

TOWARDS UNCERTAINTY QUANTIFICATION OF
PREMIXED LAMINAR FLAMES USING BAYESIAN
STATISTICS

by

Dhruvin Jasmin Naik

January 4, 2016

A thesis submitted to the
Faculty of the Graduate School of the
State University of New York at Buffalo
in partial fulfillment of the requirements for the degree of

Master of Science

Department of Mechanical and Aerospace Department

Copyright by
Dhruvin Jasmin Naik
2016

Acknowledgements

These are my acknowledgements

Contents

Acknowledgements	iii
List of Figures	viii
List of Tables	ix
Abstract	xi
1 Introduction	1
2 Mathematical Model	3
2.1 Governing Equations	3
2.2 Premixed ozone oxygen laminar flame model	4
2.3 The experimental data on laminar flame speed	4
2.4 1D oxygen ozone combustion model	5
2.5 Geometry with boundary conditions	6
2.6 Transport Model	8
2.6.1 Viscosity	8
2.6.2 Bimolecular Diffusion	8
2.6.3 Species Thermal Conductivity	9
2.6.4 Mixture Model	10
3 Finite Element Formulation	15
3.1 Weak formulation	15
3.2 Need for stability	16
3.2.1 Streamline Upwind Petrov Galerkin Method	16
3.2.2 Pressure-Stabilizing/Petrov-Galerkin (PSPG)	17
3.2.3 Stabilized Navier Stokes Equation	17
3.3 Adaptive Finite Element	17
4 Bayesian Methods	19
4.1 Review of Theory	19
4.2 Application to Problem	19
4.3 Methods of Solution	20
4.4 Software	20
5 Results	21
5.1 Estimating parameter E for reaction 3	21
5.1.1 Different surrogate sizes	21
5.1.2 Convergence Study	66

5.1.3	flamespeed Data fit	67
5.2	Estimating parameters Activation energies for reaction 2 and 3	71
5.2.1	Different surrogate sizes	71
5.2.2	Convergence Study	136
5.2.3	flamespeed Data fit	136
6	Conclusion	141
7	Appendix	143
7.1	Literature Review	143
7.2	Mathematical Model	143
7.2.1	Governing Equations	143
7.2.2	Low mach number asymptotic analysis	144
7.2.3	Asymptotic analysis	145
	Bibliography	147

List of Figures

2.1	Geometry	6
2.2	Viscocity	8
2.3	Diffusion coefficients for $O_2 - O_2$, $O_2 - O_3$, $O_3 - O_3$, $O - O$, $O - O_2$ and $O - O_3$	9
2.4	Thermal Conductivity for O , O_2 and O_3	10
2.5	Mixture Viscosity behind, inside and after the flame	11
2.6	Mixture Diffusion coefficient	12
2.7	Mixture thermal conductivity	13
5.-1	Results for sample size 1e5	24
5.-2	Results for sample size 5e5	27
5.-3	Results for sample size 1e6	30
5.-4	Results for sample size 5e6	33
5.-5	Results for sample size 1e7	36
5.-6	Results for sample size 1e5	39
5.-7	Results for sample size 5e5	42
5.-8	Results for sample size 1e6	45
5.-9	Results for sample size 5e6	48
5.-10	Results for sample size 1e7	51
5.-11	Results for sample size 1e5	54
5.-12	Results for sample size 5e5	57
5.-13	Results for sample size 1e6	60
5.-14	Results for sample size 5e6	63
5.-15	Results for sample size 1e7	66
5.-14	Convergence for surrogate size 1000	67
5.-16	Flamespeed Data fit	71
5.-16	Results for sample size 1e5	75
5.-16	Results for sample size 5e5	78
5.-16	Results for sample size 1e6	81
5.-16	Results for sample size 5e6	84
5.-16	Results for sample size 1e7	87
5.-16	Results for sample size 1e5	91
5.-16	Results for sample size 5e5	94
5.-16	Results for sample size 1e6	97
5.-16	Results for sample size 5e6	100
5.-16	Results for sample size 1e7	103
5.-16	Results for sample size 1e5	107
5.-16	Results for sample size 5e5	110
5.-16	Results for sample size 1e6	113
5.-16	Results for sample size 5e6	116
5.-16	Results for sample size 1e7	119

5.-16 Results for sample size 1e5	123
5.-16 Results for sample size 5e5	126
5.-16 Results for sample size 1e6	129
5.-16 Results for sample size 5e6	132
5.-16 Results for sample size 1e7	135
5.-15 Convergence for surrogate size 100	136
5.-17 Flamespeed Data fit	140

List of Tables

2.1 Experimental laminar flame speed given by A.G. Streng and A.V. Grosse	5
---	---

Abstract

This is my abstract

Chapter 1

Introduction

It is important to understand the dynamics of reacting flows as it is inherent in number of areas of science and engineering such as combustion, surface chemistry and reentry flows . To understand these systems in detail, it is necessary to use numerical simulations. These simulations require simultaneous numerical resolution of chemical reactions; diffusive transport and fluid mechanics. The combination of these three factors make simulations demanding of computational resources. In the deflagration regime where the burning speed also known as laminar flame speed and associated velocity scales are much smaller than the speed of sound in the fluid, the problem is acute.

For low speed combustion flows, Low Mach number asymptotics of the flow equations exploit the inherent separation of scales in such systems by analytically eliminating acoustic wave propagation entirely from the dynamics, while preserving the important compressibility effects arising from reactions and transport.

We need models that provide predictive and explanatory power. These models should be complex enough to explain the observed phenomena. Also, these models should be simple enough to generalise to future observations. Bayesian inference provides a systematic framework to infer such models from the observed data. In this work, We aim at doing uncertainty quantification for chemical parameters in the ozone oxygen combustion model. Experiments[3] have successfully measured the flamespeed for premixed ozone oxygen fuel at various concentrations starting from 17 percent ozone to 100 percent ozone. We take this data in our model and try to infer the chemical parameters that would fit this data. In bayesian approach, we take into consider our prior knowledge about the parameters and the likelihood of observing the data given the parameters. The resulting answer is the probability distribution of the parameters given the data.

A.G Streng and A.V. Grosse [3] studied the ozone oxygen flame experimentally. The stability of ozone and the rates of decomposition or explosion were investigated by Armour research foundation. Ozone was burned to oxygen from a simple burner tip in the range from 17 percent to 100 percent initial concentration of ozone in the mixture. The flame temperatures were calculated from enthalpy data and dissociation constants of oxygen using kelley's tables. The concentration of ozone was kept constant with error of 0.2 percent. Two methods were used to determine burning velocity i.e open tube method and the burning tip method. We will be using experimental burning velocity of the burning tip method. The burner tip experiments were carried out in standard apparatus, using pyrex glass aluminium tips with an inner diameter of 3 to 0.65mm. The flames were readily observed by the standard schlieren method at all concentrations above 30 mole percent. The measurements were all carried out in the laminar flow region and the reynolds number of the flow was below 2000. The initial conditions are 300K temperature and 1.0 atmosphere pressure. The results of burning

velocities of ozone flames were compared with theoretical burning velocities of Dr. Von Karman and his associates. They were found to be in close agreements.

Chapter 2

Mathematical Model

A.G Streng and A.V. Grosse [3] studied the ozone oxygen flame experimentally. The stability of ozone and the rates of decomposition or explosion were investigated by Armour research foundation. Ozone was burned to oxygen from a simple burner tip in the range from 17 percent to 100 percent initial concentration of ozone in the mixture. The flame temperatures were calculated from enthalpy data and dissociation constants of oxygen using kelley's tables. The concentration of ozone was kept constant with error of 0.2 percent. Two methods were used to determine burning velocity i.e open tube method and the burning tip method. We will be using experimental burning velocity of the burning tip method. The burner tip experiments were carried out in standard apparatus, using pyrex glass aluminium tips with an inner diameter of 3 to 0.65mm. The flames were readily observed by the standard schlieren method at all concentrations above 30 mole percent. The measurements were all carried out in the laminar flow region and the reynolds number of the flow was below 2000. The initial conditions are 300K temperature and 1.0 atmosphere pressure. The results of burning velocities of ozone flames were compared with theoretical burning velocities of Dr. Von Karman and his associates. They were found to be in close agreements.

2.1 Governing Equations

The final equation obtained by from asymptotic analysis is given below. These quantities are non dimensionalised.

$$-\nabla \cdot u = \frac{1}{p^0} \frac{dp^0}{dt} - \frac{1}{T} \frac{DT}{Dt} \quad (2.1)$$

$$\rho \frac{Du}{Dt} = -\frac{1}{M^2} \nabla p + \frac{1}{Re} \nabla \cdot \tau + \frac{1}{Fr^2} \rho g \quad (2.2)$$

$$\rho C_p \frac{DT}{Dt} = -\frac{1}{RePr} \nabla \cdot (k \nabla T) + \frac{1}{\gamma - 1} \frac{dp^0}{dt} \quad (2.3)$$

(2.4)

The species conservation equation is given as

$$\frac{\partial \rho_i}{\partial t} + \nabla \cdot (\rho_i v) = \nabla \cdot (\rho D_{ij} \nabla Y_i) + w_i \quad (2.5)$$

Where, the rate of production for species i is given by the following

Where

$$w_i = M w_i \sum_{k=1}^6 (v''_{k,i} - v'_{k,i}) B_k T^{\alpha_k} e^{\frac{-E_a}{R_u T}} \prod_{j=1}^3 \left(\frac{X_j p}{RT} \right)^{v'_{j,k}}$$

The above equation considers all reactions for all the species.

From atomic species conservation

$$\sum_{i=1}^N v_i' M_i \rightleftharpoons \sum_{i=1}^N v_i'' M_i$$

Where E_a is the activation energy, R_u is the universal gas constant, X_j is the molar concentration of the reactant j , Mw_i is the molecular weight of the reactant. $v_{j,k}'$ is the moles of reactant j in the reaction k . $v_{j,k}''$ is the number of moles of product.

The overall continuity equation, species conservation equation and energy conservation equation are solved to calculate the flame parameters. The energy equation considers that the pressure is constant throughout the reaction zone. The viscous dissipation is negligible and there is no body force work.

The Diffusion equation is given

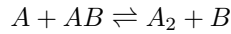
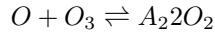
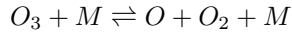
$$\frac{\partial X_k}{\partial x} = \sum_{j=1}^3 \frac{X_k X_j}{D_{jk}} (V_j - V_k) \quad (2.6)$$

Where D_{jk} is the fick's diffusion coefficient. V is the diffusion velocities.

The boundaries are defined by specifying the concentration of O_3 , O_2 at the inlet.

2.2 Premixed ozone oxygen laminar flame model

We shall use Heimerl and coffee's contemporary method for modelling combustion flame problem. A one dimensional, premixed, laminar, steady state ozone oxygen flame was considered in their theoretical model. The reason for choosing this model was due to its simplicity. The chemical reactions involved only three species



Where M represents the third body which could be either O , O_2 or O_3 .

2.3 The experimental data on laminar flame speed

To compare our results we have used the experimental data given by the A.G. streng and A.V. Grosse, They have done experiments with ozone flame in tube and ozone flame on the tip of the burner. We will be using the results of the later. They have shown that laminar flame speed or burning velocity varies with the initial concentration of the ozone. The table given below shows the burning velocity with respect to initial concentration of the ozone. We concentrate on two specific cases where initial concentration of ozone is 53 percent and 100 percent. The laminar flame speed for 53 percent is measured in the burner with inner diameter 1.3mm and rate of 7.7 cc/sec. The laminar flame speed for 100 percent ozone is taken on .66 inner diameter tip 0.66 mm and the flow rate of 8.23 cc/sec. The measured laminar flame speed is given below. Laminar flame measurements are carried out at 300K and 1 atmosphere pressure.

Table 2.1: Experimental laminar flame speed given by A.G. Streng and A.V. Grosse

Initial Concentration of O_3 ($\pm 0.2\%$)	Laminar Flame Speed (cm/s)
17	9.2
20	18.2
28	52.2
40	125
46	166
53	210
75	331
100	475

2.4 1D oxygen ozone combustion model

The governing equations are given in one dimensional and time dependent forms as follows

The Overall continuity equation is given as

$$\frac{\partial \rho}{\partial t} + \frac{\partial \rho u}{\partial x} = 0 \quad (2.7)$$

The species continuity equation

$$\rho \frac{Y_k}{\partial t} + \rho u \frac{Y_k}{\partial x} = -\frac{\partial(\rho Y_k V_k)}{\partial x} + w_k \quad (2.8)$$

Where $k = 1, 2 \text{ or } 3$ for O , O_2 or O_3 respectively.

Energy Equation

$$\rho C_p \frac{\partial T}{\partial t} + \rho u C_p \frac{T}{\partial x} = \frac{1}{\rho} \left(\lambda \frac{\partial T}{\partial x} \right) - \sum_{k=1}^N w_k \Delta h_{fk}^0 - \rho \sum_{k=1}^N C_{p,k} Y_k V_k \frac{\partial T}{\partial x} \quad (2.9)$$

This energy equations was arrived at under assumption that the pressure is constant in the reaction zone, the viscous dissipation is negligible, and there is no body force.

The Diffusion equation is given as

$$\frac{\partial X_k}{\partial x} = \sum_{j=1}^3 \frac{X_k X_j}{D_{jk}} (V_j - V_k) \quad (2.10)$$

We have considered a free flame in a tube. The boundary conditions for the totally burned end are

$$x \leftarrow \infty : \frac{\partial T}{\partial x} = \frac{\partial Y_k}{\partial x} = 0$$

In order to avoid solving the continuity equation along with the other equations, Heirmerl and coffee[1] used a langrangian coordinate ψ and a new time coordinate τ defined by

$$\psi \equiv \int_0^x \rho(x', t) dx'$$

So by definiton of ψ and by chain, we have these expressions

$$\frac{\partial \psi}{\partial x} = \rho$$

$$\begin{aligned}\frac{\partial \tau}{\partial x} &= 0 \\ \frac{\partial \tau}{\partial t} &= 1 \\ \frac{\partial \psi}{\partial t} &= (\rho u)_{x=0} - (\rho u)_x\end{aligned}$$

By integrating the overall continuity equation from 0 to x, we obtain

$$\frac{\partial d}{\partial t} \int_0^x \rho dx + [(\rho u)_x - (\rho u)_0] = 0$$

The product ρu at $x = 0$ is the eigenvalue of the problem. It is defined as

$$m_0 = (\rho u)_0$$

The energy equation in the new coordinate system becomes

$$\frac{\partial T}{\partial t} + m_0 \frac{T}{\partial \psi} = \frac{1}{C_p} \frac{d}{\partial \psi} \left(\rho \lambda \frac{\partial T}{\partial \psi} \right) - \frac{1}{\rho C_p} \sum_{k=1}^N w_k \Delta h_{fk}^0 - \frac{1}{C_p} \sum_{k=1}^N C_{p,k} Y_k V_k \frac{\partial T}{\partial \psi} \quad (2.11)$$

The eigenvalue of m_0 or S_L was determined from the steady state solution of the problem, that is

$$\frac{\partial Y_k}{\partial t} = \frac{\partial T}{\partial t} = 0$$

Under the steady state conditons,

$$\rho u = \text{constant} = \rho_\infty u_\infty = -\rho_1 S_L$$

2.5 Geometry with boundary conditions

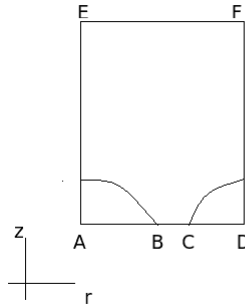


Figure 2.1: Geometry

- AB is the inlet
- BC is the thickness of the burner tube
- CD is the outside of the burner
- DE, EF is the domain of interest

- AE is the Axisymmetric line

The following assumption are made

- At the inlet, the incoming velocity has parabolic profile. i.e poissuelle flow.
- The surface chemistry at the wall of the burner is neglected.
- At the outside of the burner, the incoming air has couette flow profile.
- DE, EF are the boundaries of the domain. No change occurs after this point.

The boundary conditions are defined as follows

At the inlet (AB)

- $u_r = 0$ and $u_z = 5801.9 \text{ mm/s}$
- $C_i = 1$
- $T = 300K$
- $p = 1 \text{ atm}$

On BC

- $u_r = 0$ and $u_z = 0 \text{ mm/s}$
- $\frac{\partial C_i}{\partial r} = 0$ and $\frac{\partial C_i}{\partial z} = 0$
- $T = 300K$
- $p = 1 \text{ atm}$

On CD

- $u_r = 0$ and $u_z = 5801.9 \text{ mm/s}$
- $C_{O_2} = 21\%$
- $T = 300K$
- $p = 1 \text{ atm}$

On DF and FE

- $\frac{\partial u_r}{\partial r} = 0$ and $\frac{\partial u_z}{\partial z} = 0$
- $\frac{\partial C_i}{\partial r} = 0$ and $\frac{\partial C_i}{\partial z} = 0$
- $\frac{\partial T}{\partial r} = 0$ and $\frac{\partial T}{\partial z} = 0$
- $\frac{\partial p}{\partial r} = 0$ and $\frac{\partial p}{\partial z} = 0$

On AF

- $\frac{\partial u_r}{\partial r} = 0$
- $\frac{\partial C_i}{\partial r} = 0$
- $\frac{\partial T}{\partial r} = 0$
- $\frac{\partial p}{\partial r} = 0$

2.6 Transport Model

2.6.1 Viscosity

We have used viscosity model as derived from kinetics theory under the ideal gas assumption. The kinetic theory uses the assumption of the ideal gas law.

$$pv = nRT$$

Where p is the pressure, v is the volume, n is the number of moles of the gas, R is the universal gas constant and T is the temperature. The viscosity of the species is given by the following formula

$$\eta_s = \frac{5}{16} \sqrt{\frac{m_s k_B T}{\pi}} \frac{f_n}{\sigma_s^2 \Omega^{(2,2*)}}$$

Where m the molecular mass of the species (kg), σ is the Lennard-Jones potential diameter associated to the species (m), k_B is the Boltzmann constant, $\Omega^{(2,2*)}$ is the value of the dimensionless integrated integral from Monchick and Mason (1961). With hard sphere approximation $f_n = 1$. We have three species in our system i.e O , O_2 and O_3 . We have varied temperature from 300 K to 2700 K and plotted the viscosity V/s Temperature for all the three species. The σ values and constants for dimensionless collision number are taken from NASA CAE transport file.

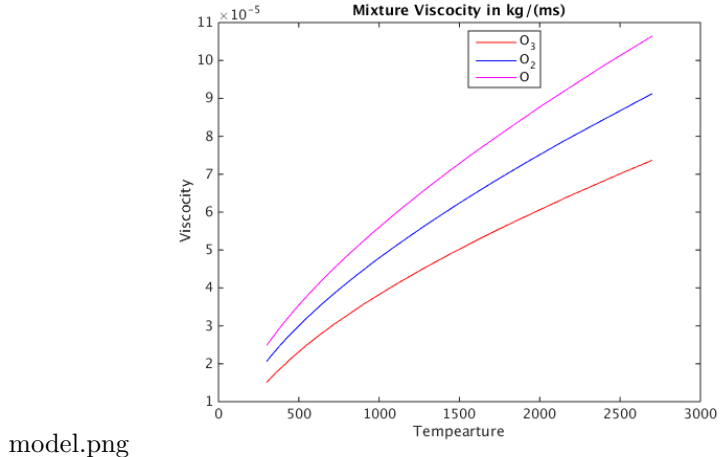


Figure 2.2: Viscosity

2.6.2 Bimolecular Diffusion

The molecular binary diffusion model is computed from kinetics theory, assuming the ideal gas hypothesis. The molecular binary diffusion coefficient ($m^2 s^{-1}$) is given by:

$$D_{ij} = \frac{3}{16} \sqrt{\frac{2k_B^3 T^3}{\pi m_{ij}}} \frac{f_n}{P \sigma_{ij}^2 \Omega^{(1,1*)}}$$

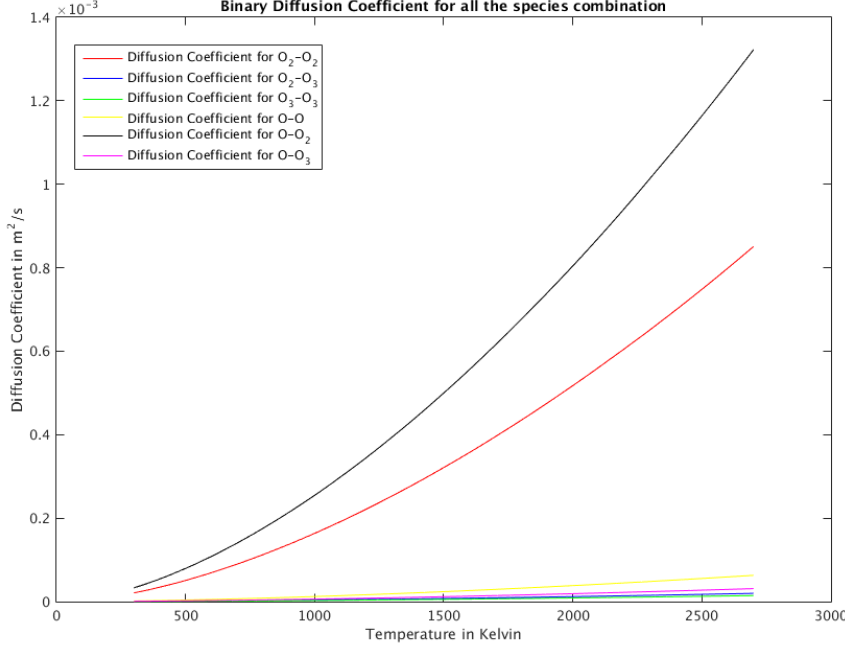
with the reduced mass

$$m_{ij} = \begin{cases} \frac{m_i m_j}{m_i + m_j} & i \neq j \\ m_i & i = j \end{cases} \quad (2.12)$$

σ_{ij} is the Lennard-Jones collision diameter between species i and j :

$$\sigma_{ij} = \frac{1}{2} (\sigma_i + \sigma_j) \xi^{-\frac{1}{6}} \quad (2.13)$$

and $\Omega^{(1,1^*)}$ the integrated collision interval, fitted from the tables given in Monchick and Mason(1961). We have varied temperature from 300 K to 2700 K and plotted the Diffusion coefficient V/s Temperature for all the combination of three species. The σ values and constants for dimensionless collision number are taken from NASA CAE transport file.



(a) Diffusion coefficient

Figure 2.3: Diffusion coefficients for $O_2 - O_2$, $O_2 - O_3$, $O_3 - O_3$, $O - O$, $O - O_2$ and $O - O_3$

2.6.3 Species Thermal Conductivity

The thermal conduction of a species i is given by

$$\begin{aligned}\lambda_i &= \lambda_i^{(\text{rot})} + \lambda_i^{(\text{trans})} + \lambda_i^{(\text{vib})} \\ \lambda_i &= \frac{\eta_i}{M_i} \left(C_{v,i}^{(\text{trans})} \lambda_i^{(\text{trans})} + C_{v,i}^{(\text{rot})} \lambda_i^{(\text{rot})} + C_{v,i}^{(\text{vib})} \lambda_i^{(\text{vib})} \right)\end{aligned}$$

with

$$\begin{aligned}\lambda_{v,i}^{(\text{vib})} &= \rho_i \frac{D_{i,i}}{\eta_i} \\ \lambda_{v,i}^{(\text{rot})} &= \rho_i \frac{D_{i,i}}{\eta_i} \left(1 + \frac{2}{\pi} \frac{A}{B} \right) \\ \lambda_{v,i}^{(\text{trans})} &= \frac{5}{2} \left(1 - \frac{2}{\pi} \frac{C_{v,i}^{(\text{rot})}}{C_{v,i}^{(\text{trans})}} \frac{A}{B} \right)\end{aligned}$$

and

$$A = \frac{5}{2} - \rho_i \frac{D_{i,i}}{\eta_i}$$

$$B = Z_{rot} + \frac{2}{\pi} \left(\frac{5}{3} \frac{C_{v,i}^{(\text{rot})}}{R} + \rho_i \frac{D_{i,i}}{\eta_i} \right)$$

the rotational relaxation number is given by

$$Z_{rot,i}(T) = Z_{rot,i}(298) \frac{F(298)}{F(T)} \quad (2.14)$$

with the function F defined as

$$F(T) = 1 + \frac{\pi^{\frac{3}{2}}}{2} \sqrt{\left(\frac{\epsilon_i}{k_B T} \right)} + \left(\frac{\pi^2}{4} + 2 \right) \left(\frac{\epsilon_i}{k_B T} \right) + \pi^{\frac{3}{2}} \left(\frac{\epsilon_i}{k_B T} \right)^{\frac{3}{2}} \quad (2.15)$$

The specific heat are given by the thermodynamic module. We have varied temperature from 300 K to 2700 K and plotted the thermal conductivity V/s Temperature for all the three species. The σ values and constants for dimensionless collision number are taken from NASA CAE transport file.

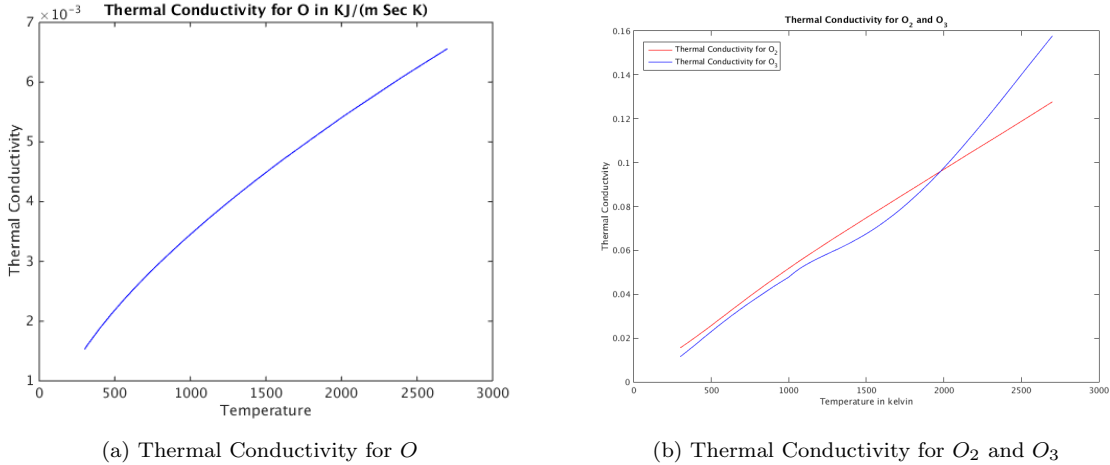


Figure 2.4: Thermal Conductivity for O , O_2 and O_3

2.6.4 Mixture Model

The Wilke formula for viscosity, independent of the viscoicity model, is

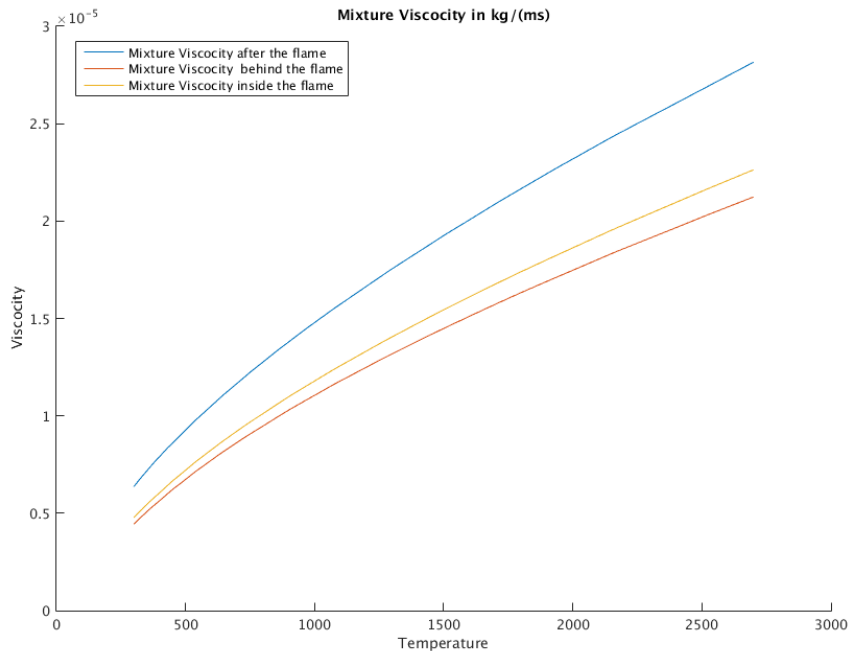
$$\eta_{\text{mixture}} = \sum_{s=1}^n \frac{x_i \eta_i}{\sum_{j=1}^n x_j \Phi_{ij}} \quad (2.16)$$

with

$$\Phi_{ij} = \frac{\left[1 + \sqrt{\frac{\eta_i}{\eta_j} \sqrt{\frac{M_j}{M_i}}} \right]^2}{\sqrt{8 \left(1 + \frac{M_i}{M_j} \right)}} \quad (2.17)$$

We have varied temperature from 300 K to 2700 K and plotted the mixture viscocity V/s Temperature for all the three species. The σ values and constants for dimensionless collision number are taken from NASA CAE transport file. We have considered three cases- behind the flame where

concentration of O_3, O_2 and O are taken to be .53, .47 and 0 respectively. Second case of the inside of the flame where concentrations are 0.5, 0.4 and 0.1 respectively. The third case is of the behind the flame where ozone and oxygen radical are absent and there will be only O_2



(a) Mixture Viscosity behind the flame

Figure 2.5: Mixture Viscosity behind, inside and after the flame

For the bimolecular diffusion model, we use:

$$D_i = \frac{1 - y_i}{\sum_{j \neq i}^n \frac{x_i}{D_{ji}}} = \frac{\sum_{j \neq i}^n x_j M_j}{M_{\text{mixture}} \sum_{j \neq i}^n \frac{x_j}{D_{ji}}} \quad (2.18)$$

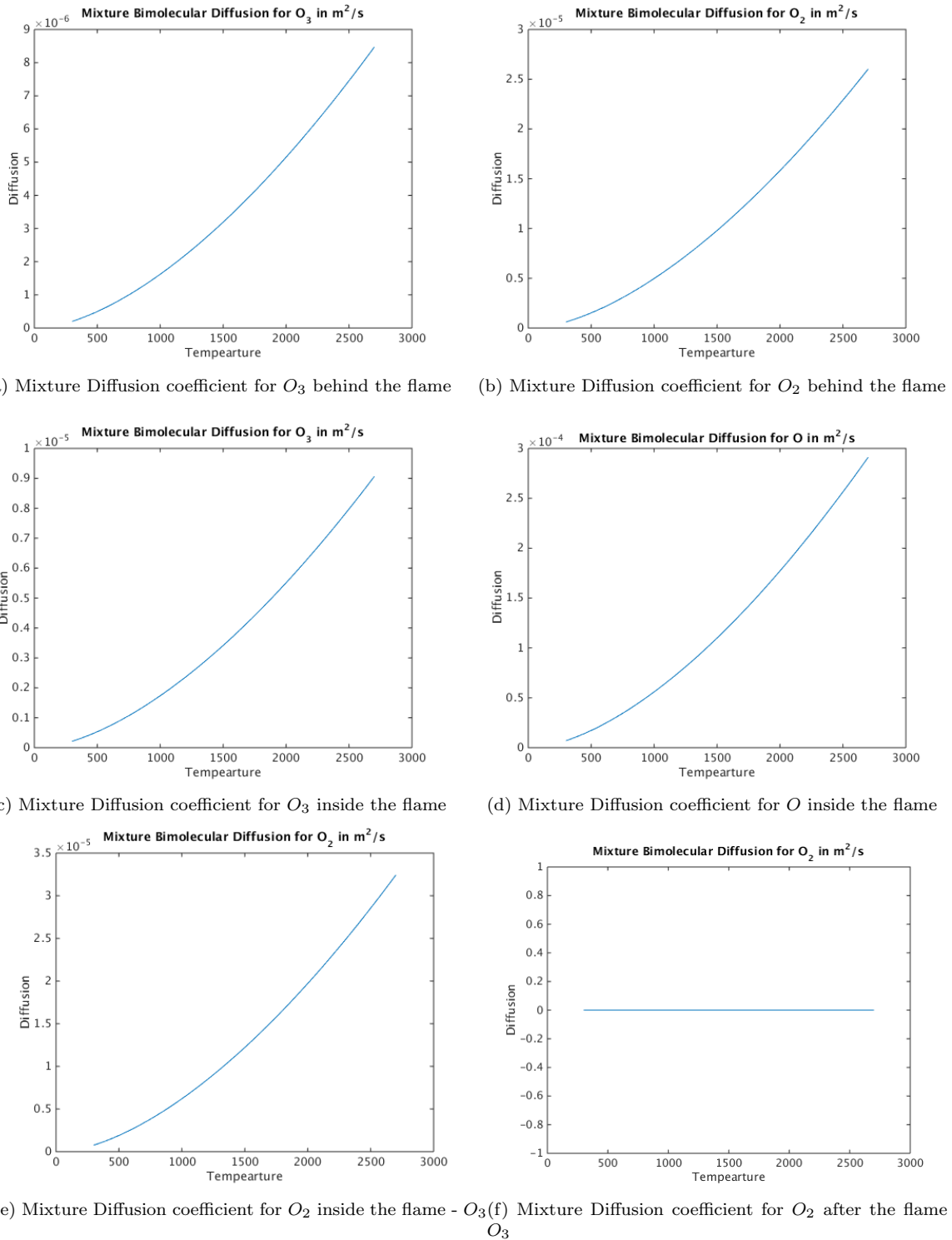


Figure 2.6: Mixture Diffusion coefficient

The thermal conductivity of the mixture is given by

$$\lambda_{\text{mixture}} = \sum_{s=1}^n \frac{x_i \lambda_i}{\sum_{j=1}^n x_j \Phi_{ij}} \quad (2.19)$$

We have varied temperature from 300 K to 2700 K and plotted the mixture thermal conductivity V/s Temperature for all the three species. The σ values and constants for dimensionless collision number are taken from NASA CAE transport file. We have considered three cases- behind the flame where concentration of O_3, O_2 and O are taken to be .53, .47 and 0 respectively. Second case of the inside of the flame where concentrations are 0.5, 0.4 and 0.1 respectively. The third case is of the behind the flame where ozone and oxygen radical are absent and there will be only O_2

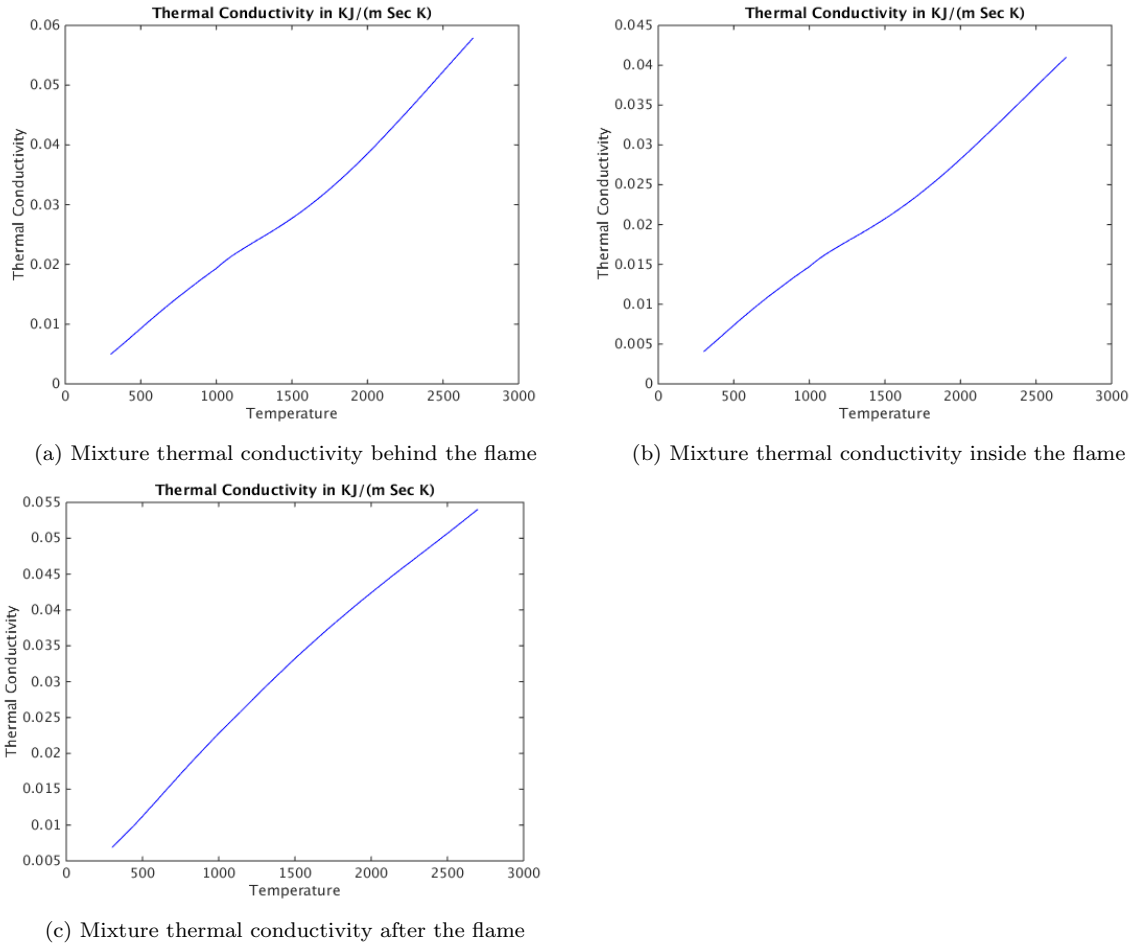


Figure 2.7: Mixture thermal conductivity

Chapter 3

Finite Element Formulation

3.1 Weak formulation

The final equation obtained by applying various thermodynamic properties are following

$$-\nabla \cdot u = \frac{1}{p^0} \frac{dp^0}{dt} - \frac{1}{T} \frac{DT}{Dt} \quad (3.1)$$

$$\rho \frac{Du}{Dt} = -\frac{1}{M^2} \nabla p + \frac{1}{Re} \nabla \cdot (\mu(\nabla u + (\nabla u)^T) - \frac{2}{3} \mu \nabla \cdot u I) + \frac{1}{Fr^2} \rho g \quad (3.2)$$

$$\rho C_p \frac{DT}{Dt} = -\frac{1}{RePr} \nabla \cdot (k \nabla T) + \frac{1}{\gamma - 1} \frac{dp^0}{dt} \quad (3.3)$$

(3.4)

The 2D finite element weak form is given as

$$\begin{aligned} \int_0^L \int_0^L \rho \frac{\partial u^h}{\partial t} \psi + \int_0^L \int_0^L (\rho u^h \cdot \nabla u^h) \psi &= \int_0^L \int_0^L -\frac{1}{M^2} (\nabla p^h) \phi + \int_0^L \int_0^L \frac{1}{Re} (\nabla \cdot \tau^h) \psi + \\ &\quad \int_0^L \int_0^L \frac{1}{Fr^2} (\rho g) \psi \\ \int_0^L \int_0^L \rho C_p \frac{\partial T^h}{\partial t} \varphi + \int_0^L \int_0^L \rho C_p (u^h \cdot \nabla T^h) \varphi &= \int_0^L \int_0^L -\frac{1}{RePr} (\nabla \cdot k \nabla T^h) \varphi + \int_0^L \int_0^L \frac{1}{\gamma - 1} \frac{dp^h}{dt} \phi \end{aligned}$$

Integrating by parts and applying boundary conditions

$$\begin{aligned} \int_0^L \int_0^L \rho \dot{u}^h \psi_i \psi_j + \int_0^L \int_0^L \rho u^h \cdot \nabla u^h \psi_i &= \int_0^L \int_0^L -\frac{1}{M^2} \nabla p^h \phi_i - \int_0^L \int_0^L \frac{1}{Re} \tau^h \nabla \psi + [\tau \psi]_0^L + \\ &\quad \int_0^L \int_0^L \frac{1}{Fr^2} \rho g \psi \\ \int_0^L \int_0^L \rho C_p \dot{T}^h \varphi_i \varphi_j + \int_0^L \int_0^L \rho C_p u^h \cdot \nabla T \varphi_i &= \int_0^L \int_0^L + \frac{1}{RePr} (k \nabla T^h) \nabla \varphi - \frac{1}{RePr} [k \nabla T^h \varphi]_0^L \\ &\quad + \int_0^L \int_0^L \frac{1}{\gamma - 1} \frac{dp^h}{dt} \phi \end{aligned}$$

3.2 Need for stability

Using numerical methods in a straightforward way for the approximation of arbitrary differential equations may cause severe problems. There are Oscillations, locking, singular matrices and other problems in the result in certain concrete problem. Thus, stabilization is needed. To obtain satisfactory approximations stabilization may be needed. The matrix of the advective term is non-symmetric (non-self adjointness of the convective operator) and the best approximation property is lost . As a result Bubnov-Galerkin methods applied to these problems are far from optimal and show spurious oscillations in the solutions, worsening with growing convection-domination.

To characterize the relative importance of convective and diffusive effects in a given flow problem, it is useful to introduce the mesh Peclet number.

$$Pe = \frac{ah}{2\nu}$$

which expresses the ratio of convective to diffusive transport. The Galerkin solution is corrupted by non-physical oscillations when the Peclet number is larger than one. The Galerkin method loses its best approximation property when the non-symmetric convection operator dominates the diffusion operator in the transport equation, and consequently spurious node-to-node oscillations appear. All stabilization schemes applied are Petrov-Galerkin approaches. They all add perturbations to the original Bubnov-Galerkin weak form. These perturbations are formulated in terms of modifications of the Bubnov-Galerkin test functions. They are multiplied with the residuals of the differential equations and thereby ensure consistency. Additionally, a stabilization parameter ξ weights the influence of the added stabilization terms.

3.2.1 Streamline Upwind Petrov Galerkin Method

To ensure that the solution of the differential equation is also a solution of the weak form, it is necessary to stabilize the convective term in a consistent manner. To accomplish this an extra term over the element interiors is added to the Galerkin weak form. This term has to be a function of the residual of the differential equation or else the equation will not be consistent. It introduces a certain amount of artificial diffusion in streamline direction only. The latter aspect ensures that no diffusion perpendicular to the flow direction is introduced, which was the reason for excessive over diffusion in other methods.

Stabilization through a product of a perturbation and the residual is a fundamental aspect of successful stabilization schemes and is realized in all stabilization method applied here. The following term is added to the galerkin weak form of the differential equation.

$$\sum_e \int_{\Omega^e} P(w)\xi R(u)d\Omega$$

Where $P(w)$ is a certain operator applied to the test function, ξ is the stabilization parameter (also called intrinsic time), and $R(u)$ is the residual of the differential equation. The stabilization techniques are characterized by the definition of $P(w)$

The SUPG stabilization technique is defined by taking

$$P(w) = a \cdot \nabla w$$

where a is the convection velocity. w is the test function. This corresponds to the perturbation of the test function. The space of the test functions does not coincide with the space of the interpolation functions, hence it is called as PetrovGalerkin formulation.

For simple convection diffusion equation $\tau = \frac{\bar{v}}{\|a\|^2}$. For 1D $\bar{v} = \frac{\beta ah}{2}$ and $\beta = \coth(Re) - \frac{1}{Re}$

3.2.2 Pressure-Stabilizing/Petrov-Galerkin (PSPG)

In mixed convection-dominated problems, such as the incompressible Navier-Stokes equations with high Reynolds-numbers, SUPG and PSPG (called herein SUPG/PSPG) stabilization have to be applied to obtain satisfactory results. It should also be mentioned that the PSPG stabilization parameter does not necessarily have to be identical with the SUPG stabilization parameter

The terms associated with parameter ξ_{pspg} (pressure-stabilizing/Petrov-Galerkin) allow the use of mixed elements with equal-order interpolations for the velocity and pressure. All stabilization terms are weighted residuals, therefore ensuring the consistency of the formulation. The following term is added to the galerkin weak form of the differential equation.

$$\sum_e \int_{\Omega^e} \nabla \phi \xi_{pspg} R(u) d\Omega$$

3.2.3 Stabilized Navier Stokes Equation

From the stabilization discussions we can now write the stabilized form of Navier stokes equation. The Residual of momentum and energy equation are given as follows

$$\begin{aligned} R1(u) &= \rho \frac{Du^h}{Dt} + \frac{1}{M^2} \nabla p^h - \frac{1}{Re} \nabla \cdot (\mu^* (\nabla u^h + (\nabla u^h)^T)) - \frac{2}{3} \mu^h \nabla \cdot u^h I - \frac{1}{Fr^2} \rho g \\ R2(T) &= \rho C_p \frac{DT^h}{Dt} + \frac{1}{Re Pr} \nabla \cdot (k \nabla T^h) - \frac{1}{\gamma - 1} \frac{dp^h}{dt} \end{aligned}$$

Now adding the pressure stabilization and convection stabilization to momentum and energy equations we get the following expressions

$$\begin{aligned} \int_0^L \int_0^L \rho \dot{u}^h \psi_i \psi_j + \int_0^L \int_0^L \rho u^h \cdot \nabla u^h \psi_i + \int_0^L \int_0^L \frac{1}{M^2} \nabla p^h \phi_i + \int_0^L \int_0^L \frac{1}{Re} \tau^h \nabla \psi + \\ - \int_0^L \int_0^L \frac{1}{Fr^2} \rho g \psi + \sum_e \int_{\Omega^e} P(\psi) \xi R1(u) d\Omega + \sum_e \int_{\Omega^e} \nabla \phi \xi_{pspg} R1(u) d\Omega &= [\tau \psi]_0^L \\ \int_0^L \int_0^L \rho C_p \dot{T}^h \varphi_i \varphi_j + \int_0^L \int_0^L \rho C_p u^h \cdot \nabla T \varphi_i - \int_0^L \int_0^L \frac{1}{Re Pr} (k \nabla T^h) \nabla \varphi - \\ \int_0^L \int_0^L \frac{1}{\gamma - 1} \frac{dp^h}{dt} \phi + \sum_e \int_{\Omega^e} S(\varphi) \xi R2(T) d\Omega + \sum_e \int_{\Omega^e} \nabla \varphi \xi_{pspg} R2(T) d\Omega &= - \frac{1}{Re Pr} [k \nabla T^h \varphi]_0^L \end{aligned}$$

3.3 Adaptive Finite Element

Chapter 4

Bayesian Methods

4.1 Review of Theory

The growth of computations technology has enabled uncertainty quantification for complex engineering problems. If we incorporate data into a model, significant reduction in uncertainty of model prediction is achieved and hence a very important step in many application. Bayes' formula provides the natural way to infer the necessary uncertainty information. Mathematical model governing physical phenomenon often include parameters that need to be determined from experiments by measuring them with the help of devices. The measured values of the parameters have uncertainty in them depending upon the assumptions, noise levels, models and prior knowledge. To estimate the correct values of the parameters we should make assumptions about the noise levels, models and prior knowledge. Let y be the data which is dependent on independent parameter u .

$$y = G(u)$$

The solution of the inverse problem is the probability distribution of u given y , denoted by $P(u|y)$. The Bayes' formula is given as

$$P(u|y) = \frac{P(u)P(y|u)}{P(y)}$$

Where $P(u)$ is the prior probability distribution of u . $P(y|u)$ is the likelihood of y given u . $P(y)$ is the scaling factor. In Bayesian approach, u is treated as random variable with some specified prior probability distribution that incorporates any prior knowledge about u that we believe is true and is independent of the measured data y . The result is the posterior probability distribution of u conditional on y .

4.2 Application to Problem

We have the experimental data for flamespeed from Streng [3]. Our goal is to do uncertainty quantification for chemical parameters namely Activation Energy E and pre exponential factor A for all the three reactions involved in the ozone oxygen combustion model. We first did sensitivity analysis for flamespeed based on all the chemical parameters. We found that the activation energy and the pre exponential factor for the first reaction of the mechanism did not have significant effect

on the flamespeed. Hence moving further, we would not consider these parameters as uncertain. The remaining 4 parameters are considered uncertain.

Let us denote flamespeed by V_f , the activation energy for second and third reaction for mechanism as E_2 and E_3 respectively and the pre exponential factor as A_2 and A_3 respectively. We model our uncertain parameter as continuous random variable. By bayes theorem, the mathematical equation for uncertainty quantification for chemical parameters is written as follows.

$$P(E_1, E_2, A_2, A_3 | V_f) = \frac{P(V_f | E_1, E_2, A_2, A_3) P(E_1) * P(E_2) * P(A_2) * P(A_3)}{\int_x P(V_f | E_1, E_2, A_2, A_3) * P(E_1) * P(E_2) * P(A_2) * P(A_3)}$$

$P(E_1, E_2, A_2, A_3 | V_f)$ is the resulting posterior distribution for the uncertain parameters in the model. $P(V_f | E_1, E_2, A_2, A_3)$ is called the likelihood distribution of the data given the parameters and $P(E_1), P(E_2), P(A_2), P(A_3)$ are the prior distribution of the parameter.

In our model, we have selected uniform priors for the parameter. This means that given the range of parameter i.e from a to b, the probability of selecting a parameter is same for all the values in this range. The continuous pdf is given as

$$f(x) = \frac{1}{b - a}$$

We have selected likelihood as gaussian with the experimental data as mean and standard deviation of 10 percent of the data. The resulting pdf is given as

$$f(x) = \frac{1}{\sigma\sqrt{2\pi}} e^{-(x-\mu)^2/2\sigma^2}$$

$\int_x P(V_f | E_1, E_2, A_2, A_3) * P(E_1) * P(E_2) * P(A_2) * P(A_3)$ is the scaling factor.

4.3 Methods of Solution

We use markov chain monte carlo method for estimating the posterior distribution by simulations. Markov chain is formed from successive random selections, the stationary distribution of which is the target distribution. In the MetropolisHastings algorithm, samples are selected from an arbitrary proposal distribution and are retained or not according to an acceptance rule.

4.4 Software

Chapter 5

Results

5.1 Estimating parameter E for reaction 3

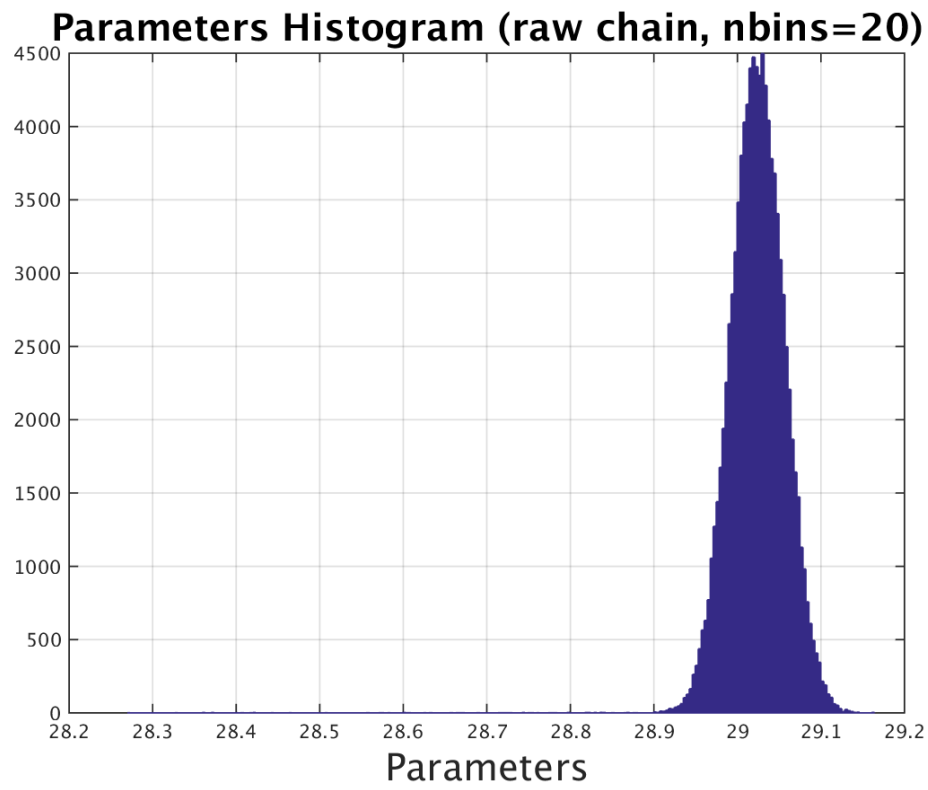
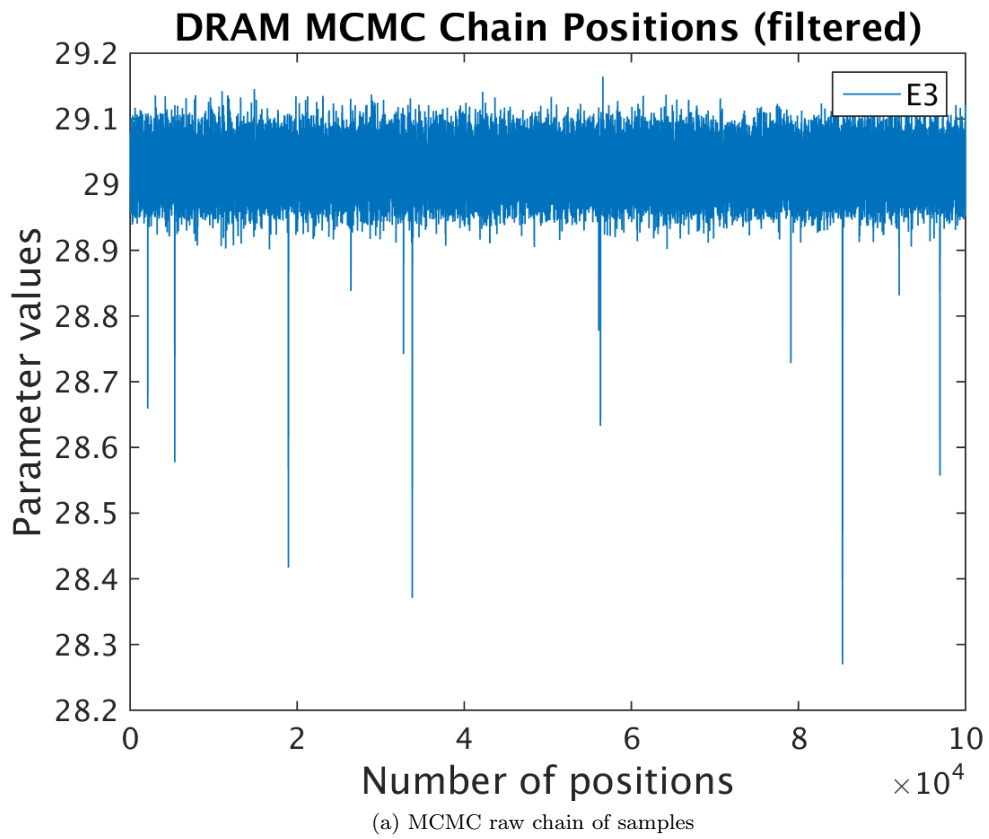
The results displayed in this section are for the uncertainty involved in the calculation of flamespeed depending only on one parameter i.e the activation energy for the fall off reaction in the ozone mechanism. The percentage of ozone is taken as 20,28,40,46,53,75 and 100 percent according to the experimental data available to us from Streng[3].The results are displayed in three section. In first section, for constant surrogate size, the number of samples are changes. In the second part of the results, convergence study is done for all samples with surrogate size 1000. In third section, we ensure that samples of the parameter which we are drawing are fitting the flamespeed values of the experiment. Also for varying size the map point of the resulting pdf does not change greatly. The surrogates for individual concentrations are constructed using linear interpolation function. The initial guess for the map point is calculated using nelder mead optimization technique. After supplying initial guess over large domain it is found that the map point is the same no matter where we start our guess.

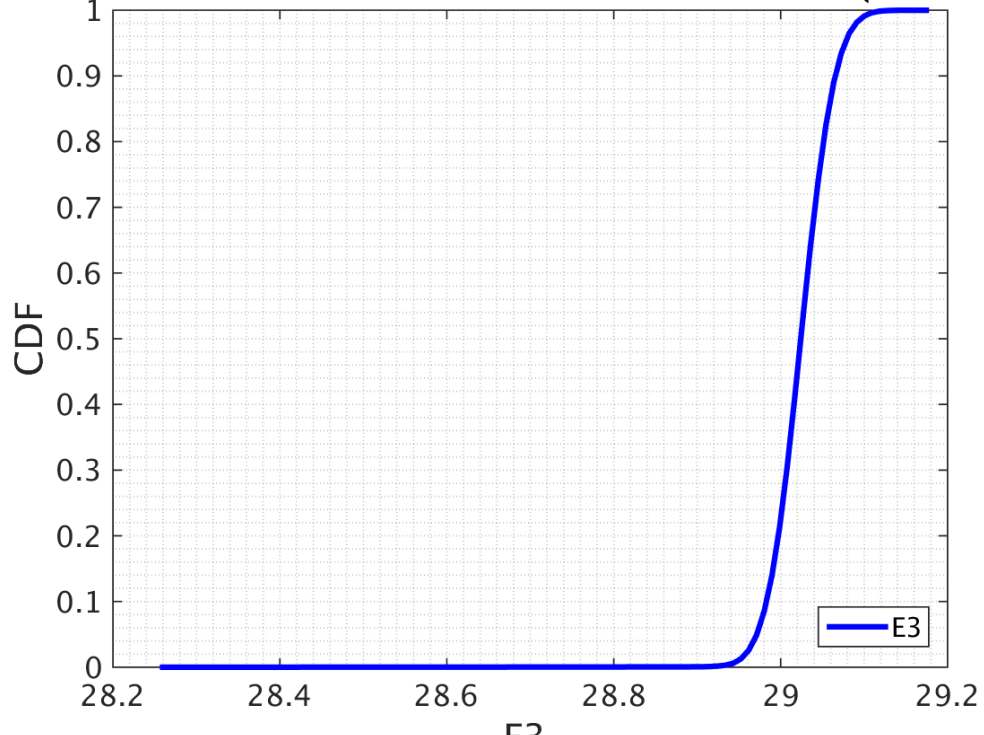
5.1.1 Different surrogate sizes

Here the surrogate size is defined as *samplesize * 1* vector. The flamespeed is calculated for given samples in the domain (-10 to 40). Other values are calculated as linear interpolation of these 1000 points. In this analysis, raw chain size of $1e5$, $5e5$, $1e6$, $5e6$ and $1e7$ is taken.

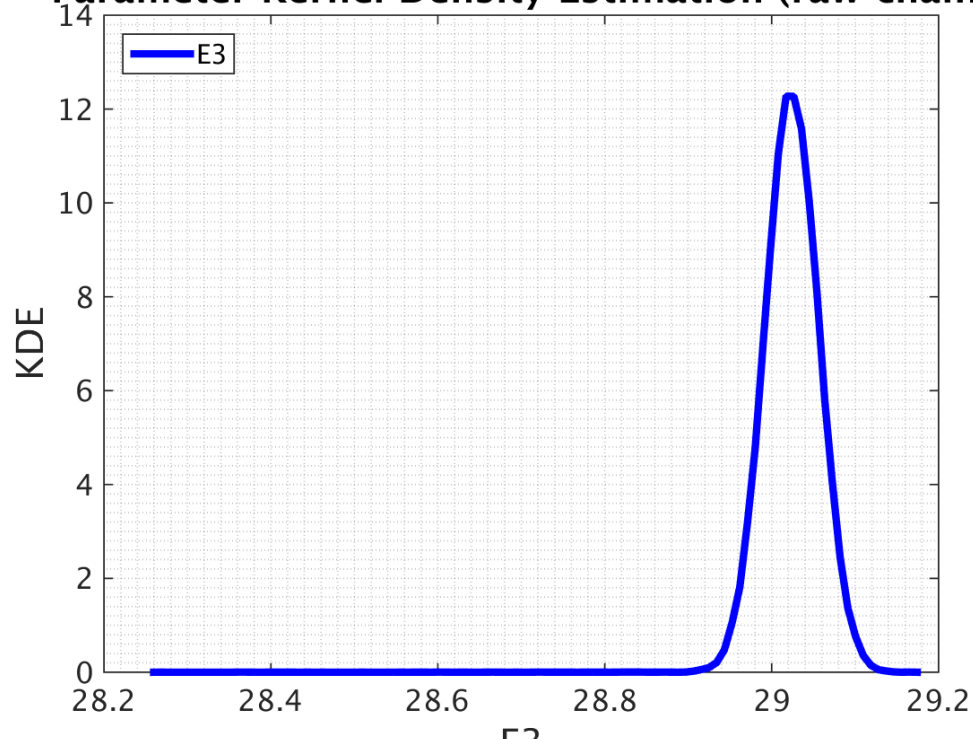
Sample size (Surrogate size) 100

In this section we calculated flamespeed values for 100 different points in the domain and the remaining values are linear combination of these 100 points. The results below are for sample size $1e5$, $5e5$, $1e6$, $5e6$ and $1e7$.



Parameter Cumulative Distribution Function (raw chair)

(c) Cummulative Density Funtion

Parameter Kernel Density Estimation (raw chain)(d) KDE
23

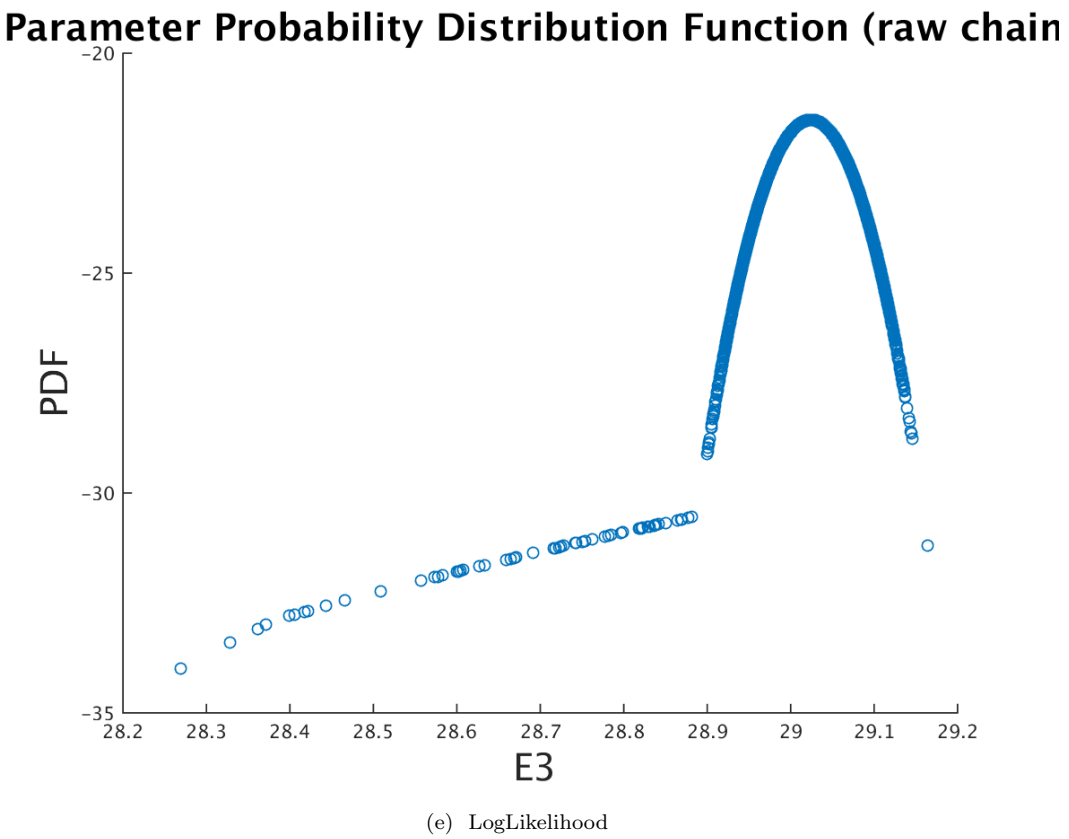
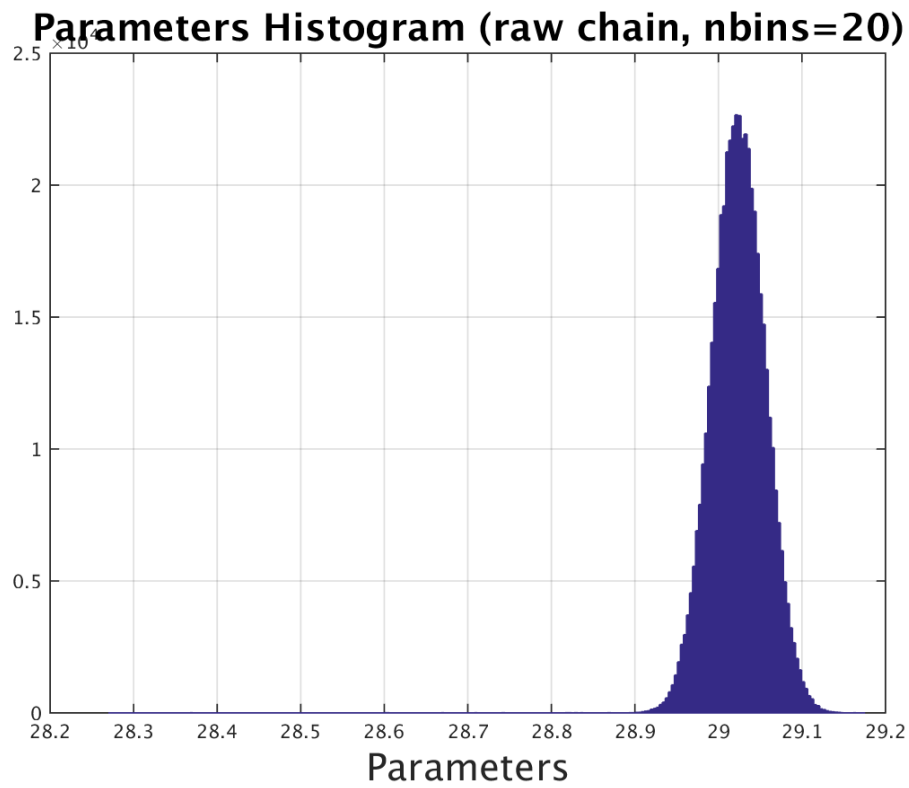
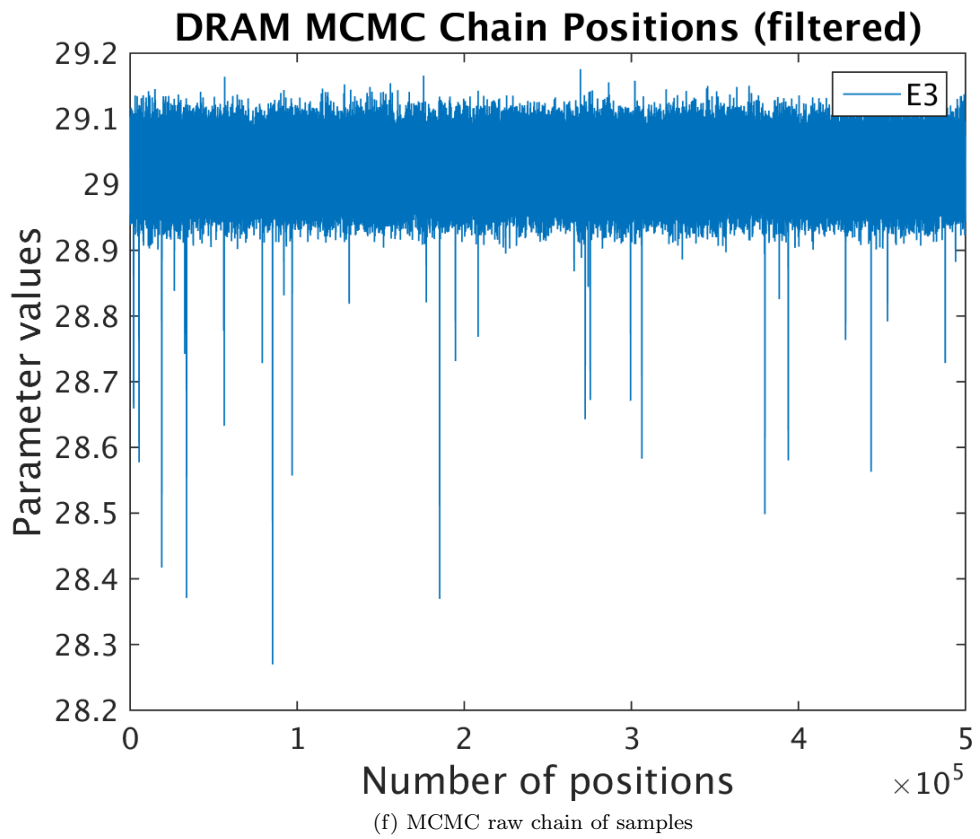
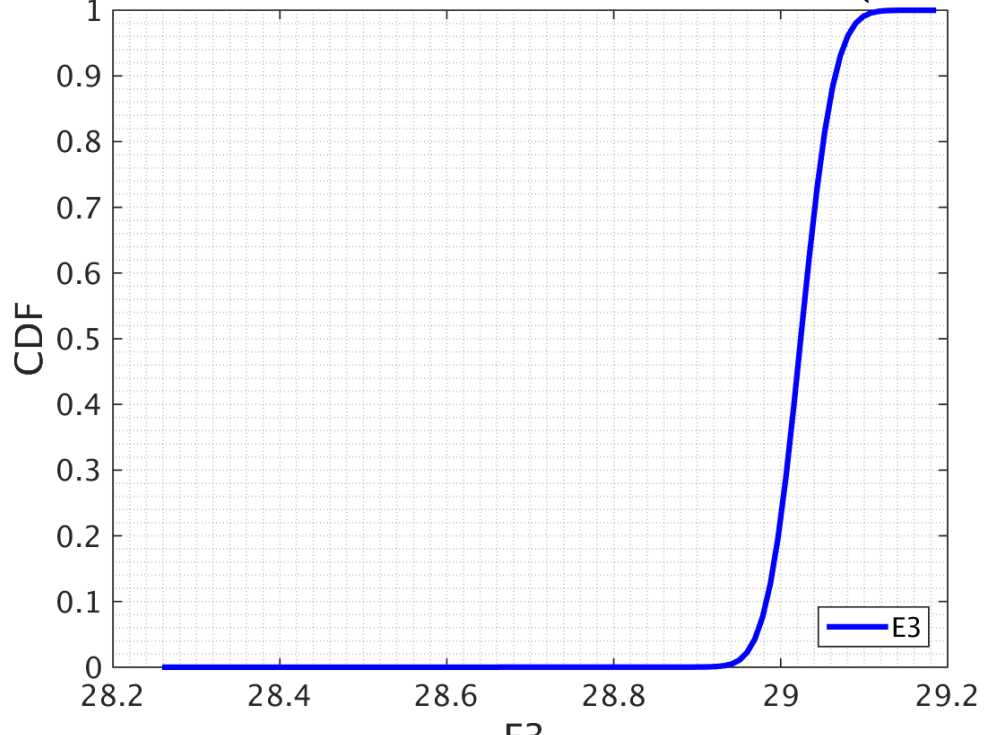
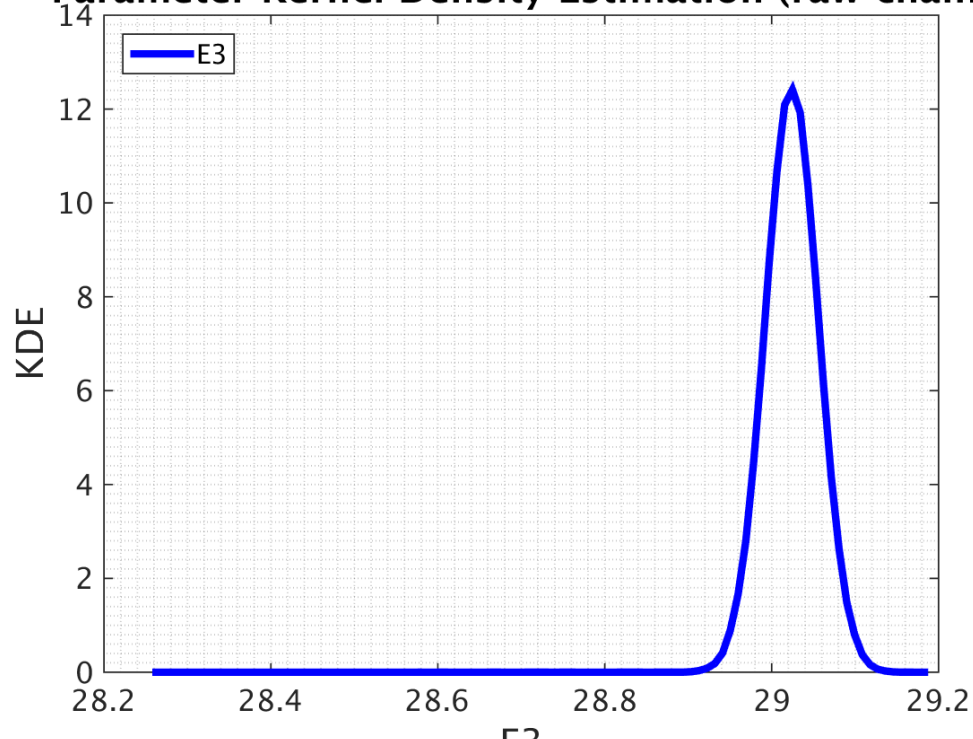


Figure 5.-1: Results for sample size 1e5



Parameter Cumulative Distribution Function (raw chair)

(h) Cummulative Density Funtion

Parameter Kernel Density Estimation (raw chain)(i) KDE
26

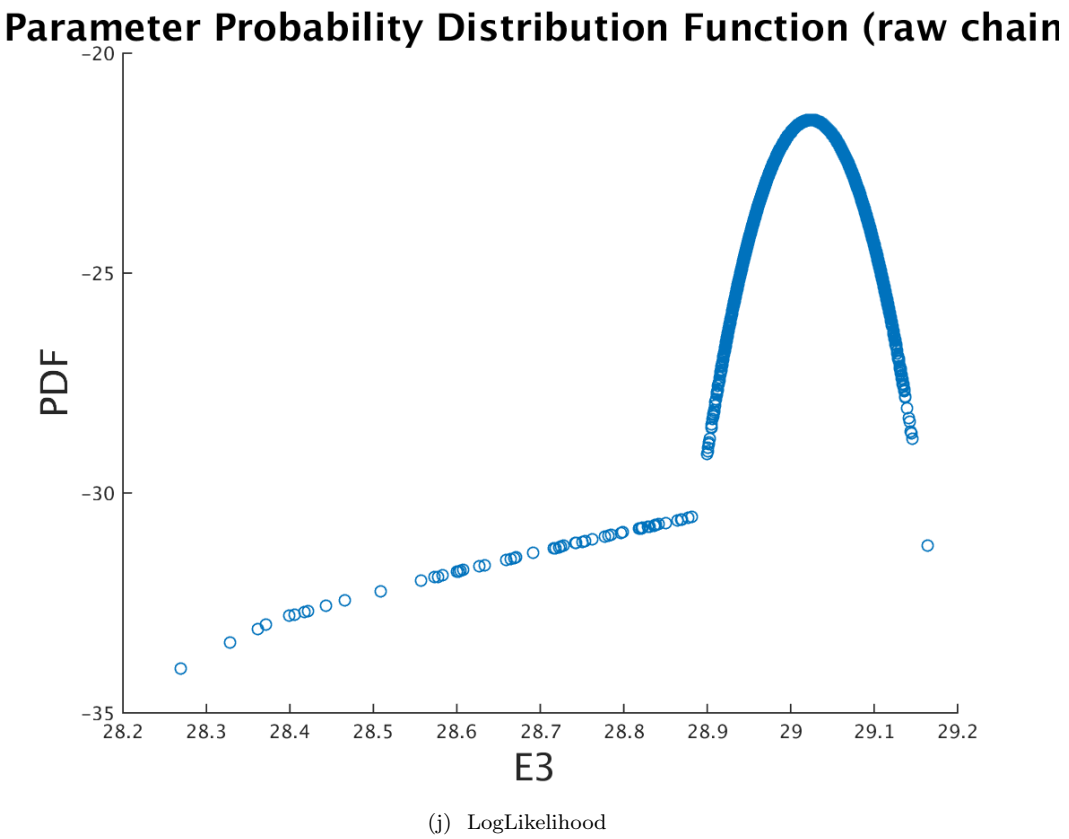
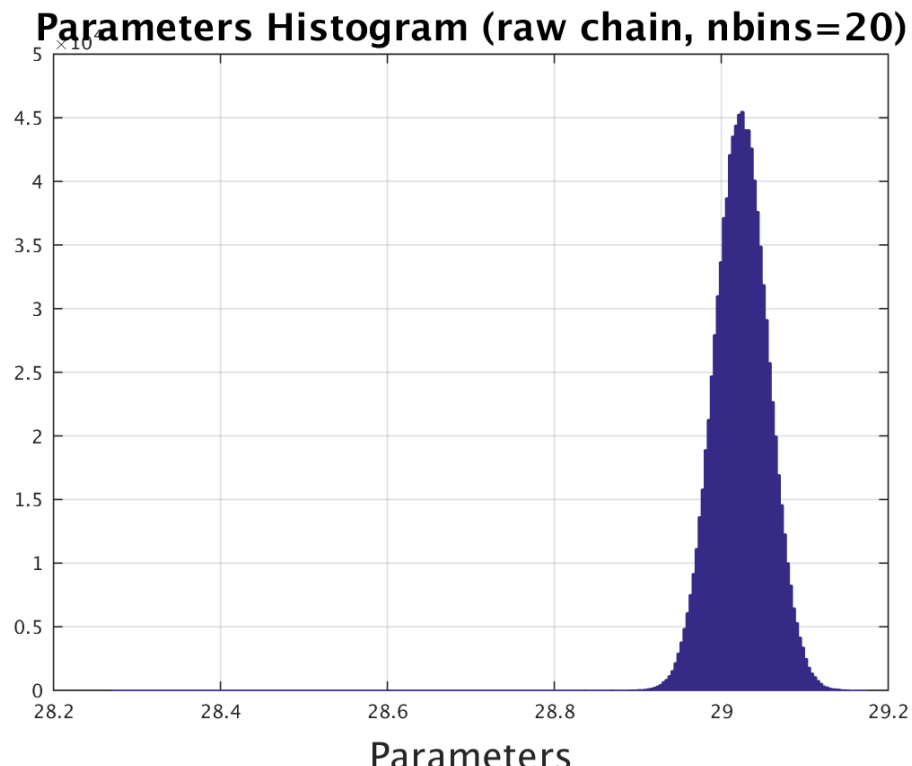
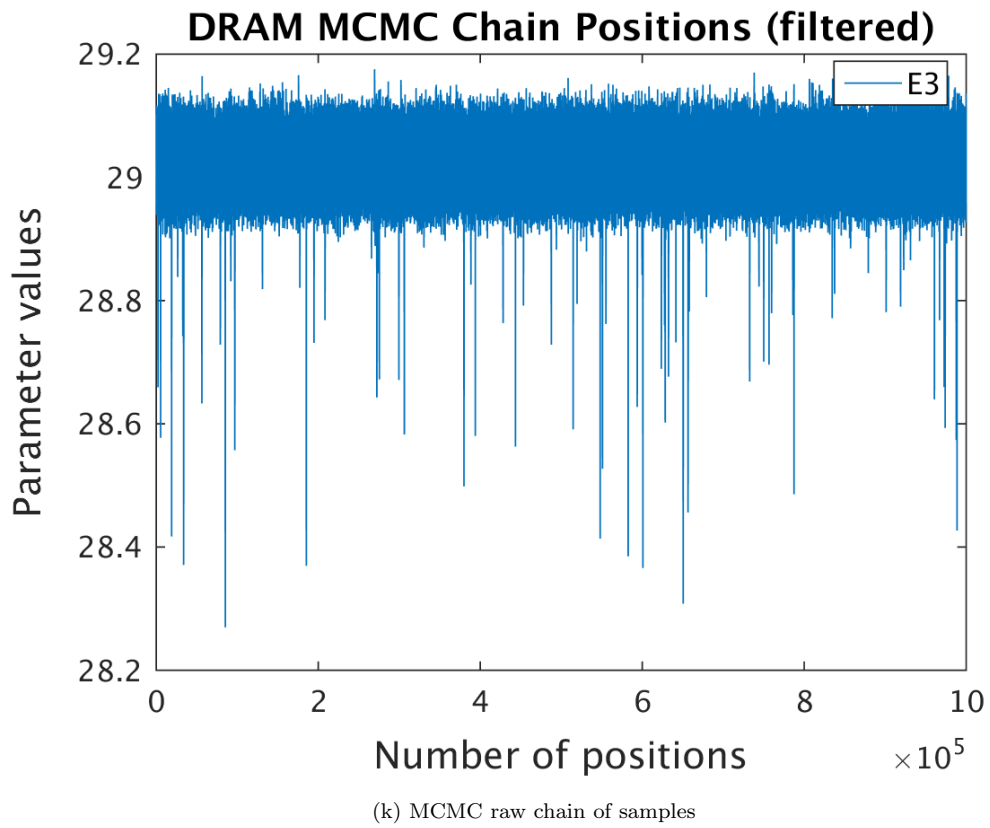
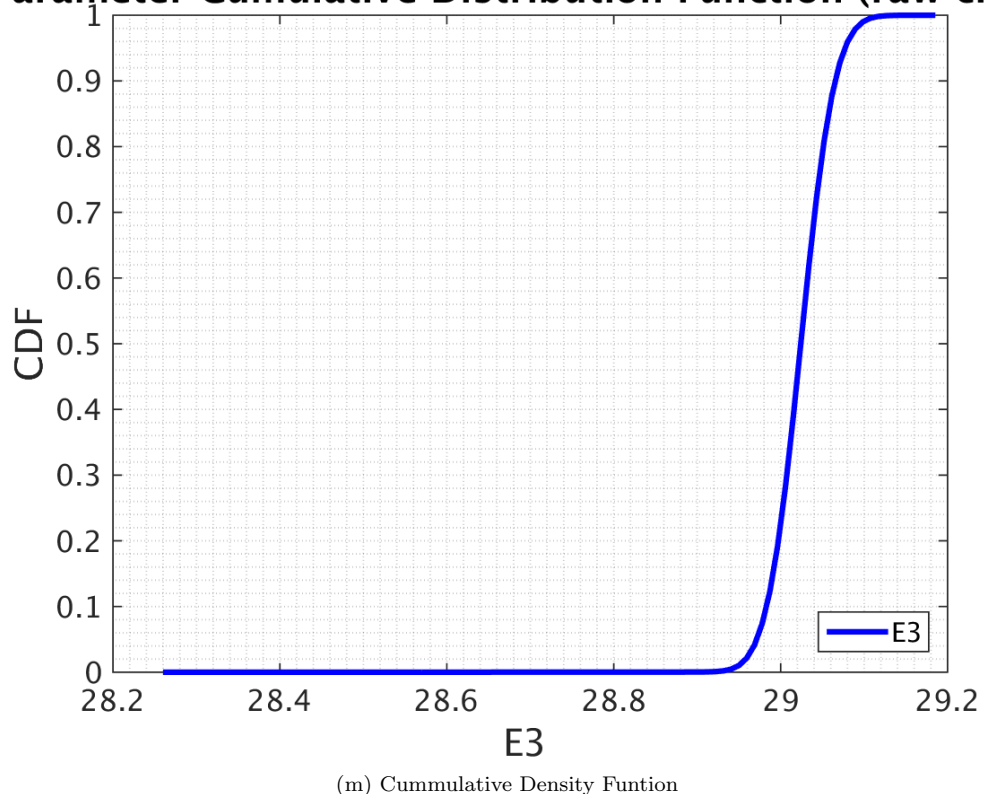
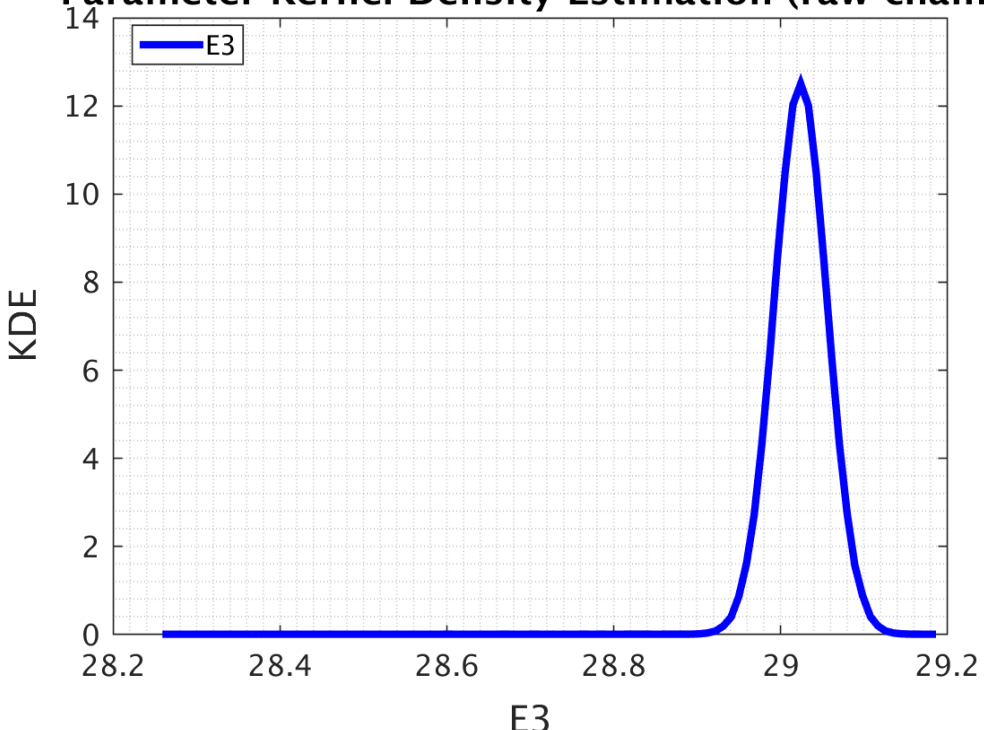


Figure 5.-2: Results for sample size 5e5



Parameter Cumulative Distribution Function (raw chair)**Parameter Kernel Density Estimation (raw chain)**

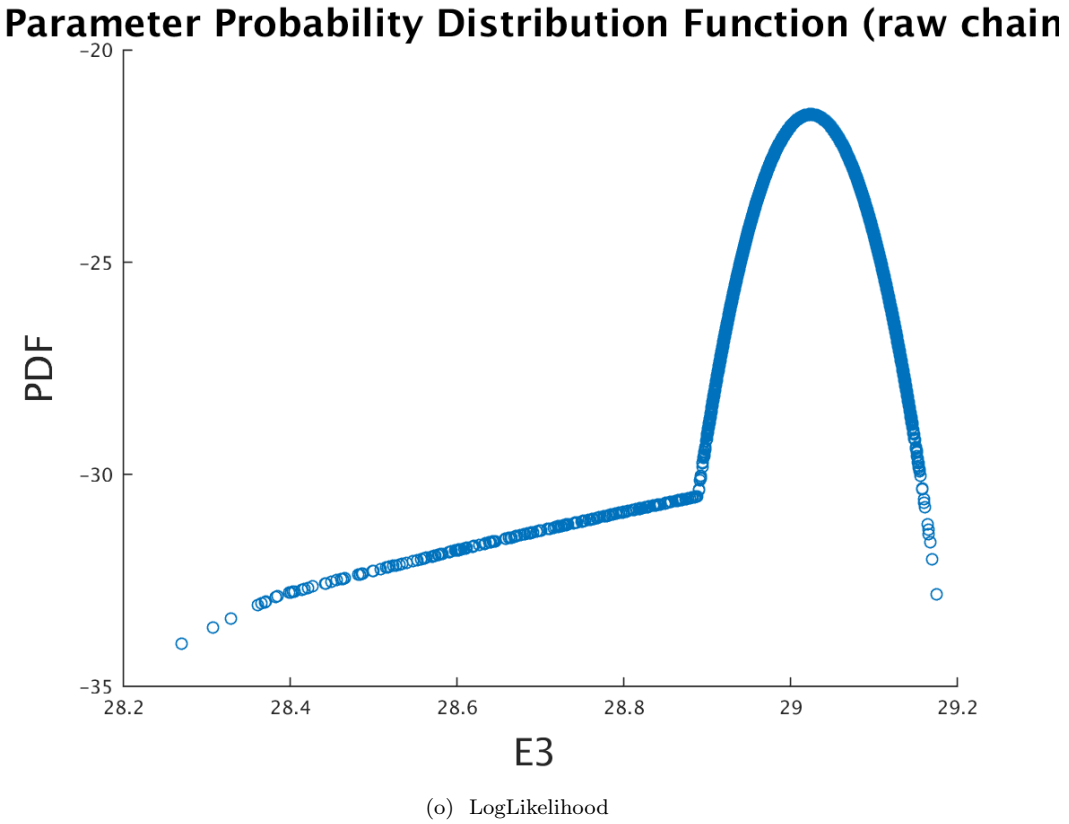
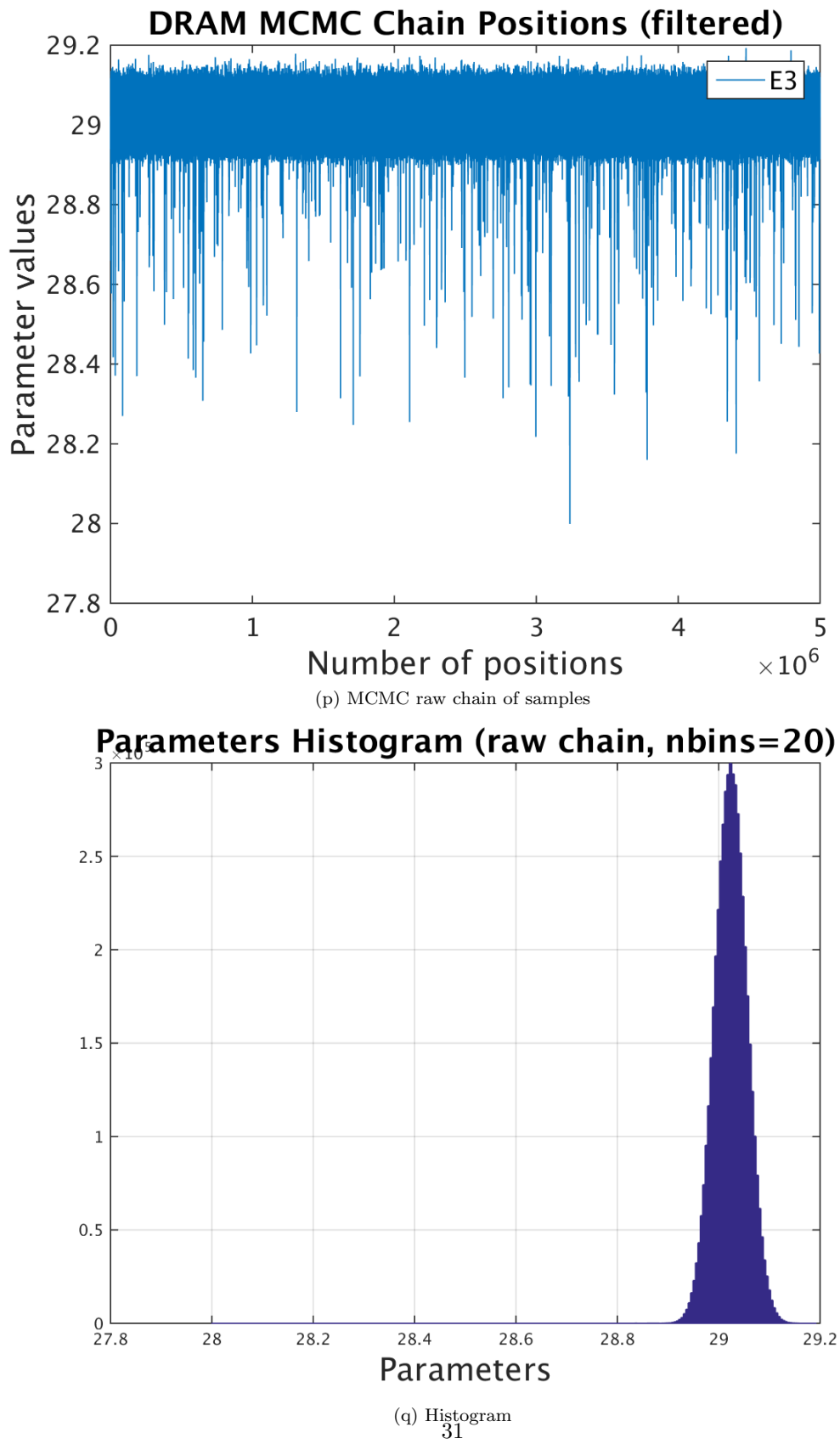
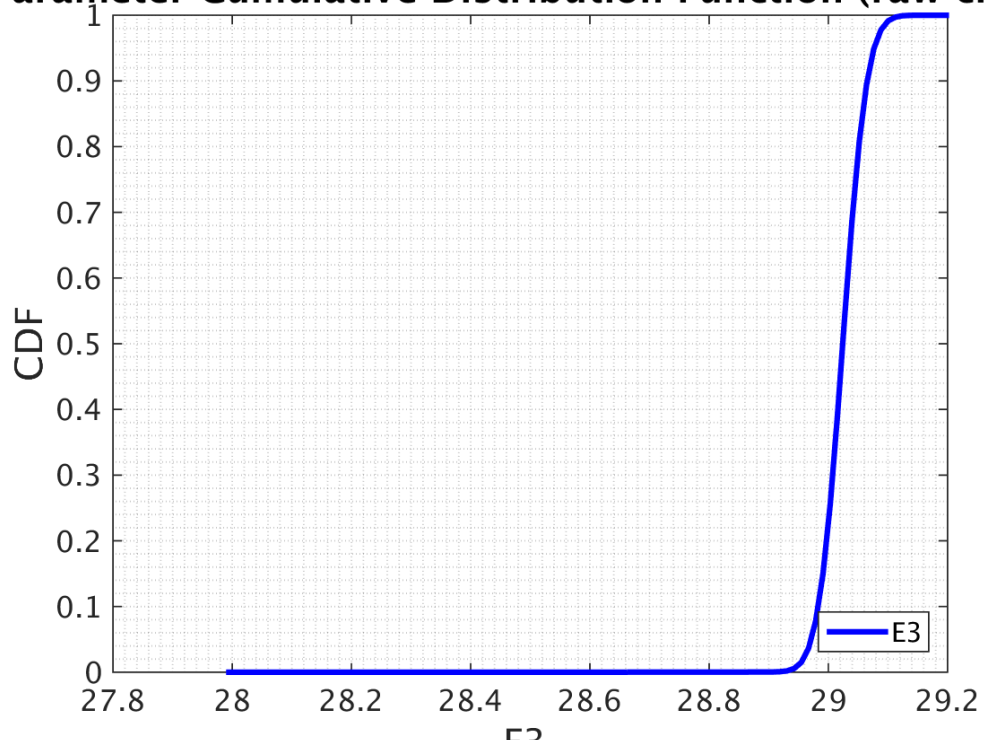
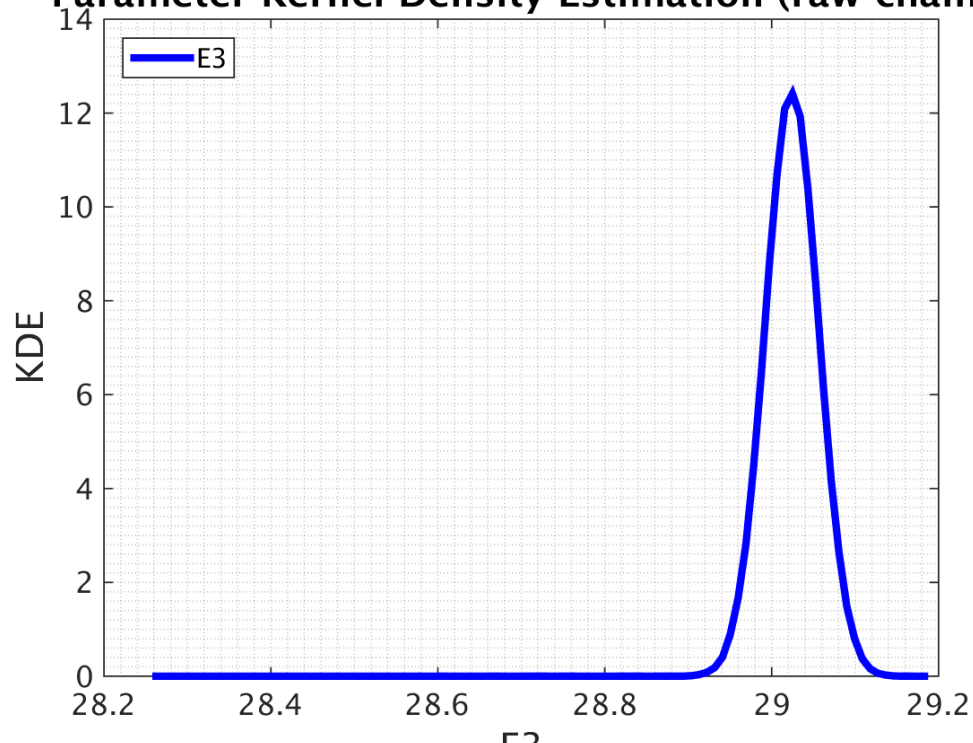


Figure 5.-3: Results for sample size 1e6



Parameter Cumulative Distribution Function (raw chair)

(r) Cummulative Density Funtion

Parameter Kernel Density Estimation (raw chain)(s) KDE
32

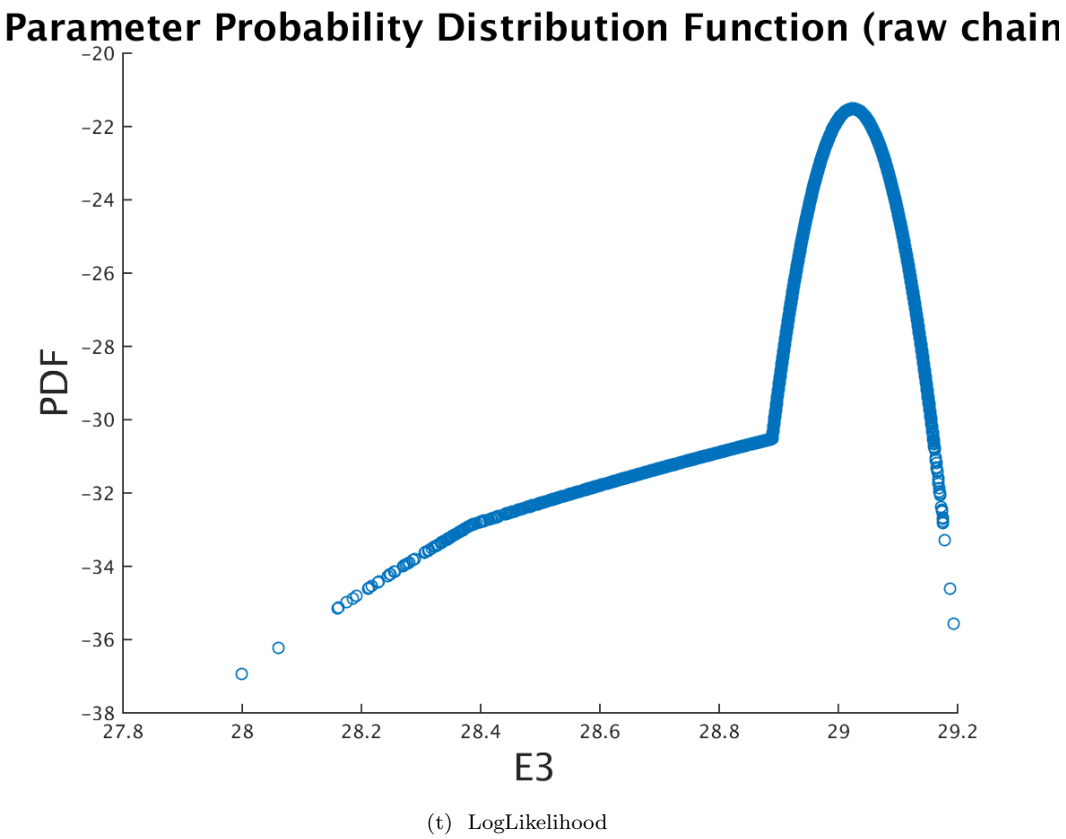
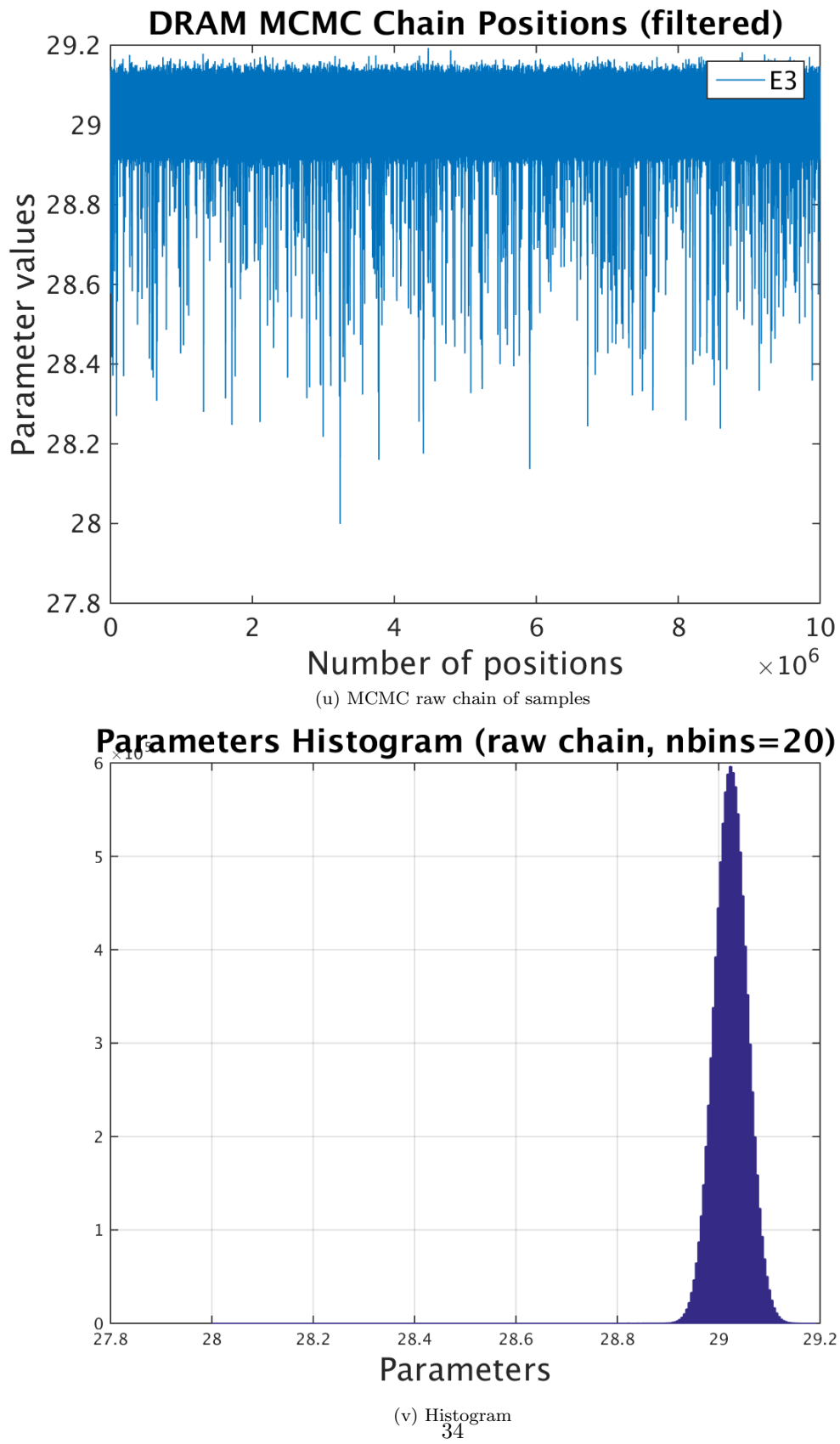
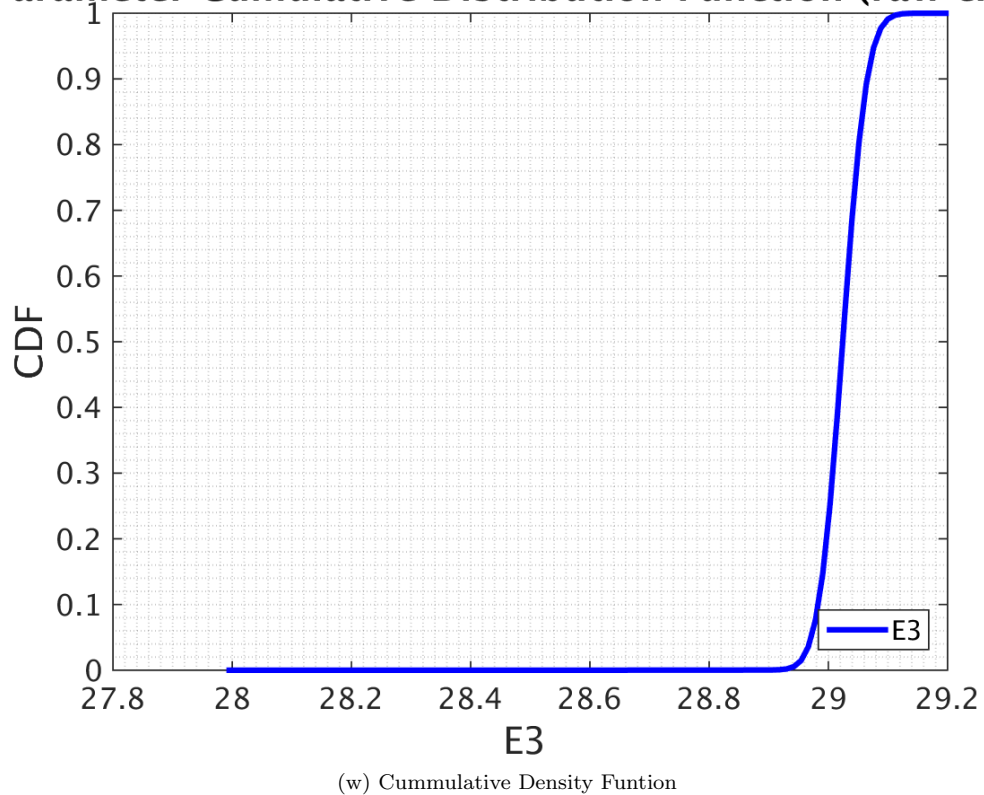
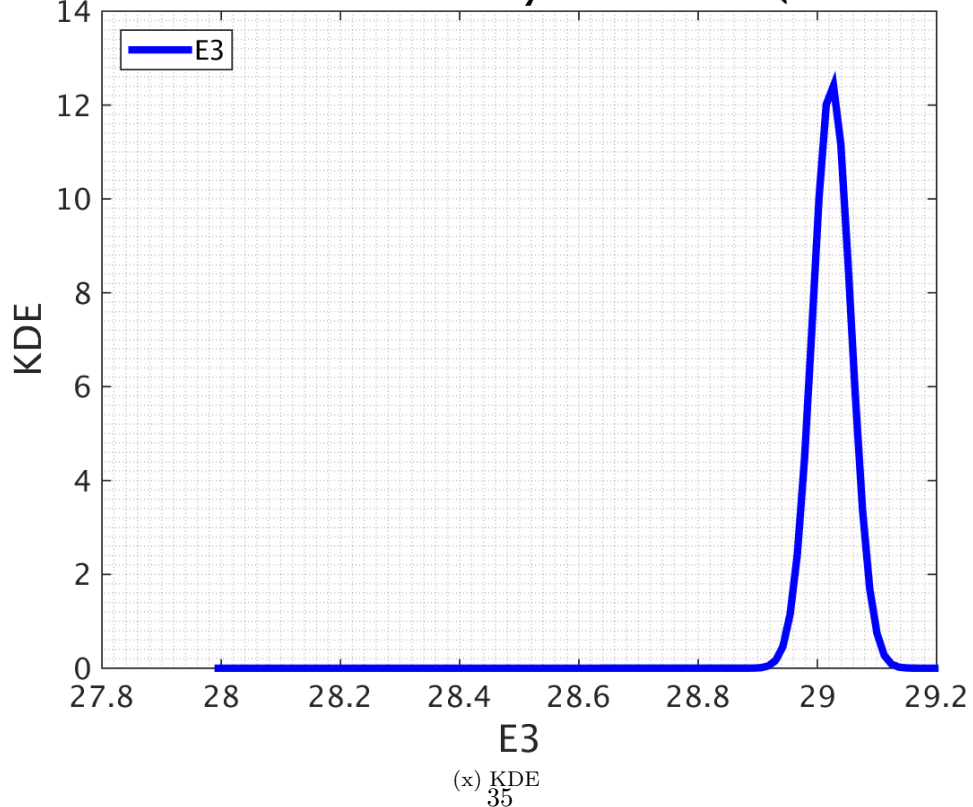


Figure 5.-4: Results for sample size 5e6



Parameter Cumulative Distribution Function (raw chair)**Parameter Kernel Density Estimation (raw chain)**

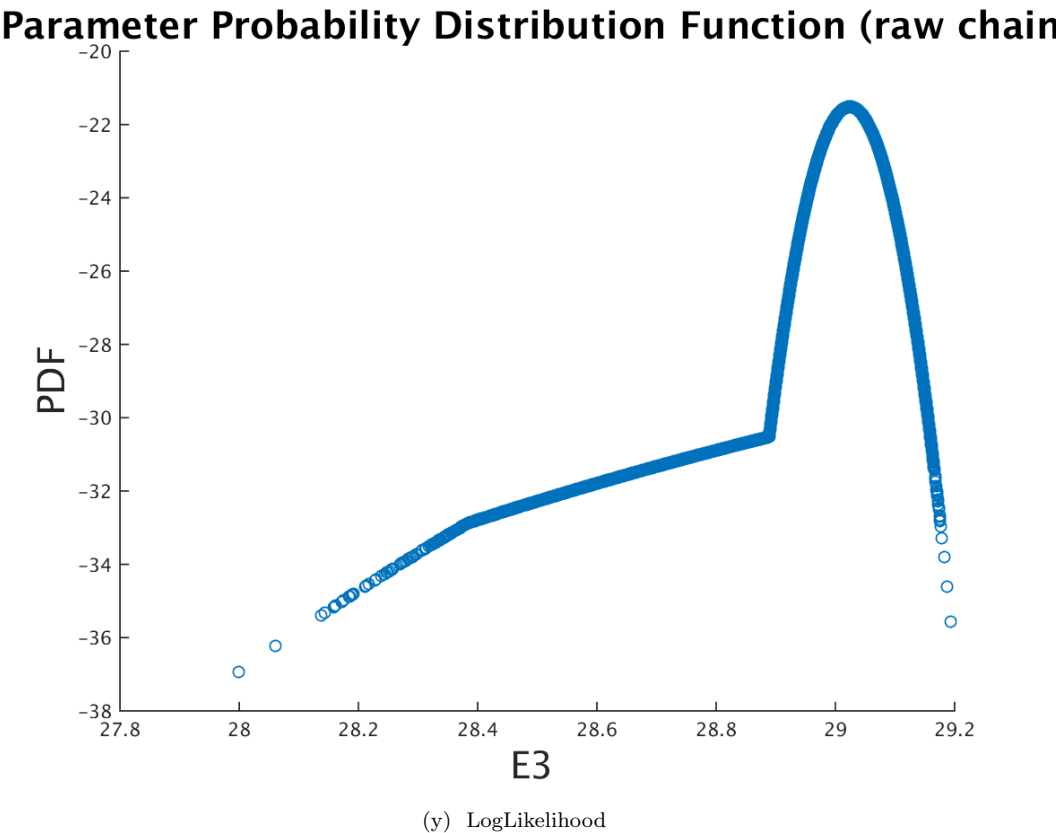
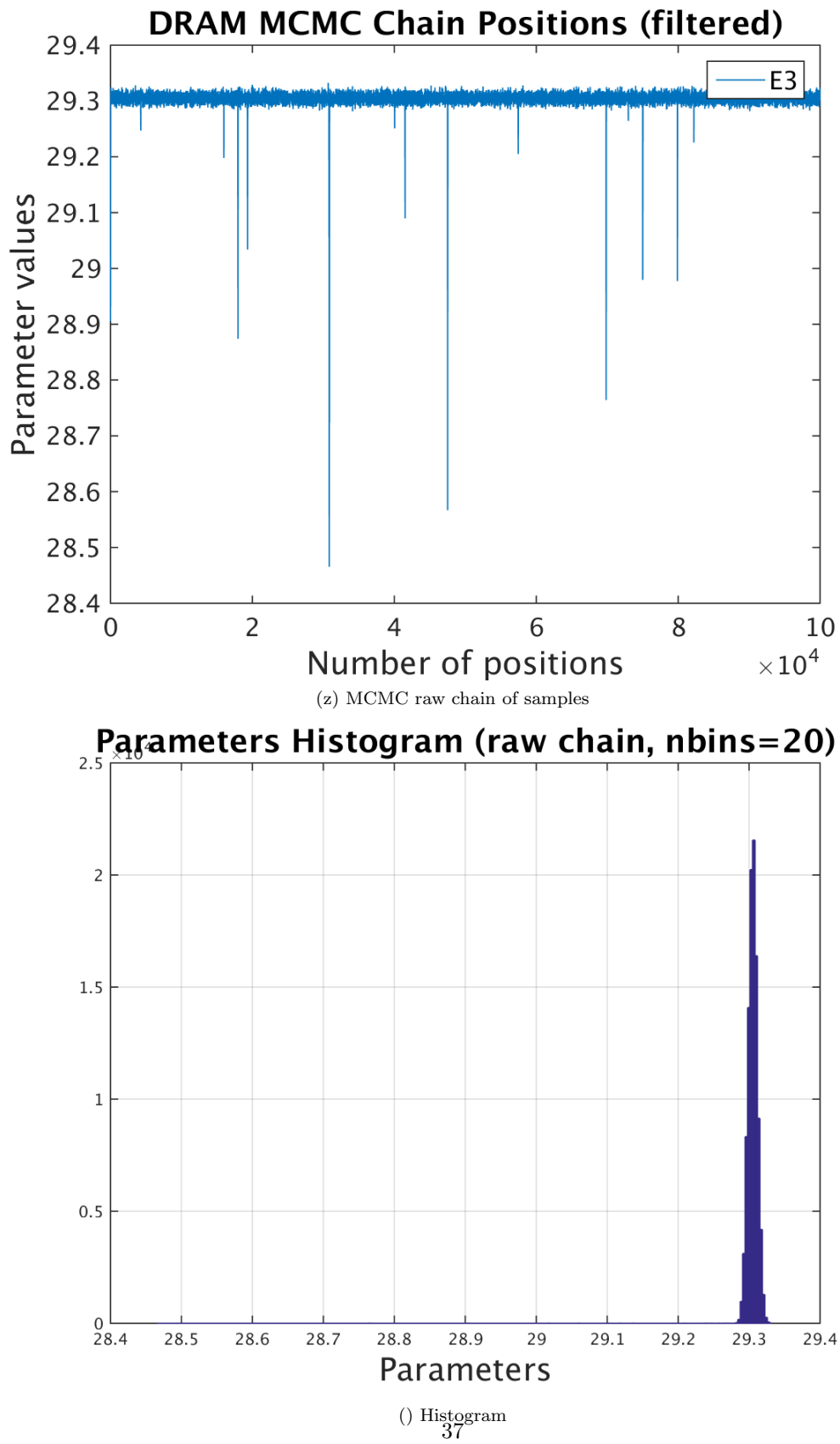
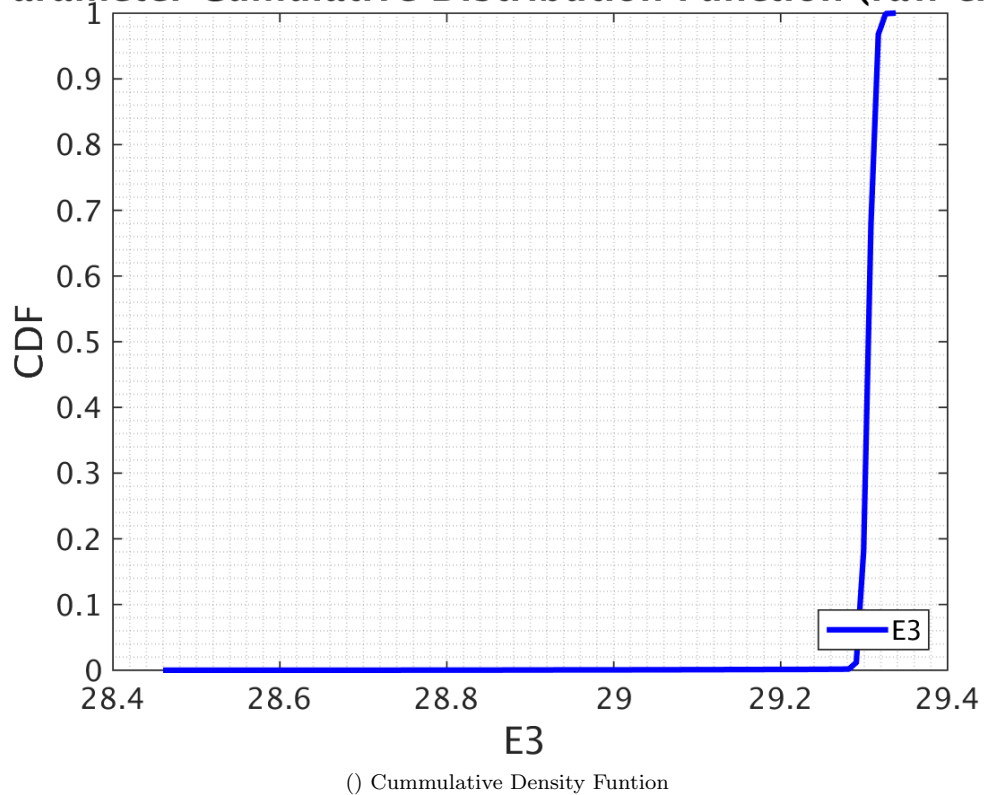
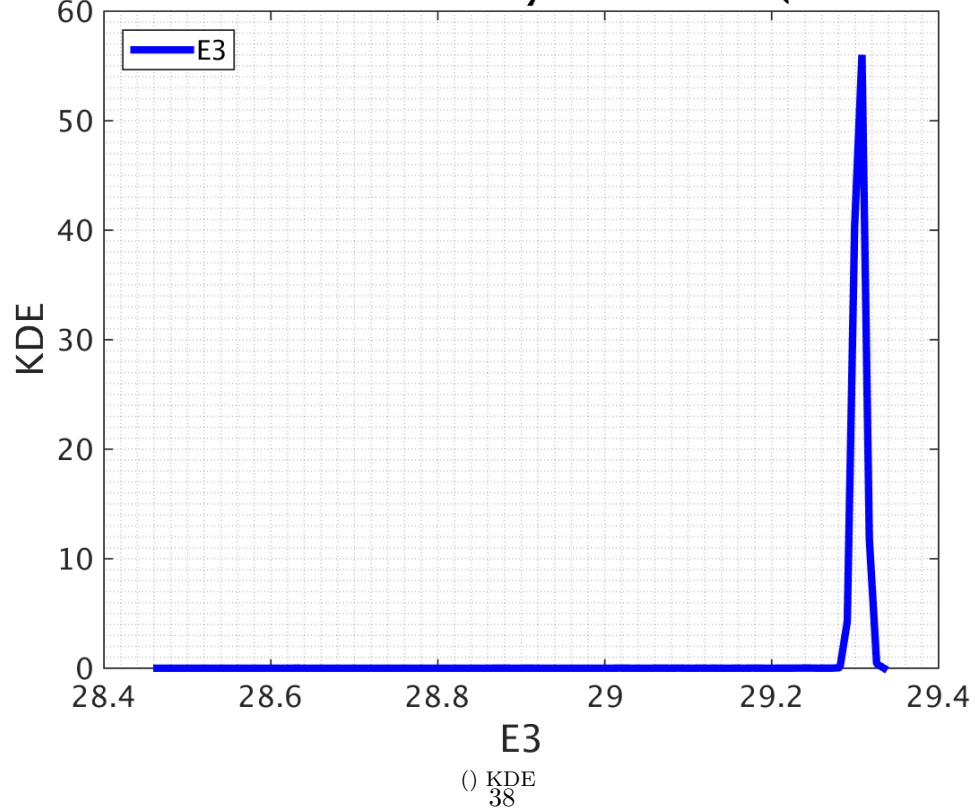


Figure 5.-5: Results for sample size 1e7

Sample size (Surrogate size) 500

In this section we calculated flamespeed values for 500 different points in the domain and the remaining values are linear combination of these 500 points. The results below are for sample size 1e5, 5e5 , 1e6, 5e6 and 1e7.



Parameter Cumulative Distribution Function (raw chair)**Parameter Kernel Density Estimation (raw chain)**

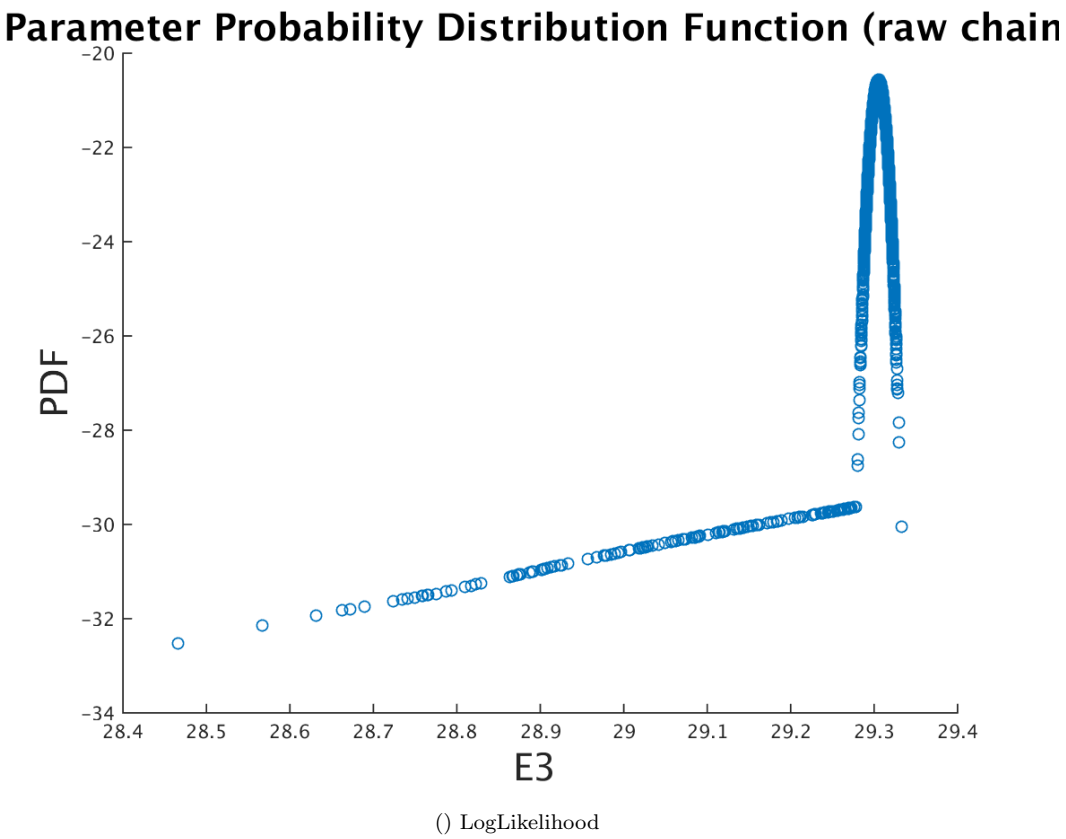
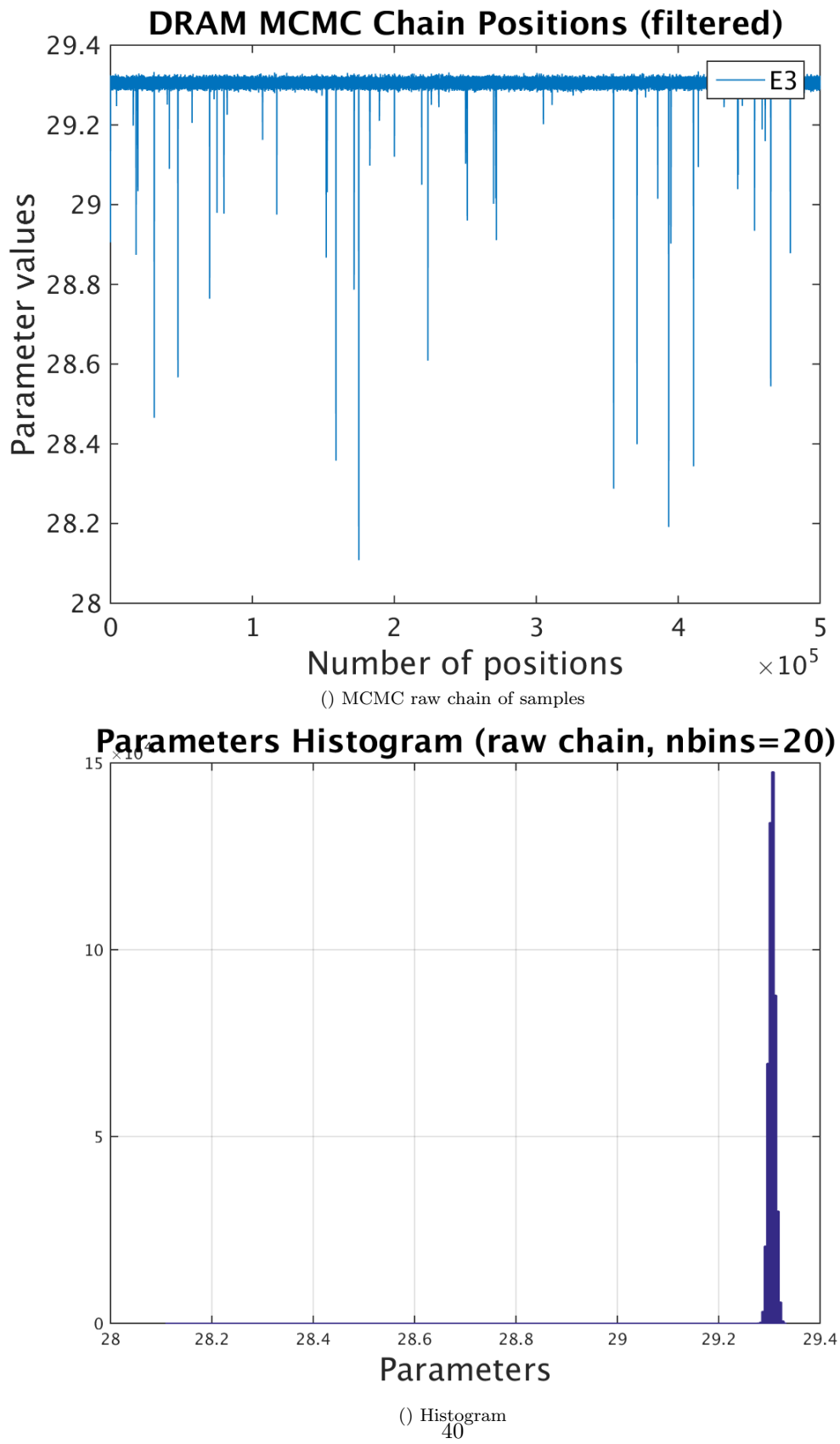
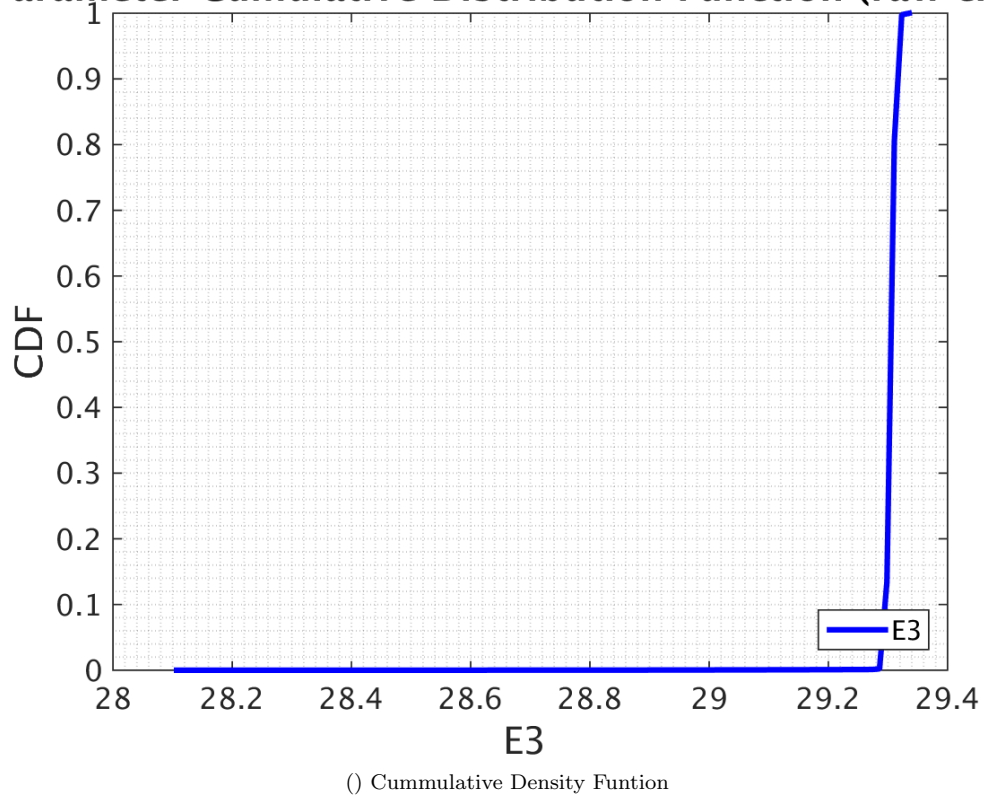
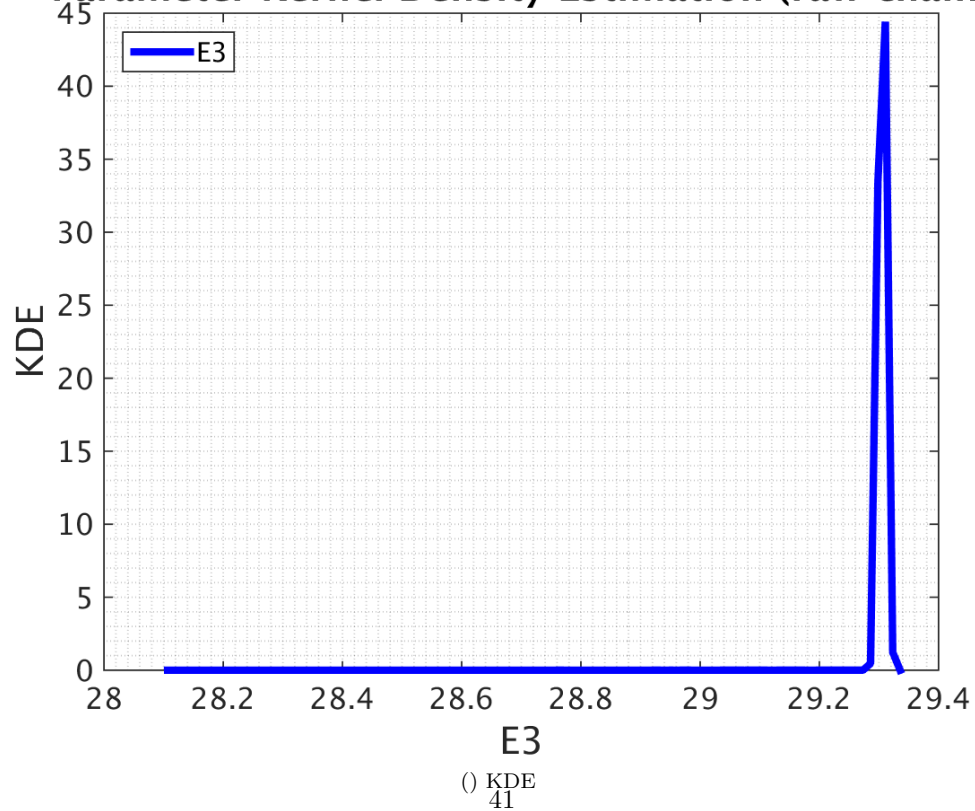


Figure 5.-6: Results for sample size 1e5



Parameter Cumulative Distribution Function (raw chair)**Parameter Kernel Density Estimation (raw chain)**

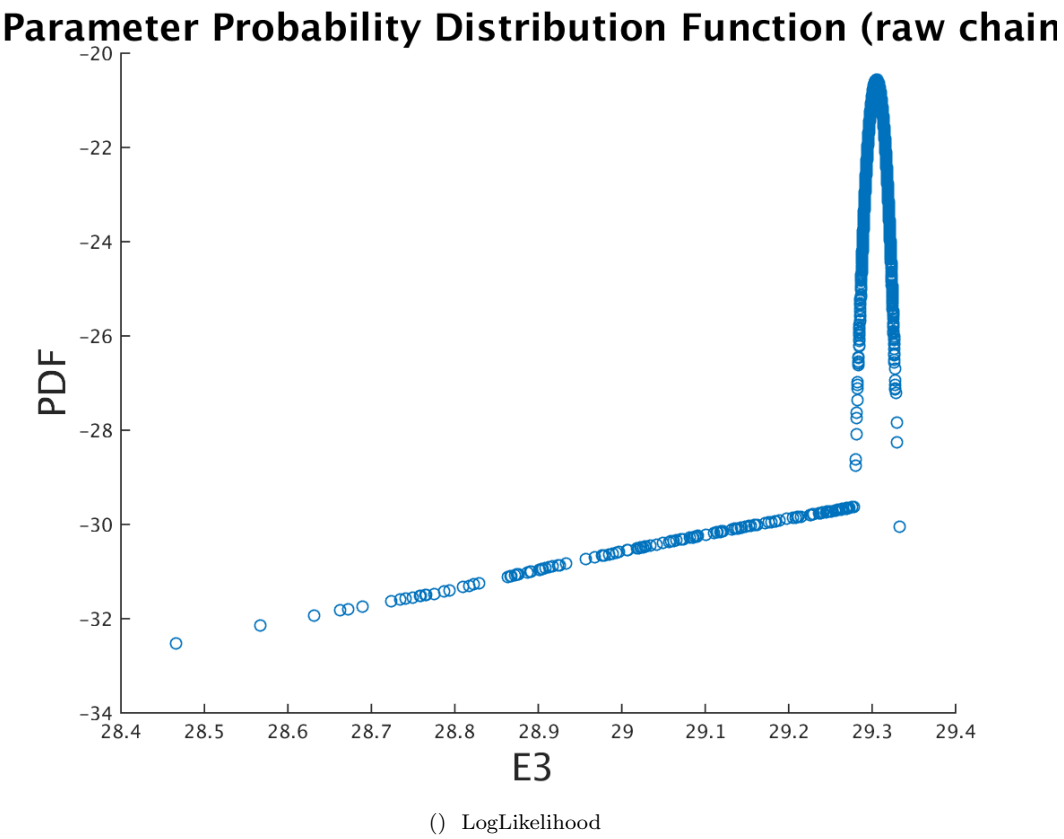
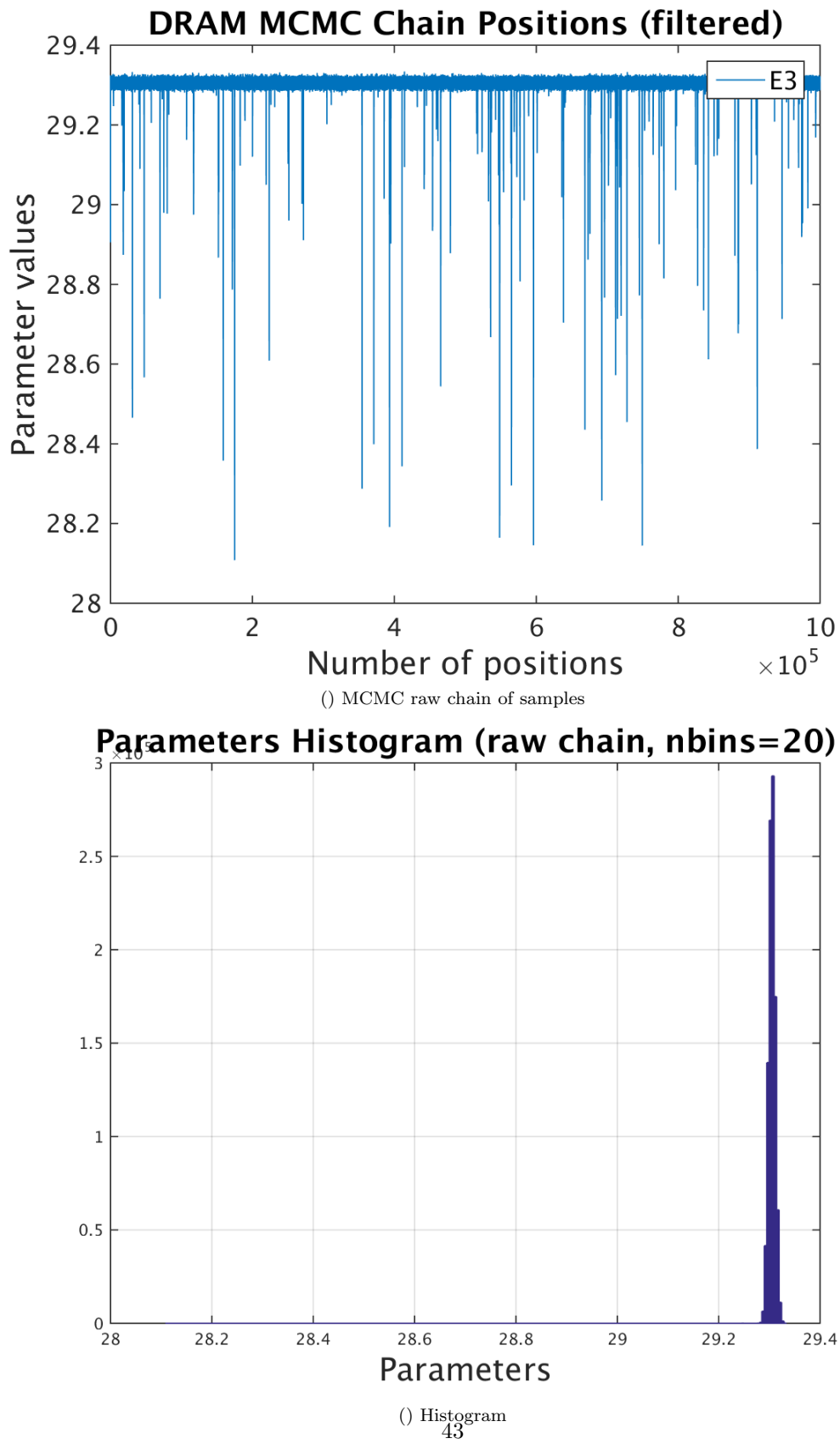
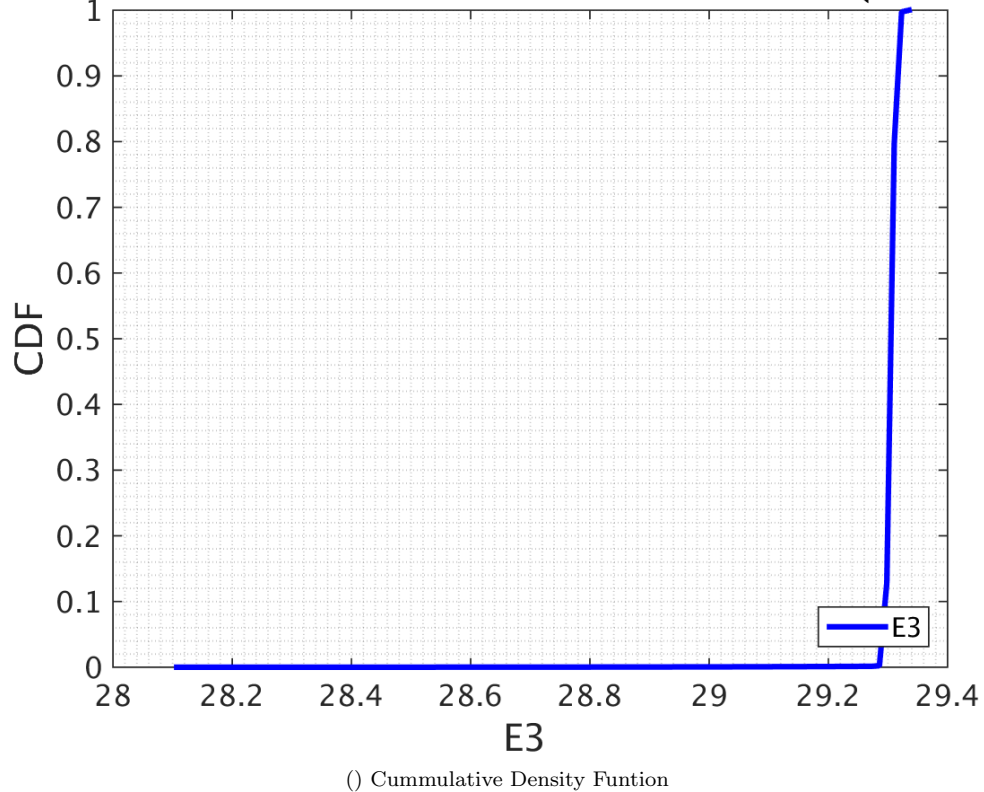
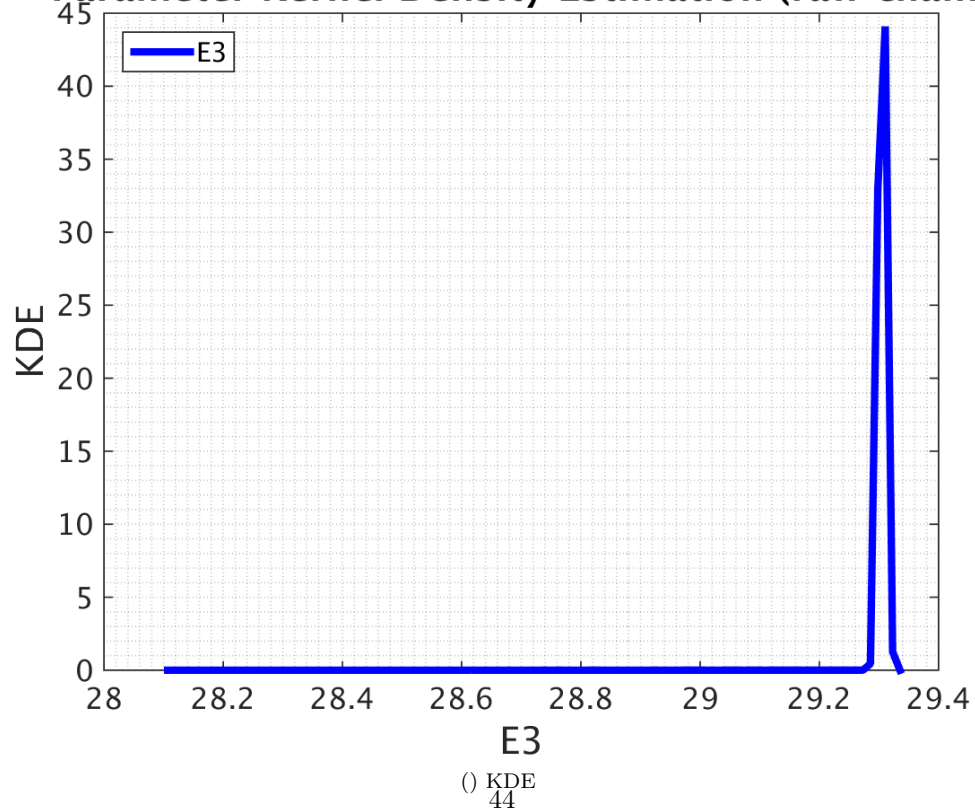


Figure 5.-7: Results for sample size 5e5



Parameter Cumulative Distribution Function (raw chair)**Parameter Kernel Density Estimation (raw chain)**

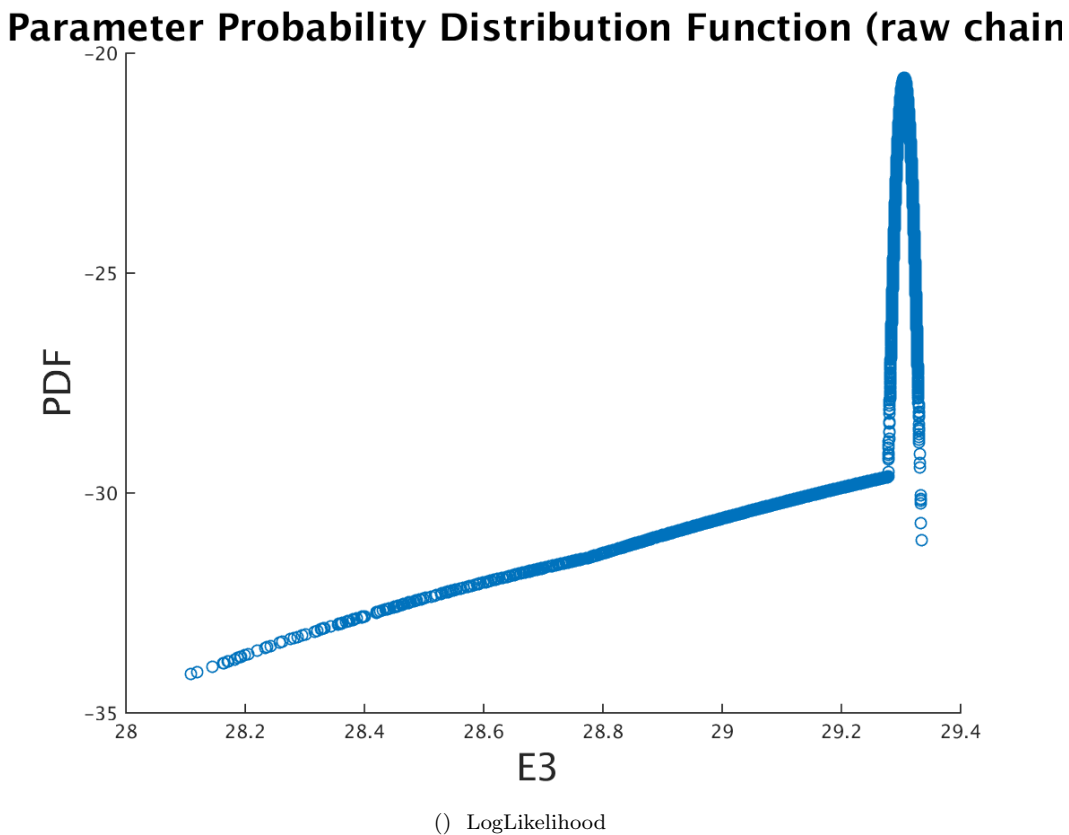
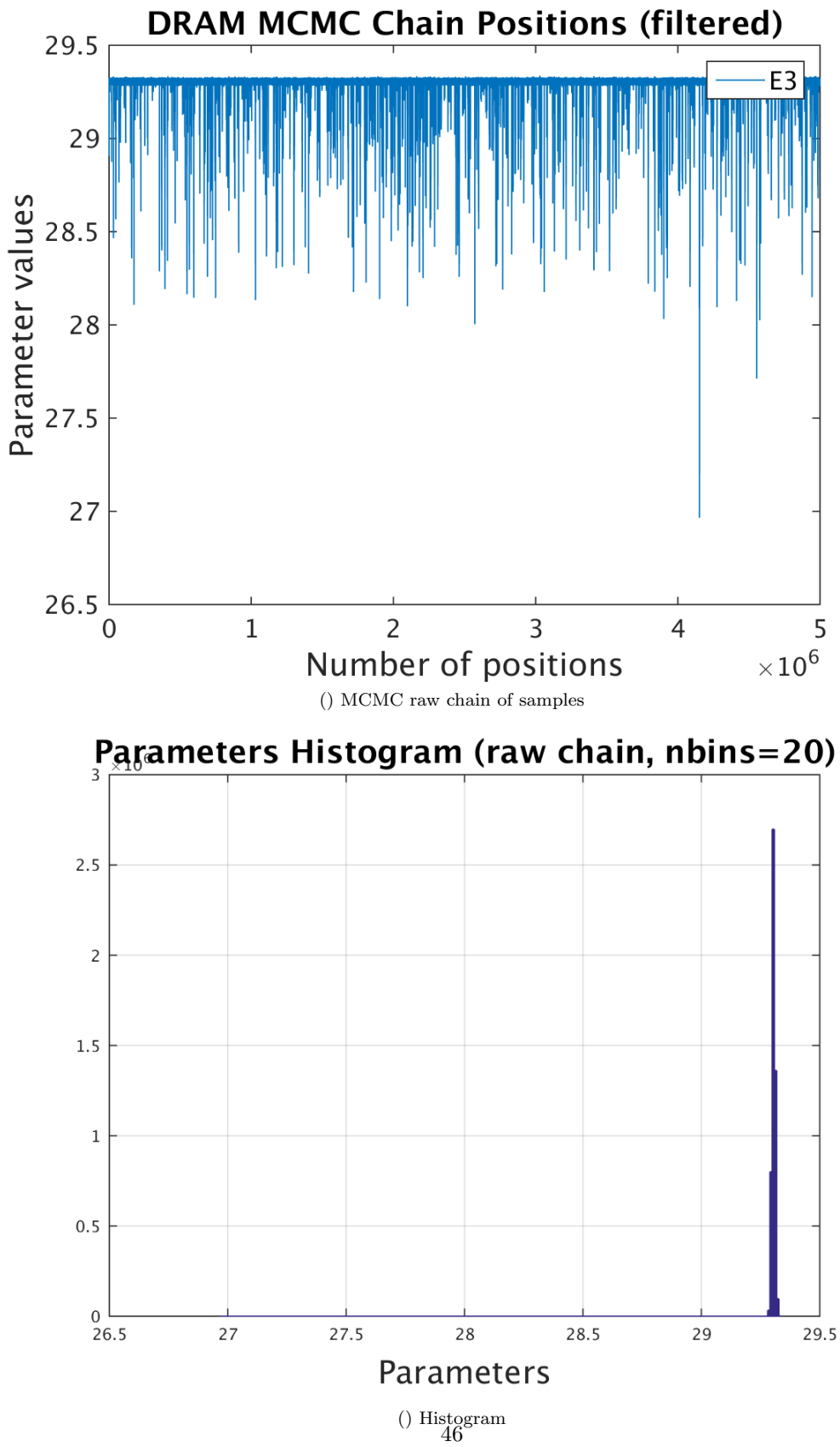
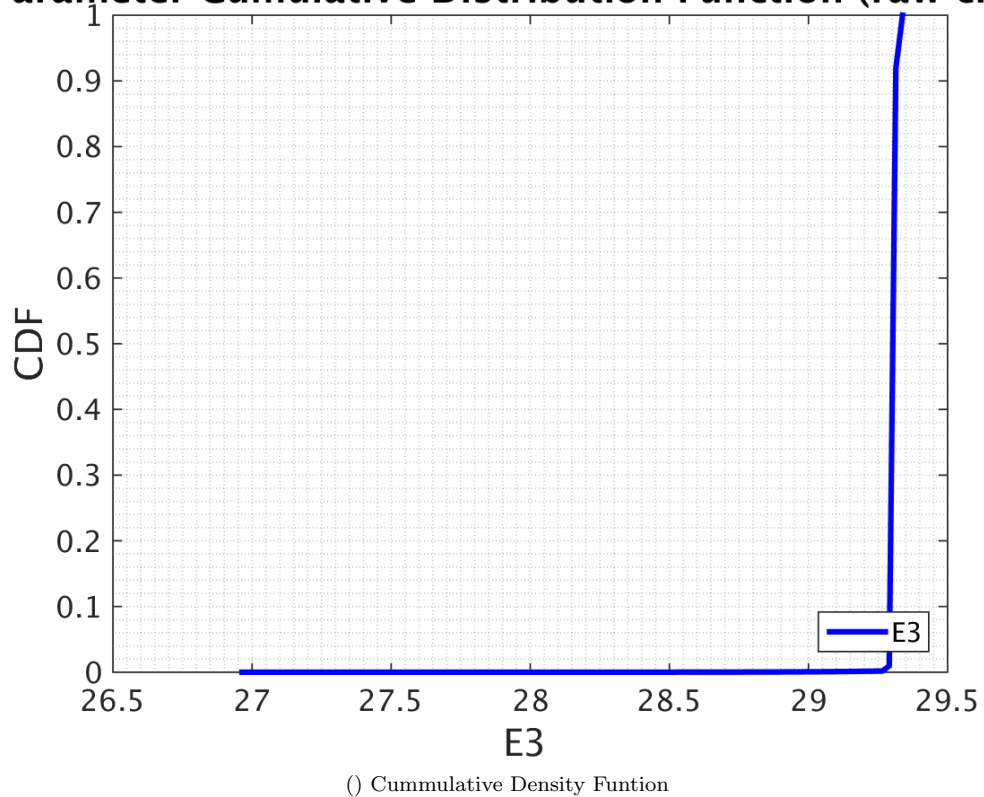
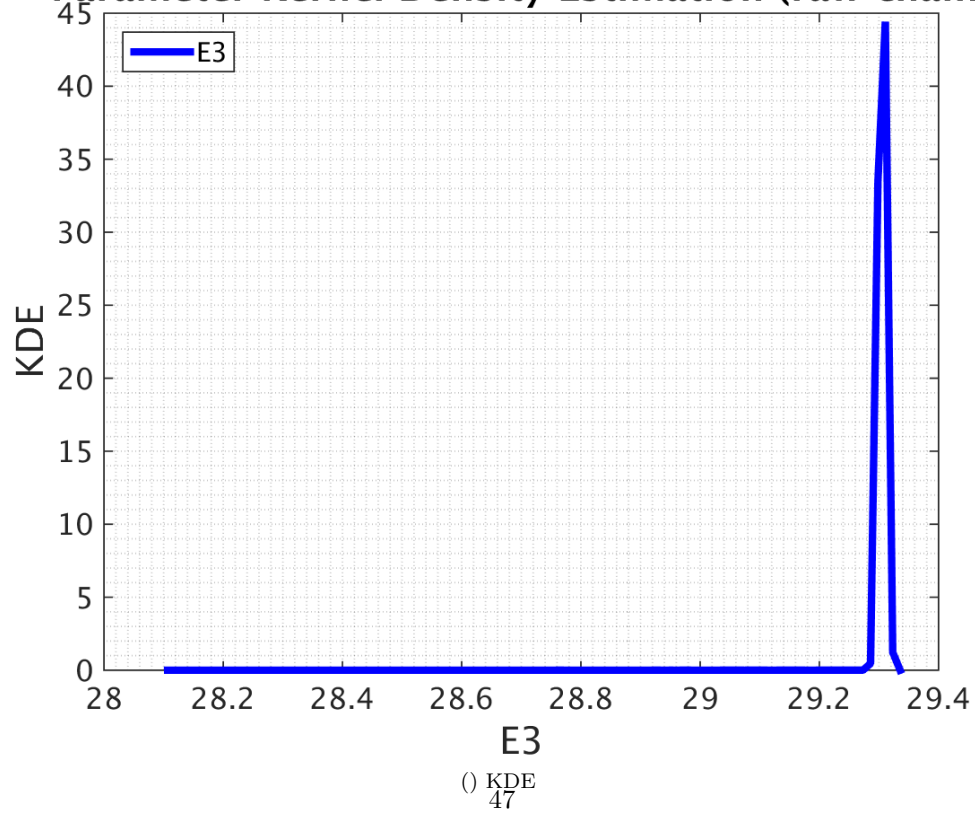


Figure 5.-8: Results for sample size 1e6



Parameter Cumulative Distribution Function (raw chair)**Parameter Kernel Density Estimation (raw chain)**

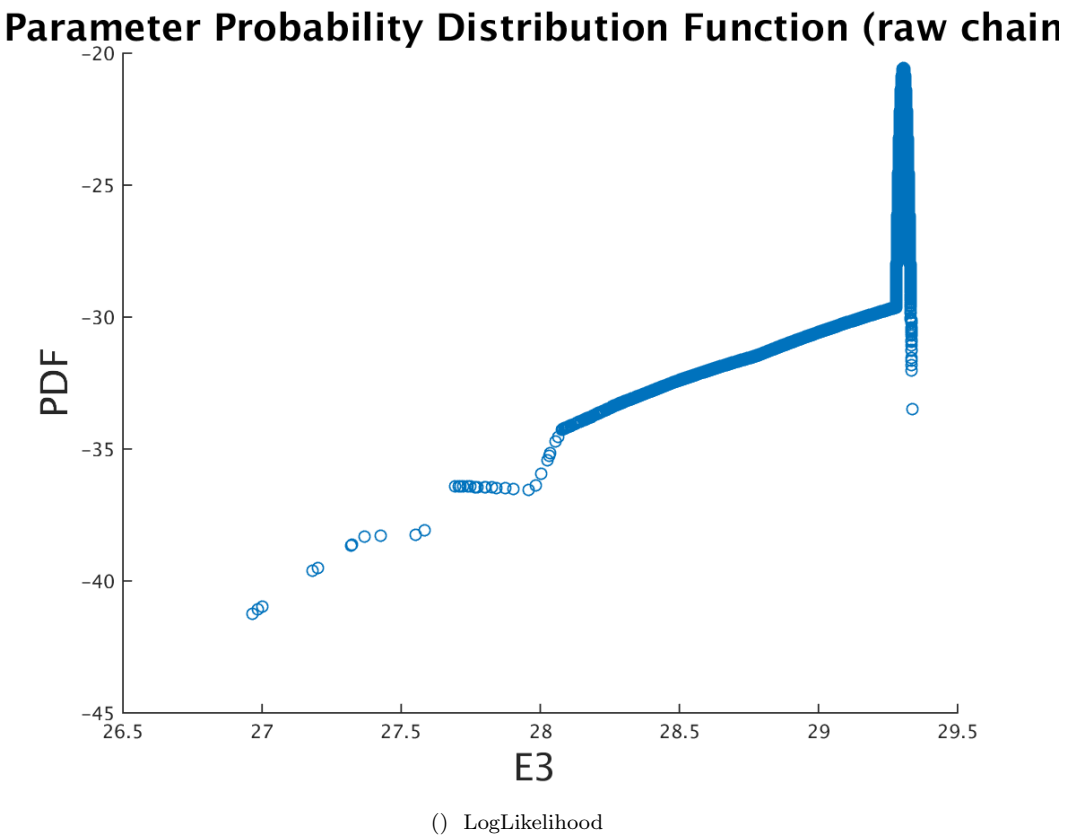
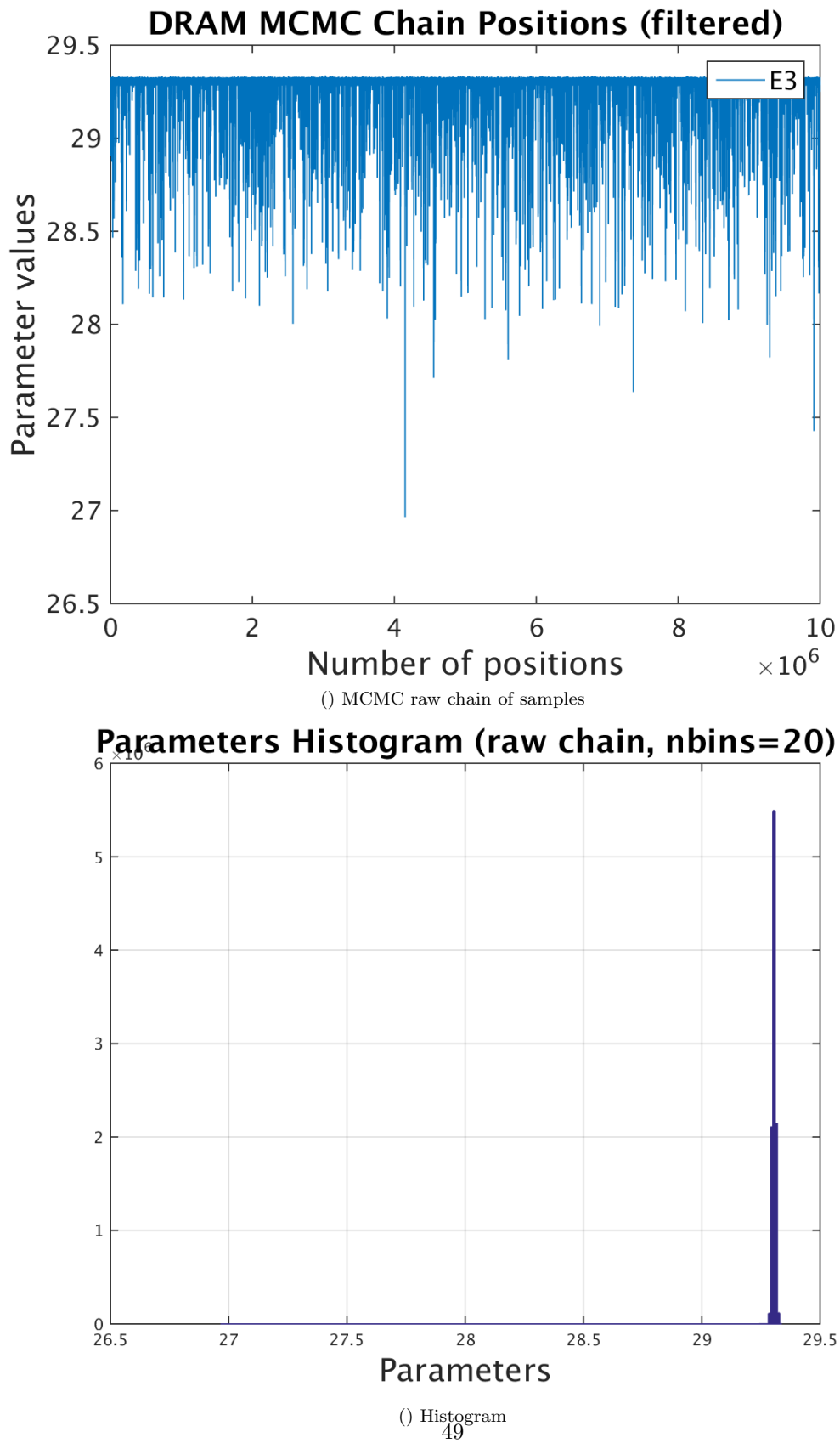
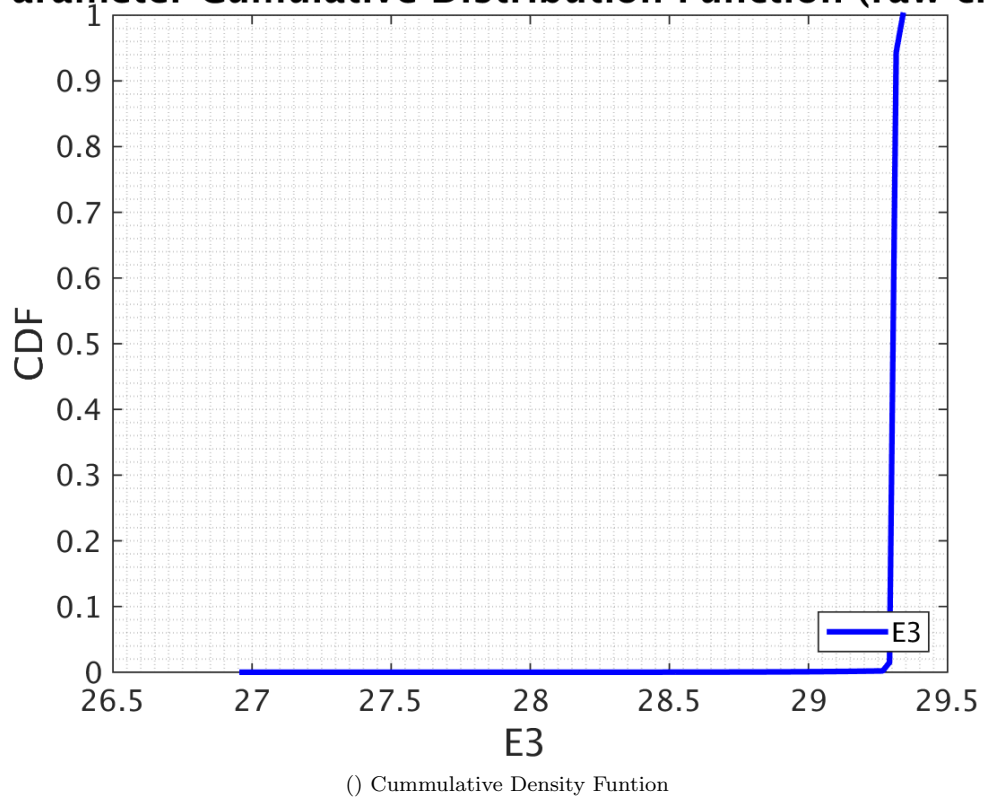
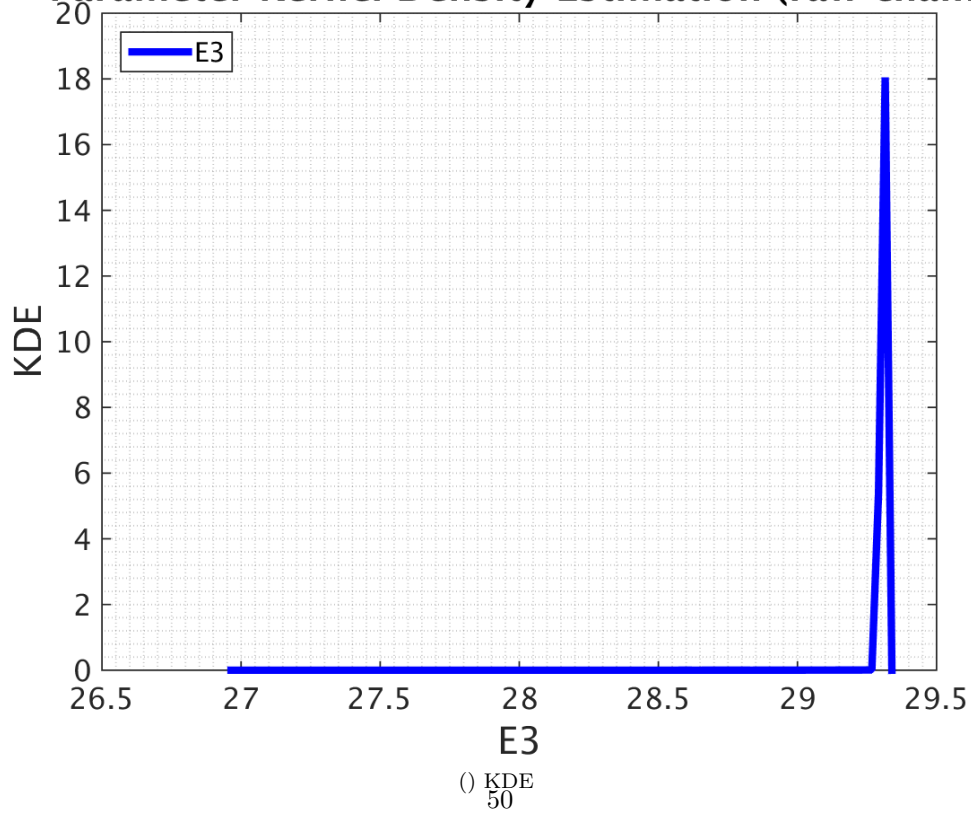


Figure 5.-9: Results for sample size 5e6



Parameter Cumulative Distribution Function (raw chair)**Parameter Kernel Density Estimation (raw chain)**

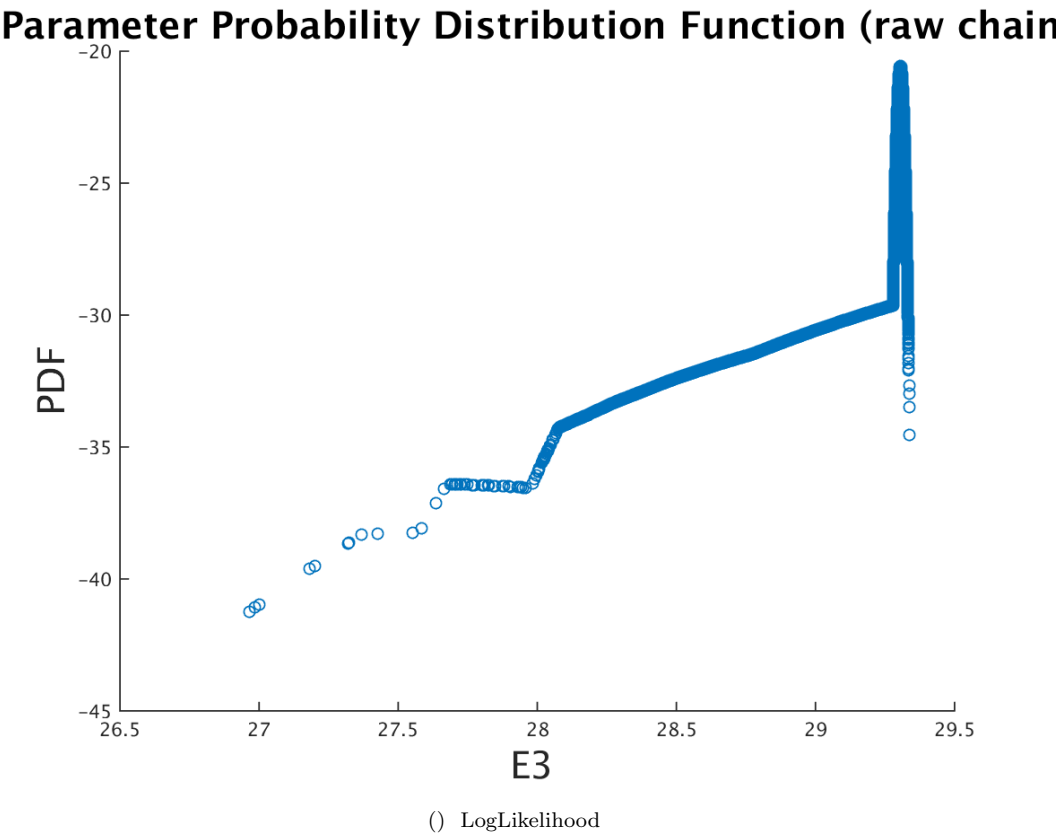
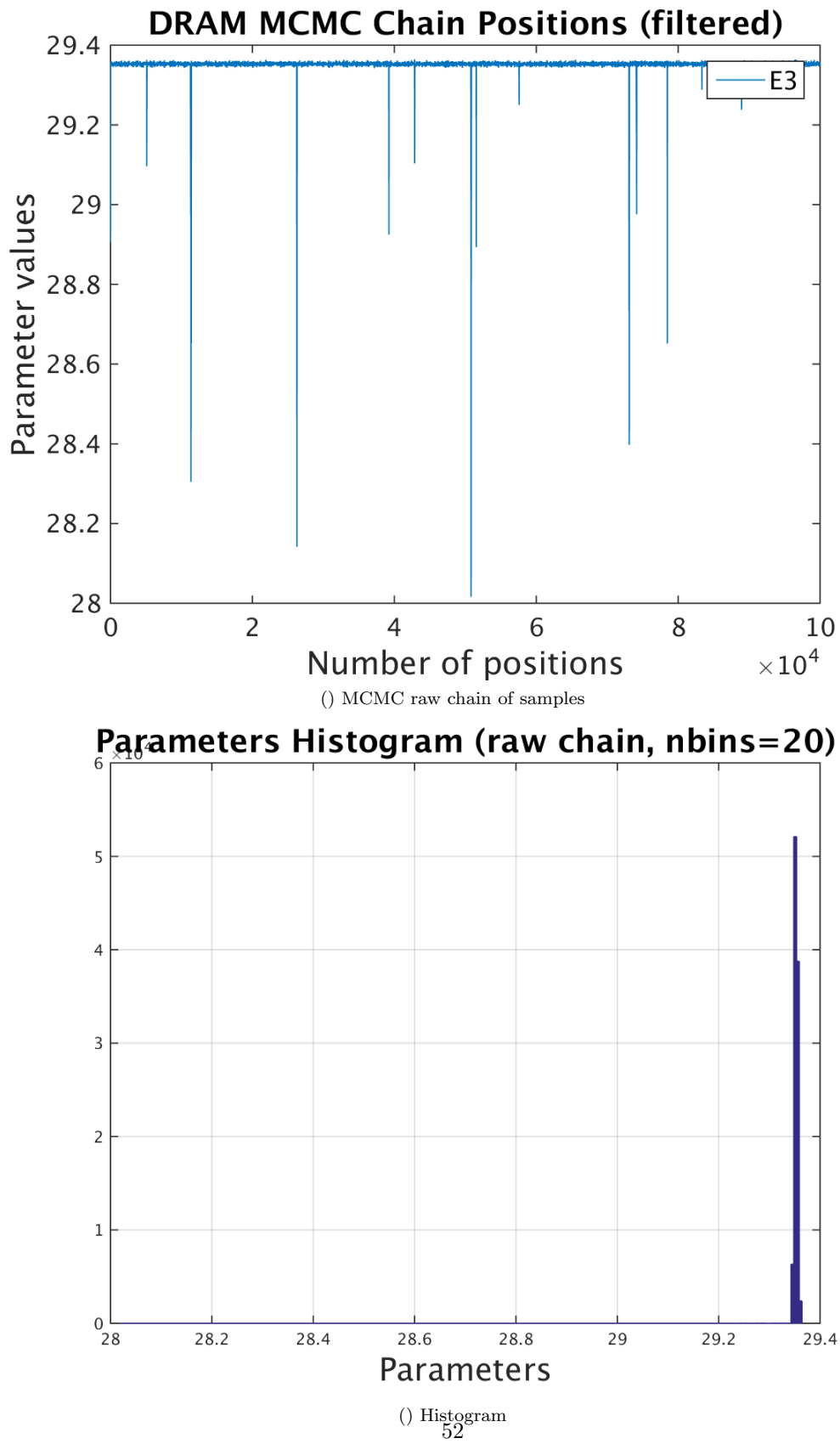
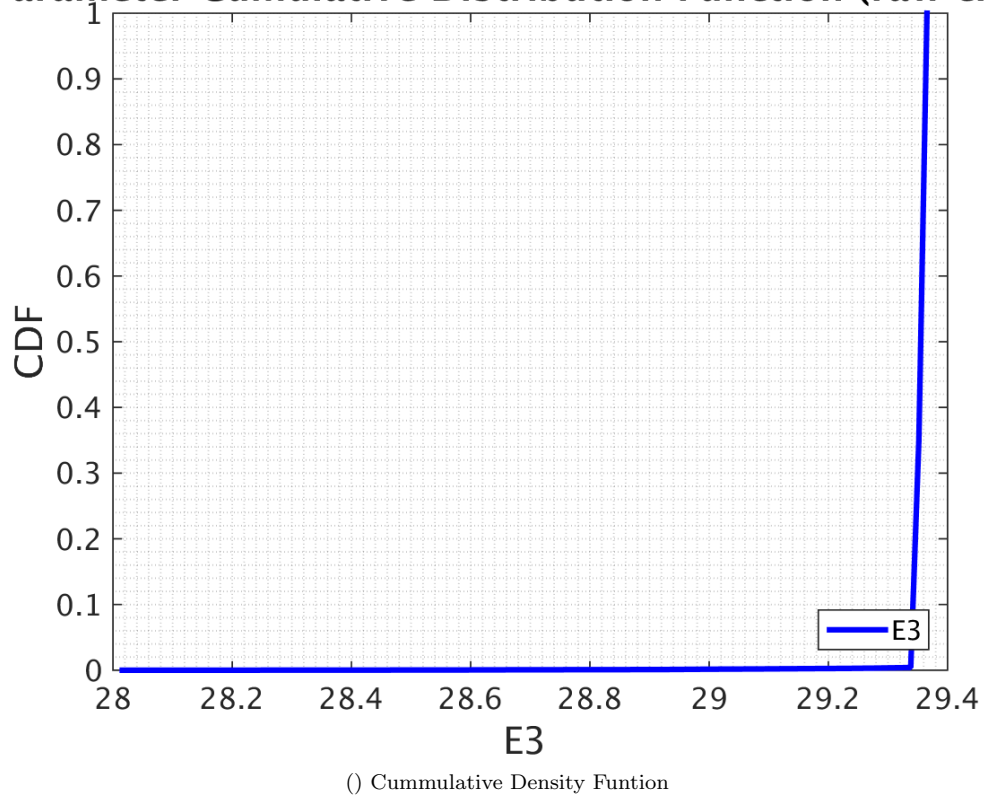
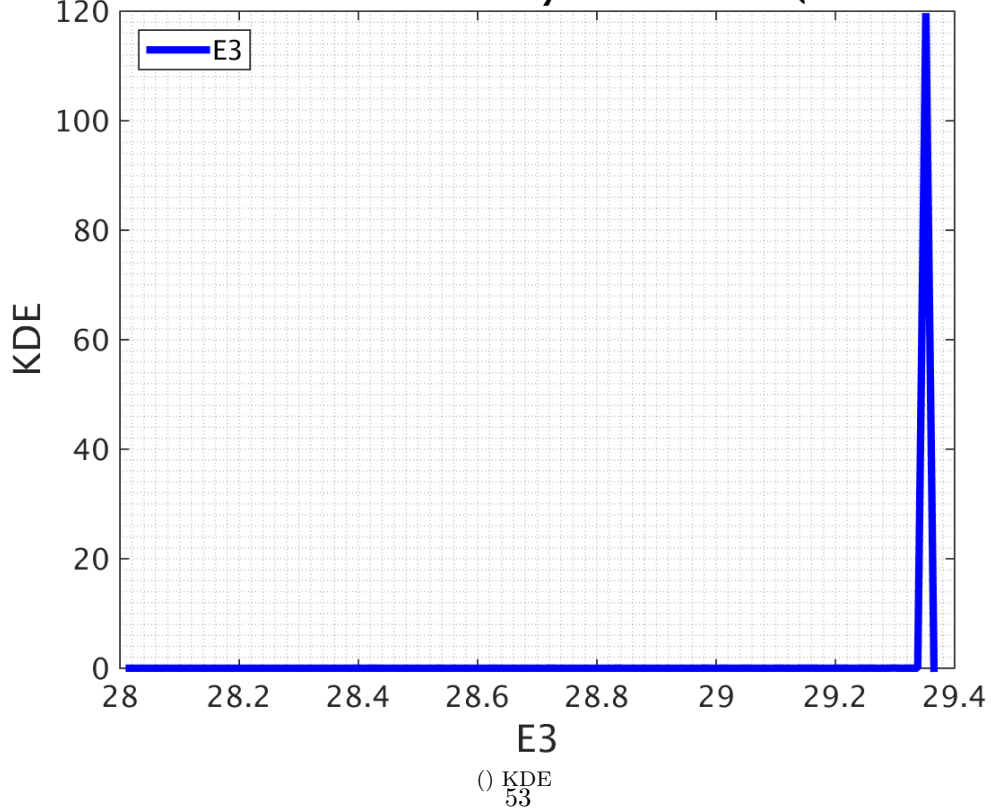


Figure 5.-10: Results for sample size 1e7

Sample size (Surrogate size) 1000

In this section we calculated flamespeed values for 1000 different points in the domain and the remaining values are linear combination of these 1000 points. The results below are for sample size 1e5, 5e5 , 1e6, 5e6 and 1e7.



Parameter Cumulative Distribution Function (raw chair)**Parameter Kernel Density Estimation (raw chain)**

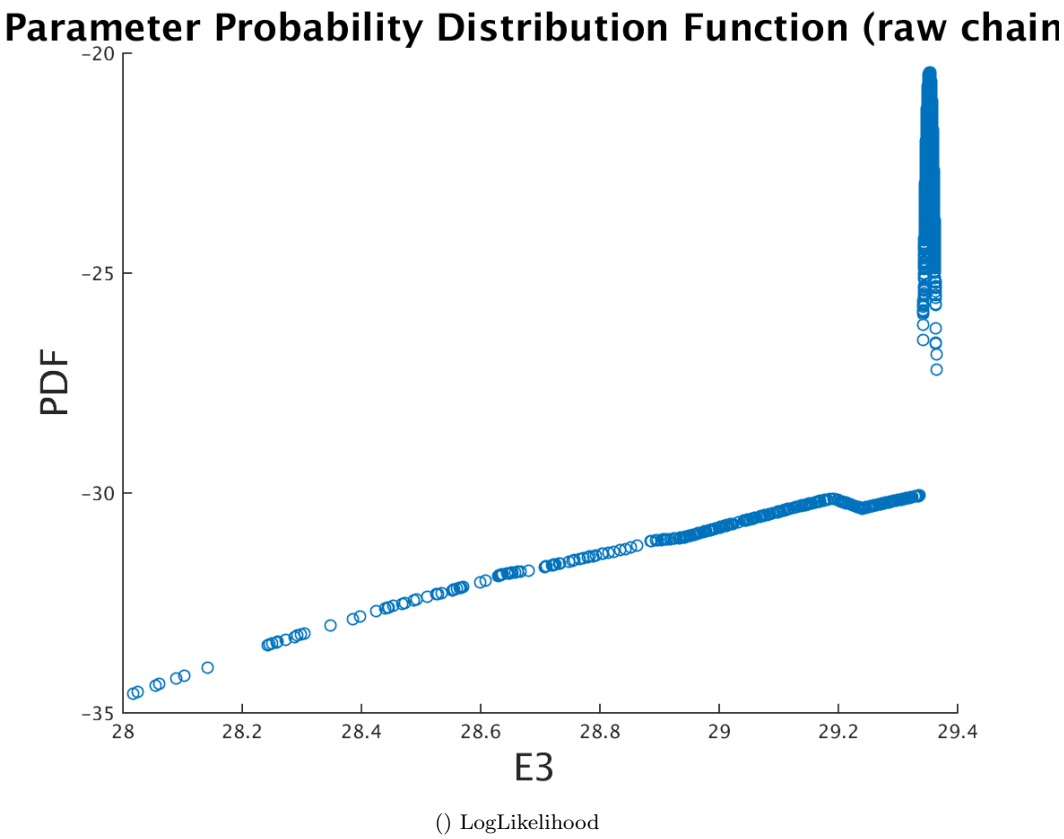
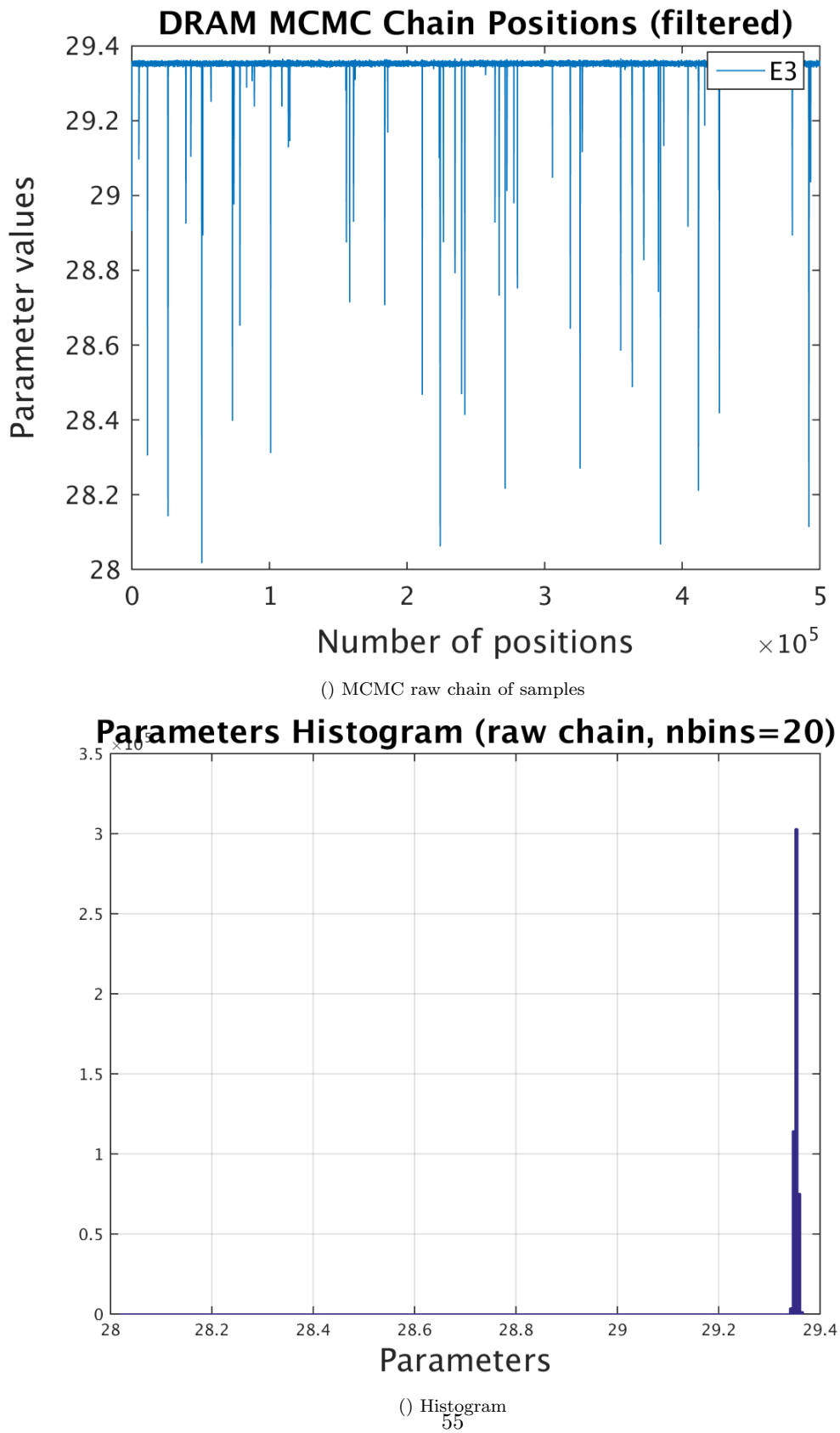
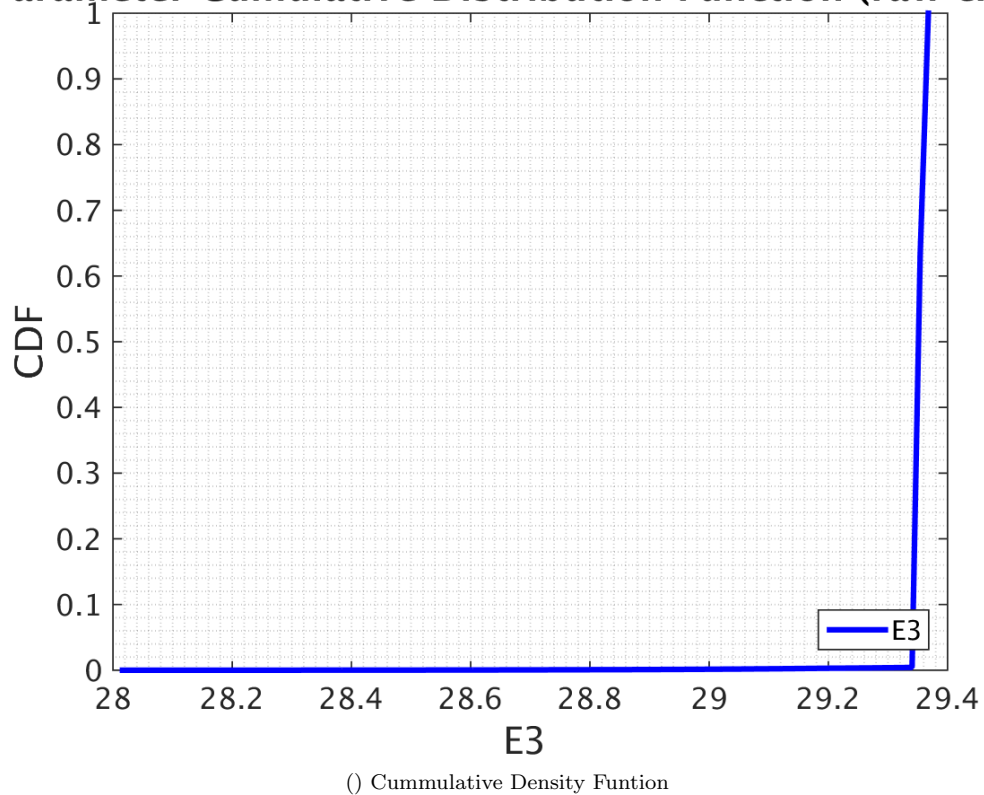
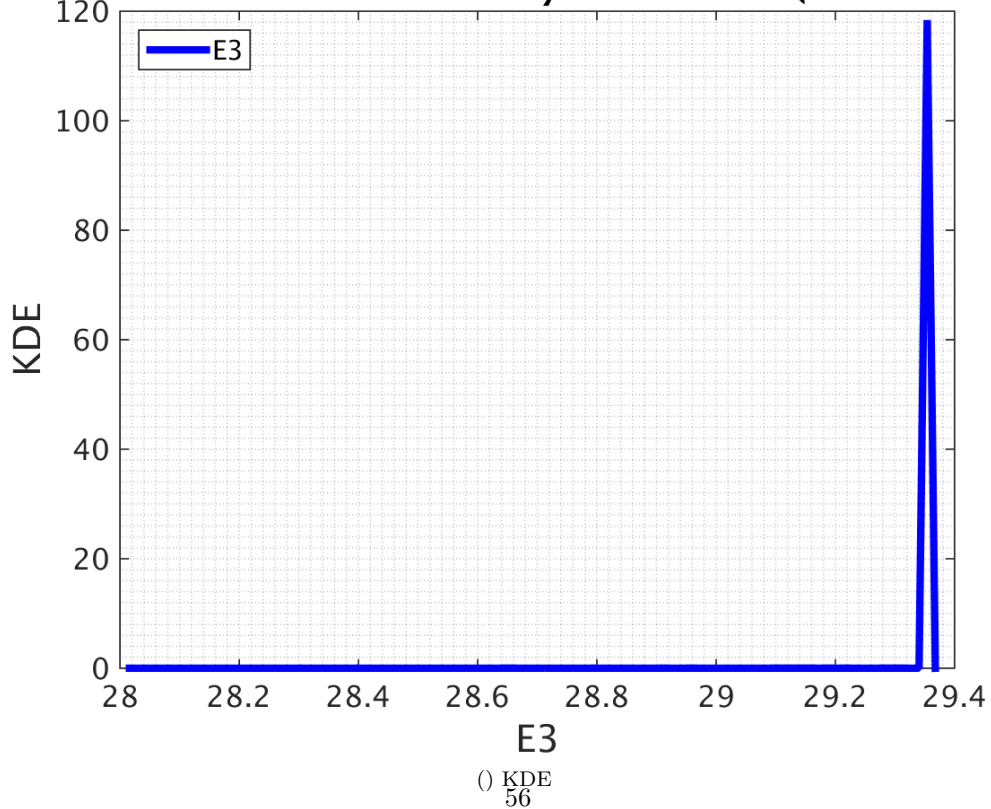


Figure 5.-11: Results for sample size 1e5



Parameter Cumulative Distribution Function (raw chair)**Parameter Kernel Density Estimation (raw chain)**

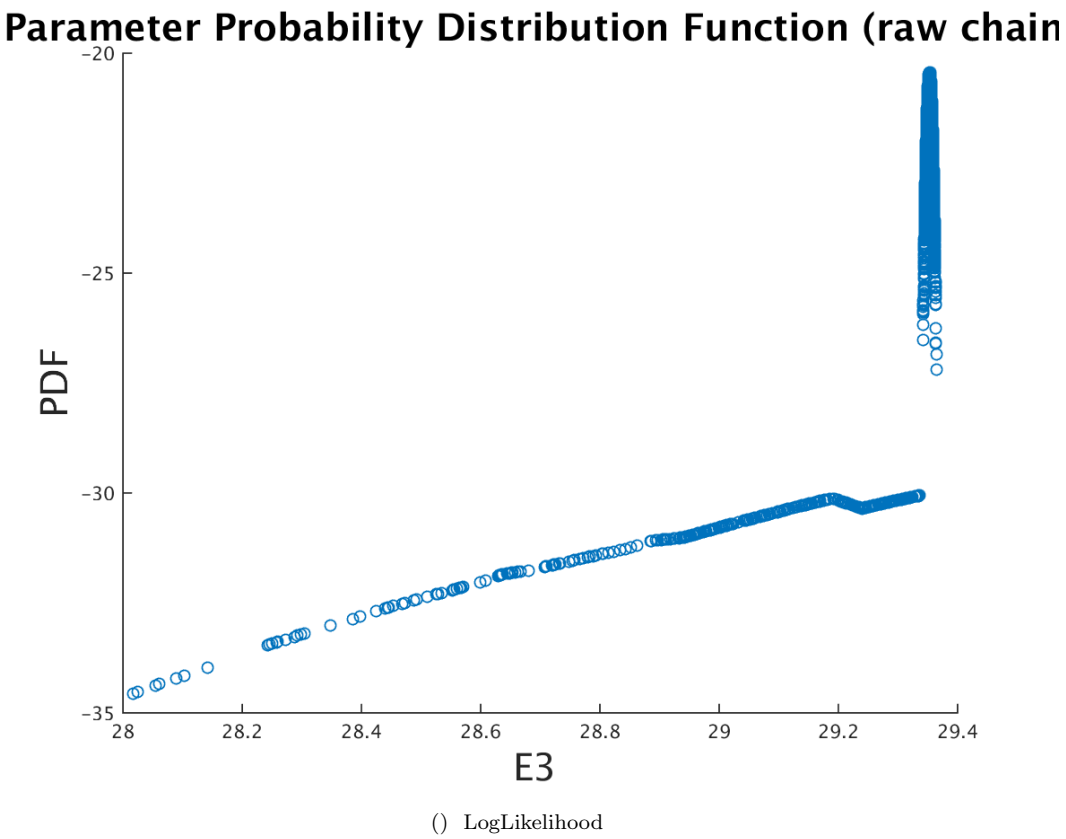
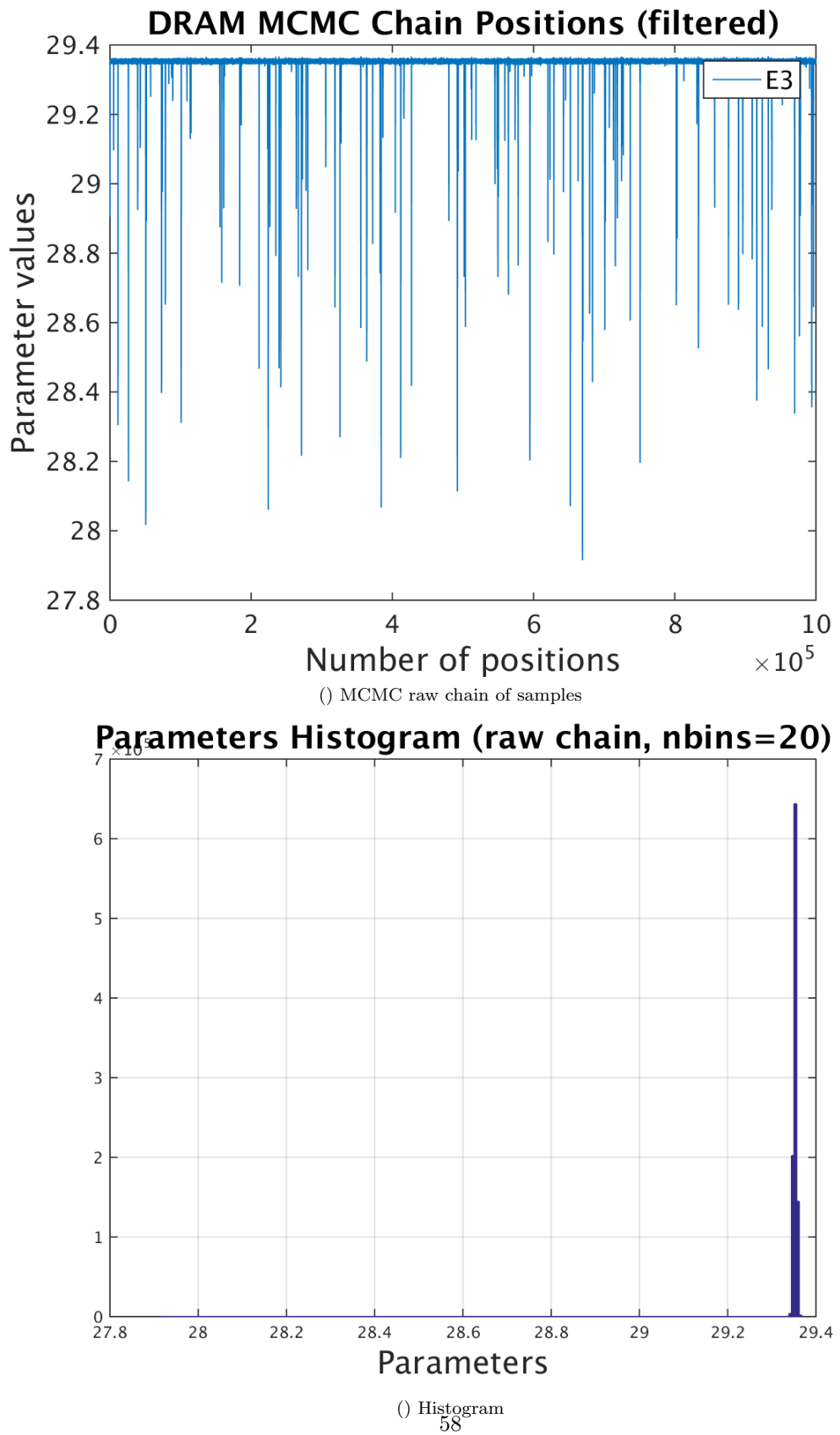
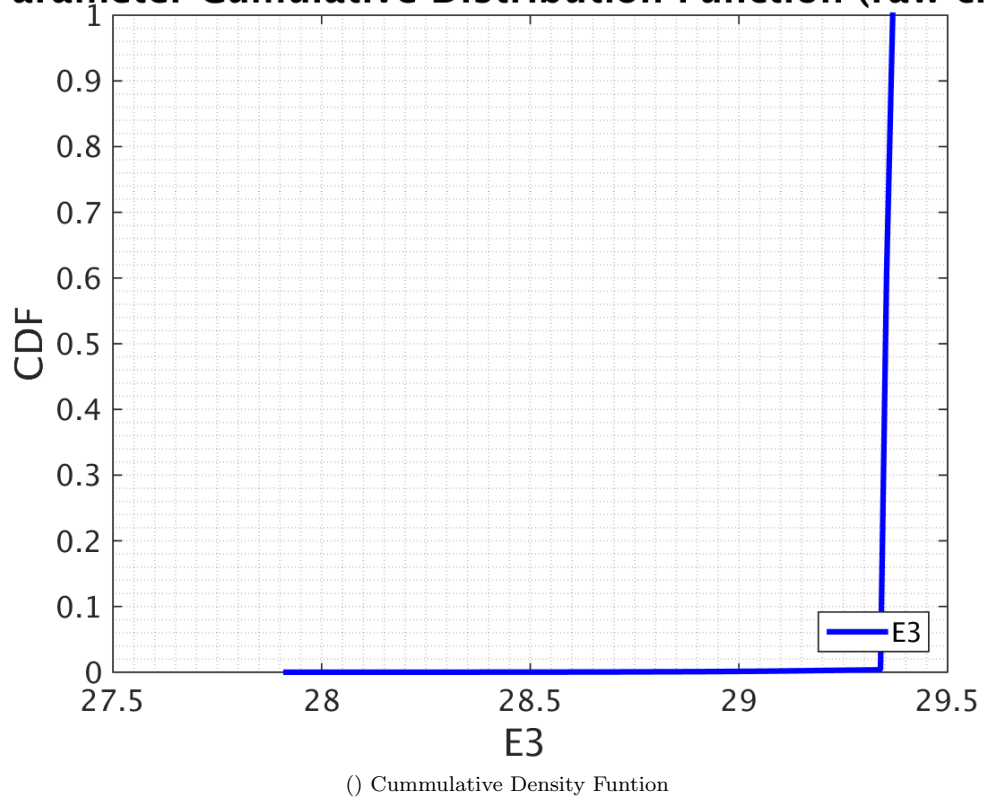
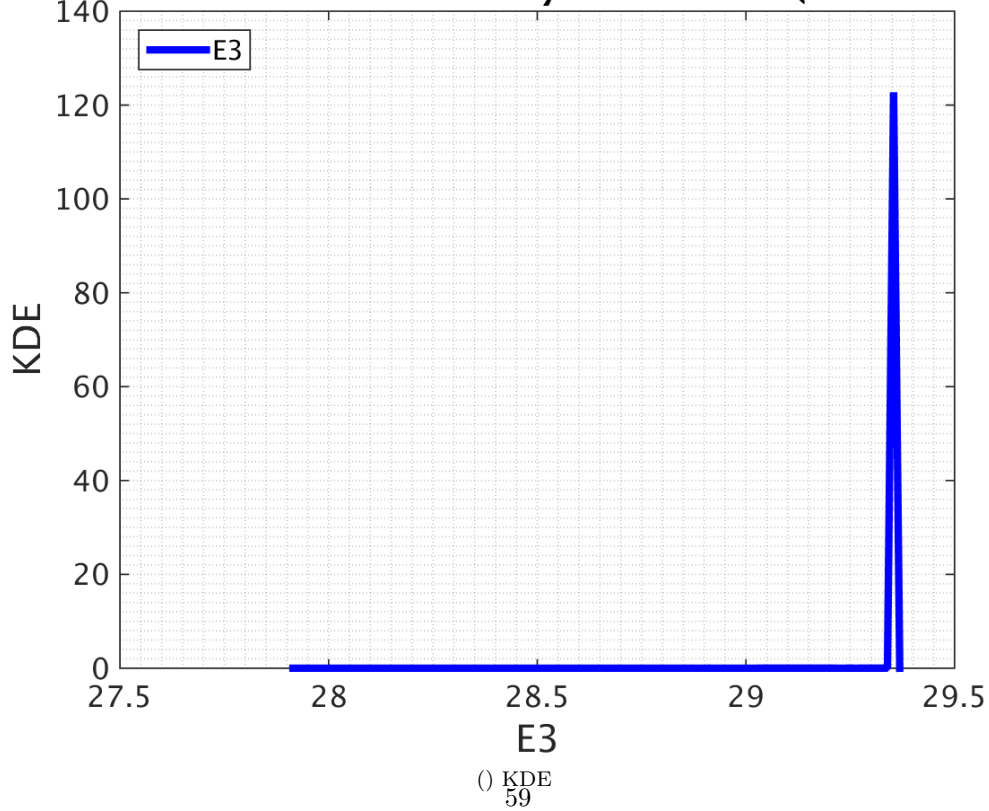


Figure 5.-12: Results for sample size 5e5



Parameter Cumulative Distribution Function (raw chair)**Parameter Kernel Density Estimation (raw chain)**

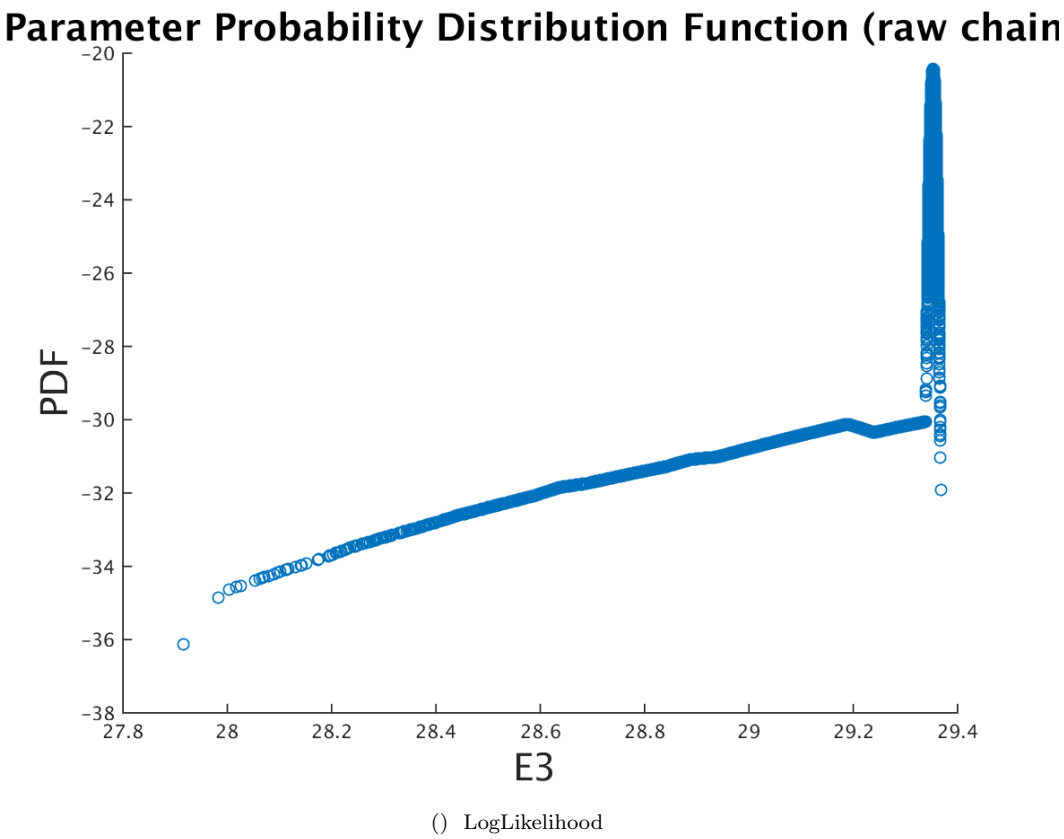
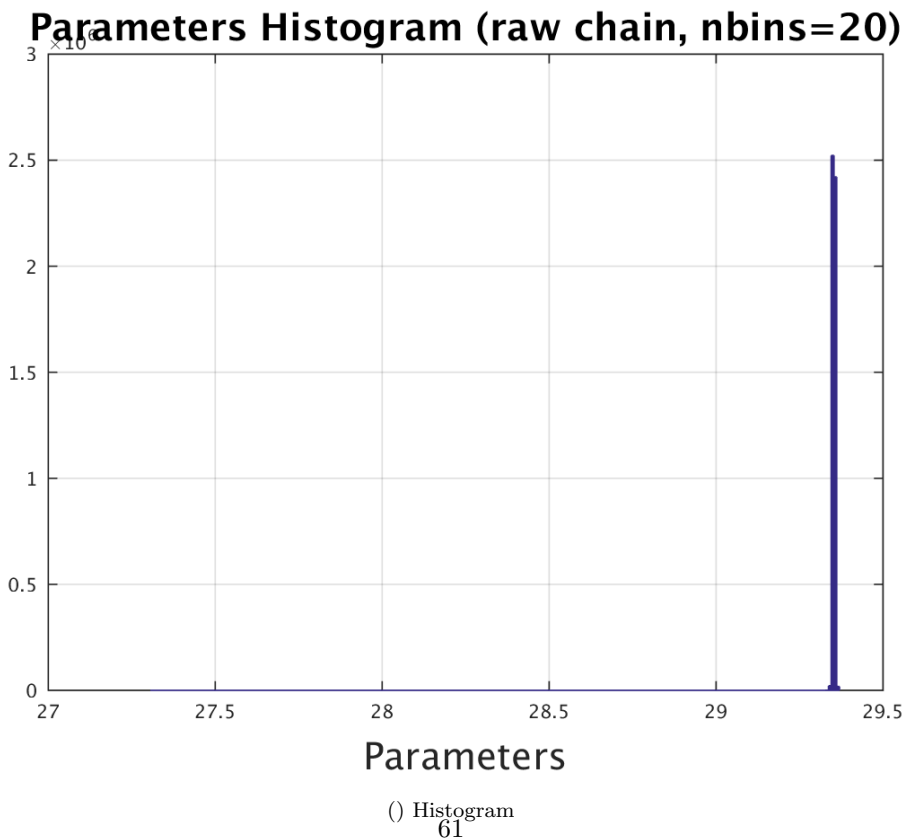
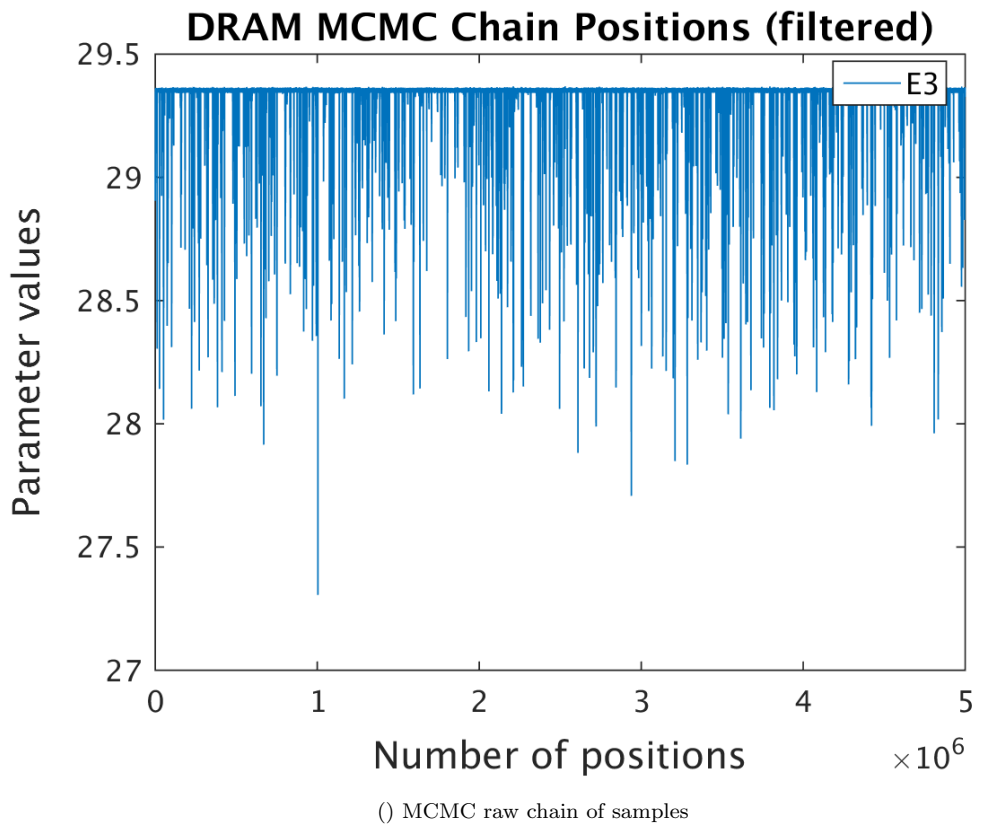
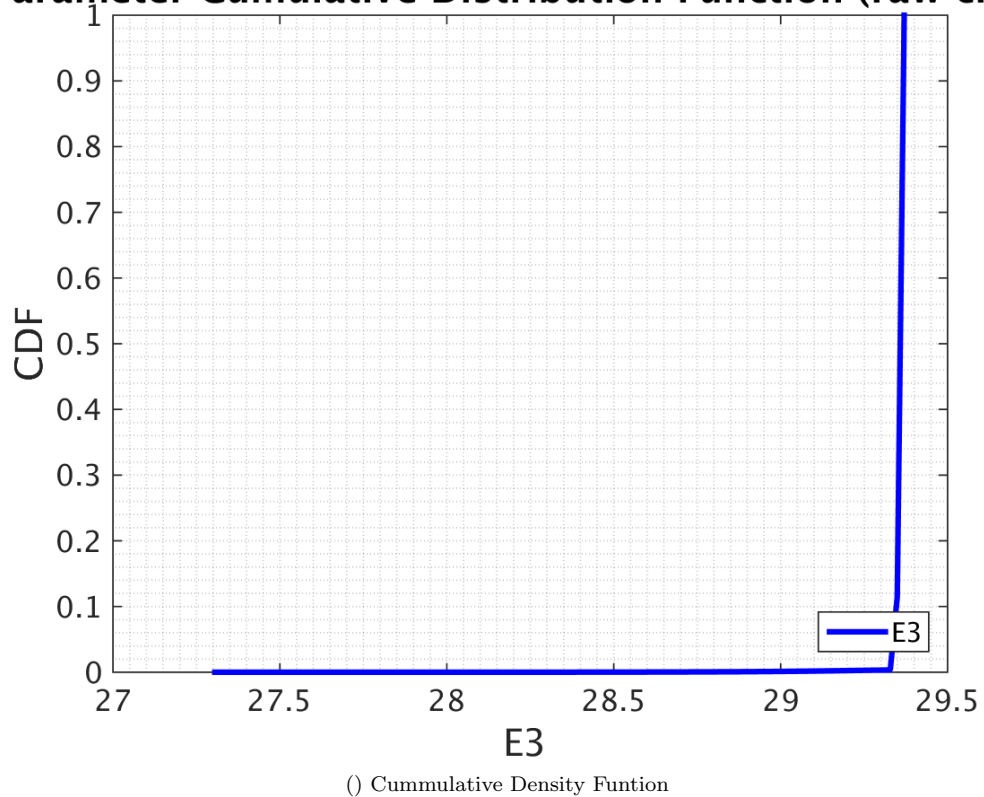
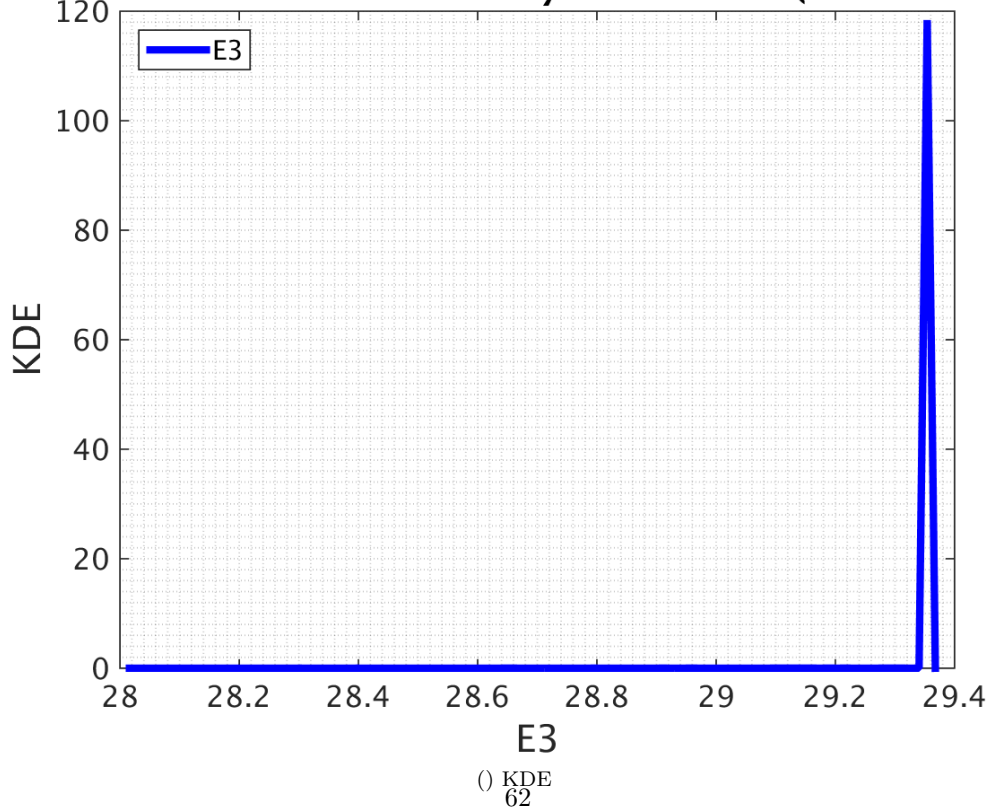


Figure 5.-13: Results for sample size 1e6



Parameter Cumulative Distribution Function (raw chair)**Parameter Kernel Density Estimation (raw chain)**

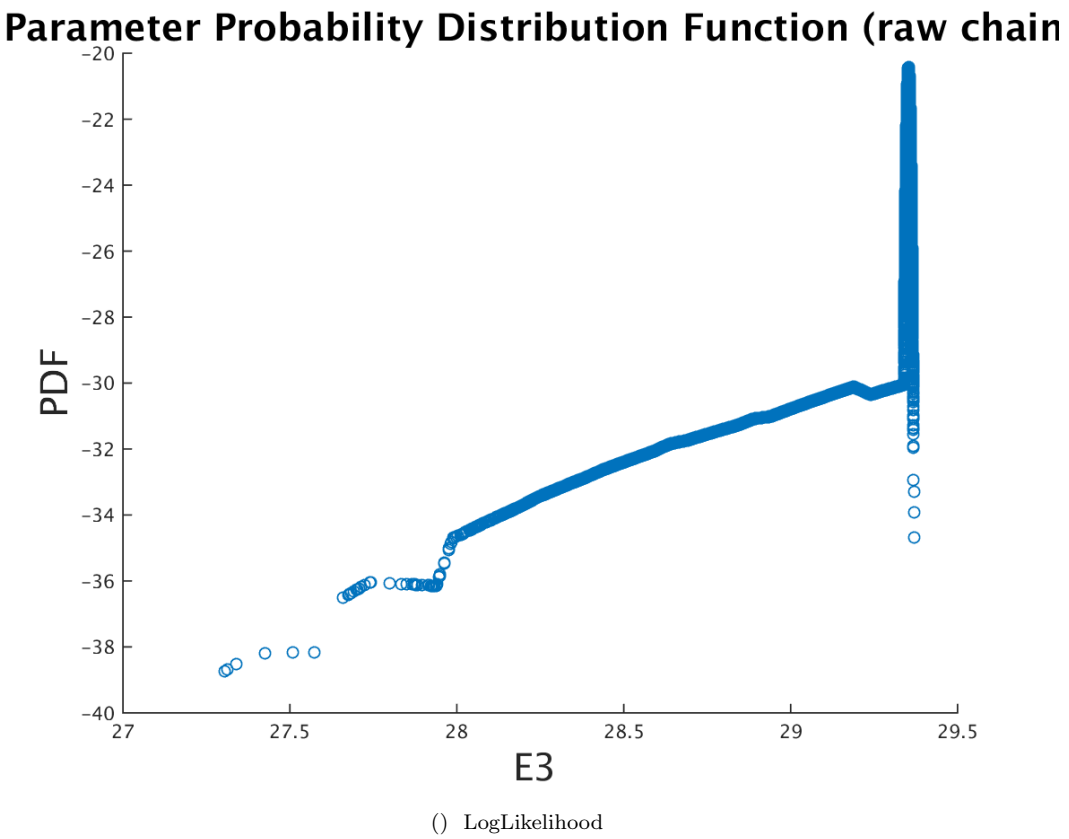
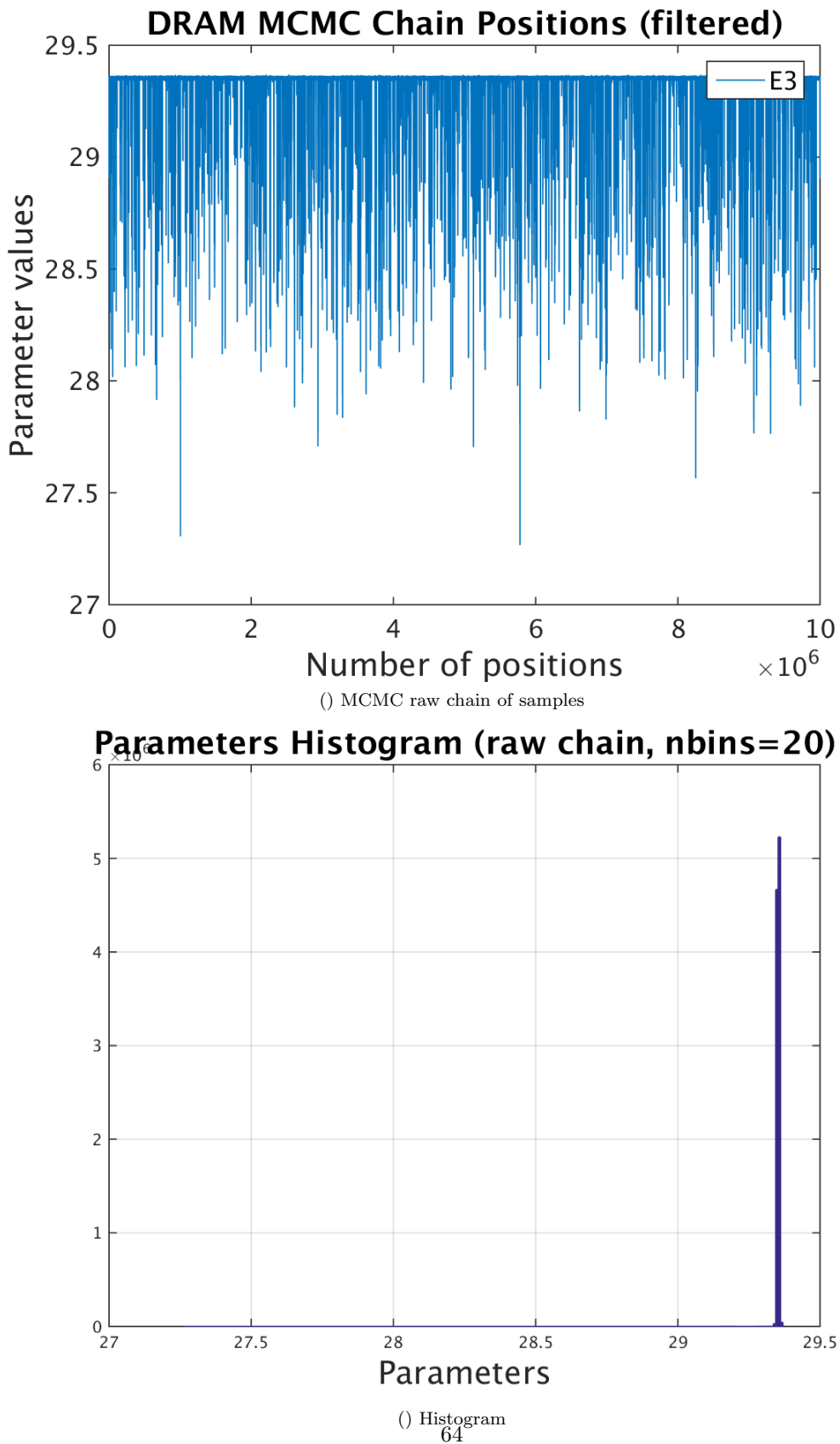
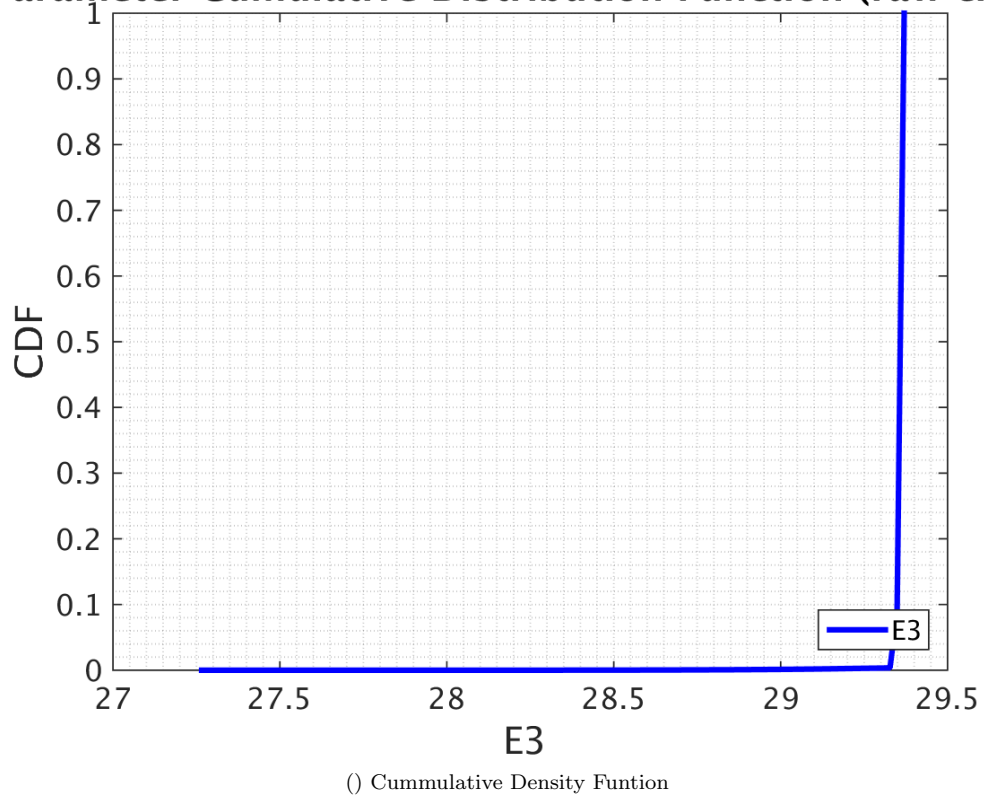
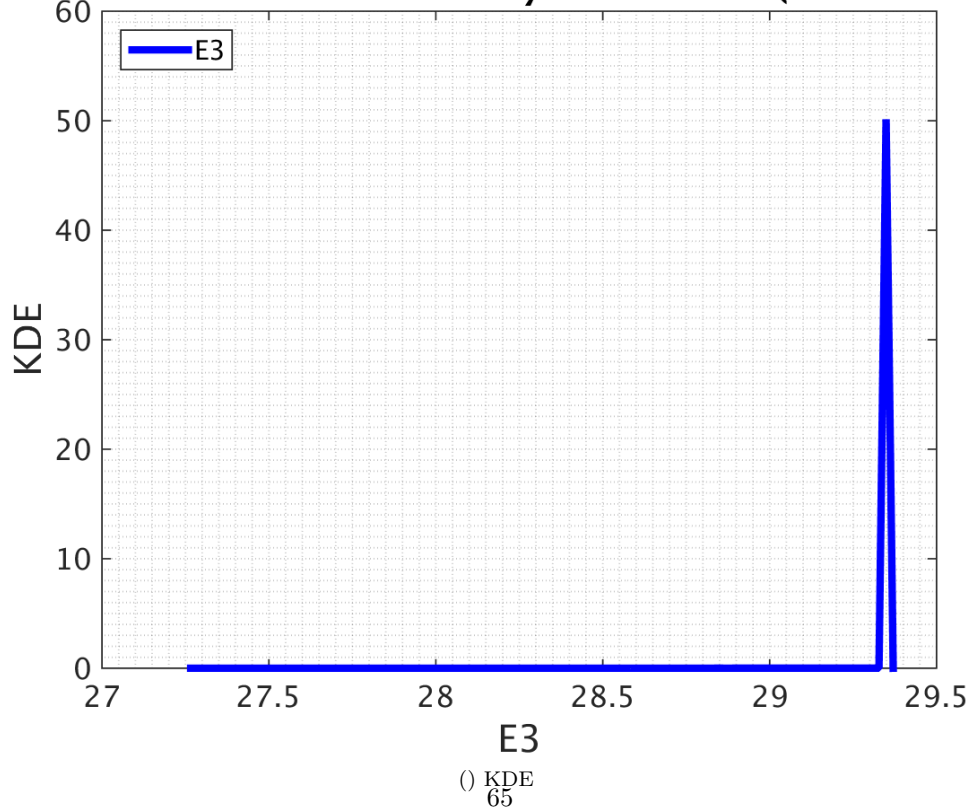


Figure 5.-14: Results for sample size 5e6



Parameter Cumulative Distribution Function (raw chair)**Parameter Kernel Density Estimation (raw chain)**

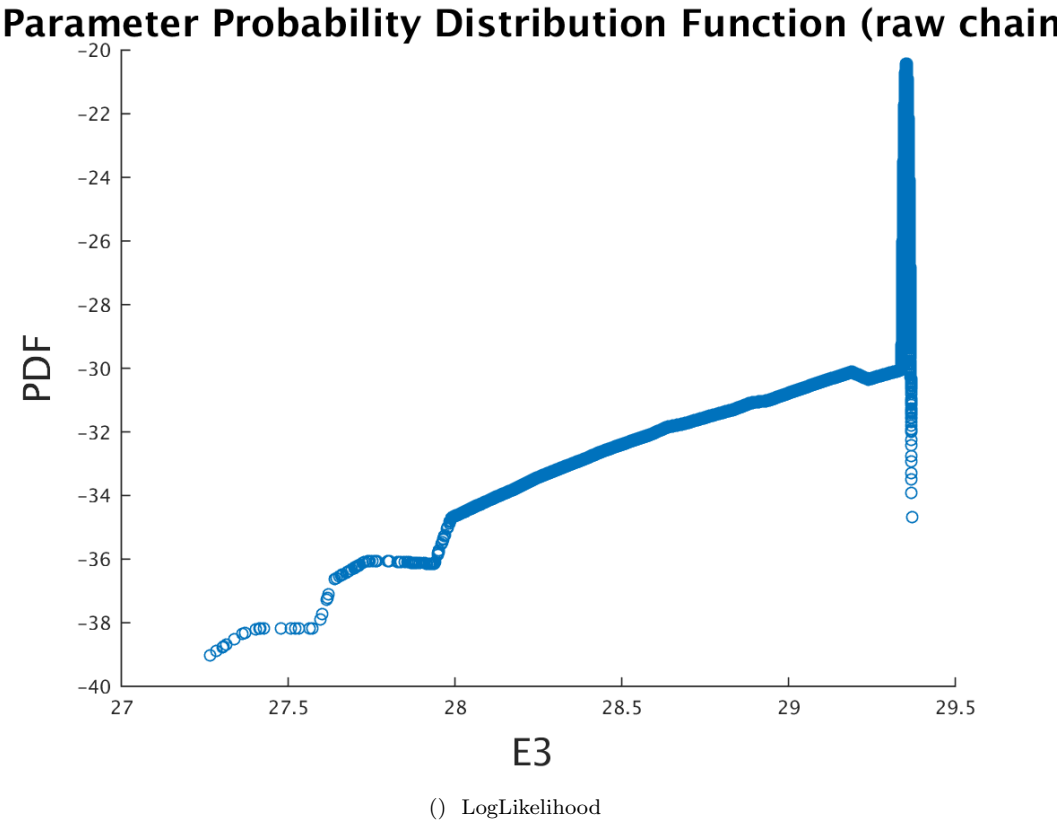


Figure 5.-15: Results for sample size 1e7

5.1.2 Convergence Study

In this section, we see the convergence of the probability distribution as we increase the raw chain sample size. The plot is done for surrogate size of 1000. In this analysis, raw chain size of 1e5, 5e5, 1e6, 5e6 and 1e7 is taken.

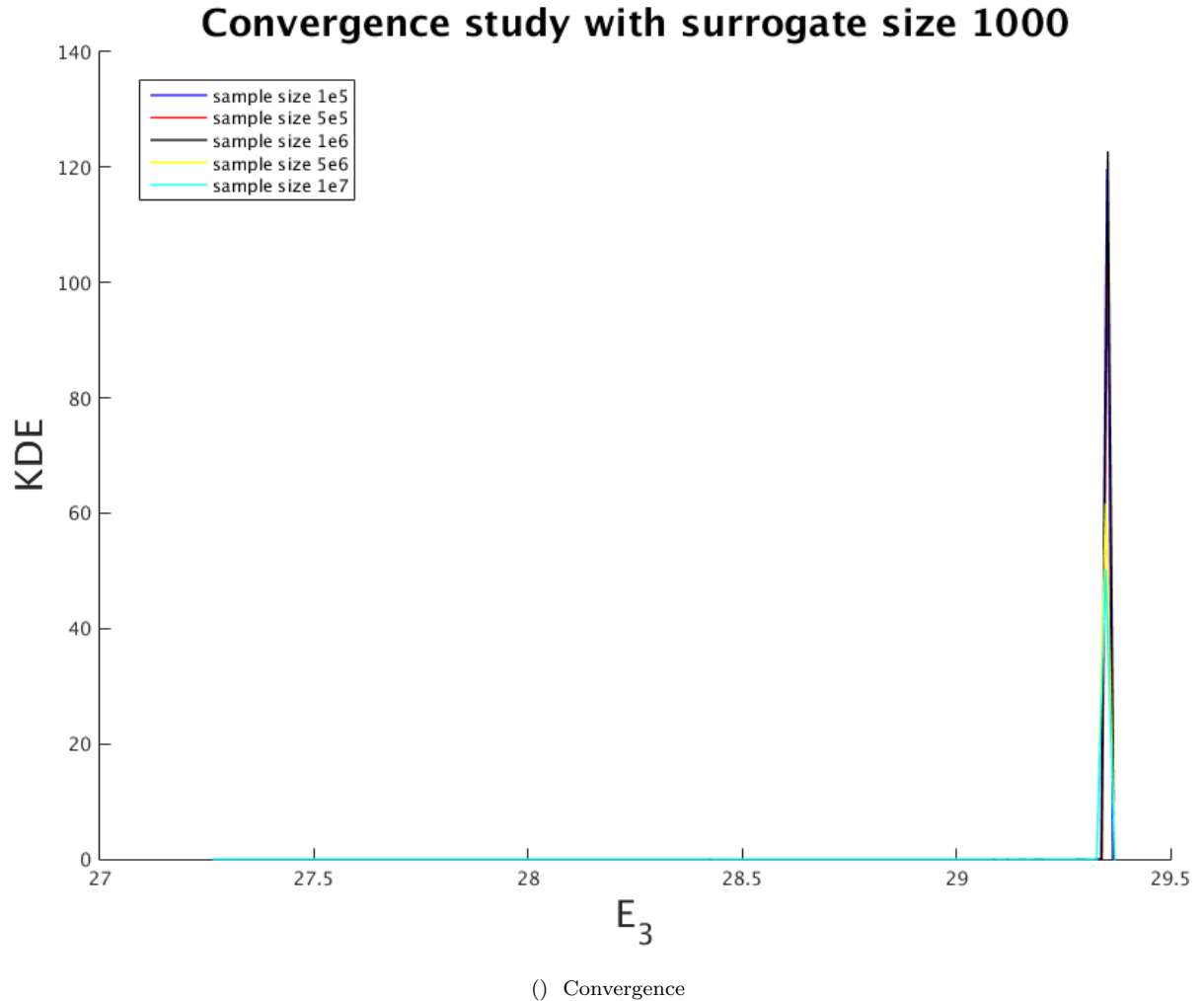
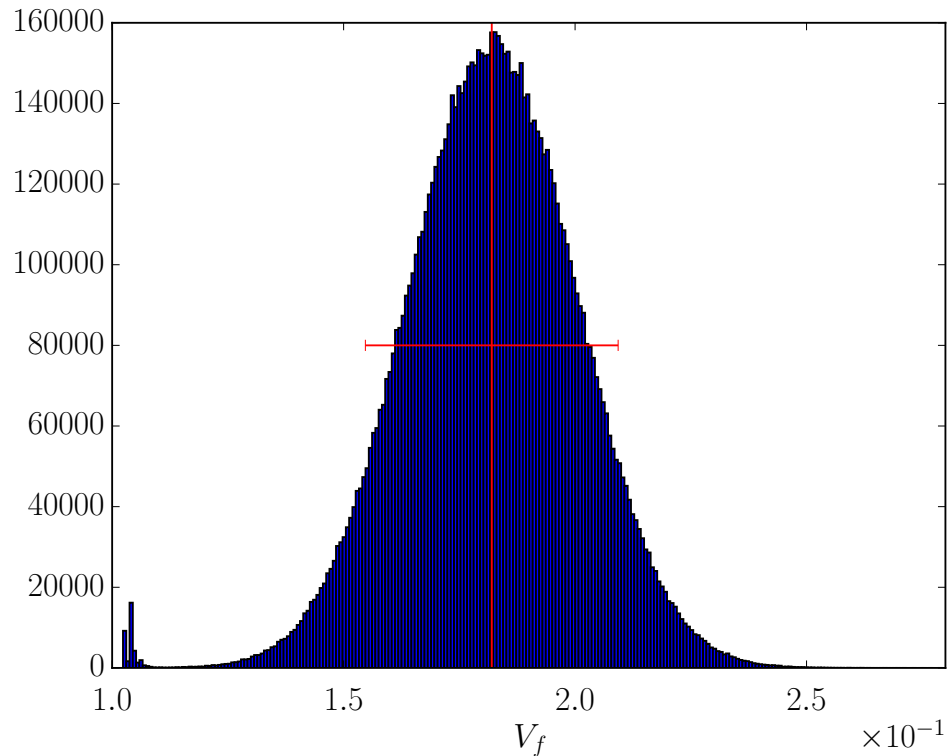


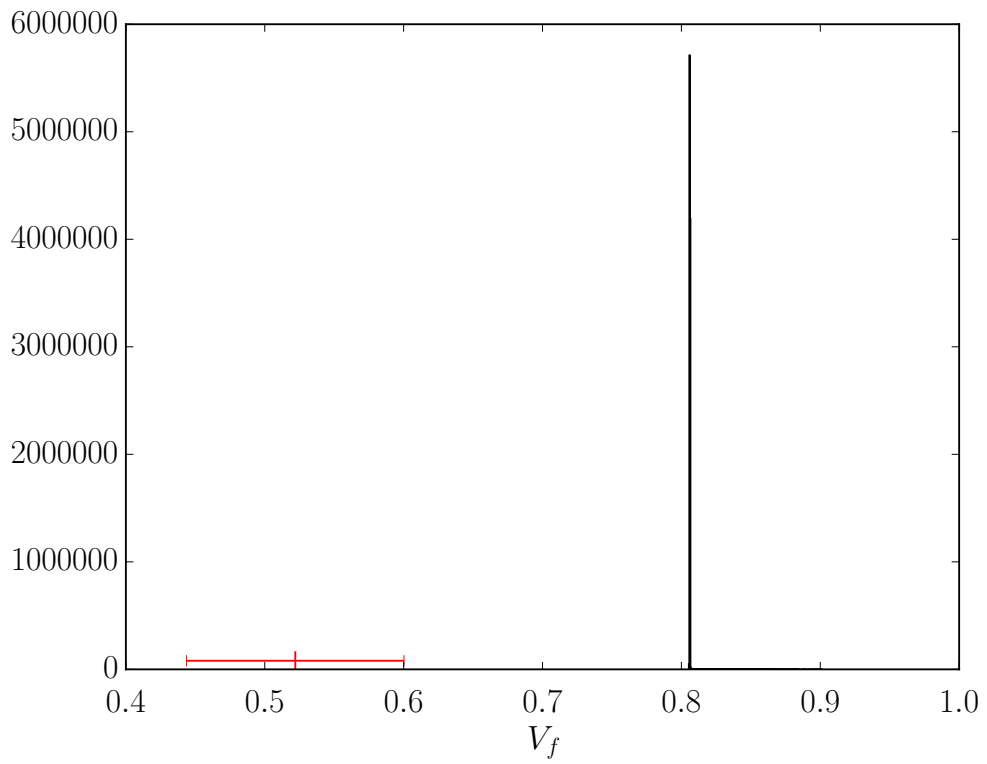
Figure 5.-14: Convergence for surrogate size 1000

5.1.3 flamespeed Data fit

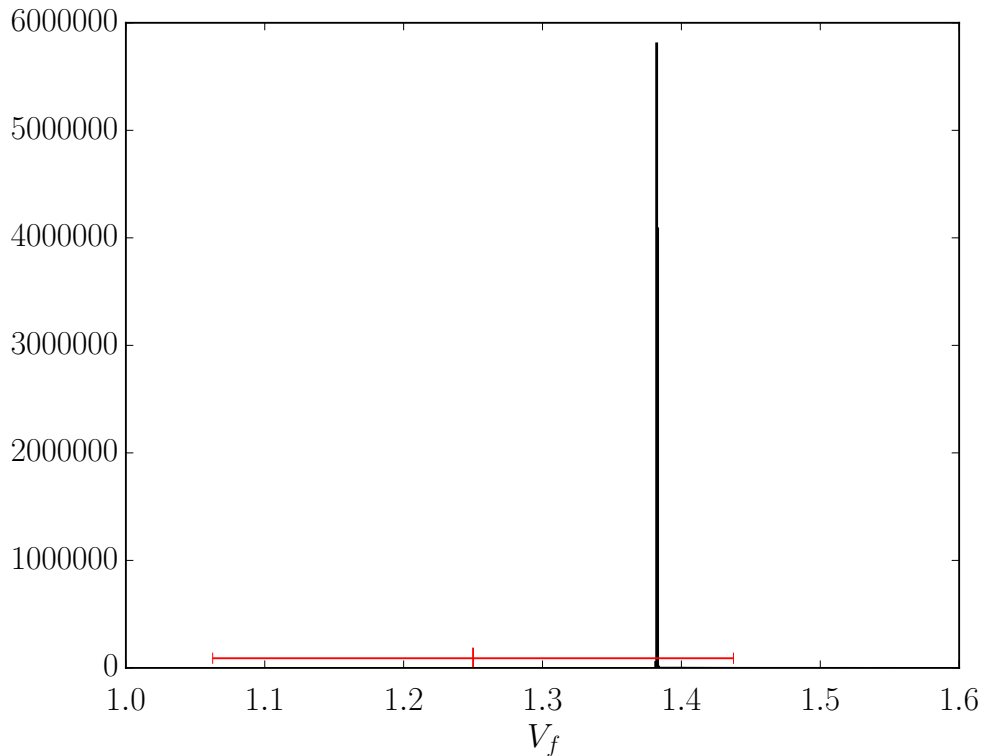
It is necessary to ensure that the samples of the parameter which we are drawing are fitting the flamespeed values of the experiment. In this section, we calculate the flamespeed for all the parameters drawn using the surrogate generated before. We have taken $1e7$ sample size and calculated flamespeed for different concentrations of ozone.



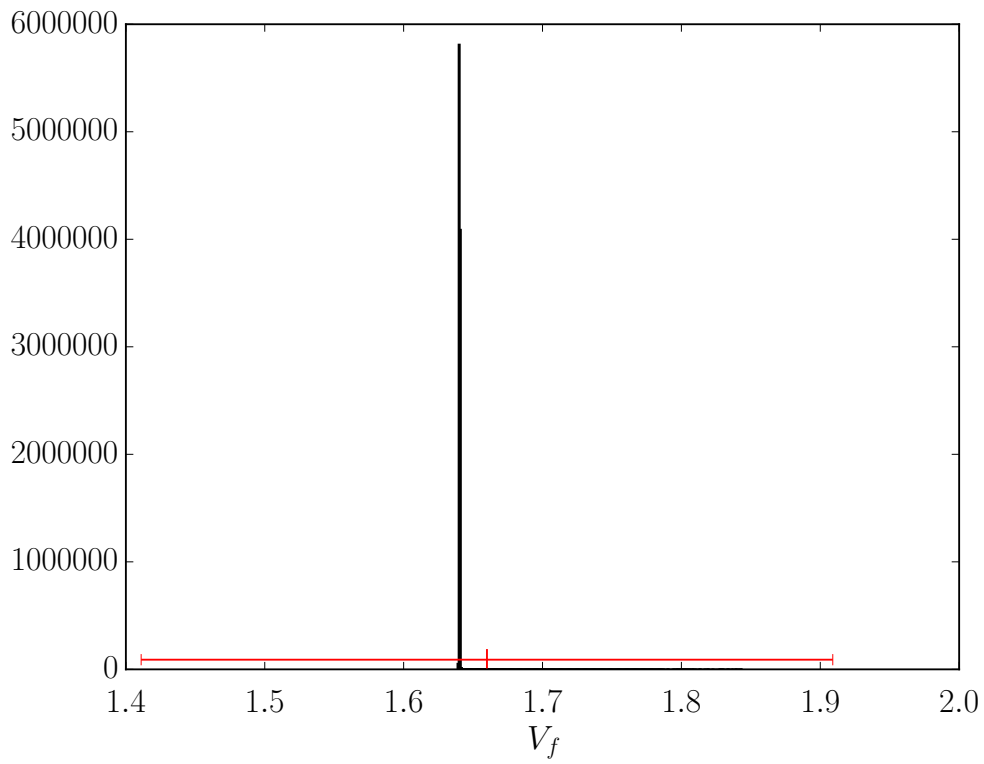
(a) Flame speed for 20 % ozone



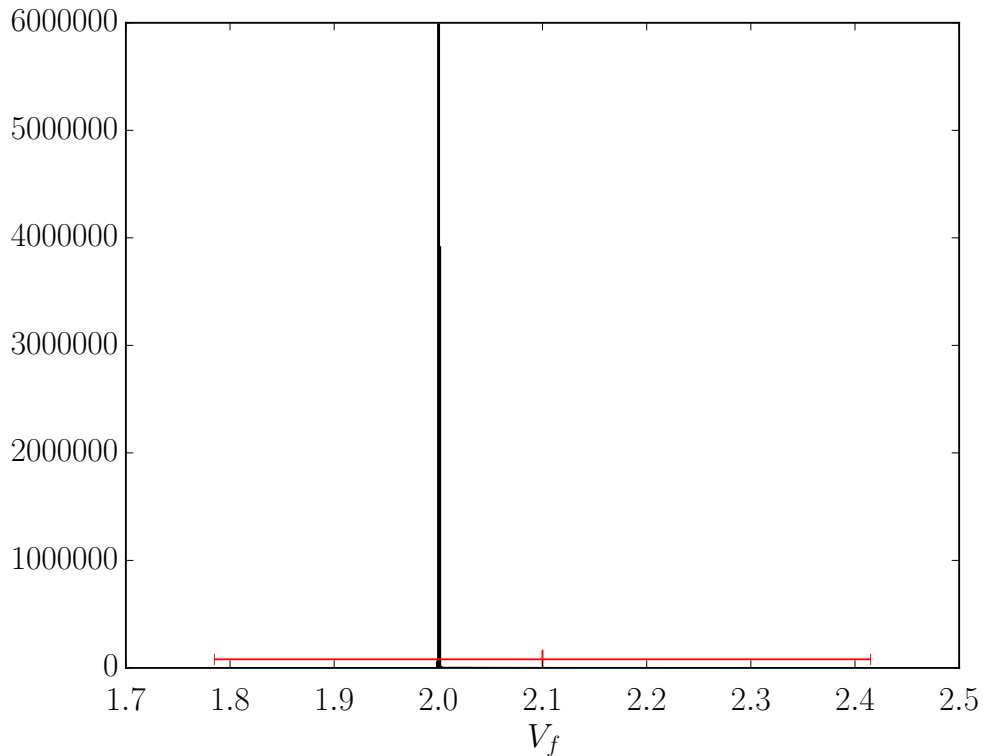
(b) Flame speed for 28 % ozone



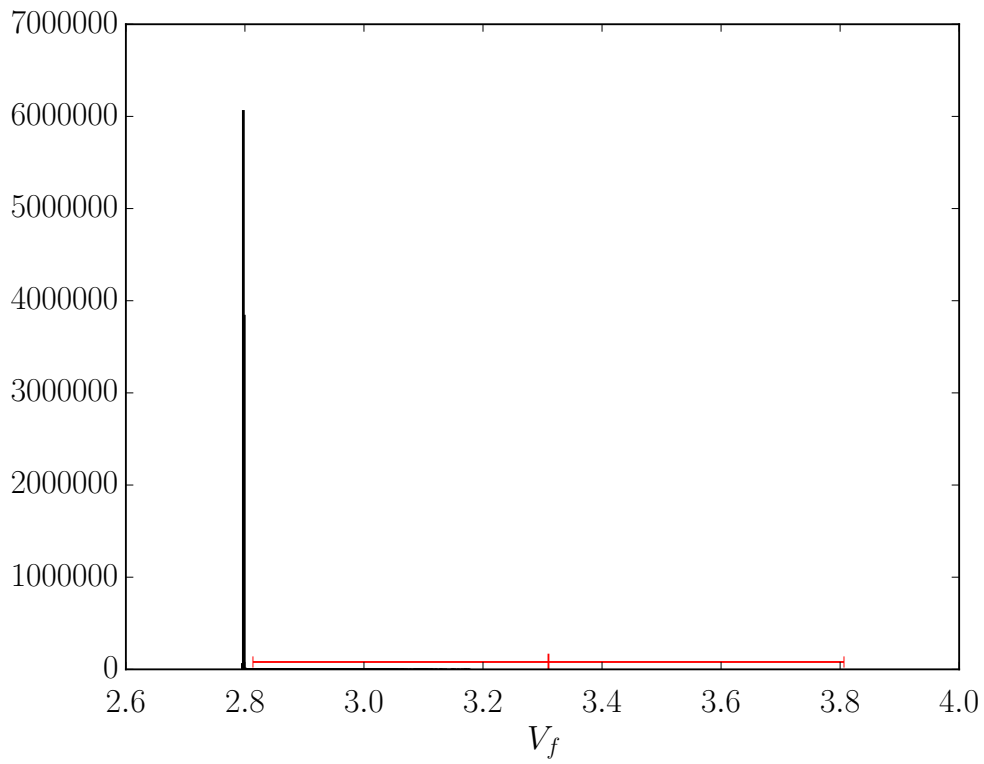
(c) Flame speed for 40 % ozone



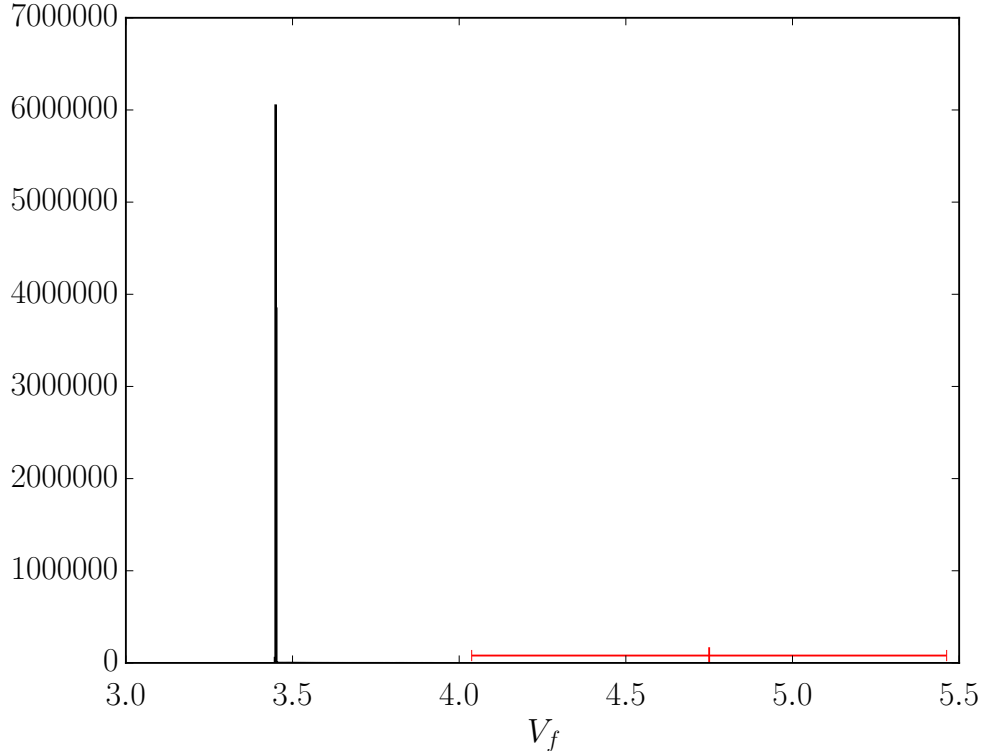
(d) Flame speed for 46 % ozone



(e) Flame speed for 53 % ozone



(f) Flame speed for 75 % ozone



(g) Flame speed for 100 % ozone

Figure 5.-16: Flamespeed Data fit

5.2 Estimating parameters Activation energies for reaction 2 and 3

The results displayed in this section are for the uncertainty involved in the calculation of flamespeed depending on two parameters i.e the activation energy for the fall off reaction and activation energy for reaction 2 in the ozone mechanism. The percentage of ozone is taken 20,28,40,46,53,75 and 100 percent according to the experimental data available to us from Streng[3]. The results are displayed in three section. In first section, for constant surrogate size, the number of samples are changes. In the second part of the results, convergence study is done for all samples with surrogate size 100*100. In third section, we ensure that samples of the parameters which we are drawing are fitting the flamespeed values of the experiment. Also for varying size the map point of the resulting pdf does not change greatly. The surrogates for individual concentrations are constructed using linear interpolation function. The initial guess for the map point is calculated using nelder mead optimization technique. After supplying initial guess over large domain it is found that the map point is the same no matter where we start our guess.

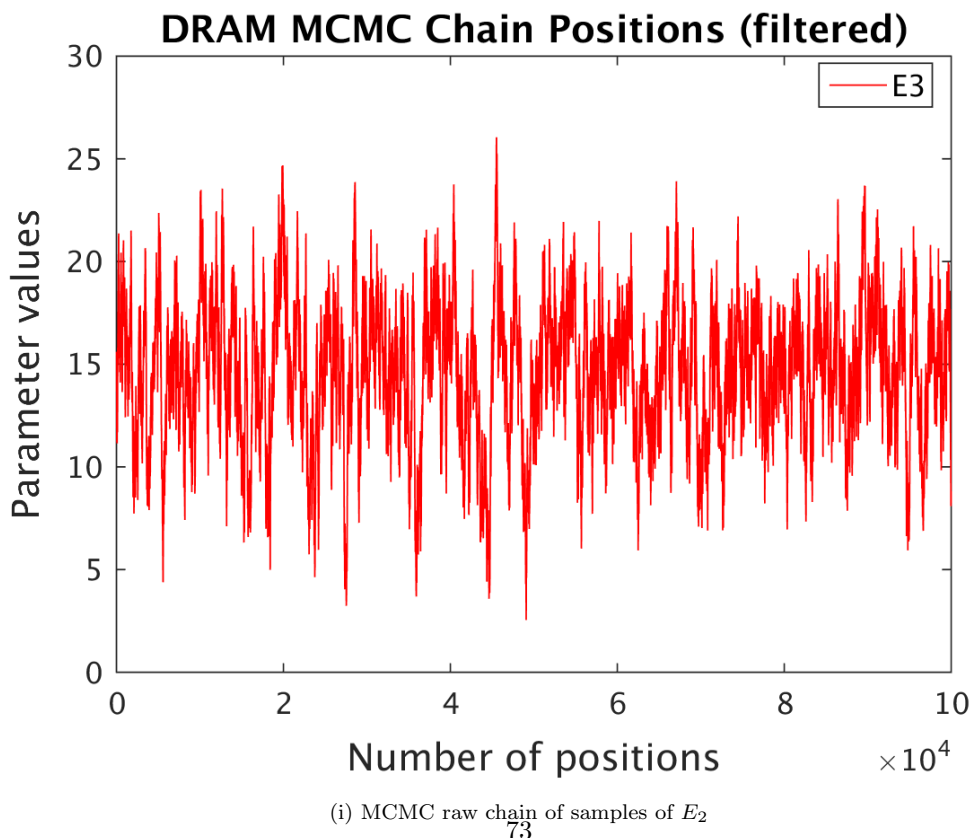
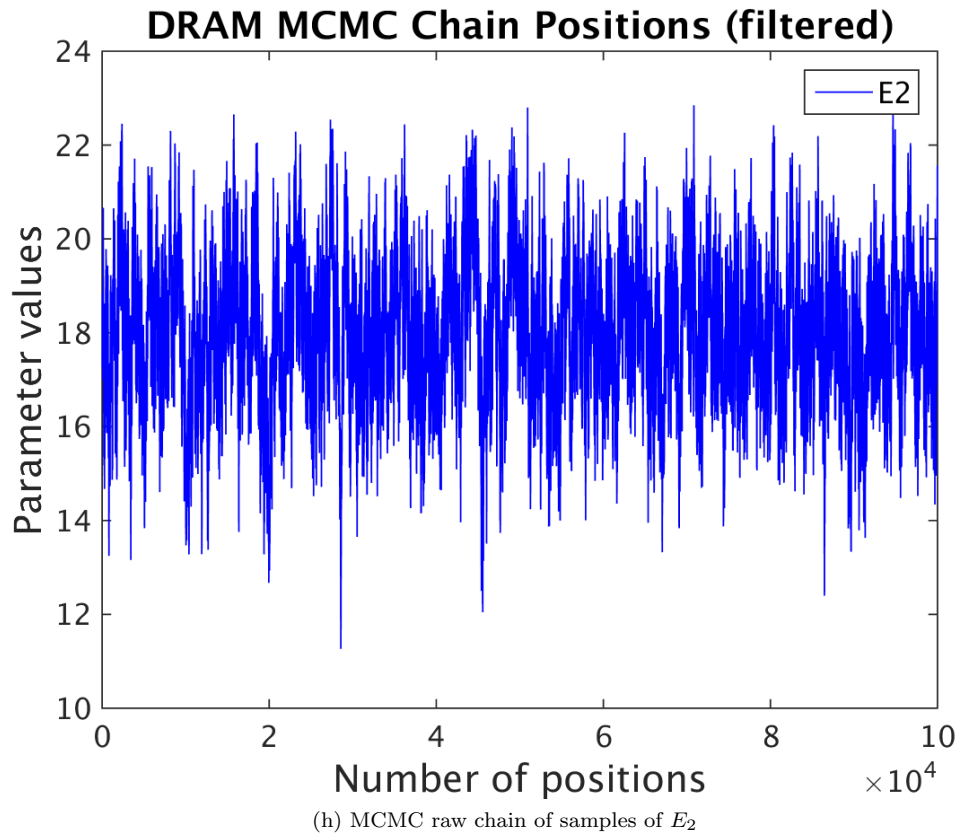
5.2.1 Different surrogate sizes

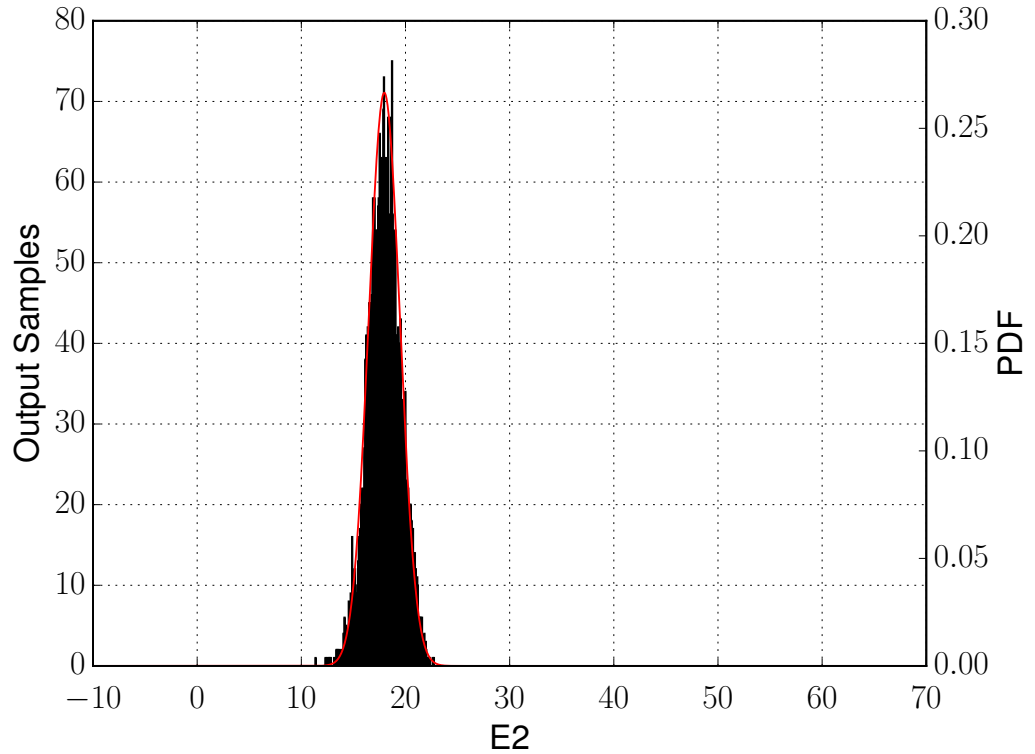
Here the surrogate size is defined as *samplesize* * 2 matrix. The flamespeed is calculated for given samples in the domain (-10 to 40) for E_2 and in the domain (-10 to 40) for E_3 . Other values are

calculated as linear interpolation of these 1000 points. In this analysis, raw chain size of $1e5$, $5e5$, $1e6$, $5e6$ and $1e7$ is taken.

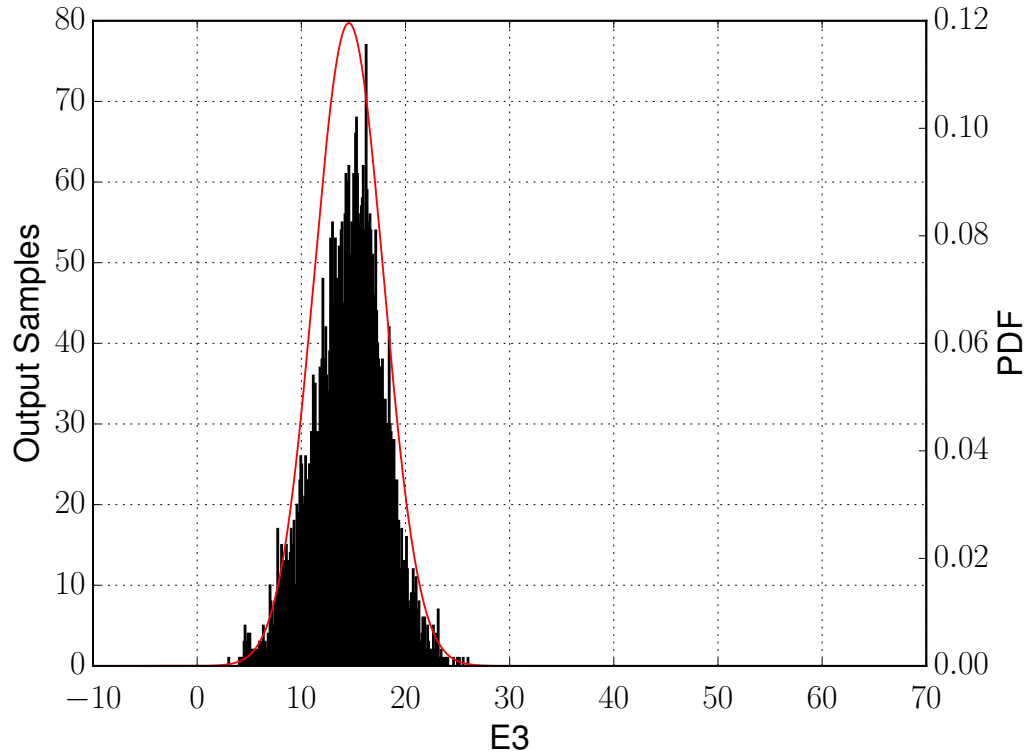
Sample size (Surrogate size) 10^*10

In this section we calculated flamespeed values for 100 (10^*10) different points in the domain and the remaining values are linear combination of these 100 points. The results below are for sample size $1e5$, $5e5$, $1e6$, $5e6$ and $1e7$.



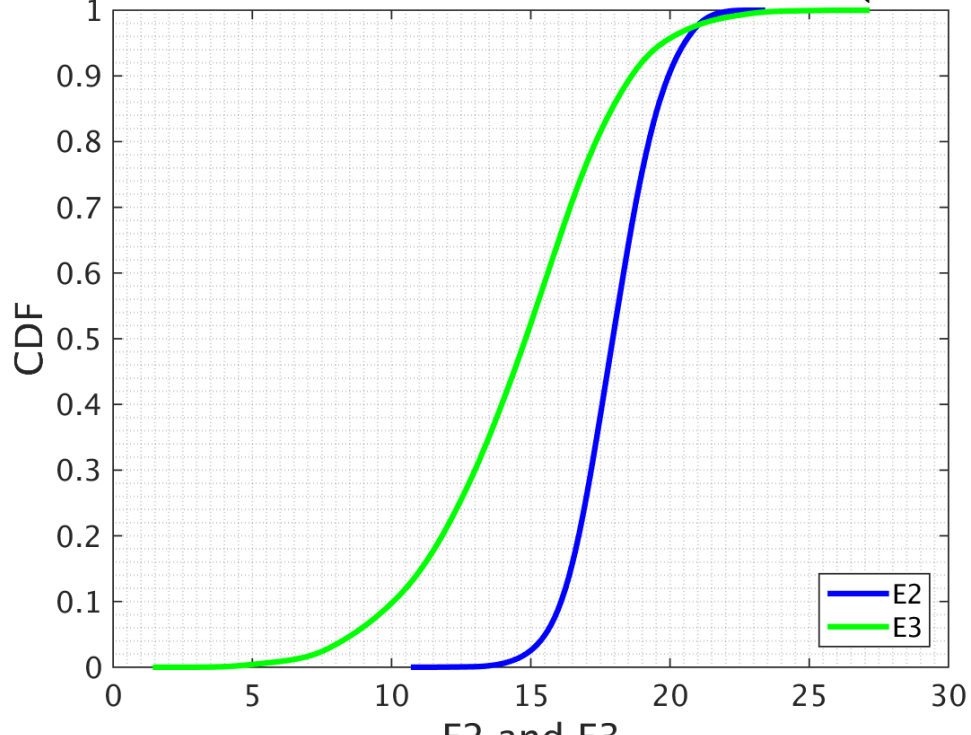


(j) Histogram for E_2



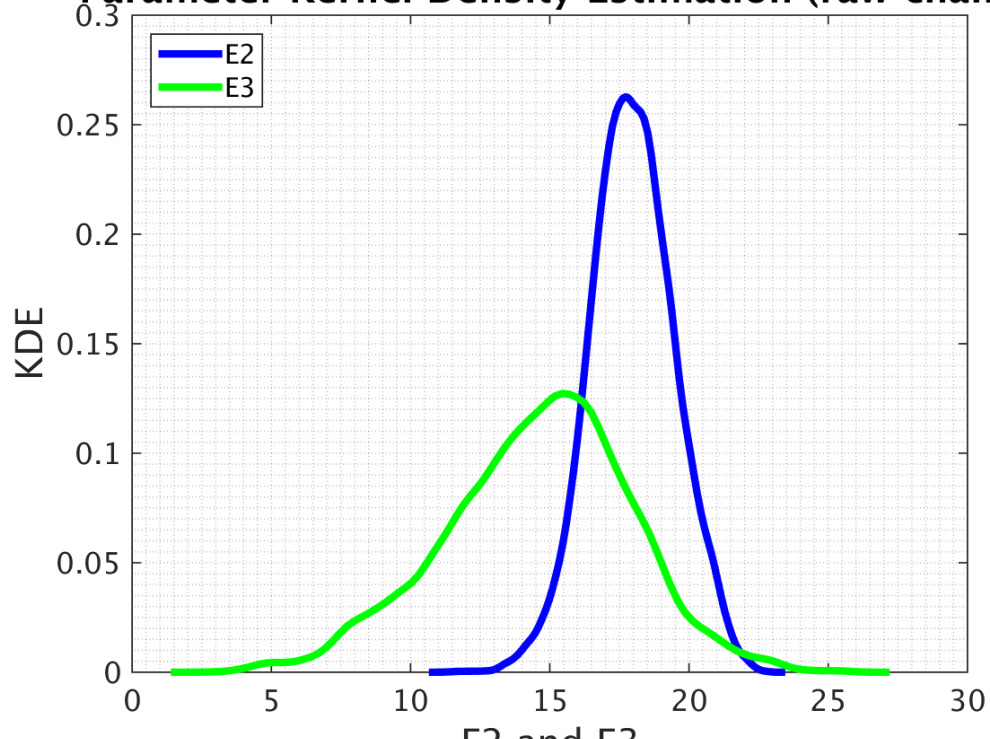
(k) Histogram for E_3

Parameter Cumulative Distribution Function (raw chair)



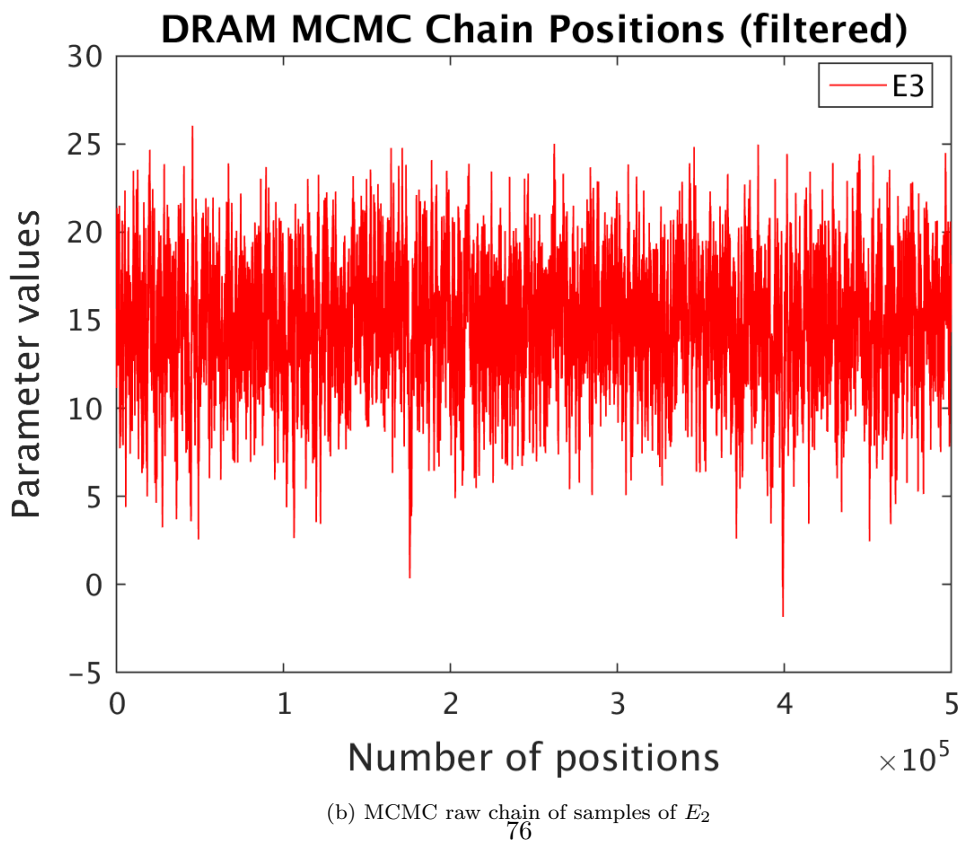
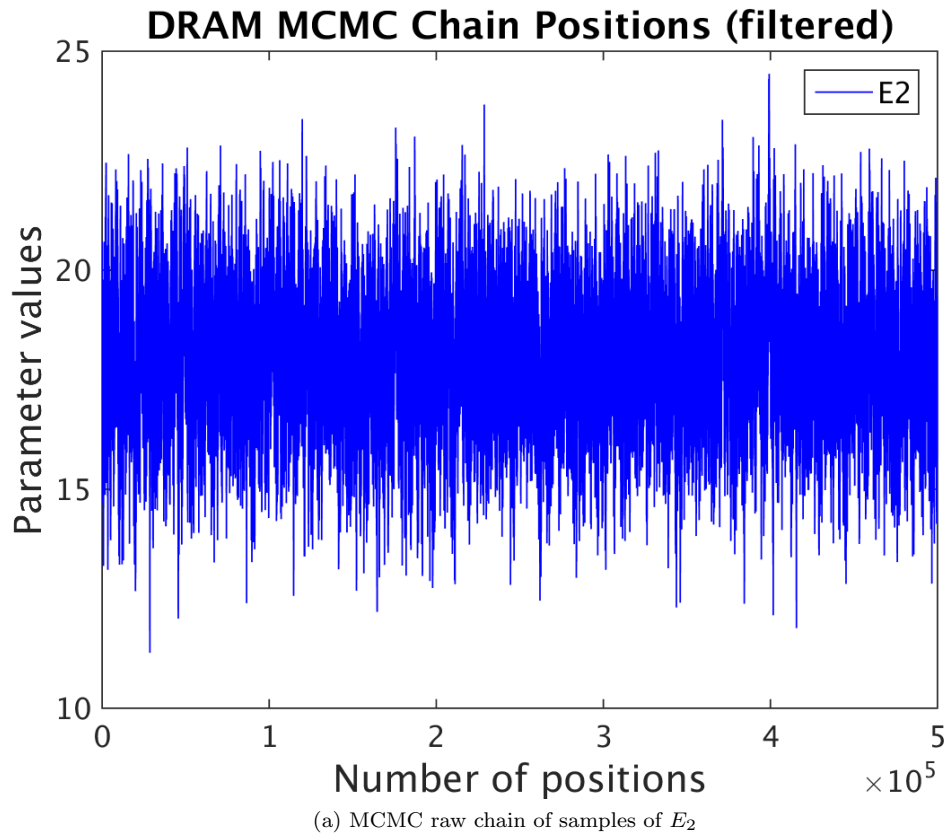
(l) Cummulative Density Funtion

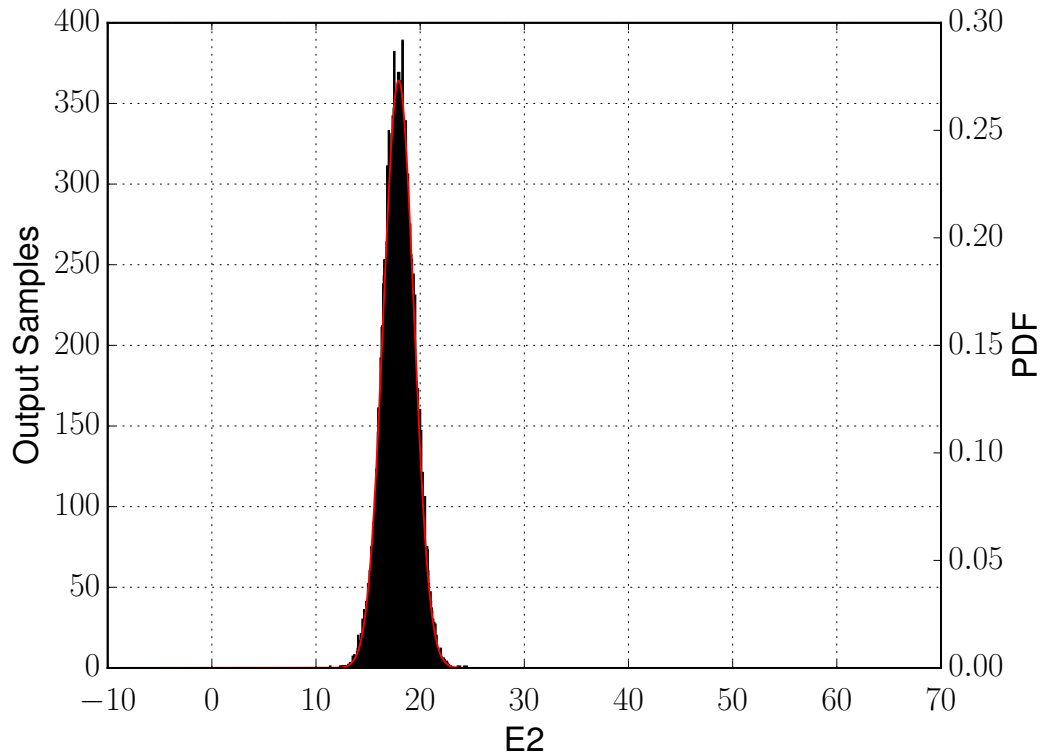
Parameter Kernel Density Estimation (raw chain)



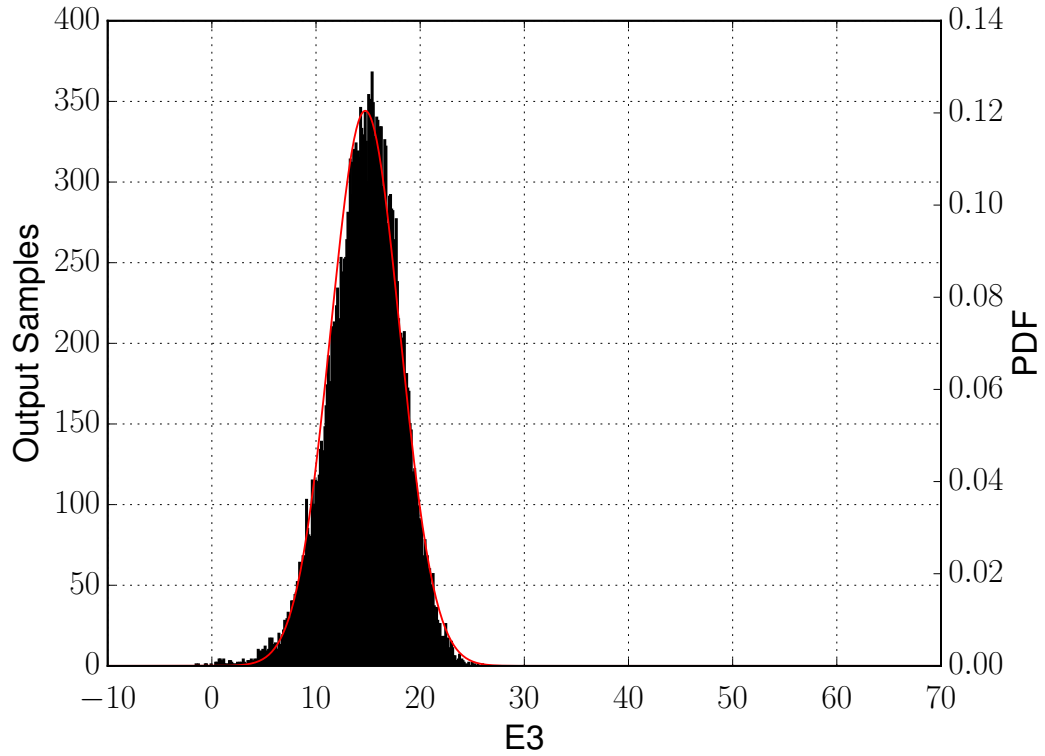
(m) KDE
75

Figure 5.-16: Results for sample size 1e5

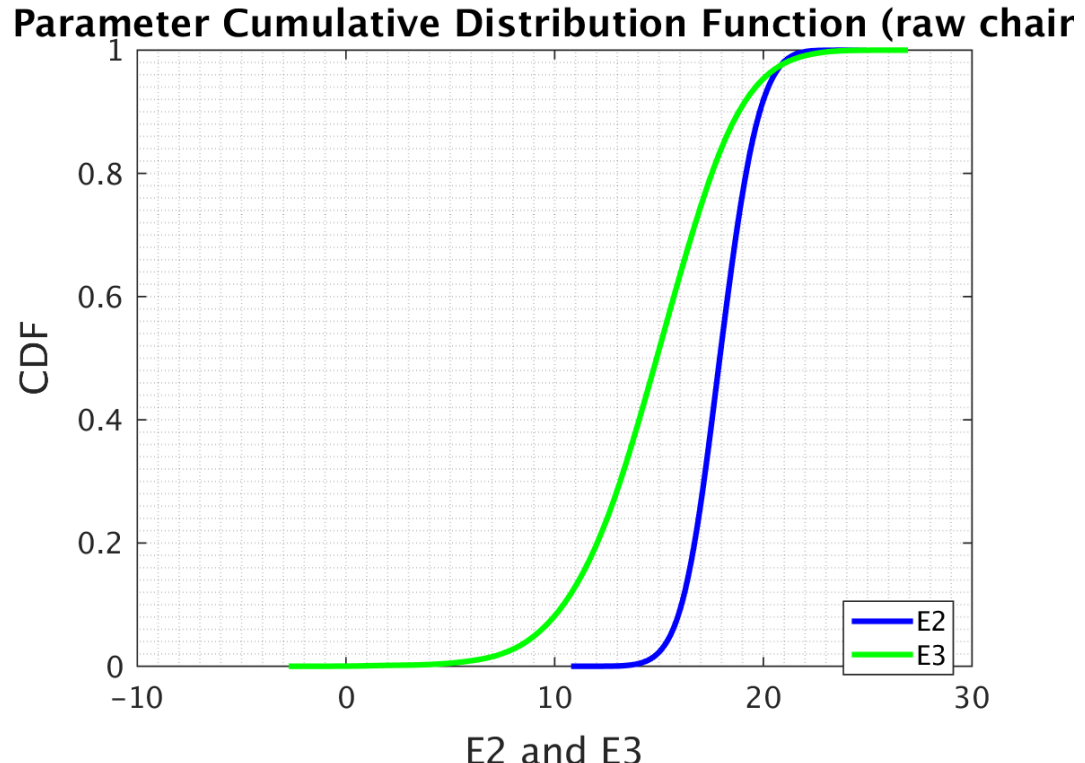




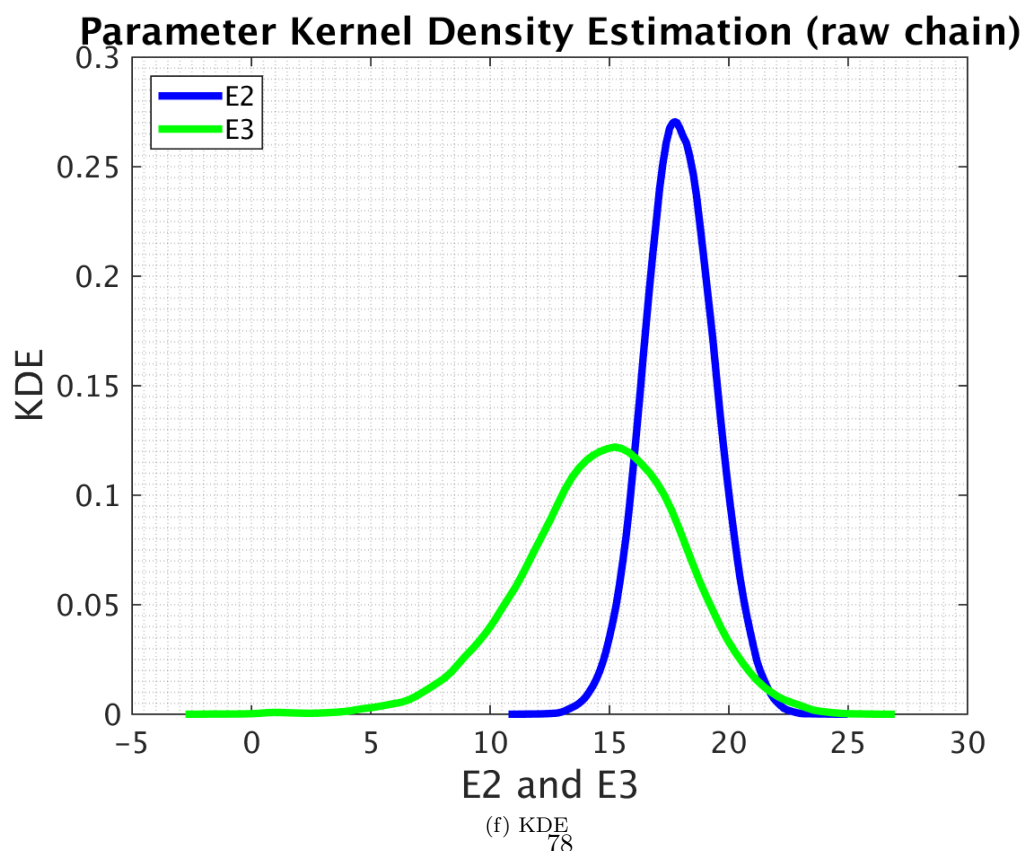
(c) Histogram for E_2



(d) Histogram for E_3

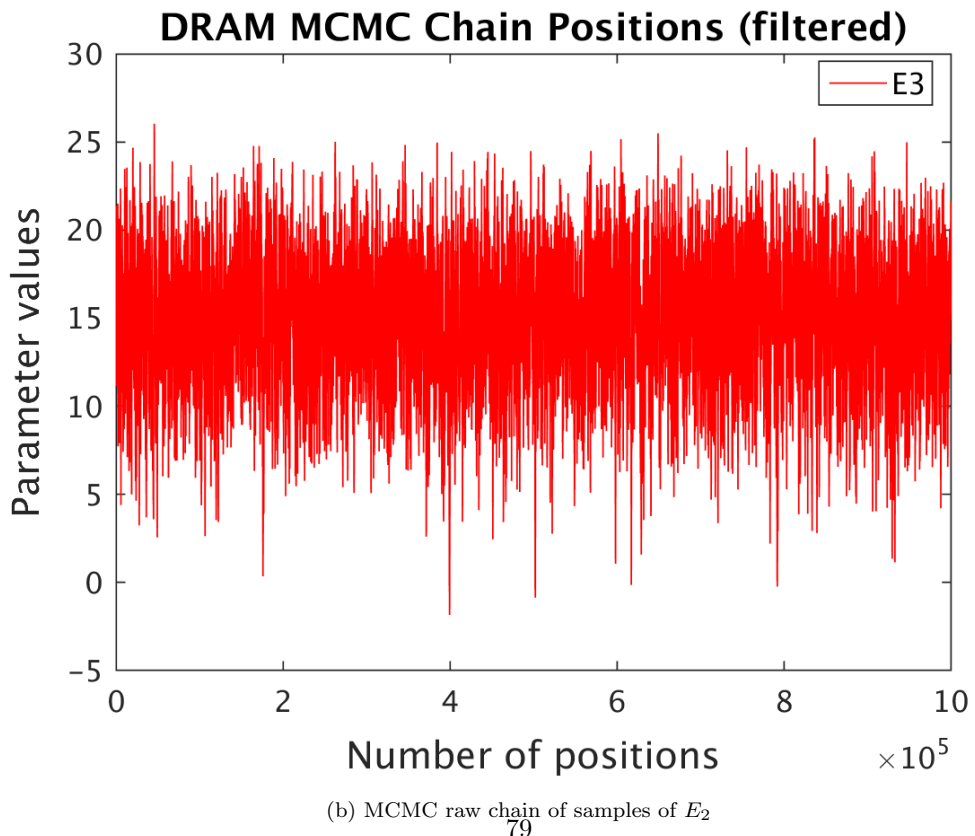
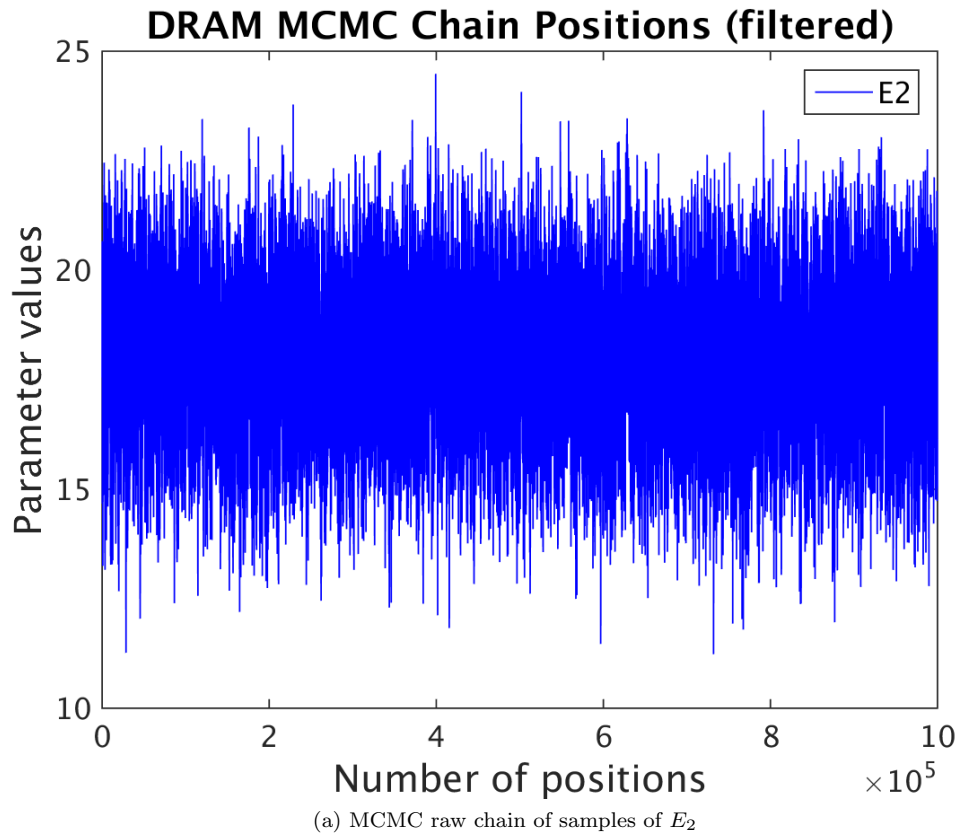


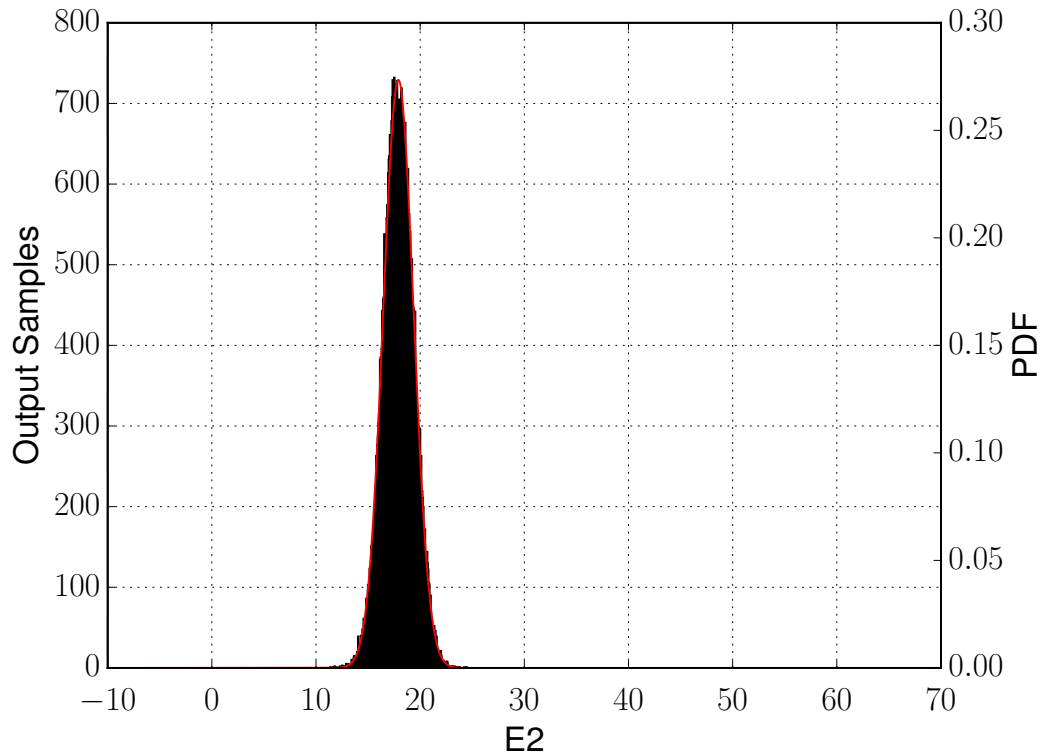
(e) Cummulative Density Funtion



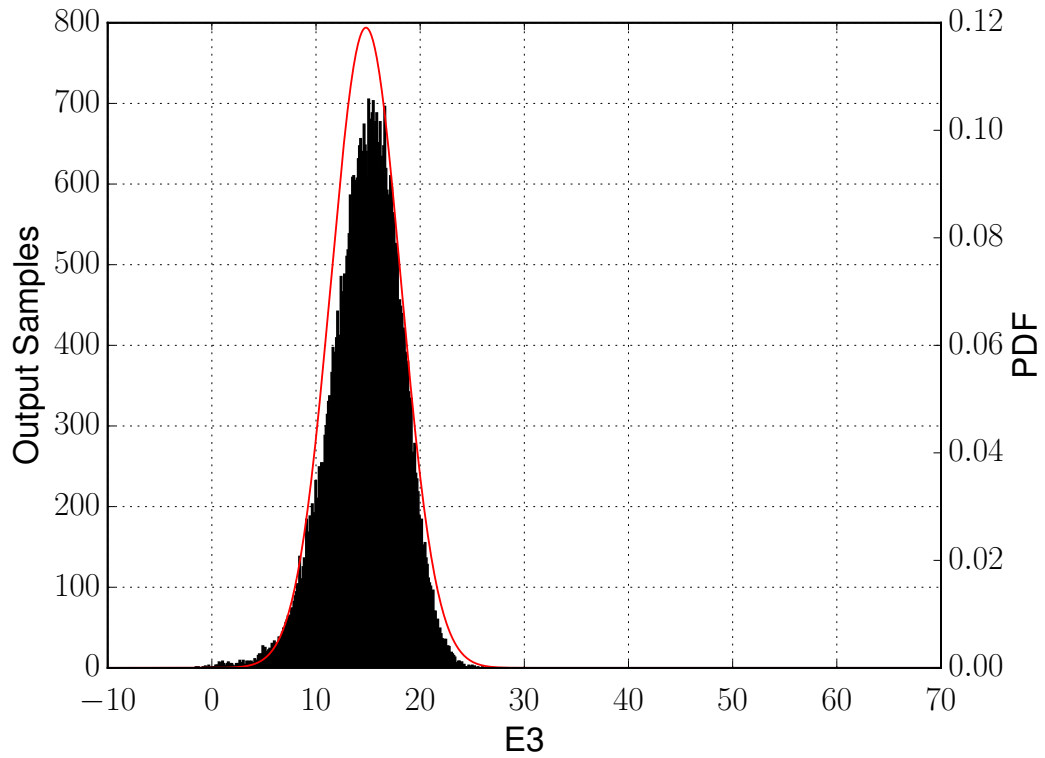
(f) KDE
78

Figure 5.-16: Results for sample size 5e5

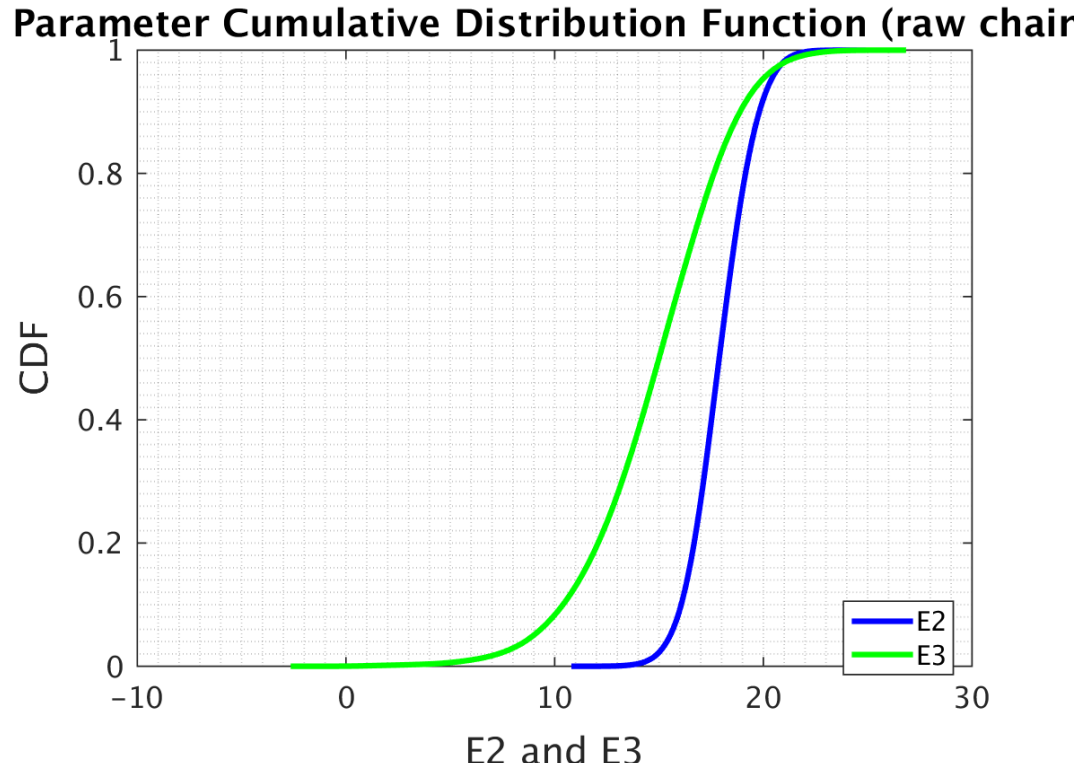




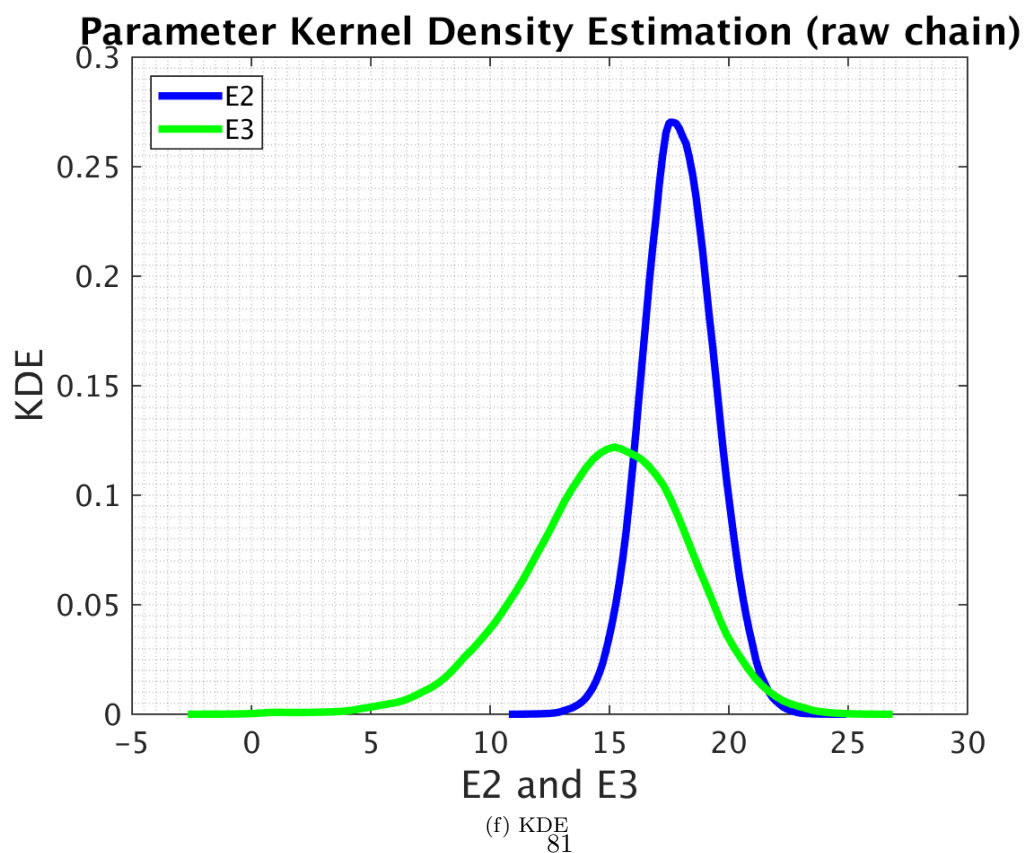
(c) Histogram for E_2



(d) Histogram for E_3

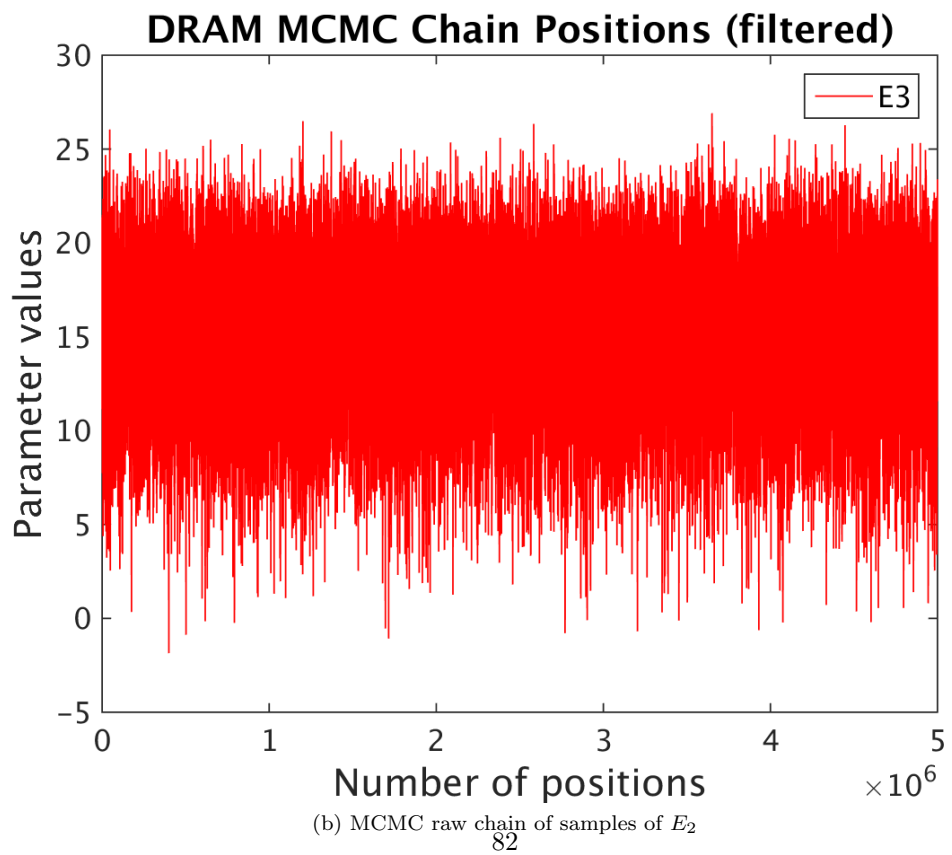
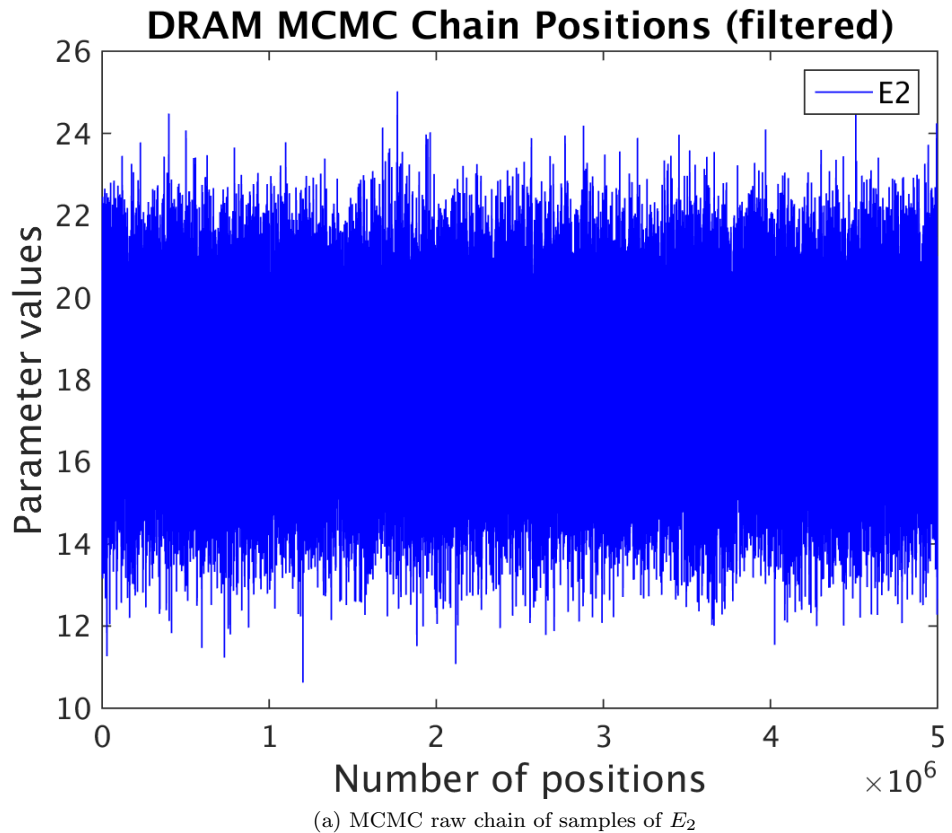


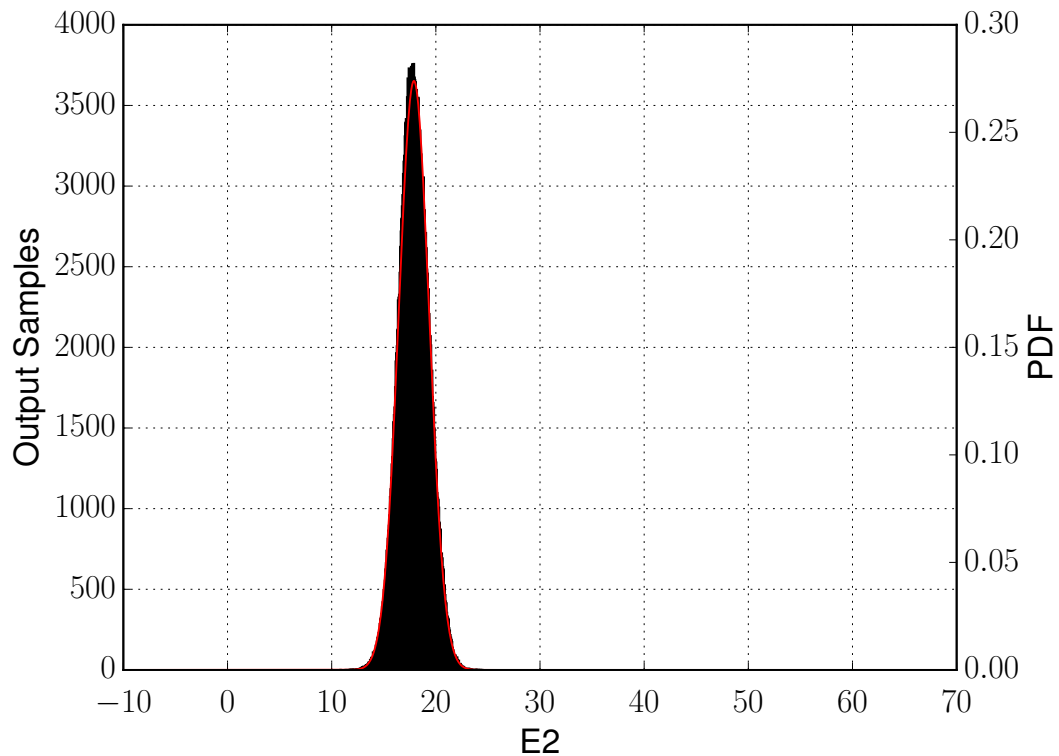
(e) Cummulative Density Funtion



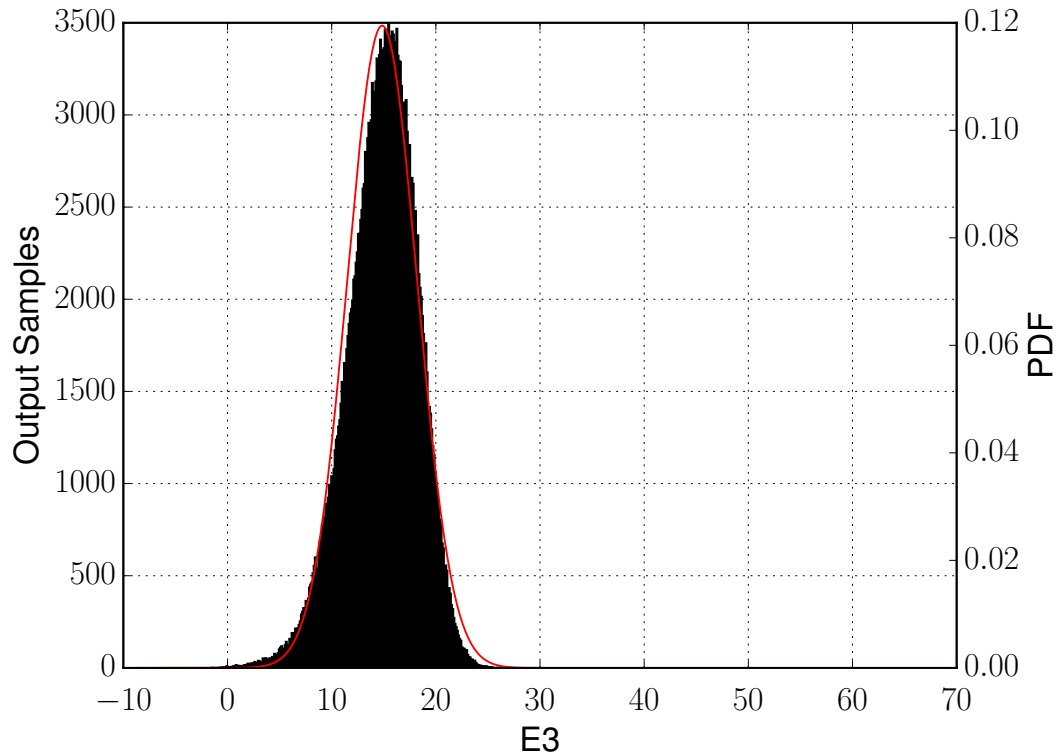
(f) KDE
81

Figure 5.-16: Results for sample size 1e6



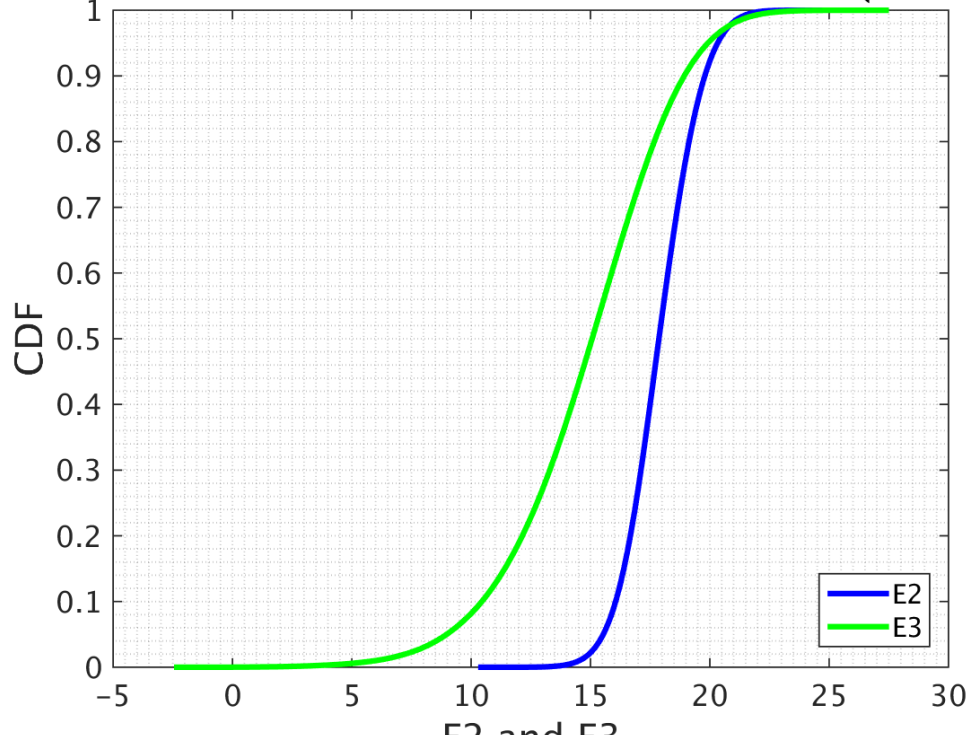


(c) Histogram for E_2



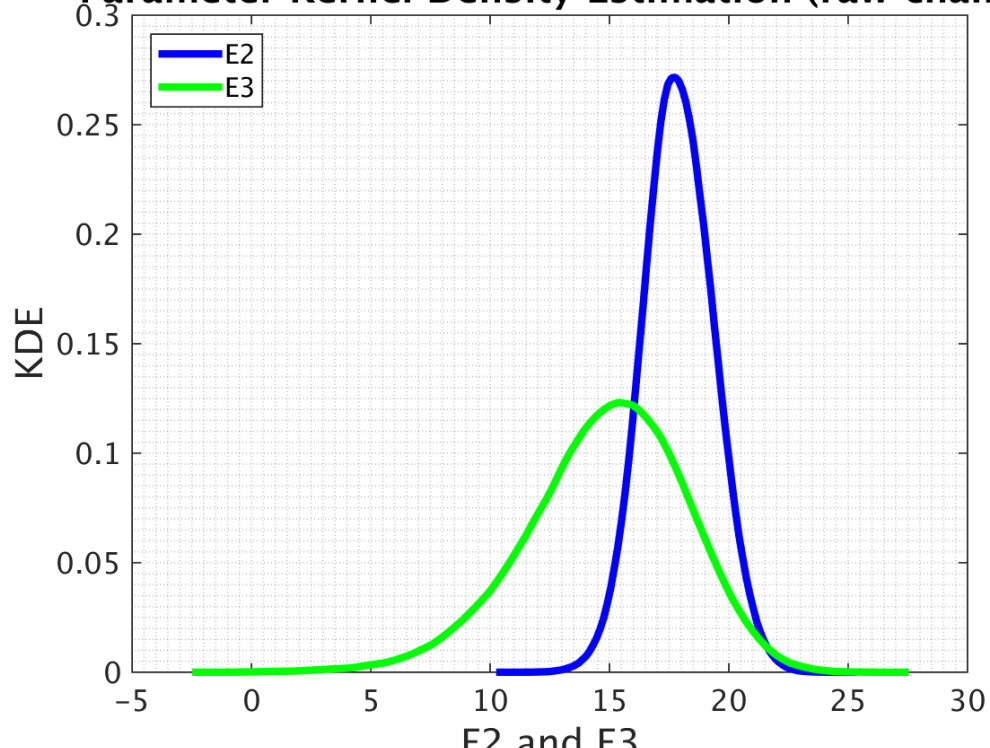
(d) Histogram for E_3

Parameter Cumulative Distribution Function (raw chain)



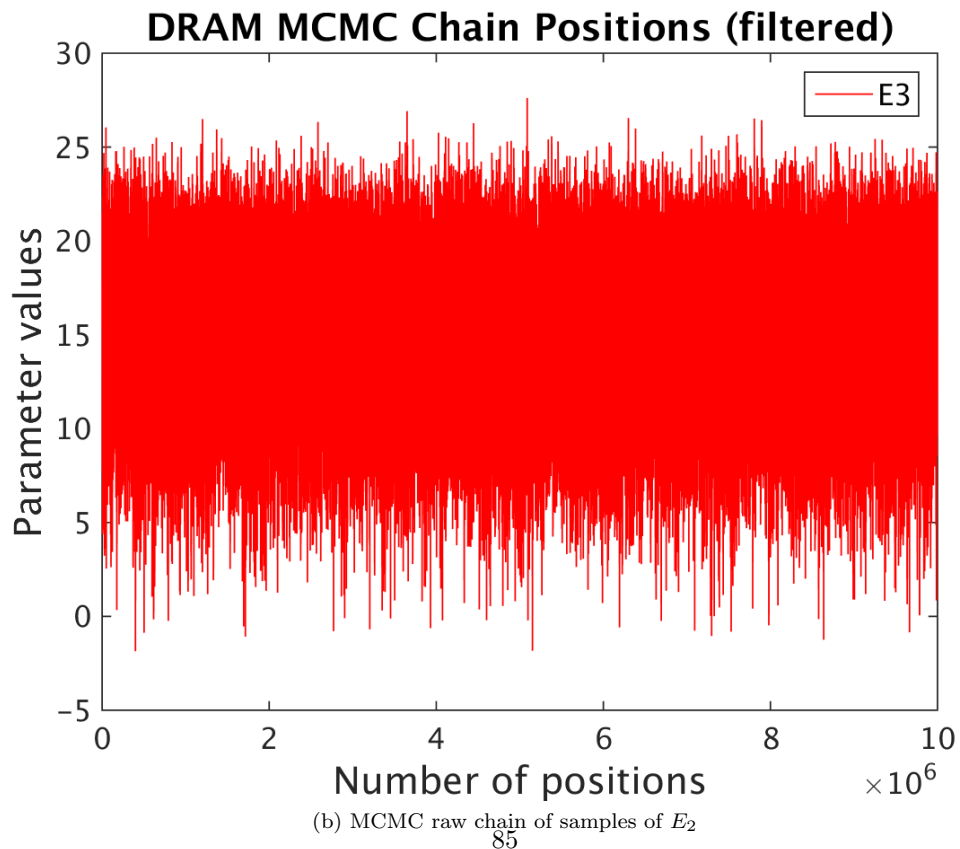
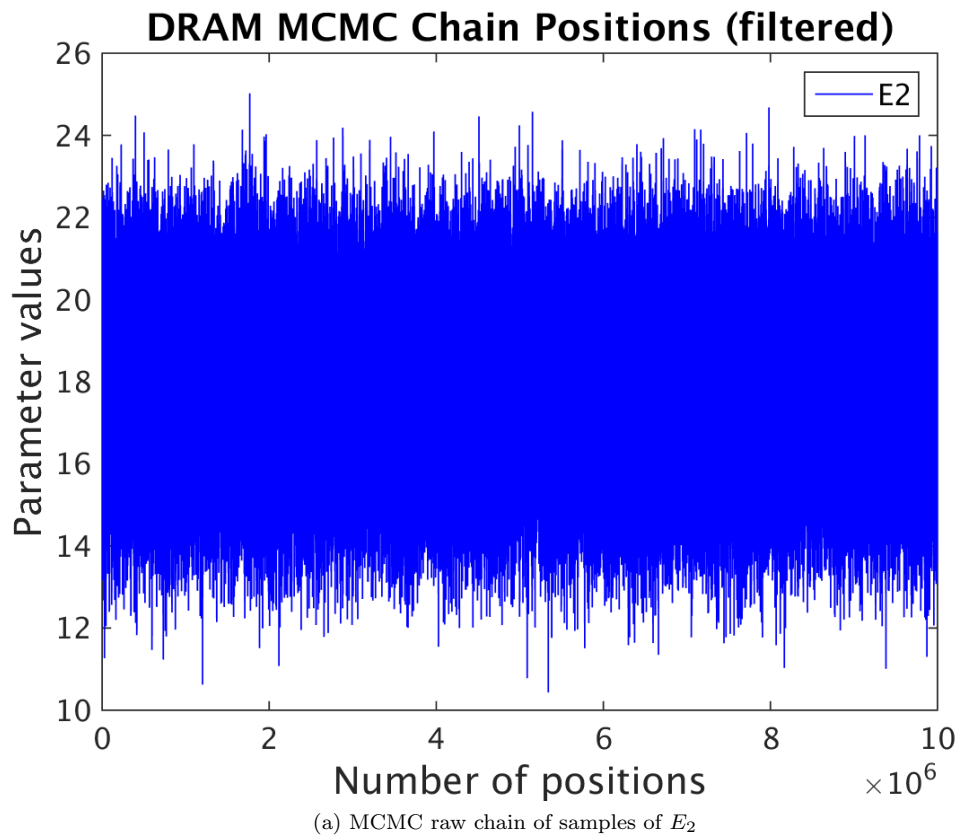
(e) Cummulative Density Funtion

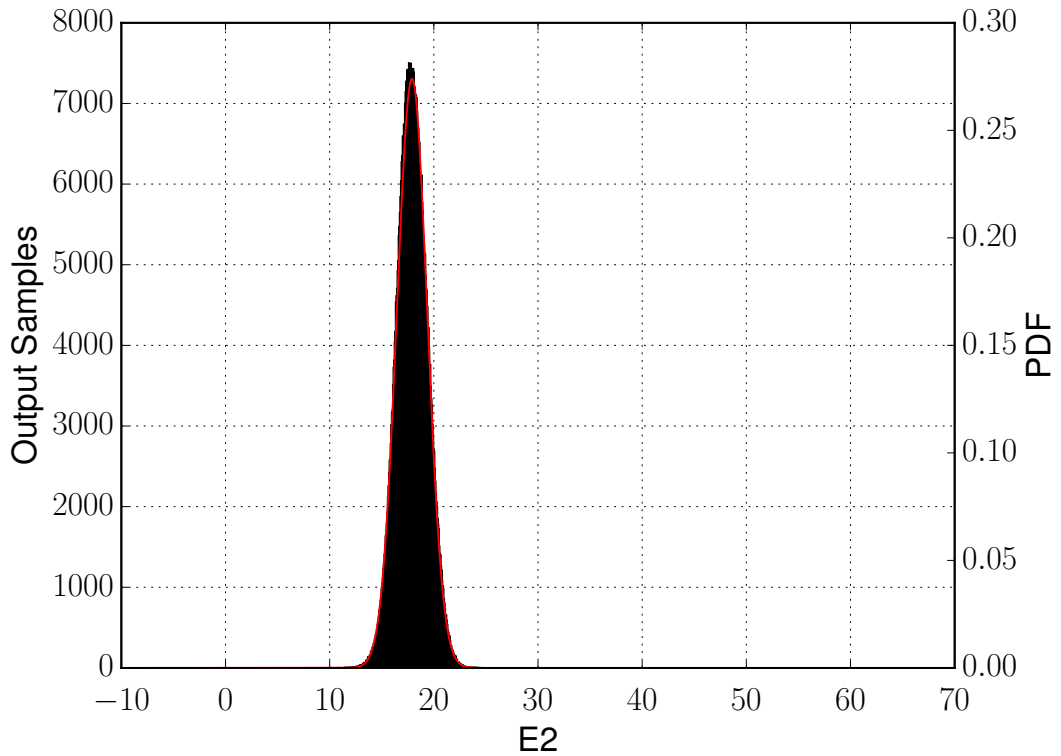
Parameter Kernel Density Estimation (raw chain)



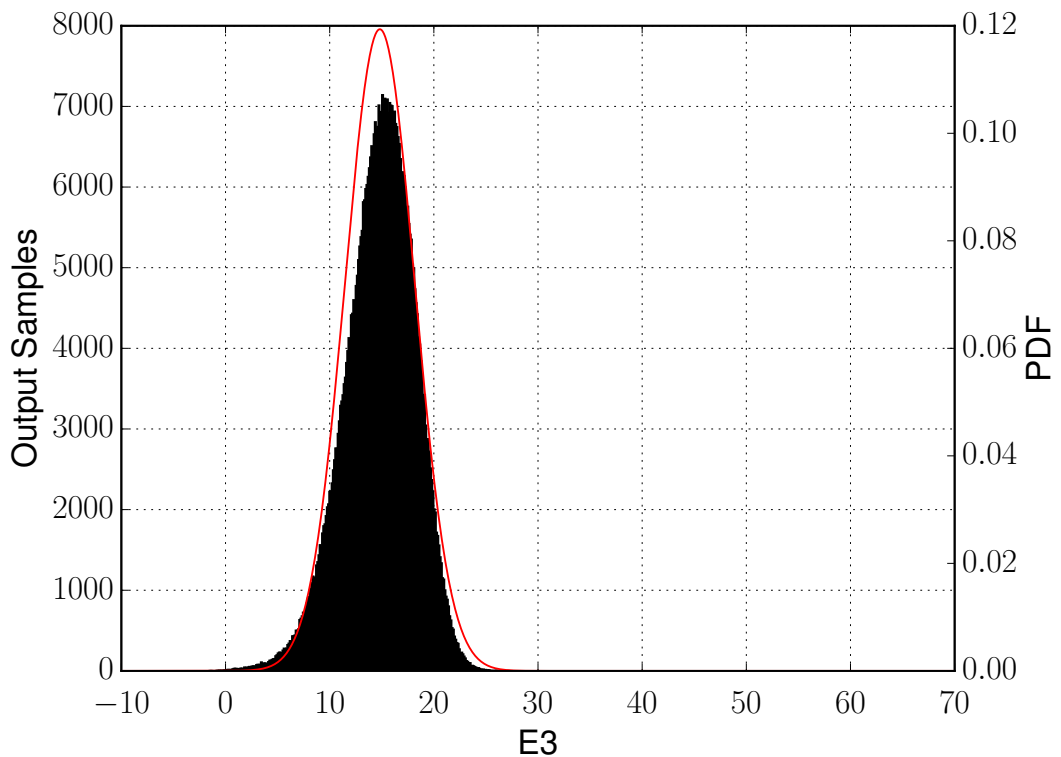
(f) KDE
84

Figure 5.-16: Results for sample size 5e6



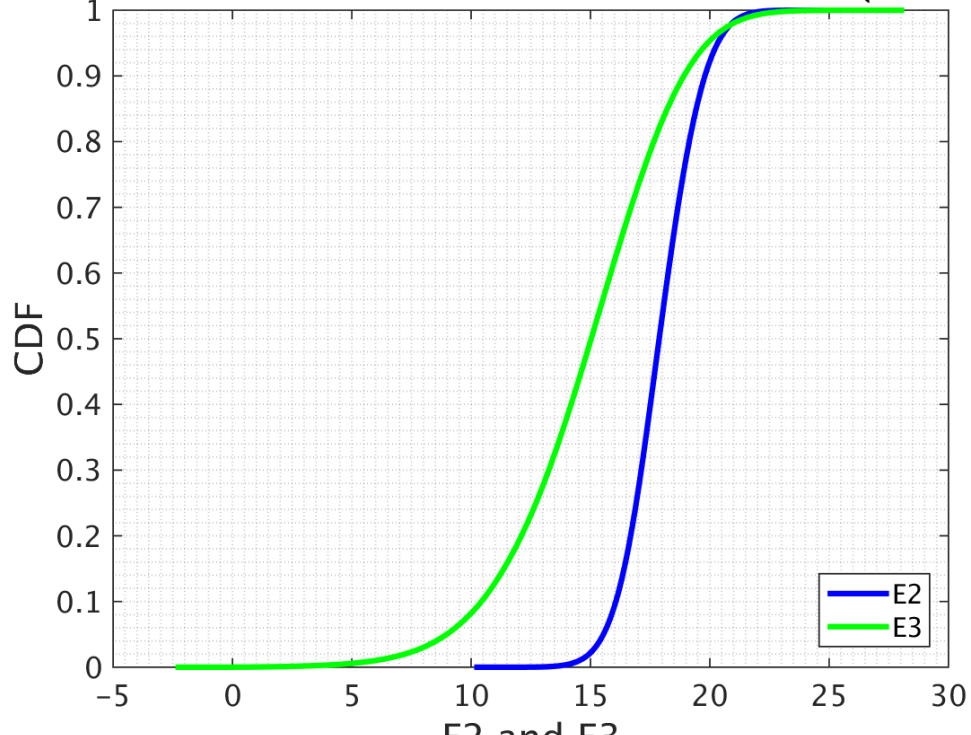


(c) Histogram for E_2



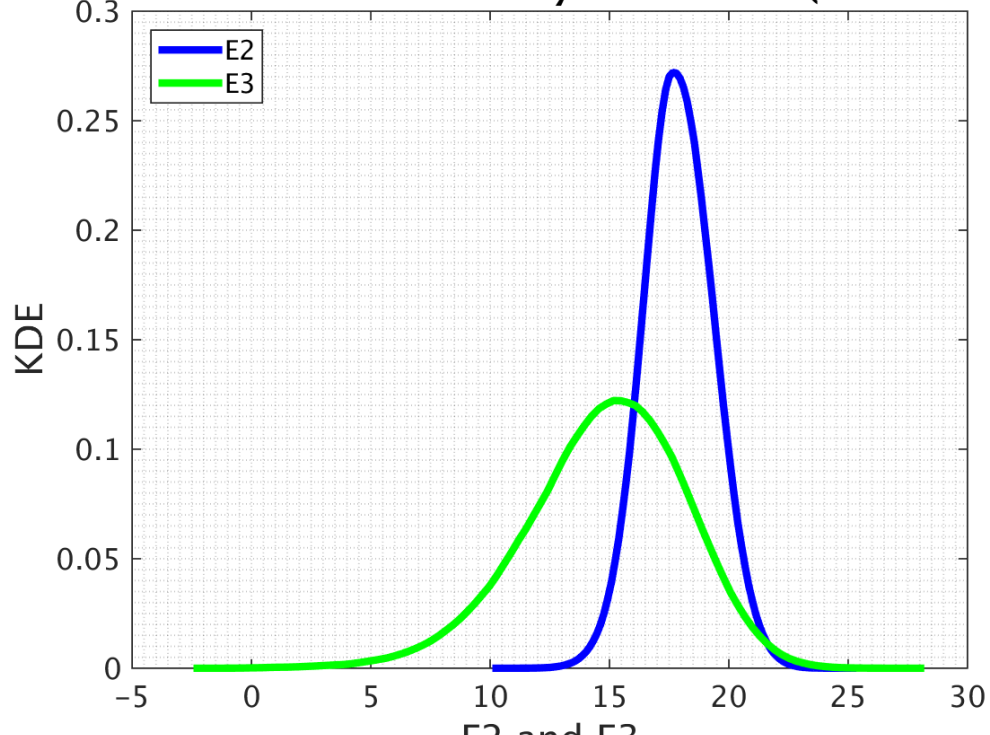
(d) Histogram for E_3

Parameter Cumulative Distribution Function (raw chain)



(e) Cummulative Density Funtion

Parameter Kernel Density Estimation (raw chain)

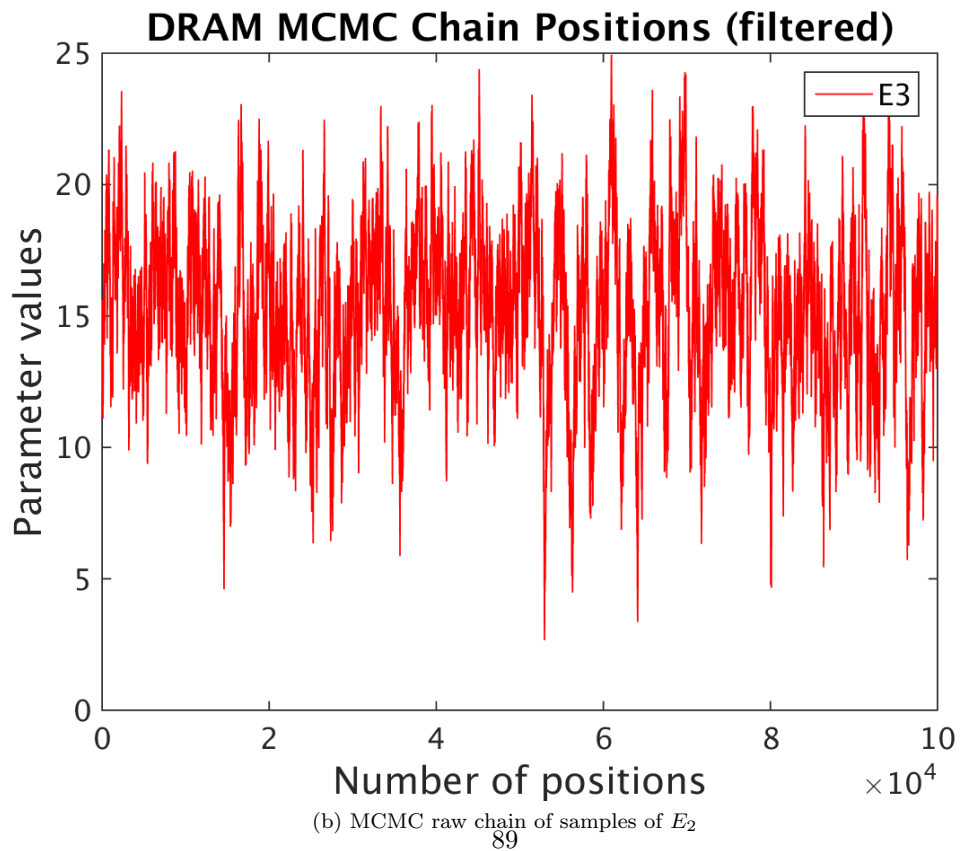
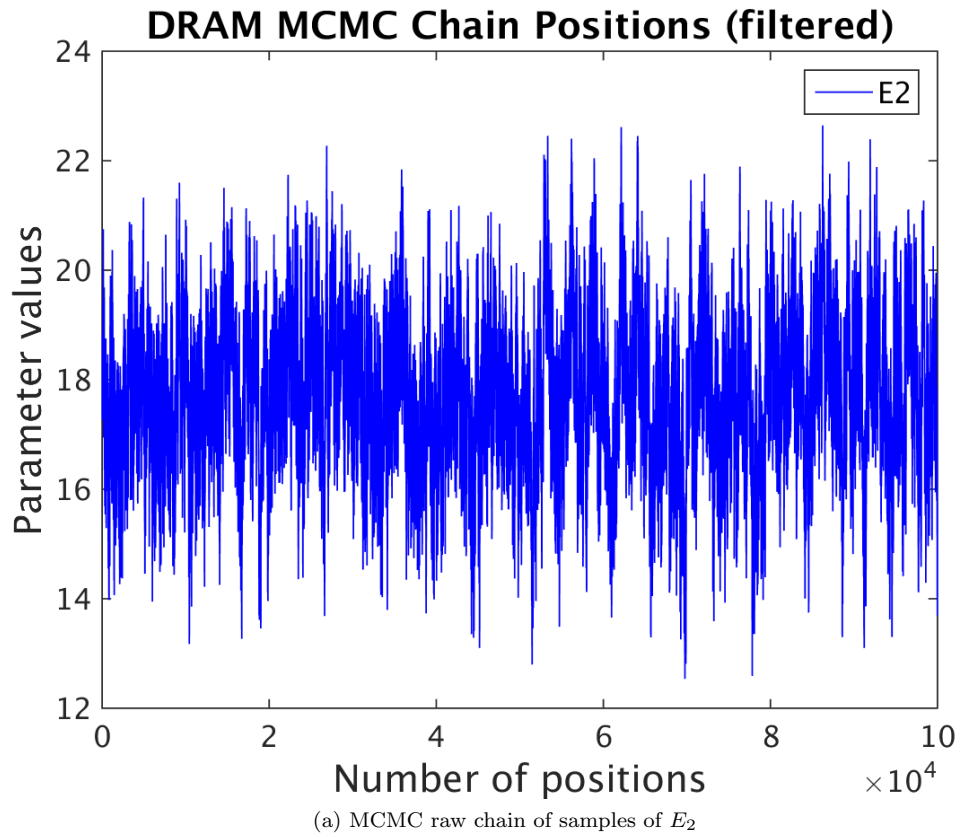


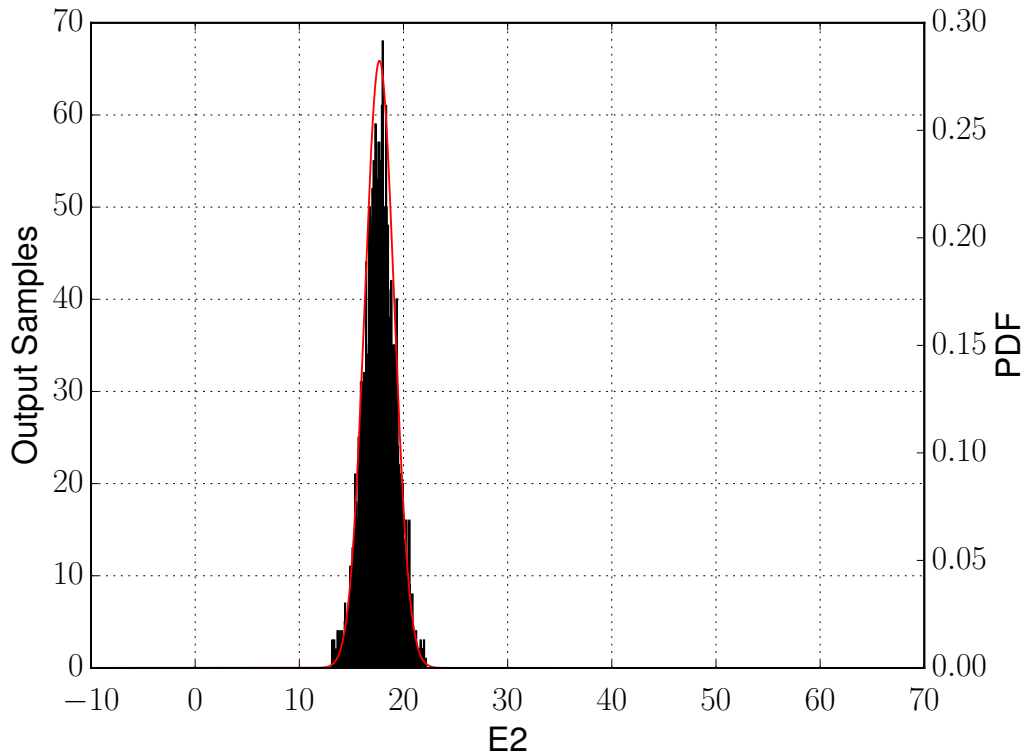
(f) KDE
87

Figure 5.-16: Results for sample size 1e7

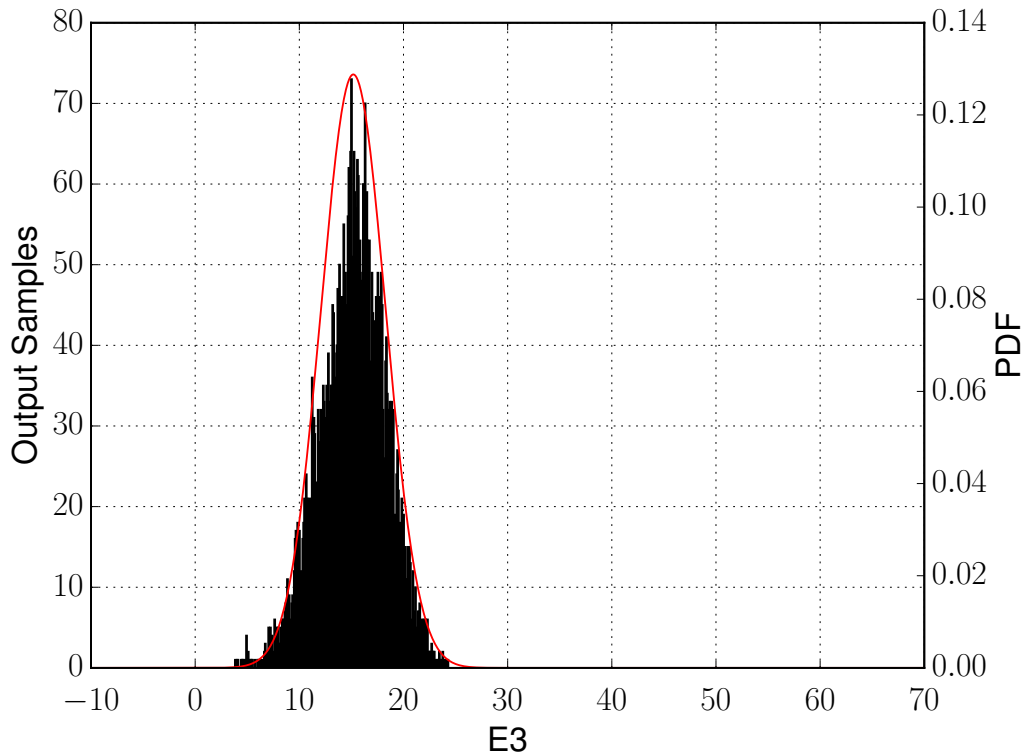
Sample size (Surrogate size) 20*20

In this section we calculated flamespeed values for 400 (20*20) different points in the domain and the remaining values are linear combination of these 400 points. The results below are for sample size 1e5, 5e5 , 1e6, 5e6 and 1e7.

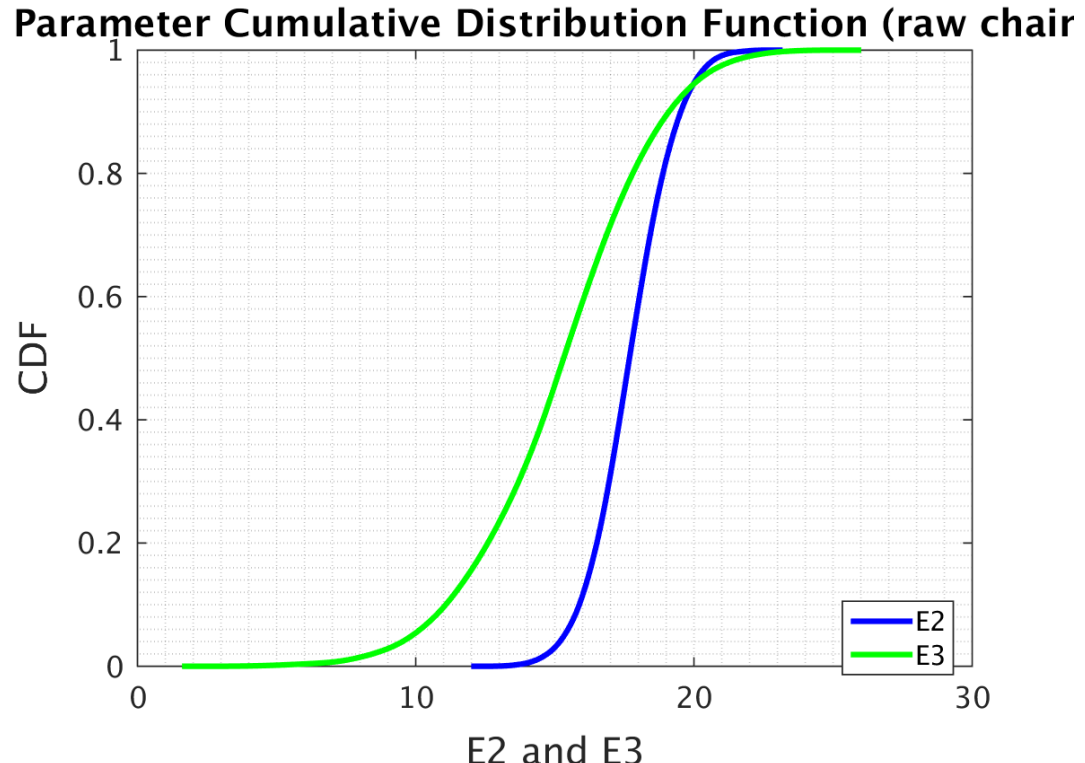




(c) Histogram for E_2



(d) Histogram for E_3



(e) Cummulative Density Funtion

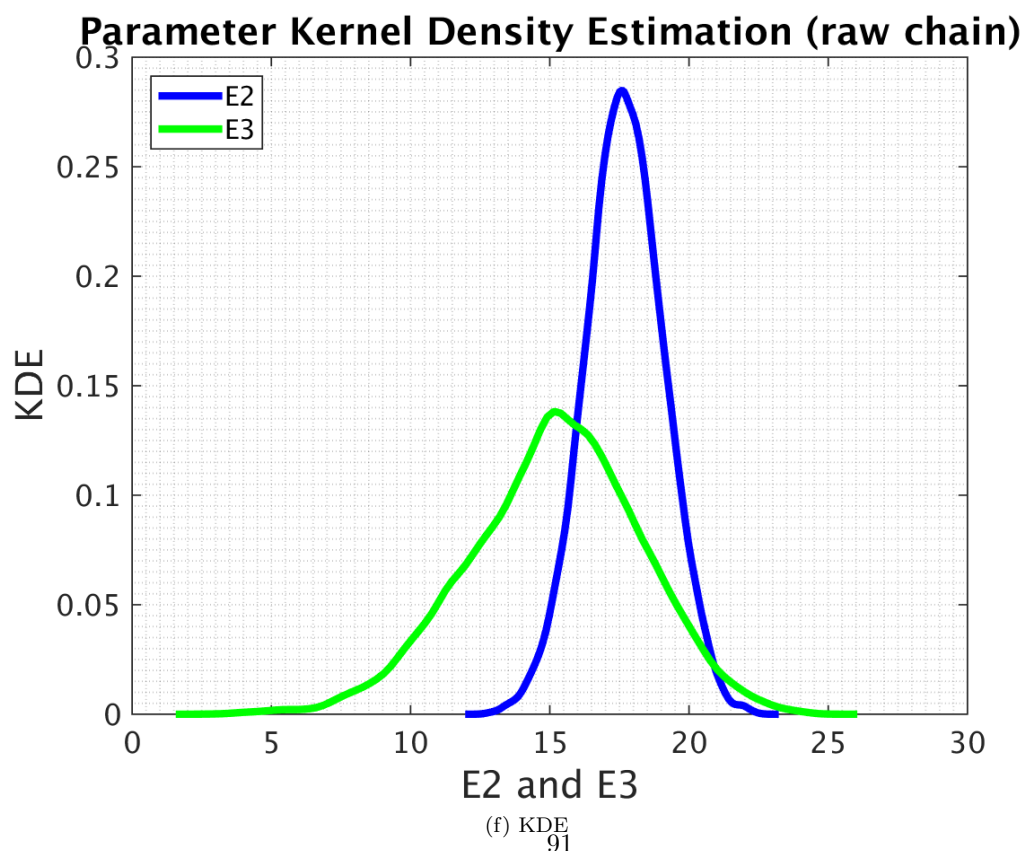
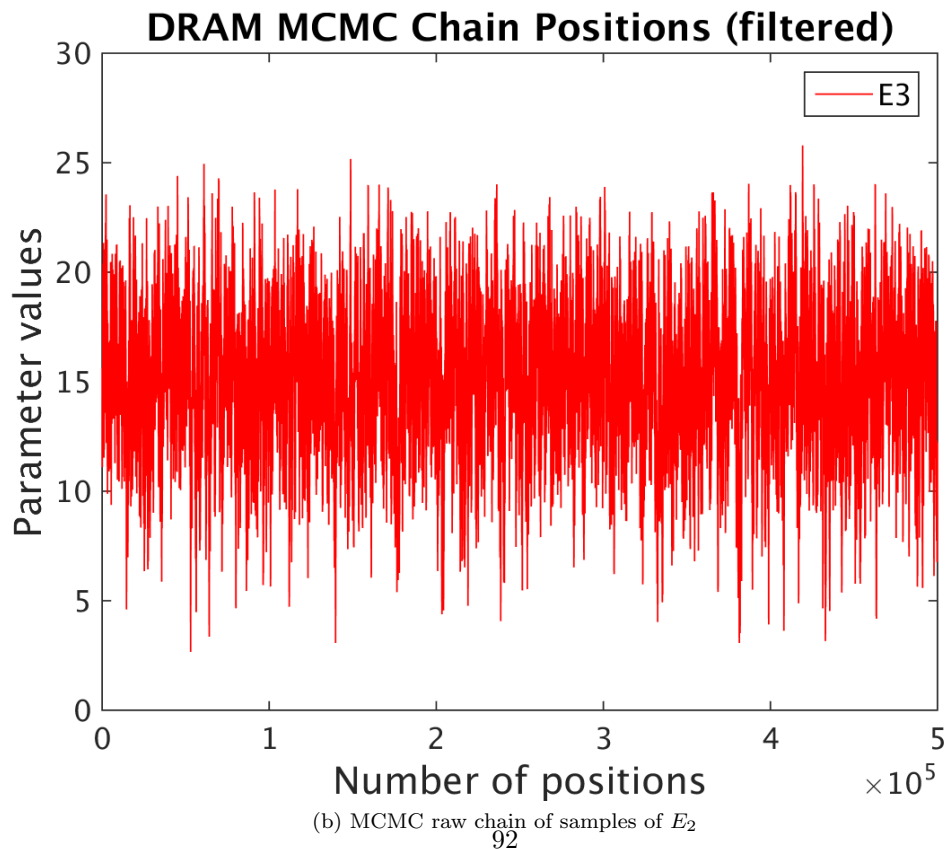
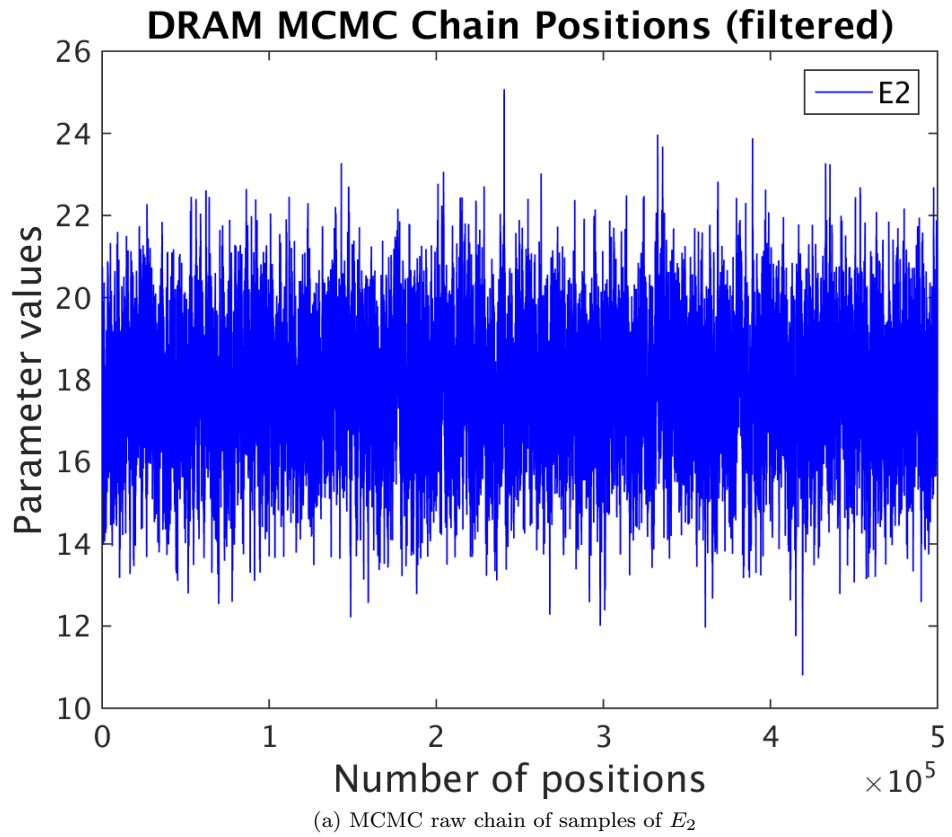
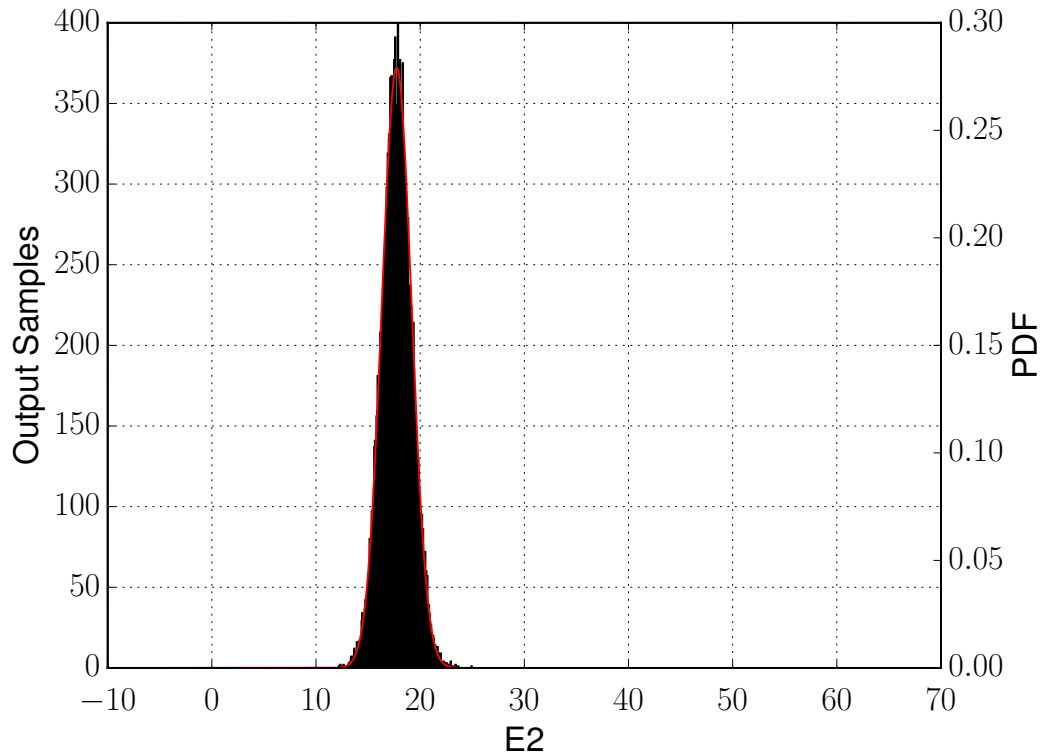
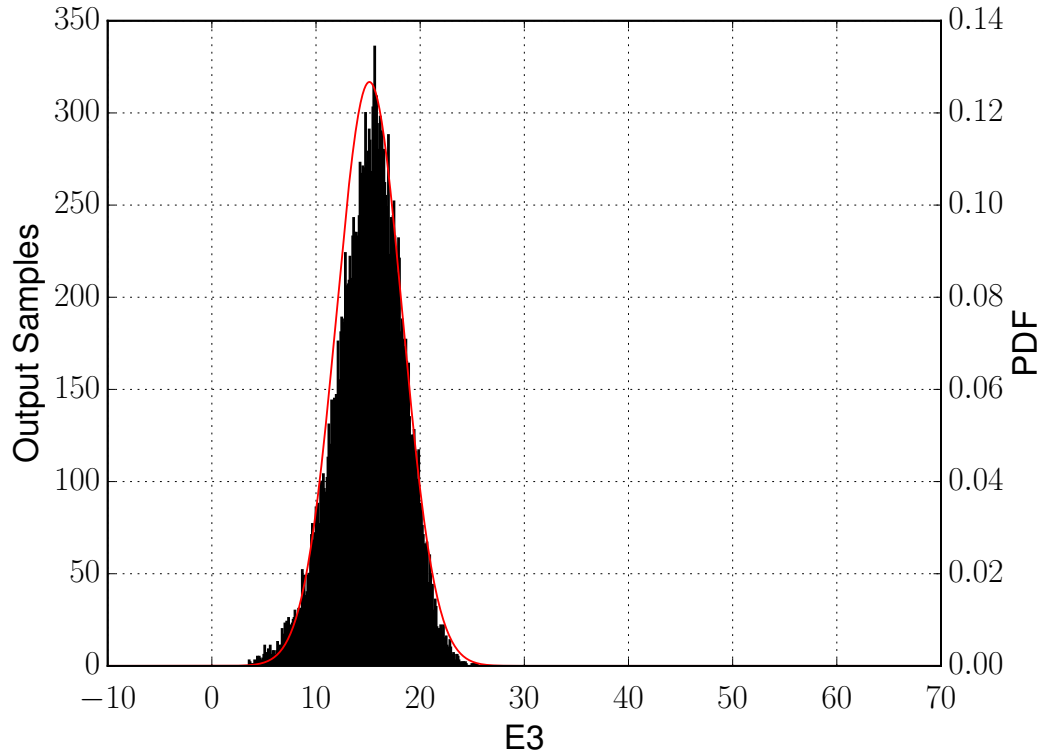


Figure 5.-16: Results for sample size 1e5



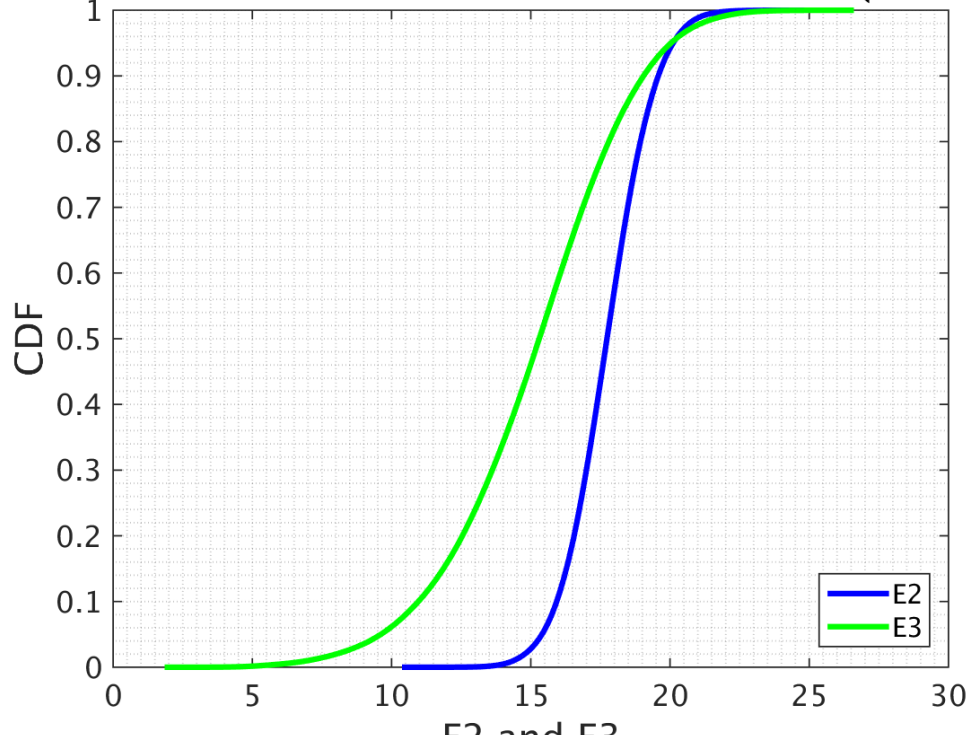


(c) Histogram for E_2



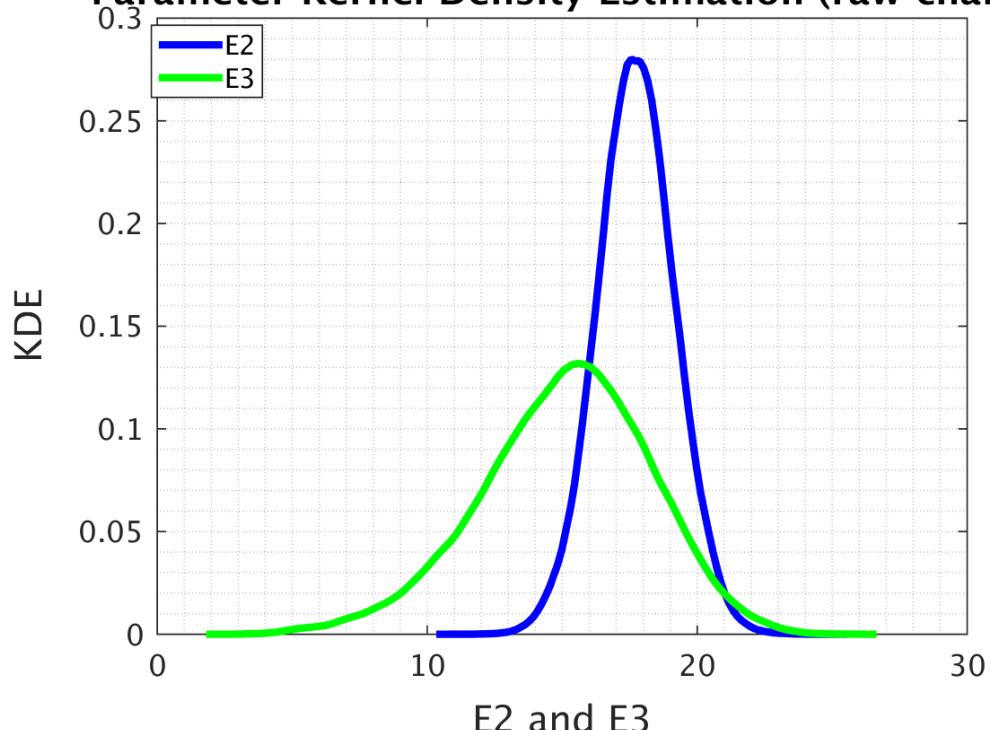
(d) Histogram for E_3

Parameter Cumulative Distribution Function (raw chair)



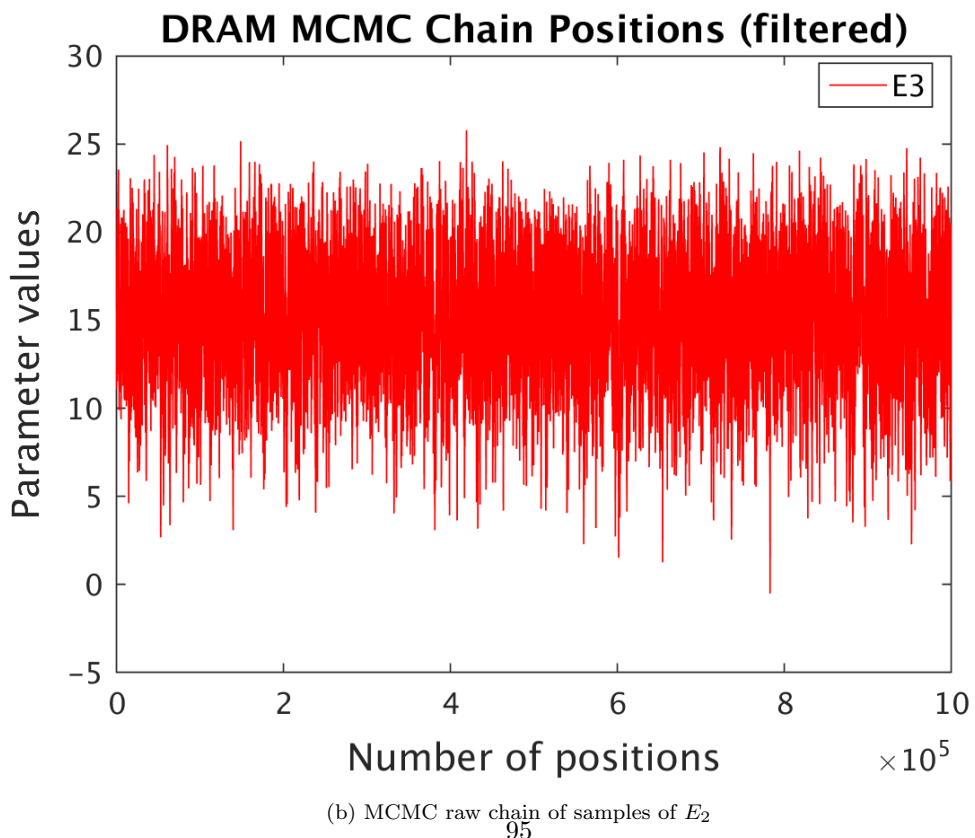
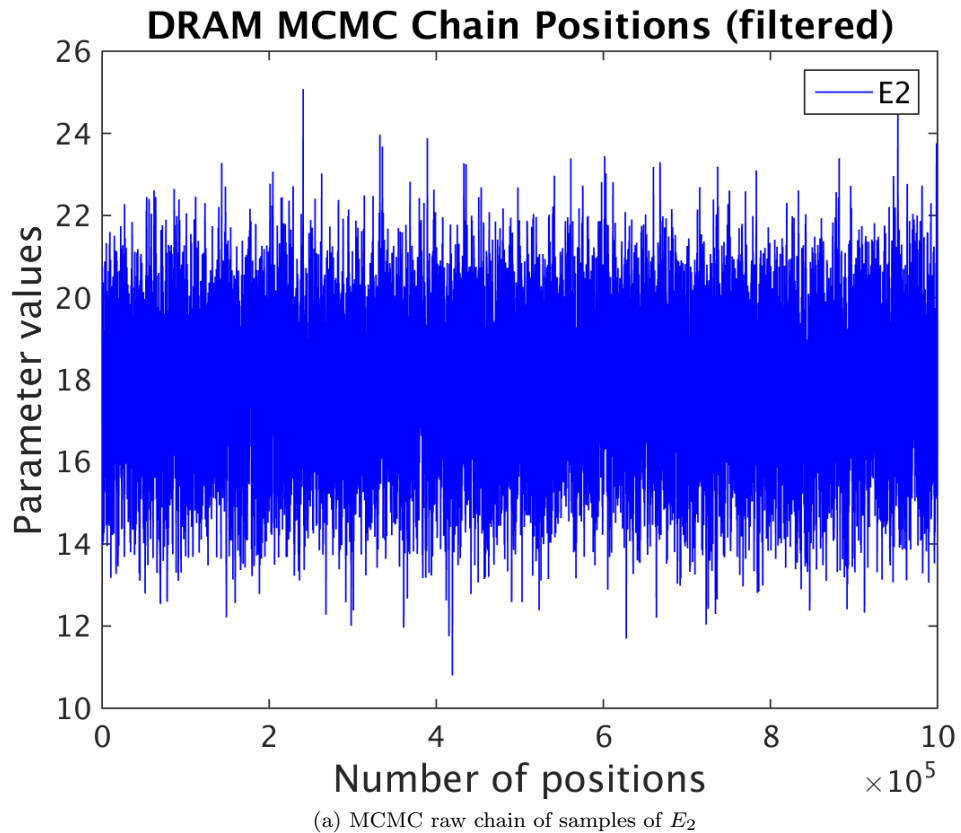
(e) Cummulative Density Funtion

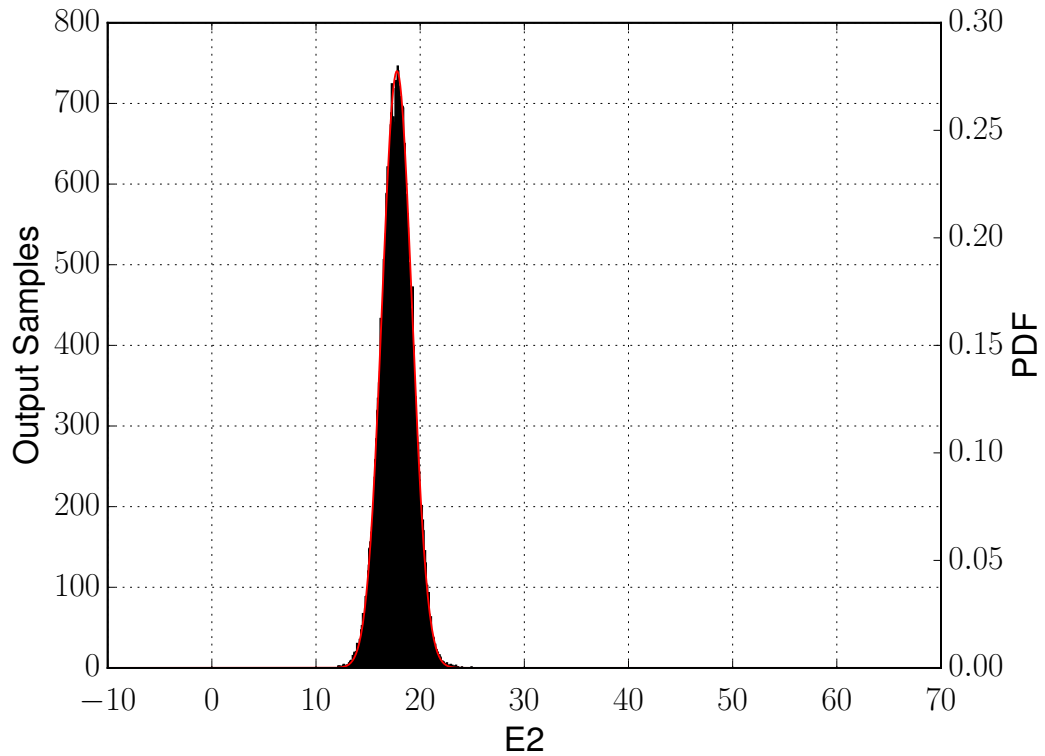
Parameter Kernel Density Estimation (raw chain)



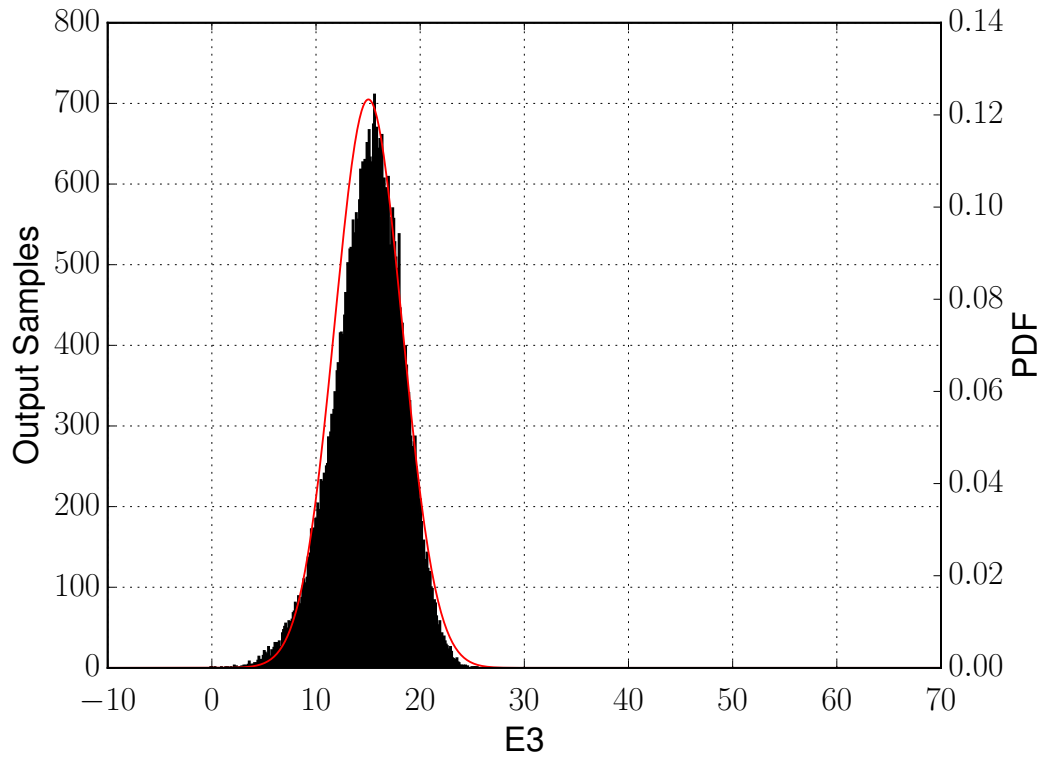
(f) KDE
94

Figure 5.-16: Results for sample size 5e5



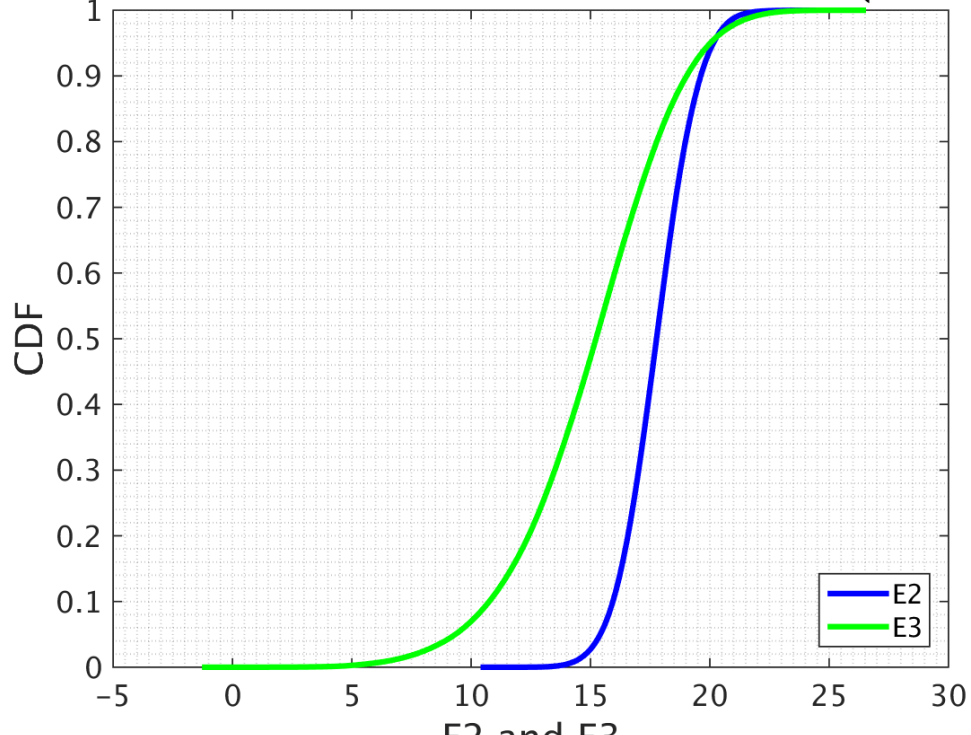


(c) Histogram for E_2



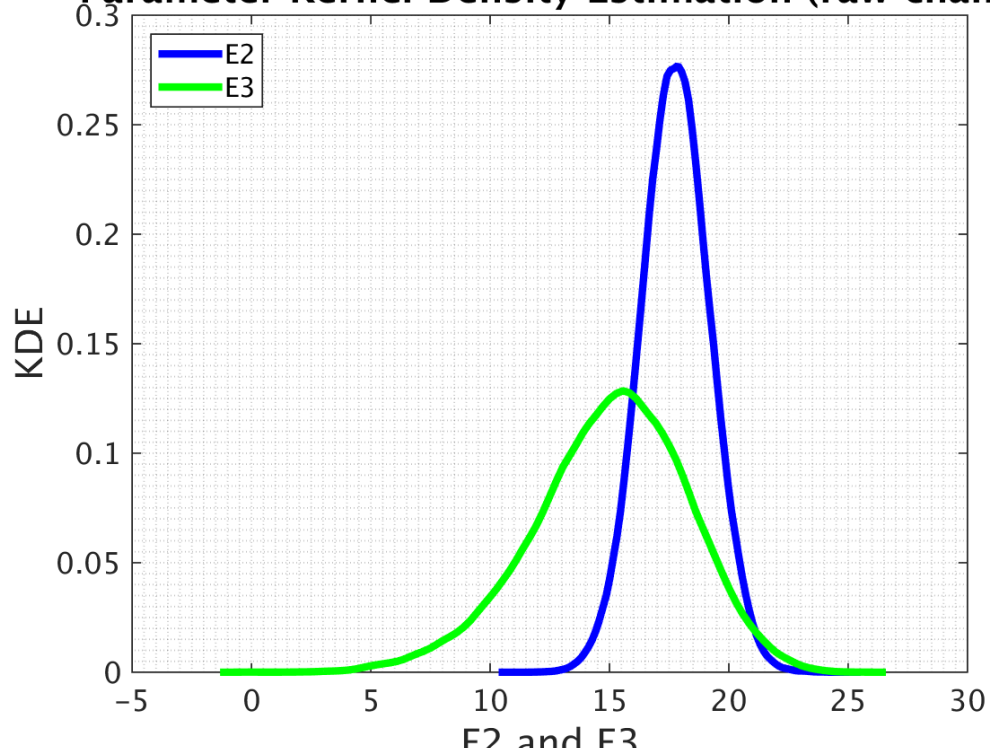
(d) Histogram for E_3

Parameter Cumulative Distribution Function (raw chain)



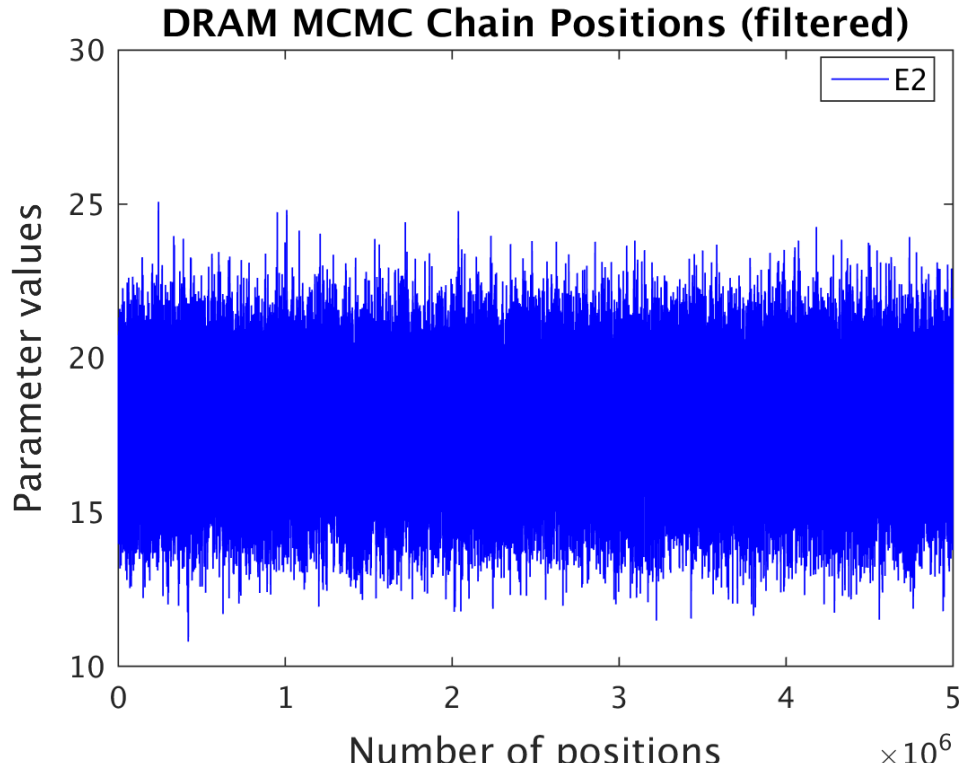
(e) Cummulative Density Funtion

Parameter Kernel Density Estimation (raw chain)

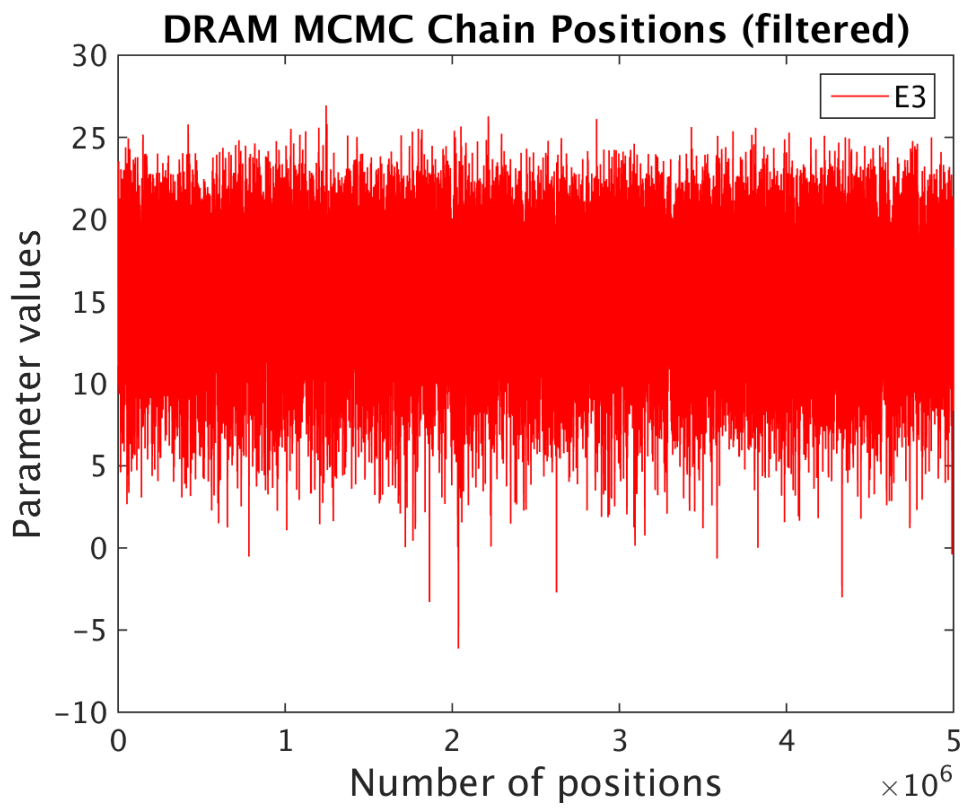


(f) KDE
97

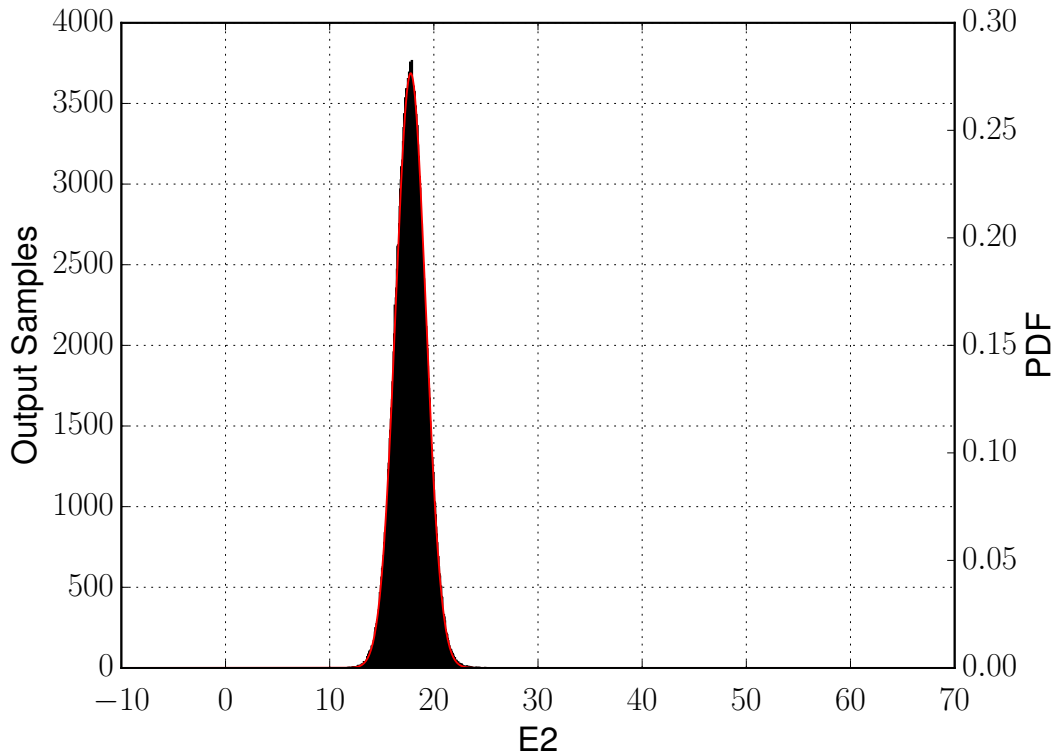
Figure 5.-16: Results for sample size 1e6



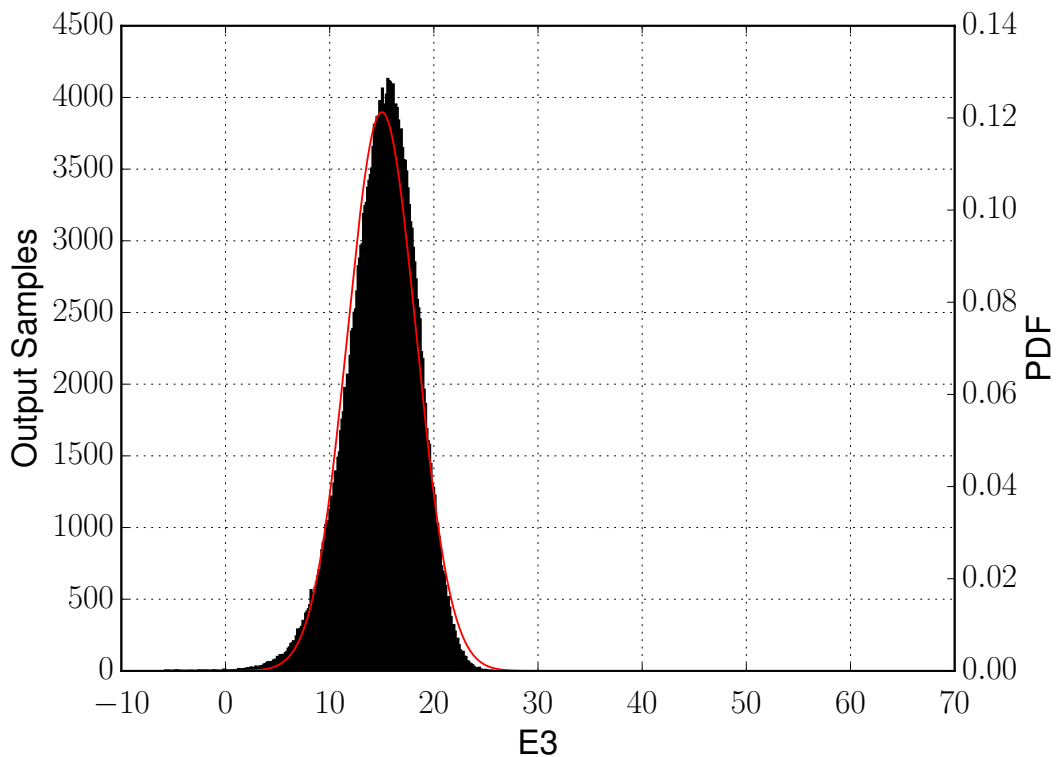
(a) MCMC raw chain of samples of E_2



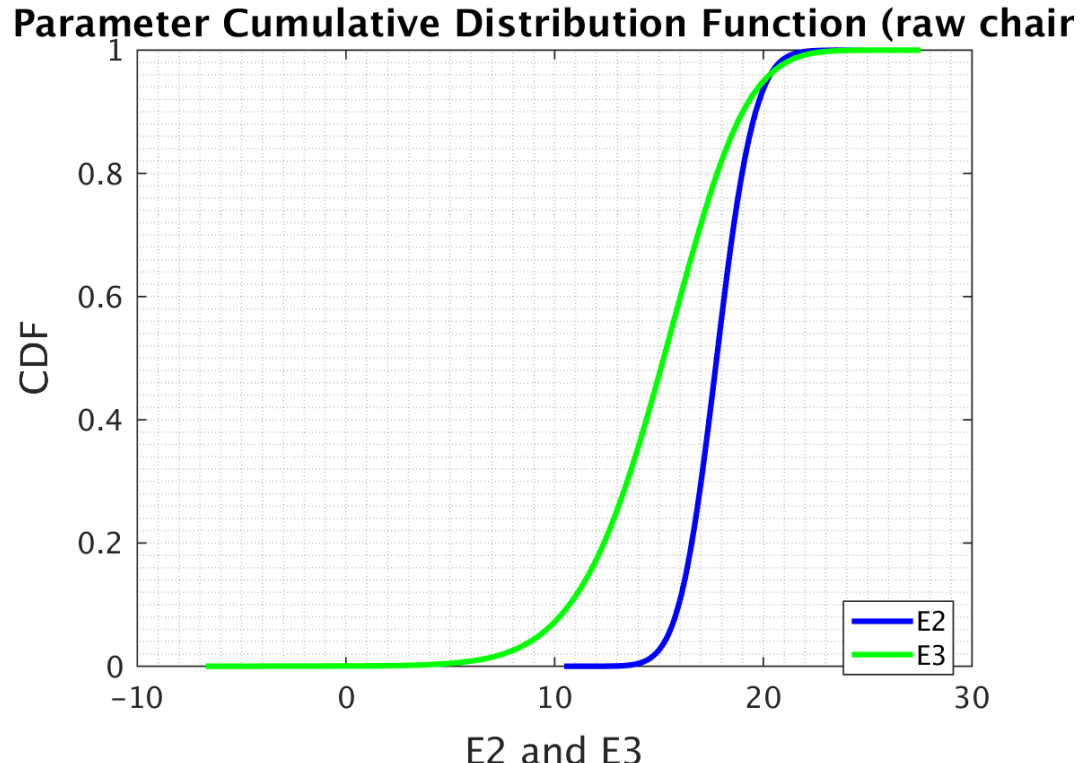
(b) MCMC raw chain of samples of E_2



(c) Histogram for E_2



(d) Histogram for E_3



(e) Cummulative Density Funtion

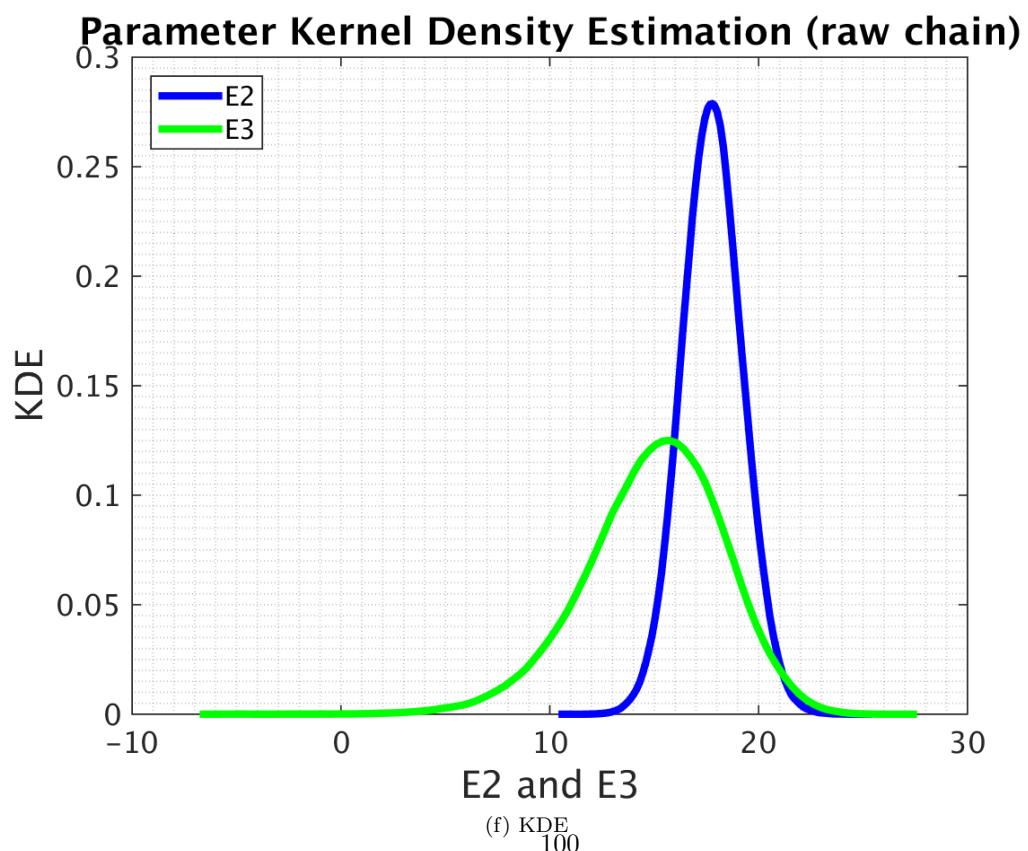
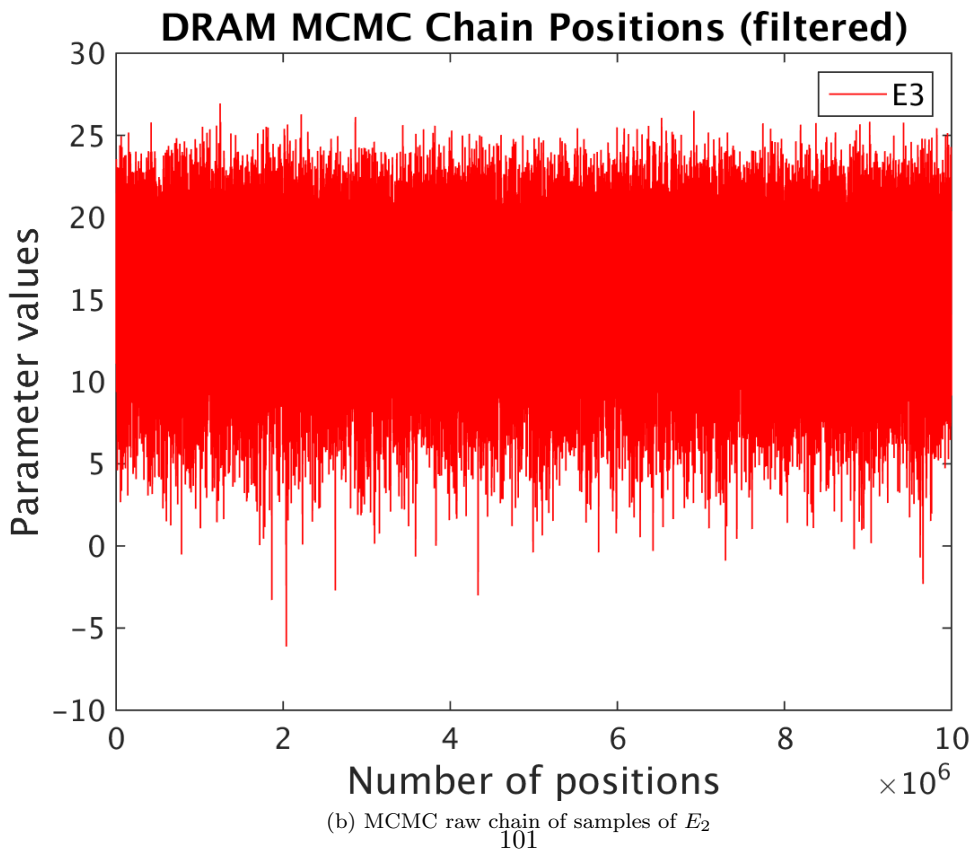
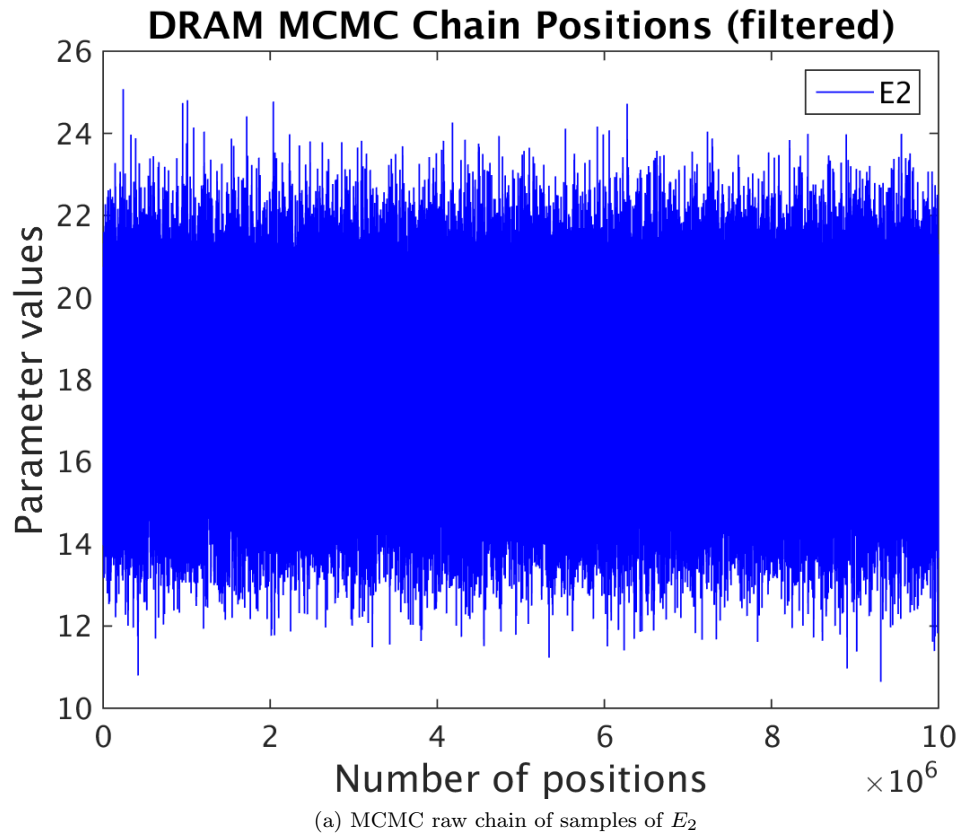
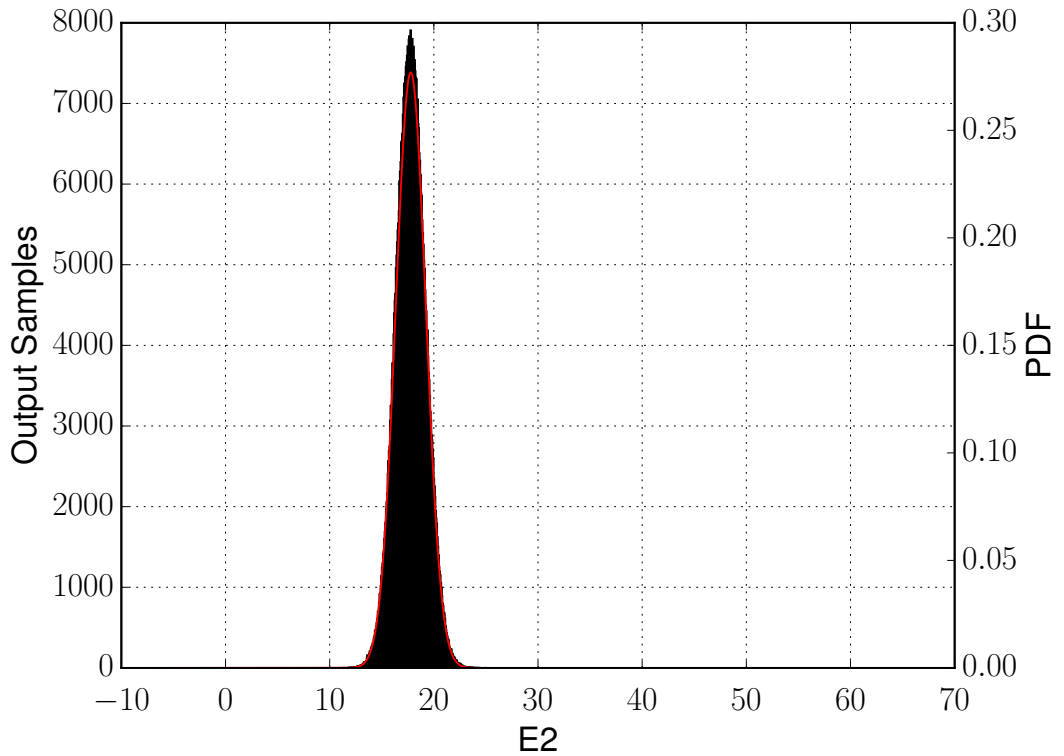
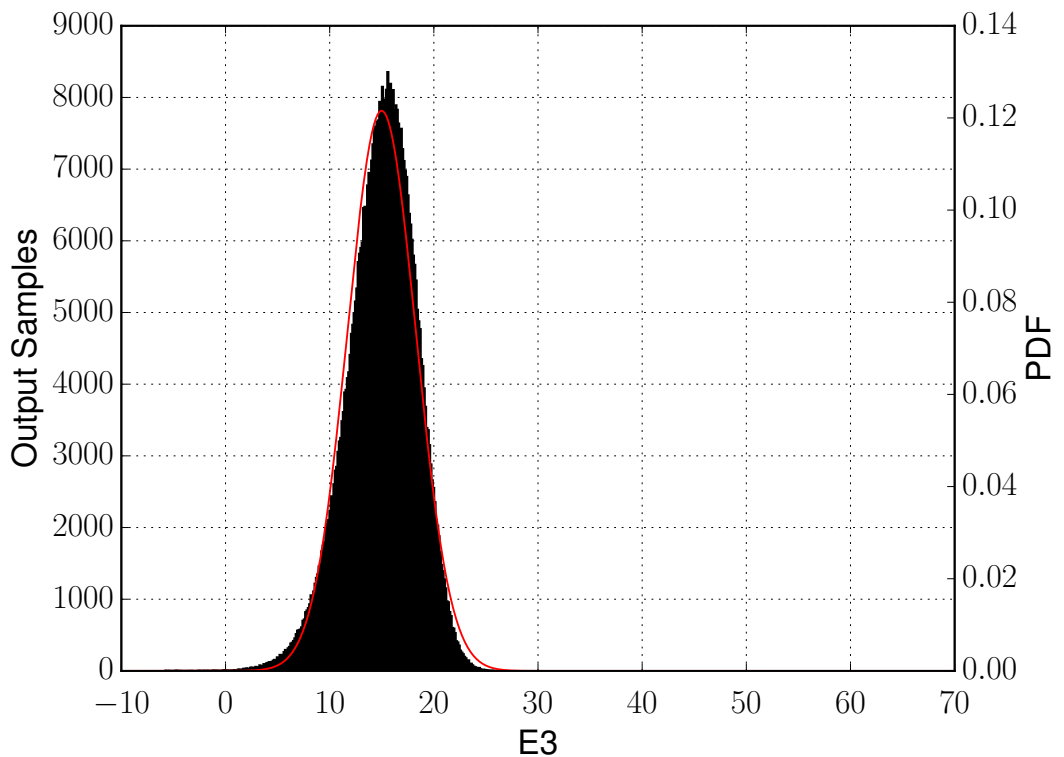


Figure 5.-16: Results for sample size 5e6



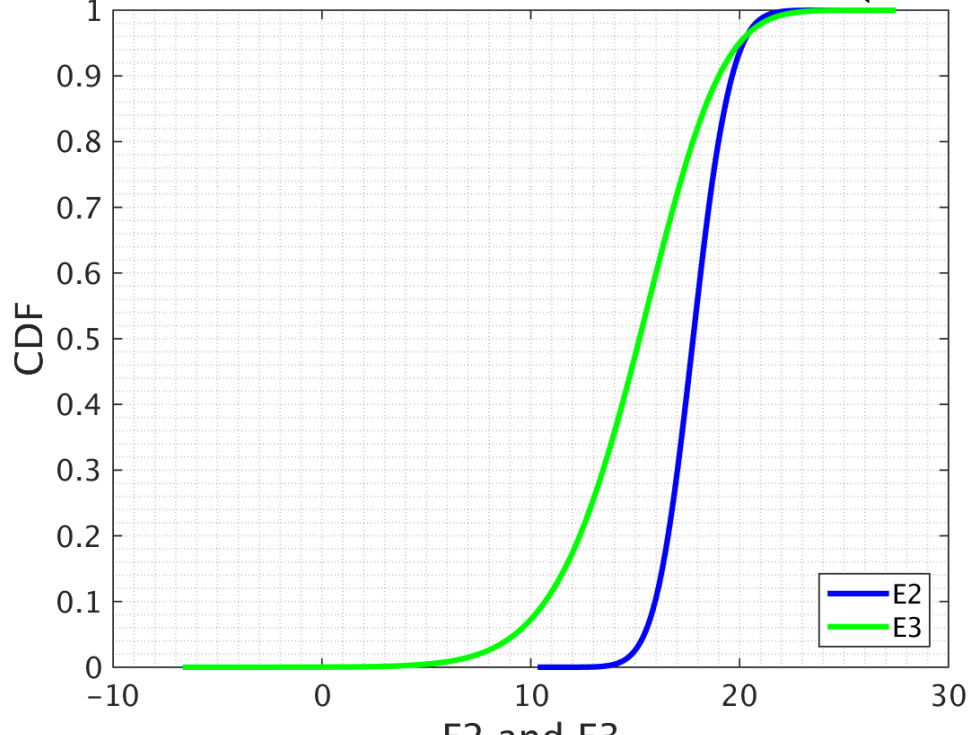


(c) Histogram for E_2



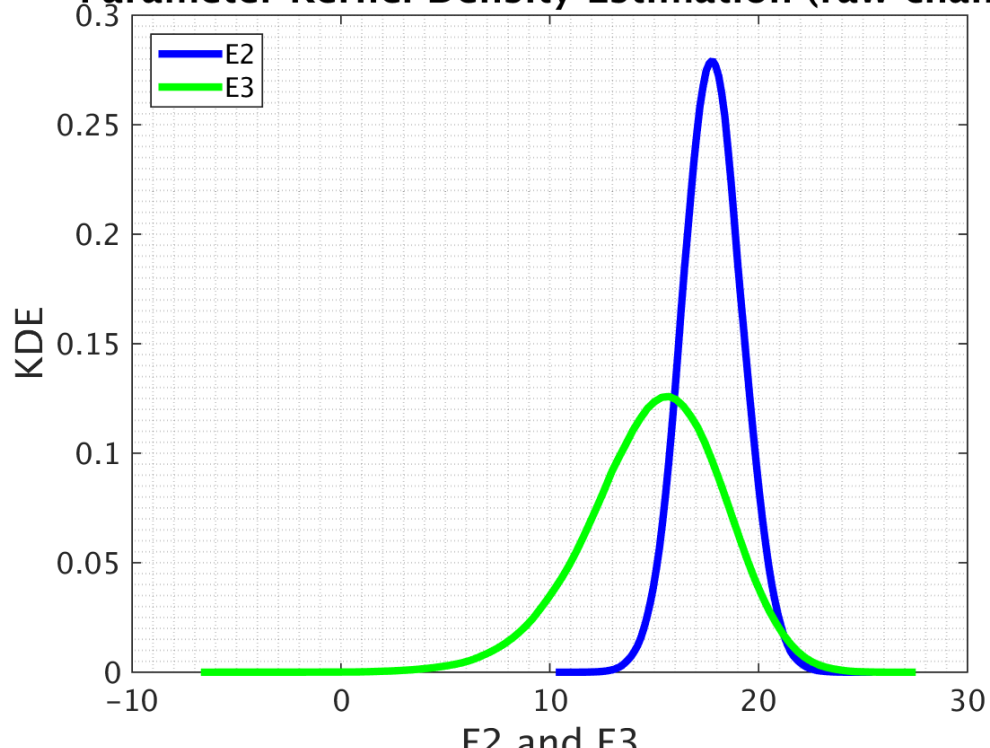
(d) Histogram for E_3

Parameter Cumulative Distribution Function (raw chain)



(e) Cummulative Density Funtion

Parameter Kernel Density Estimation (raw chain)

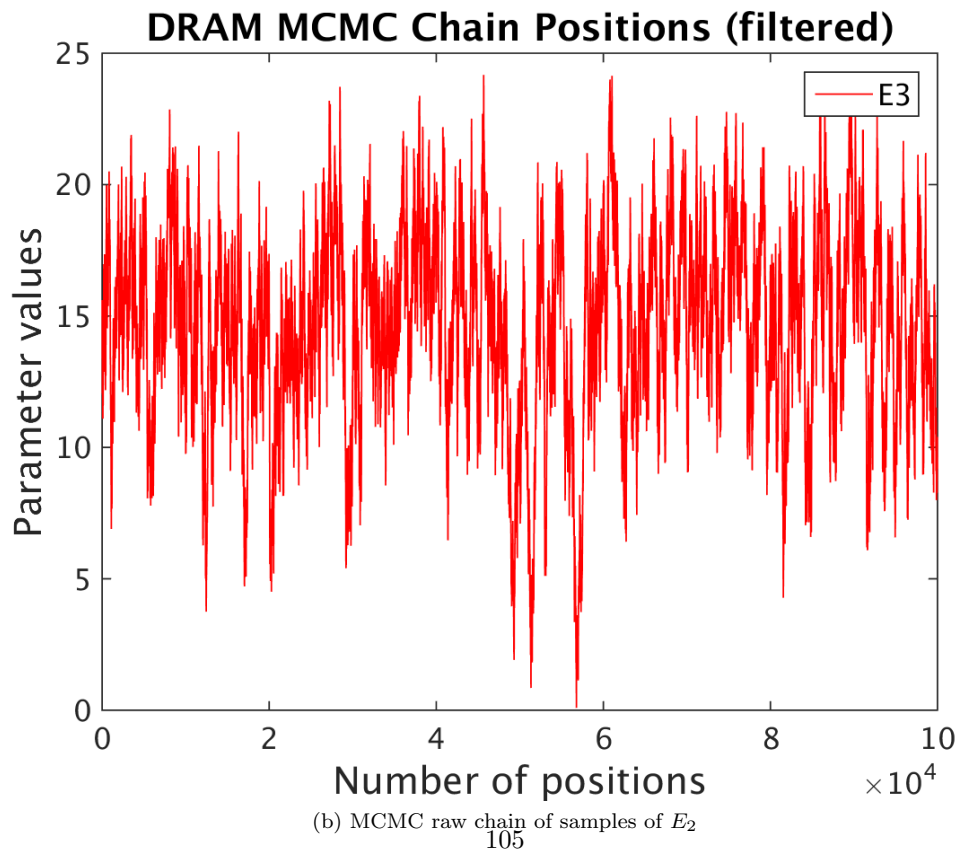
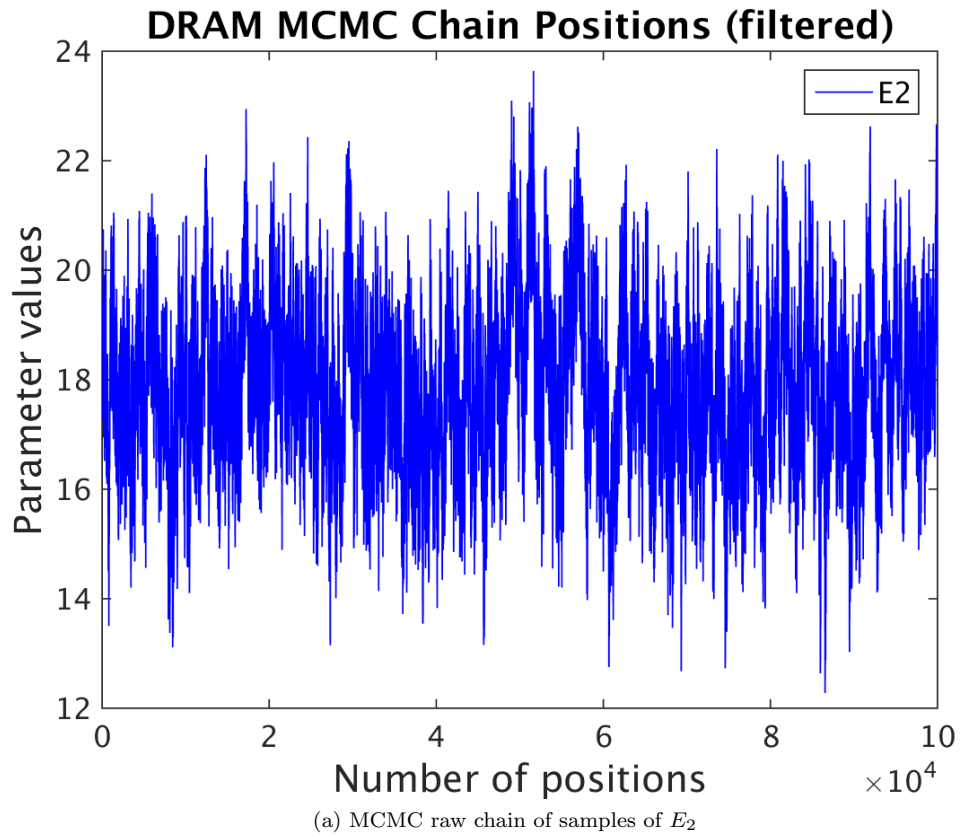


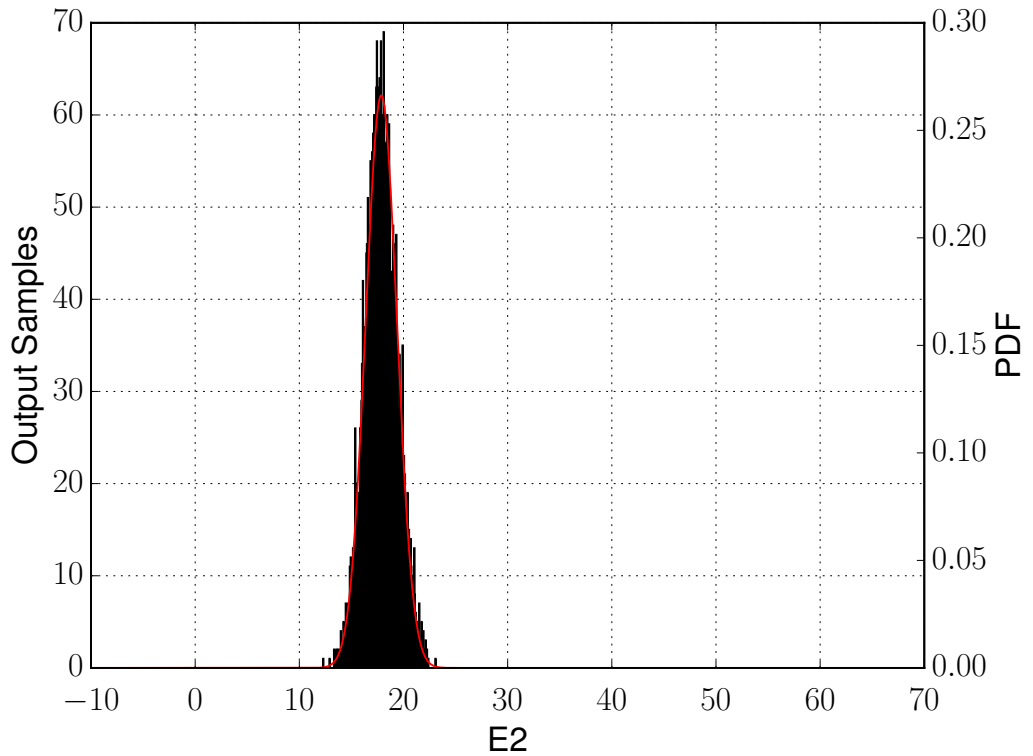
(f) $\frac{\text{KDE}}{10^3}$

Figure 5.-16: Results for sample size $1e7$

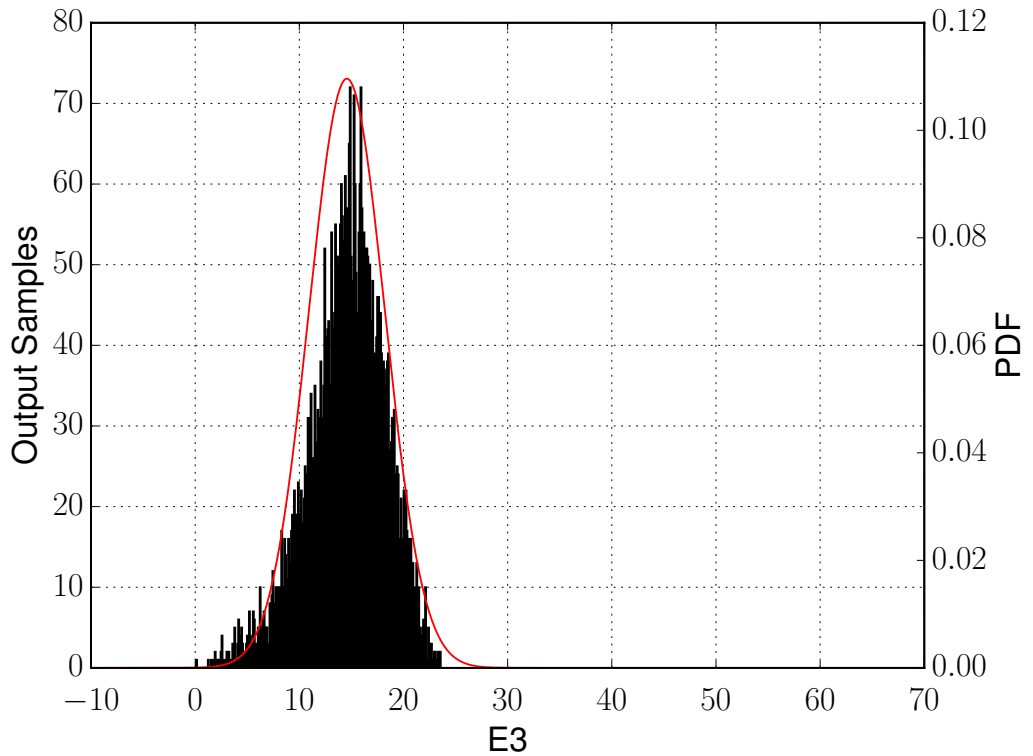
Sample size (Surrogate size) 30*30

In this section we calculated flamespeed values for 900 (30*30) different points in the domain and the remaining values are linear combination of these 900 points. The results below are for sample size $1e5$, $5e5$, $1e6$, $5e6$ and $1e7$.

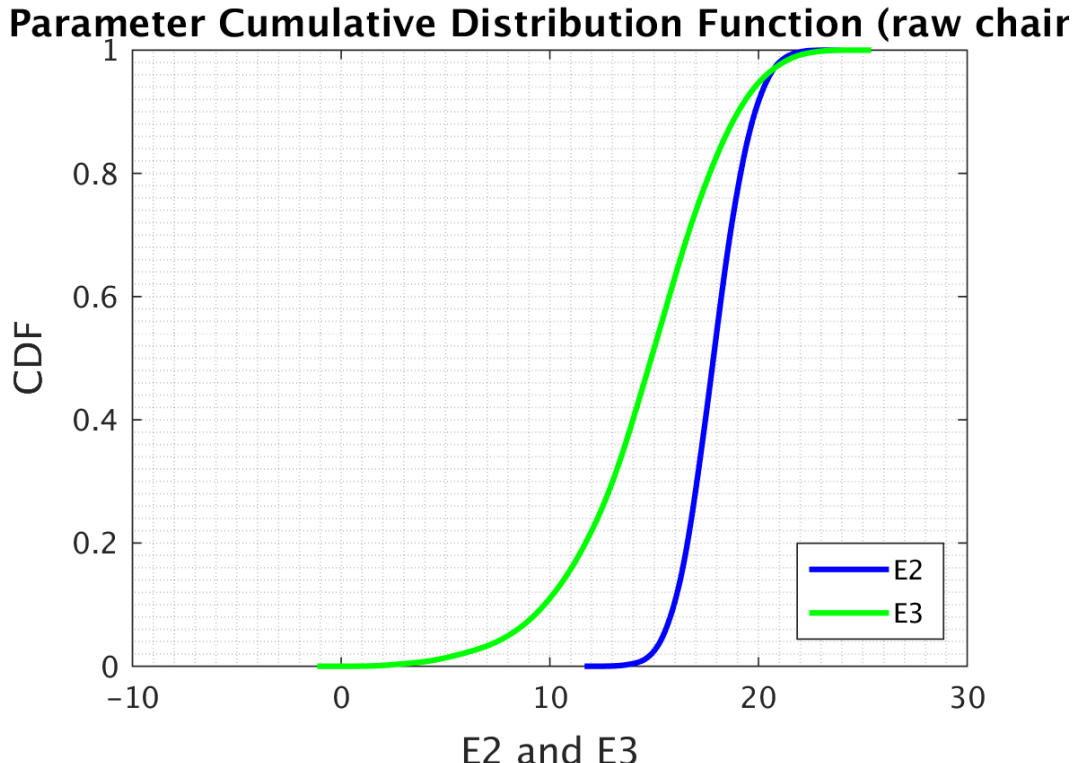




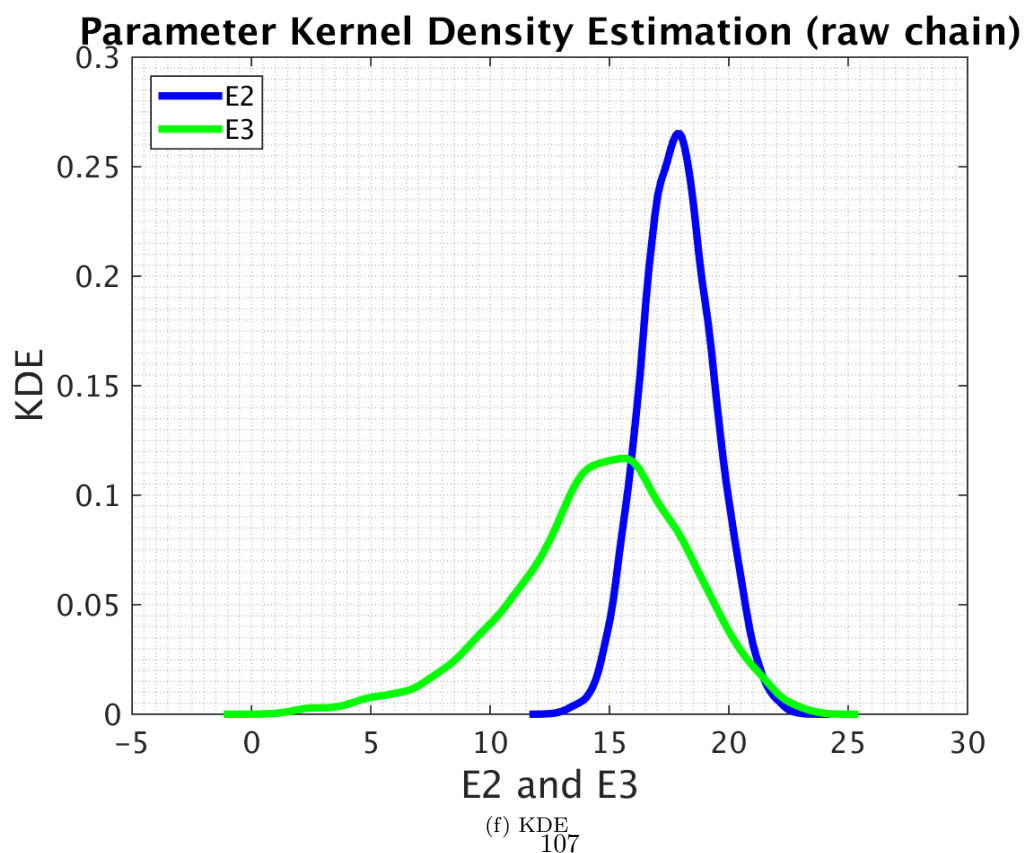
(c) Histogram for E_2



(d) Histogram for E_3

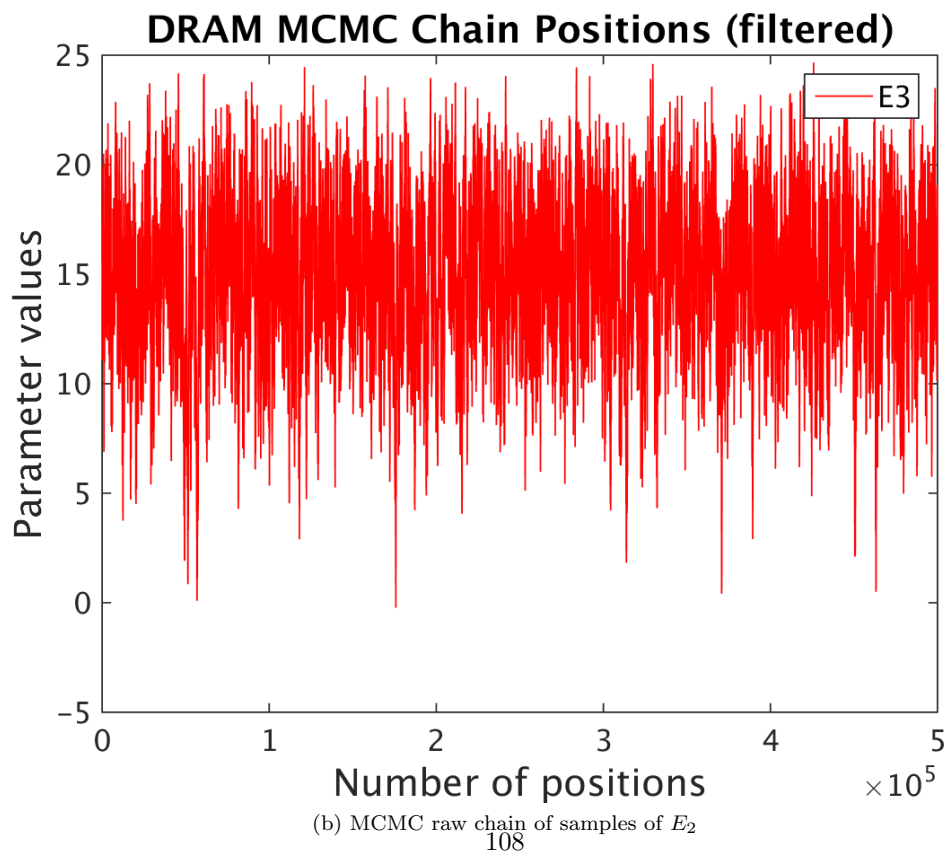
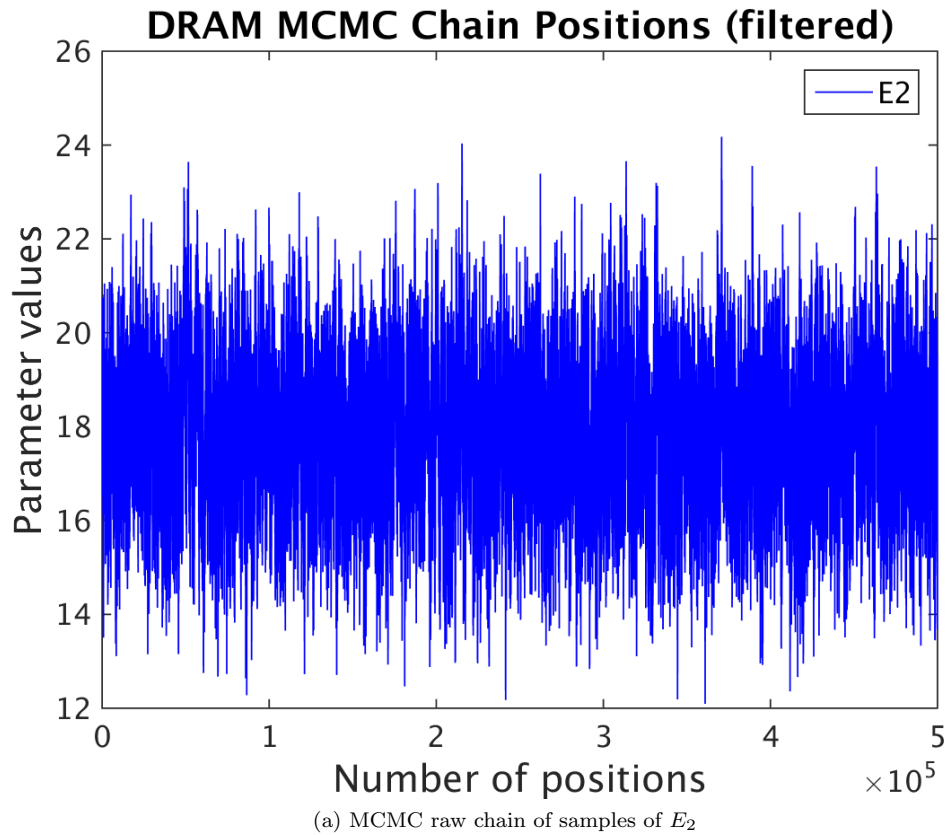


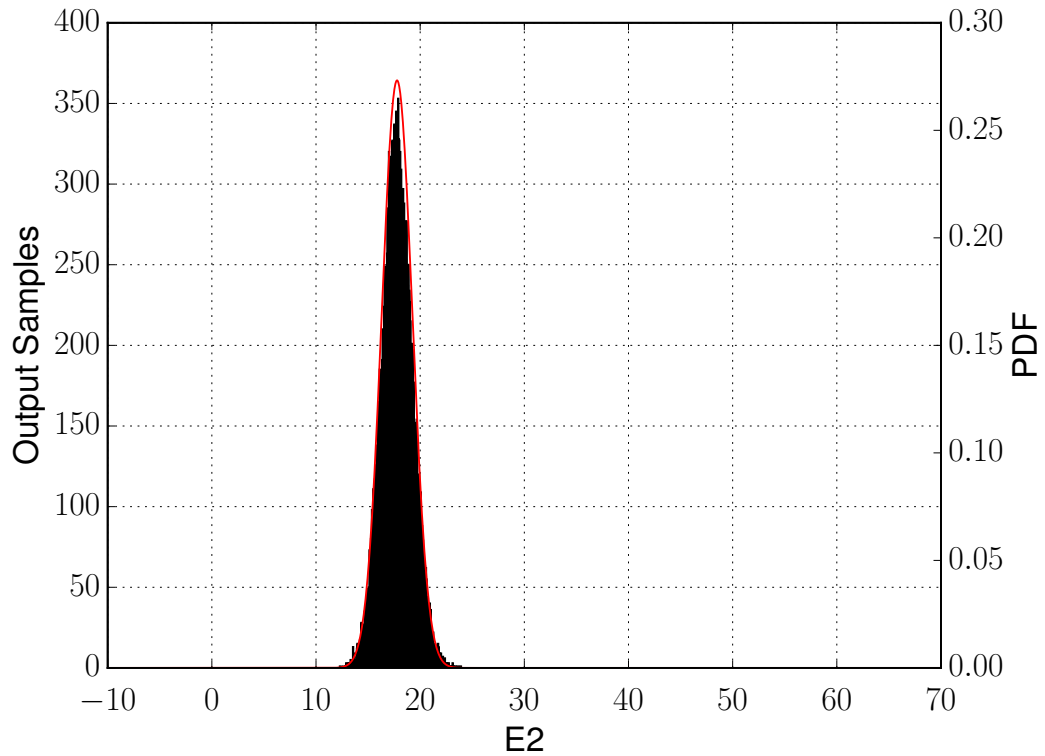
(e) Cummulative Density Funtion



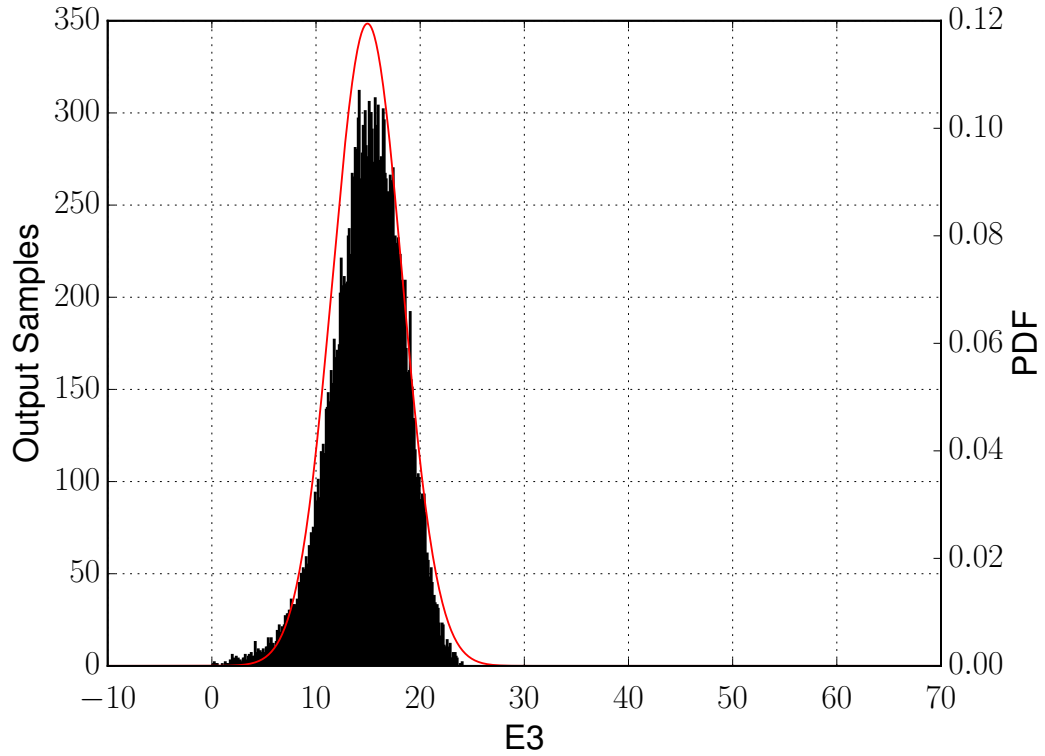
(f) $\frac{\text{KDE}}{10^7}$

Figure 5.-16: Results for sample size 1e5



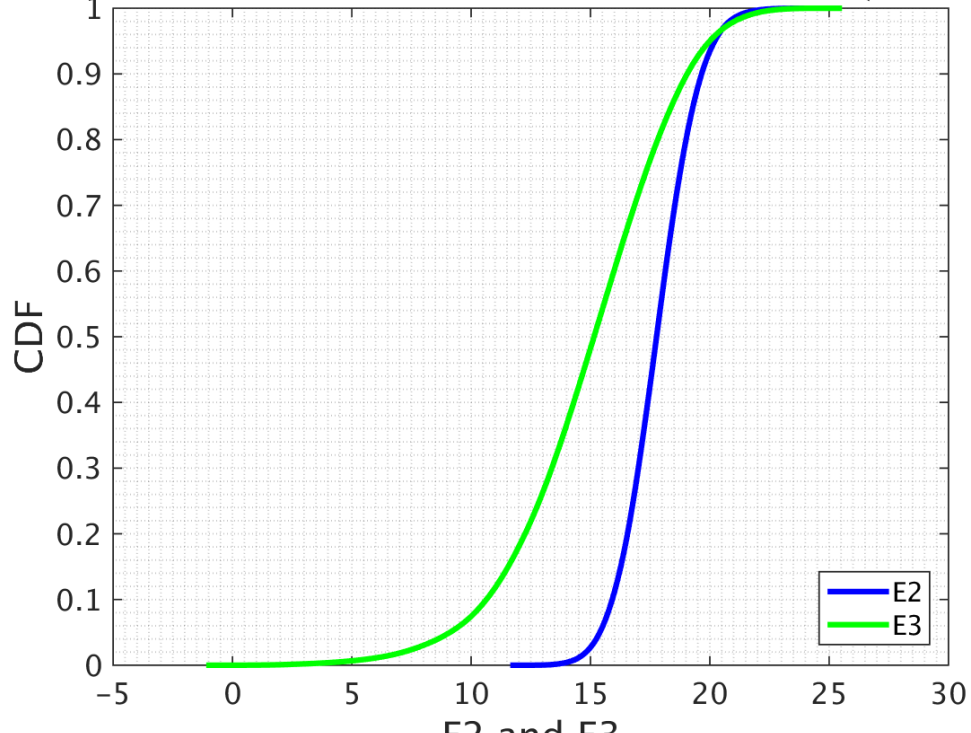


(c) Histogram for E_2



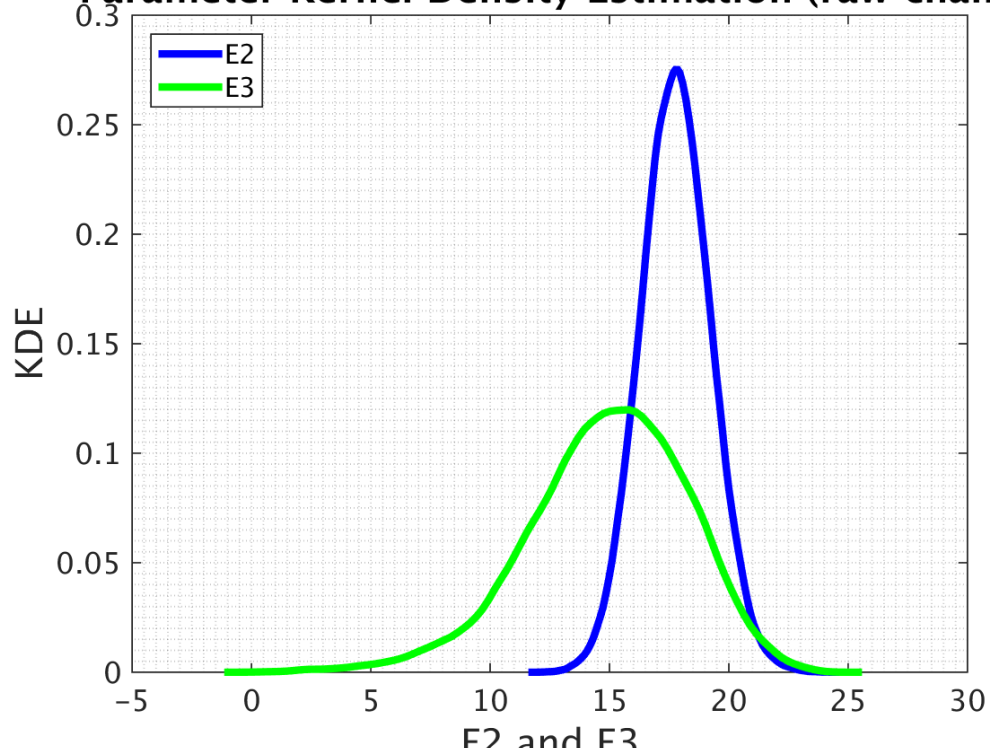
(d) Histogram for E_3

Parameter Cumulative Distribution Function (raw chain)



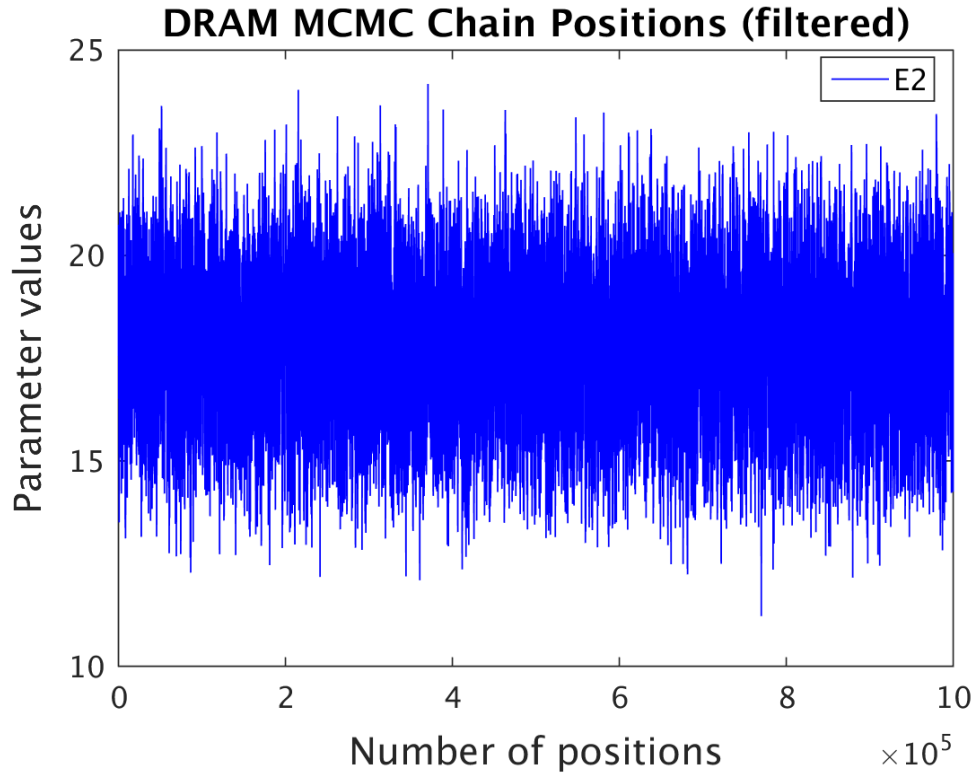
(e) Cummulative Density Funtion

Parameter Kernel Density Estimation (raw chain)

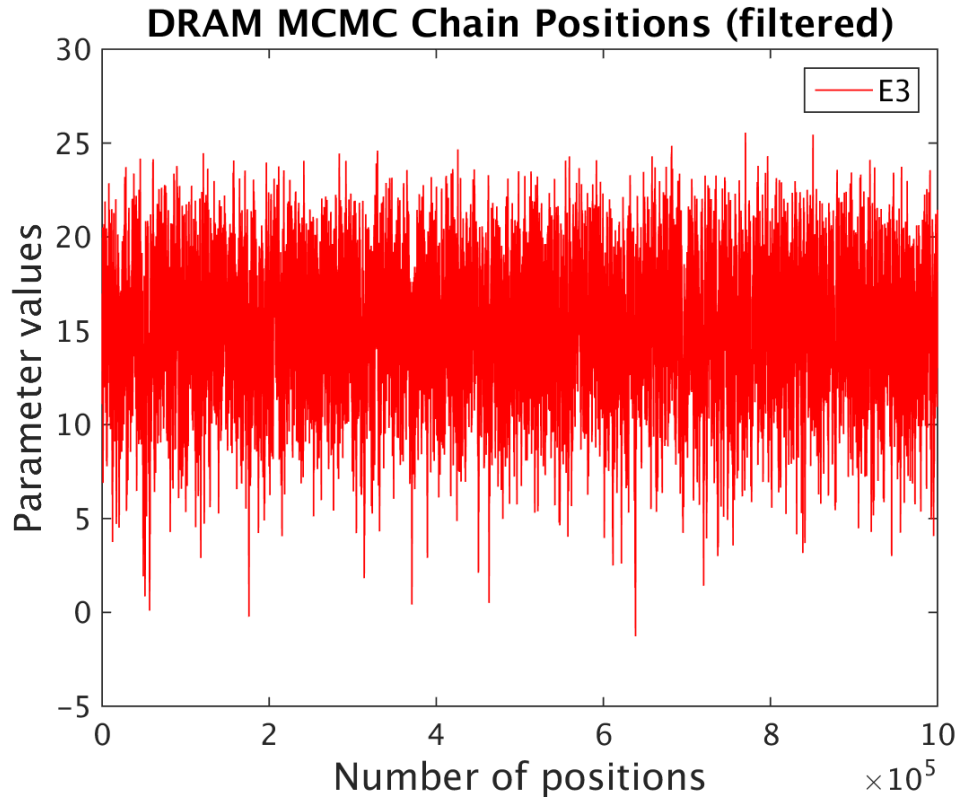


(f) KDE
110

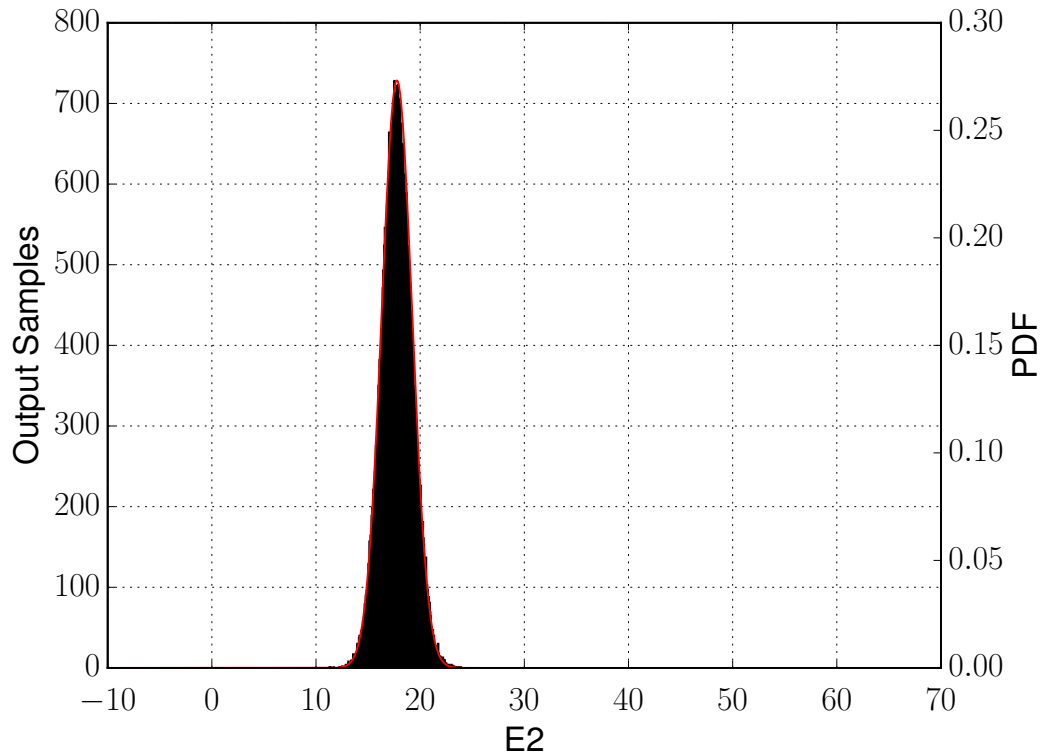
Figure 5.-16: Results for sample size 5e5



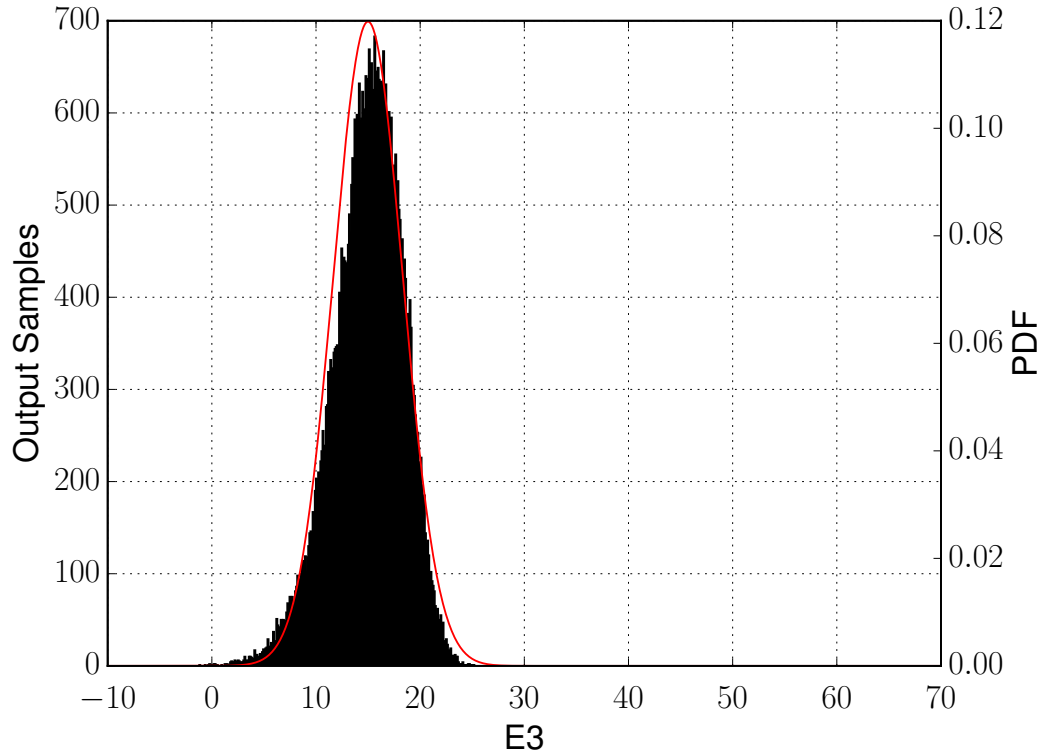
(a) MCMC raw chain of samples of E_2



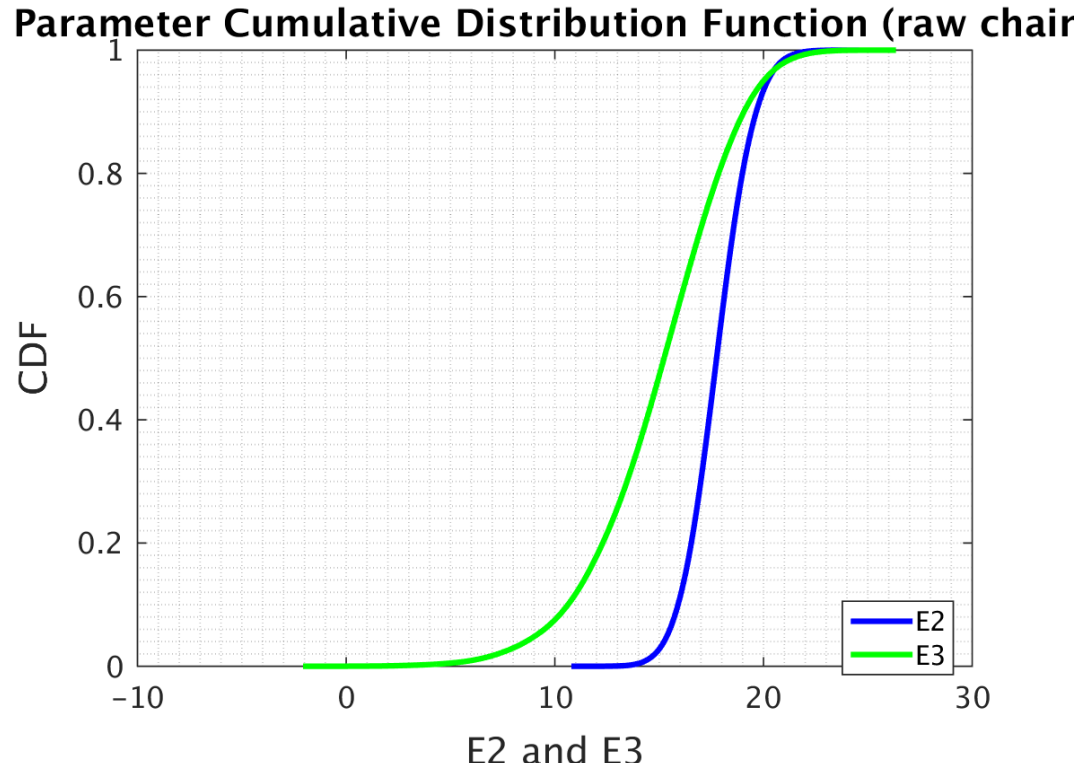
(b) MCMC raw chain of samples of E_2



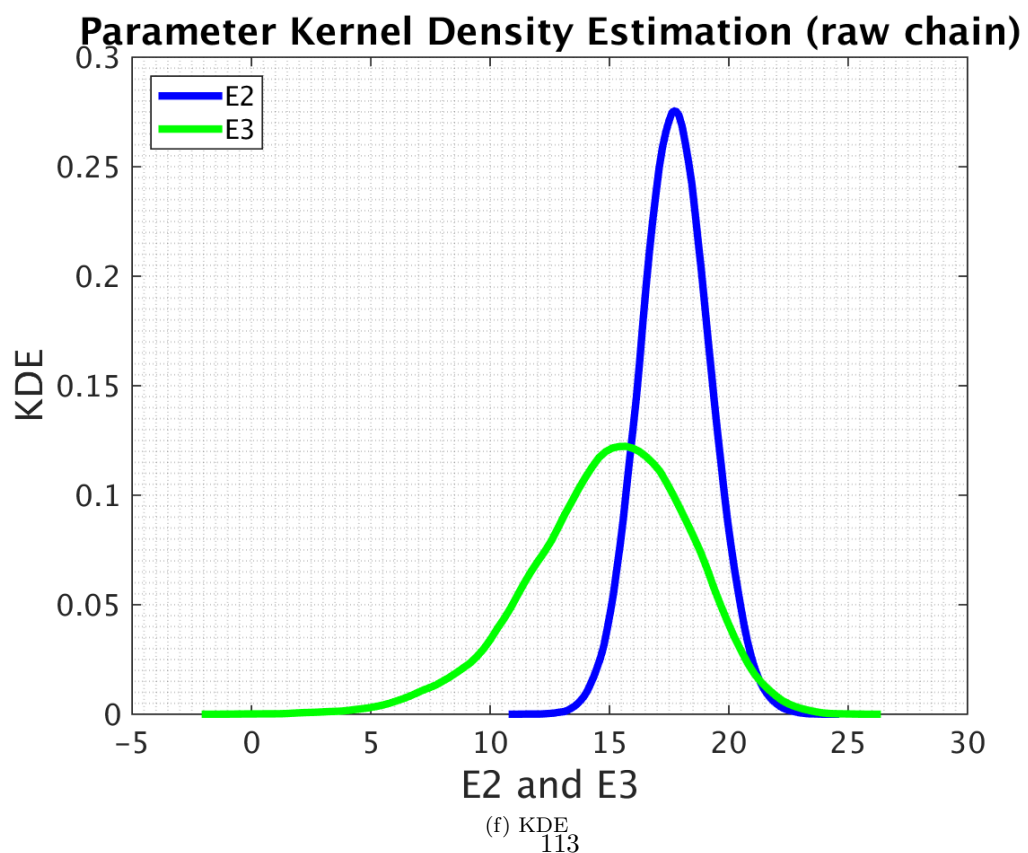
(c) Histogram for E_2



(d) Histogram for E_3

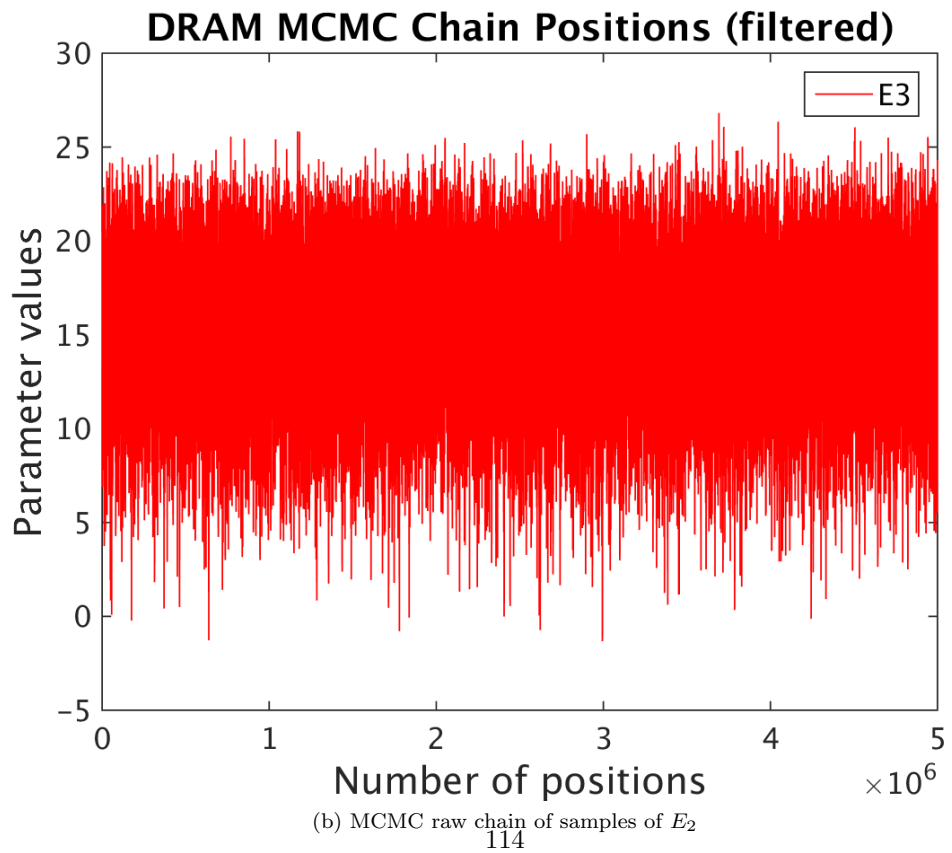
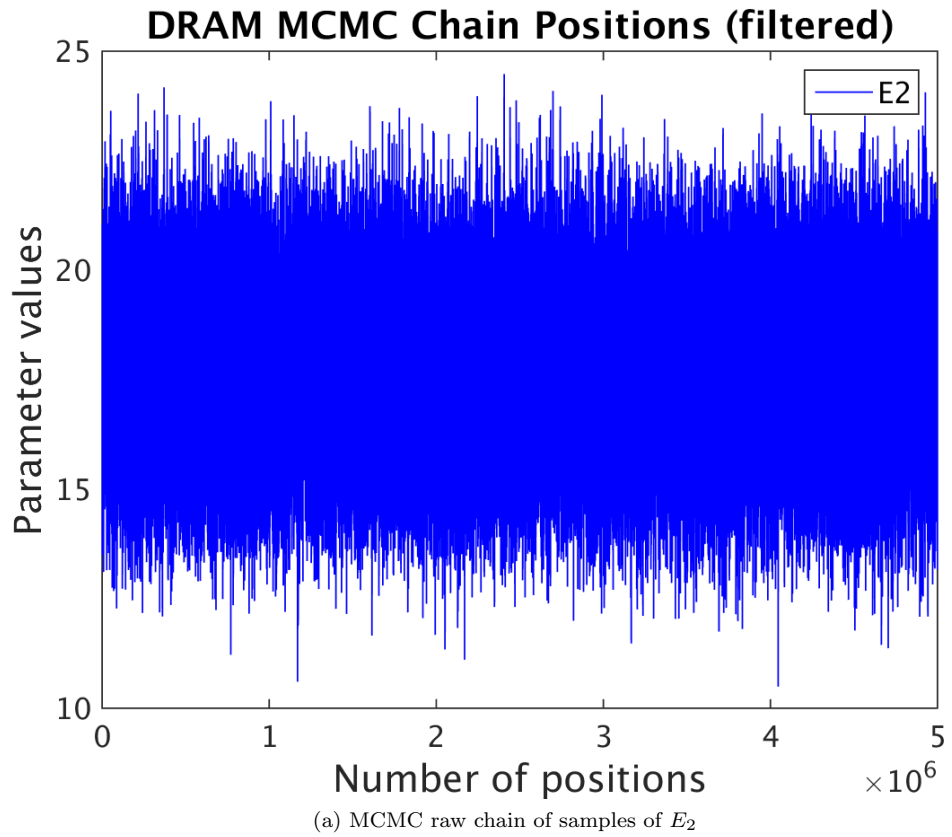


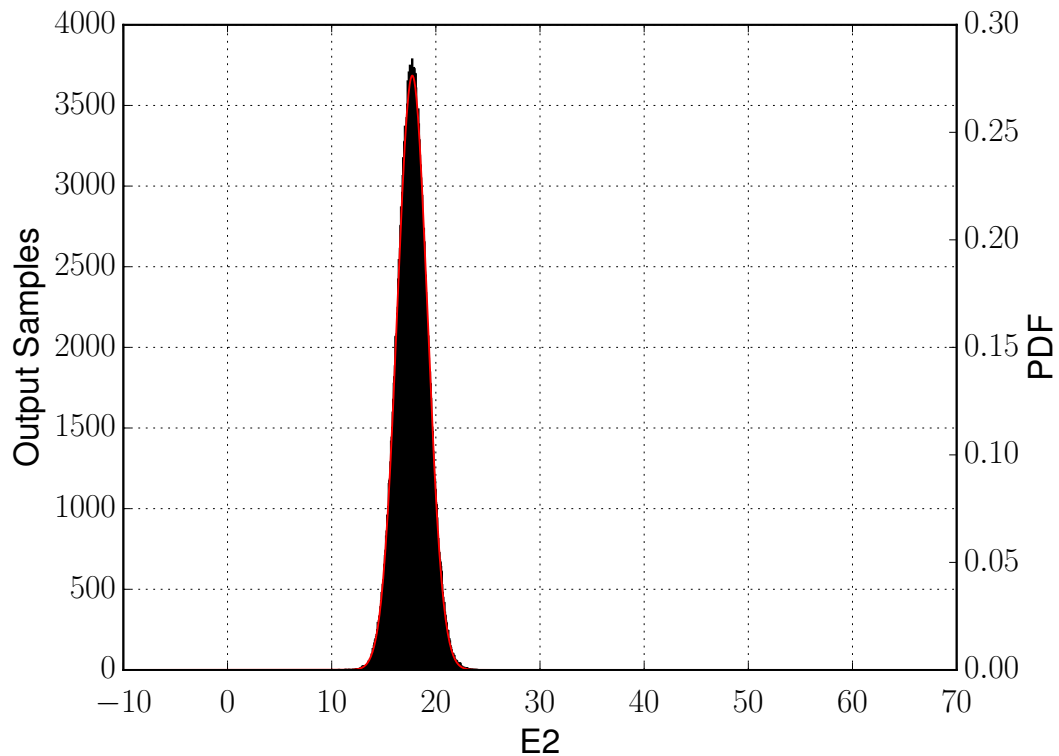
(e) Cummulative Density Funtion



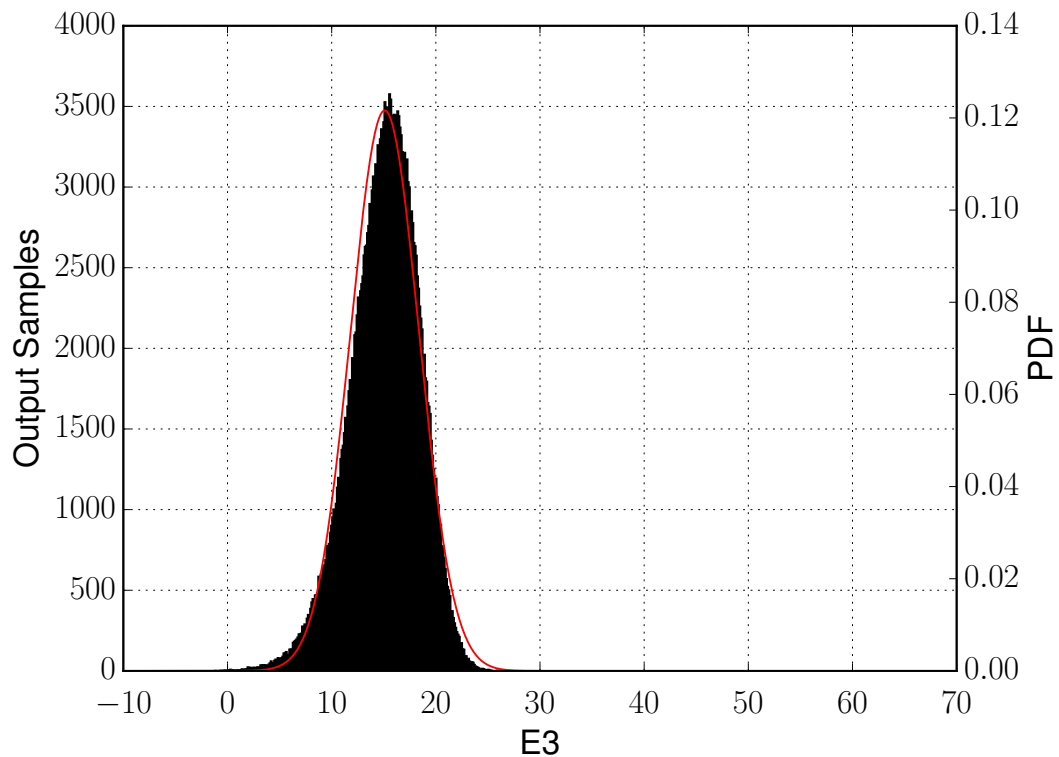
(f) KDE
113

Figure 5.-16: Results for sample size 1e6



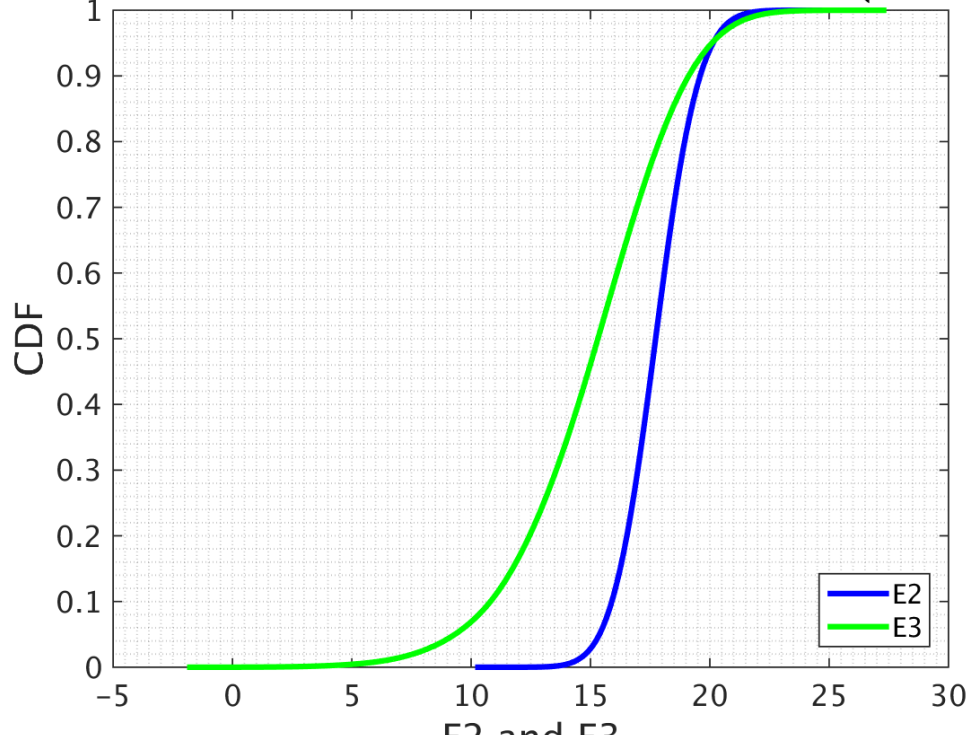


(c) Histogram for E_2



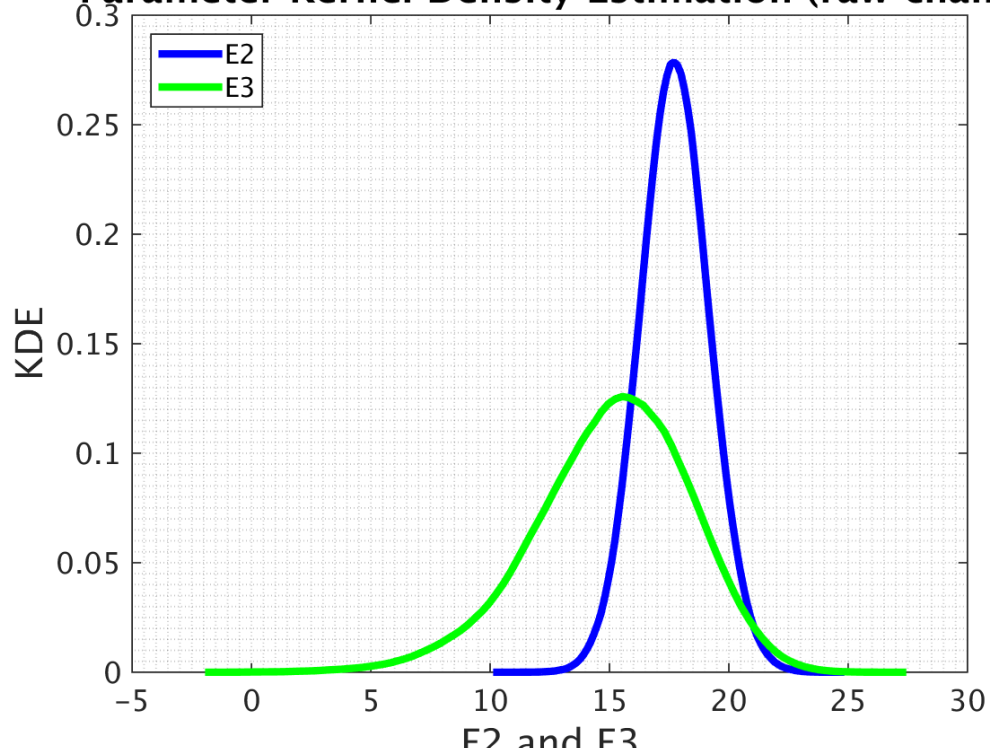
(d) Histogram for E_3

Parameter Cumulative Distribution Function (raw chain)



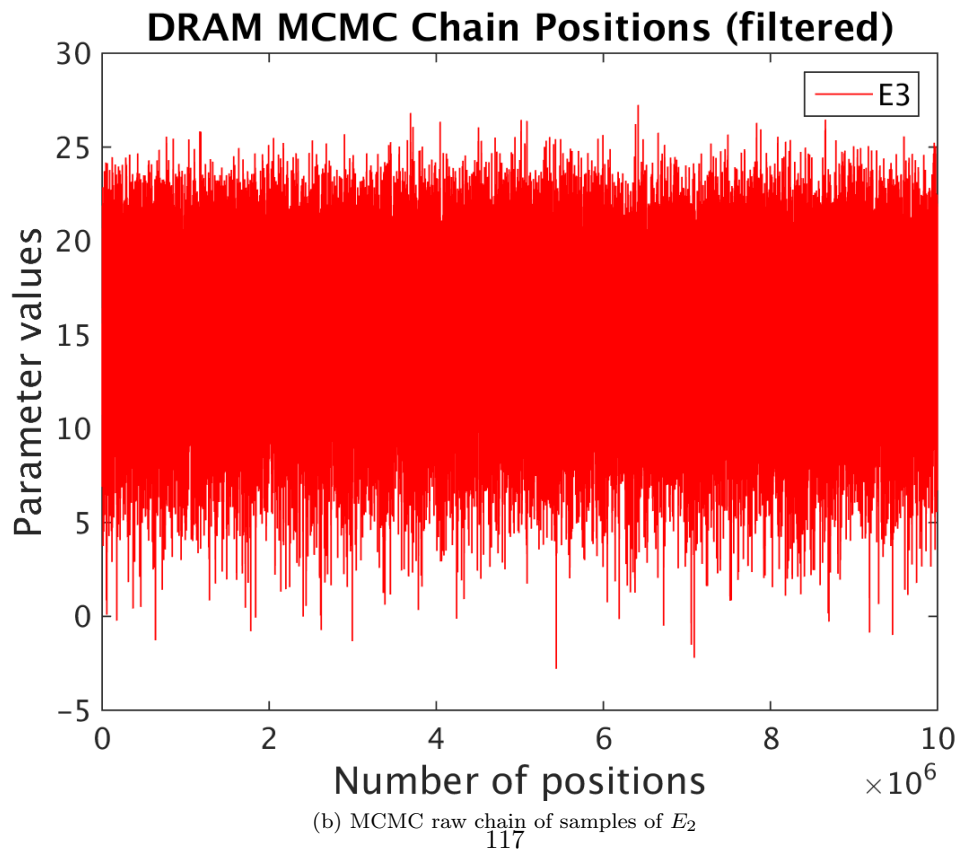
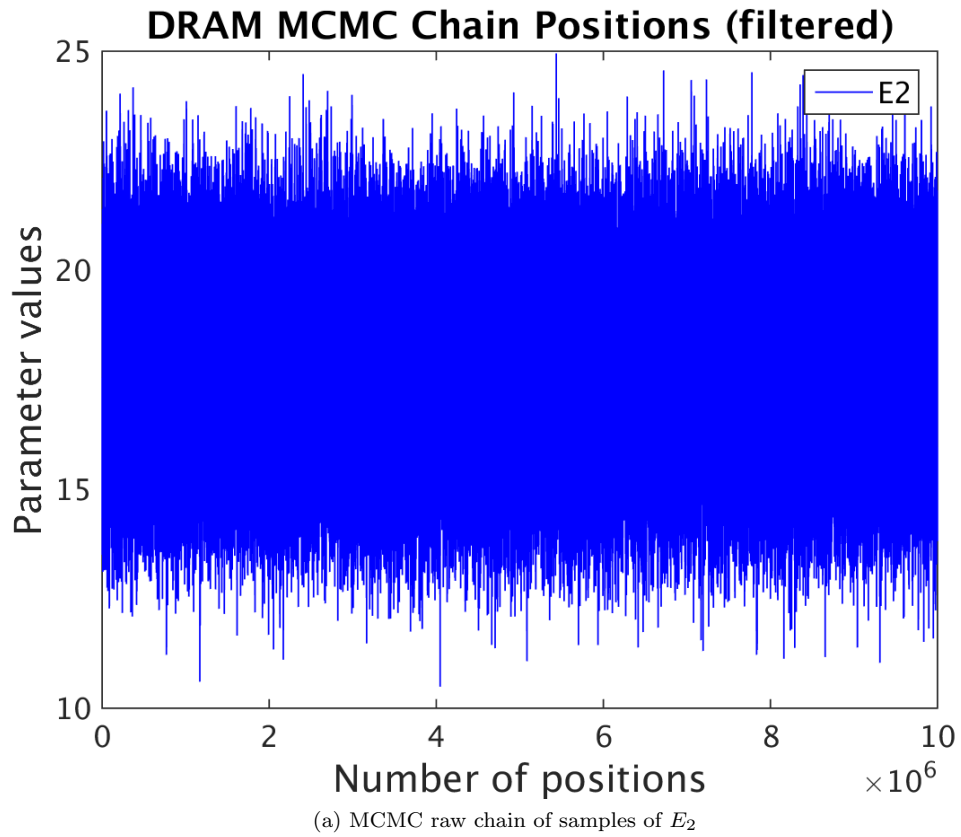
(e) Cummulative Density Funtion

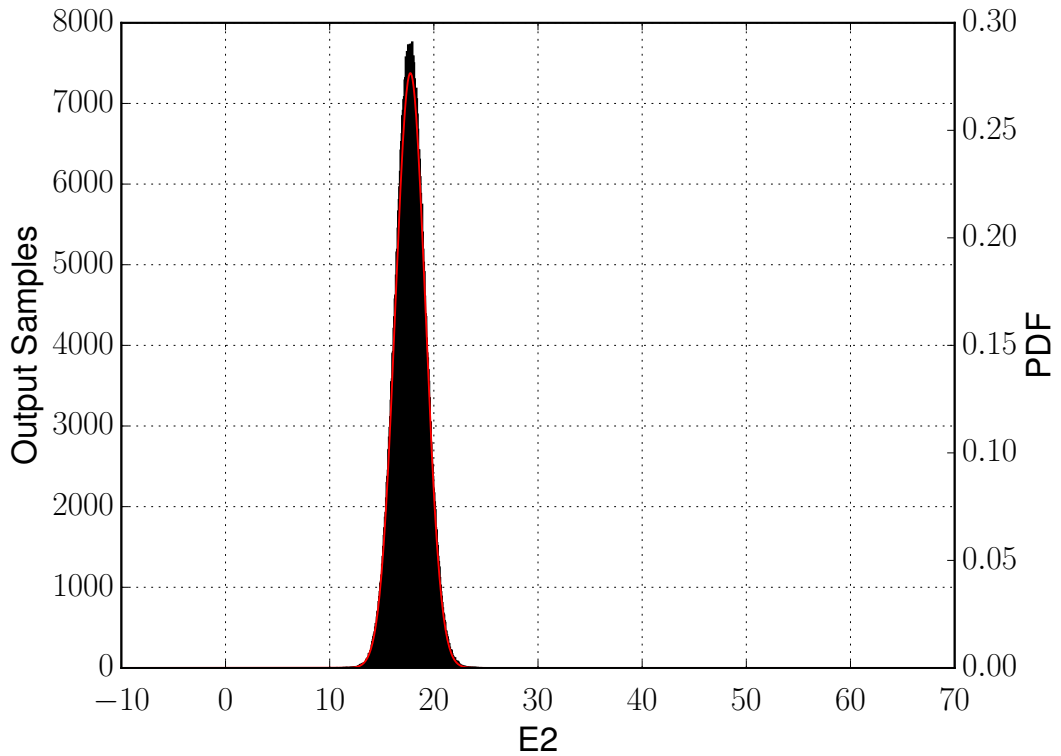
Parameter Kernel Density Estimation (raw chain)



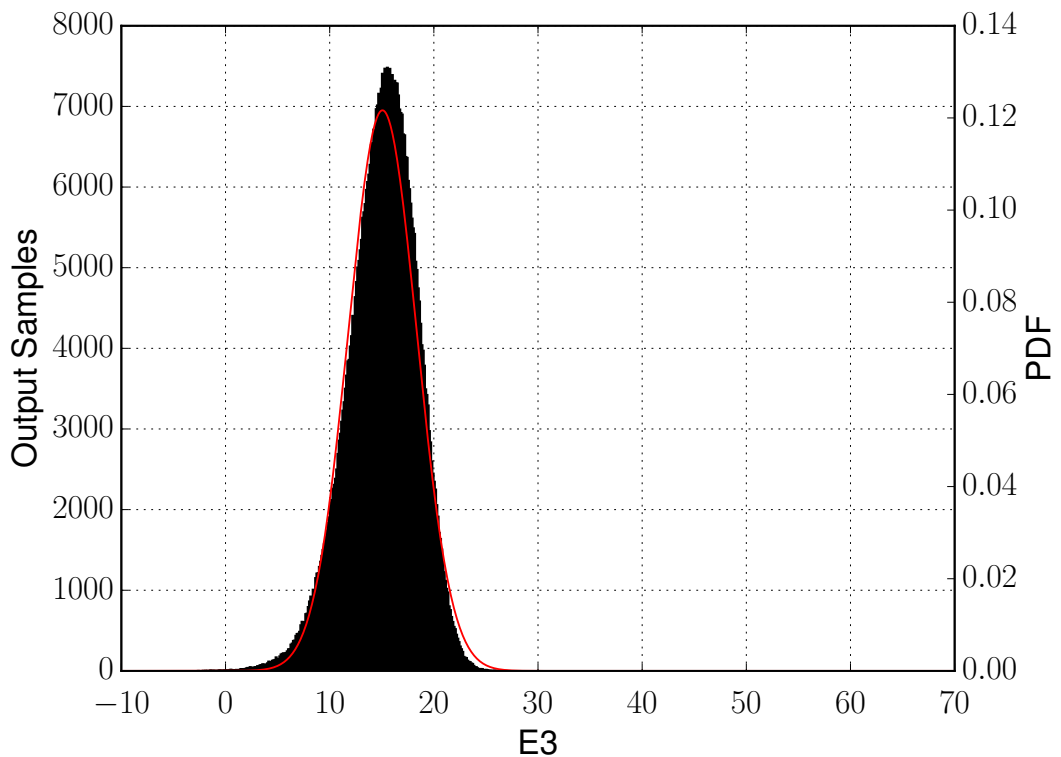
(f) KDE
116

Figure 5.-16: Results for sample size 5e6



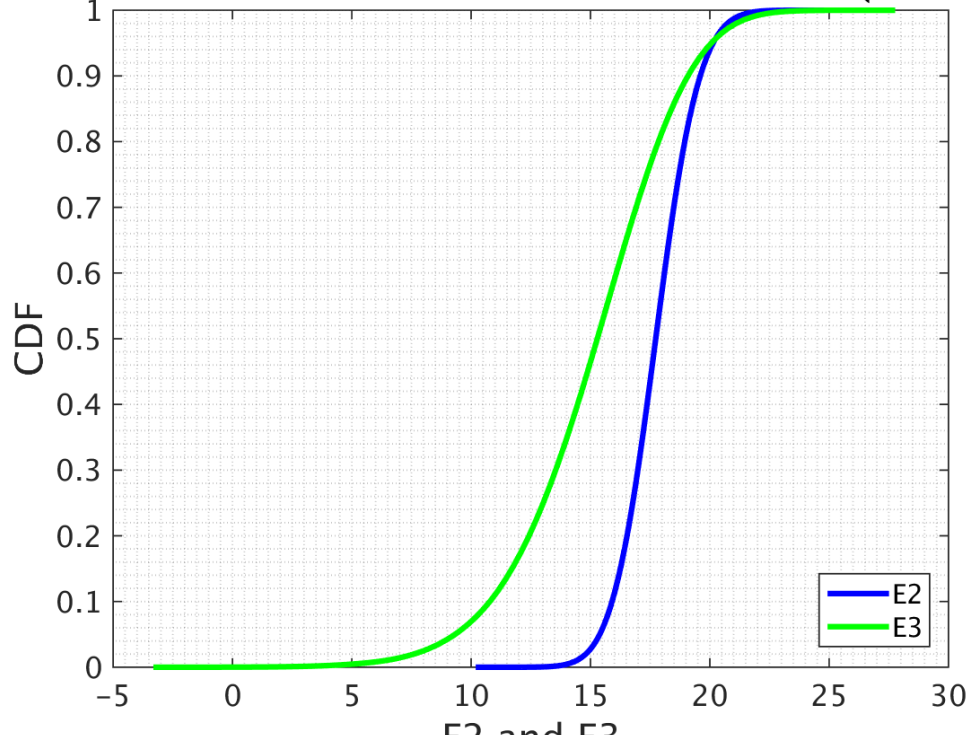


(c) Histogram for E_2



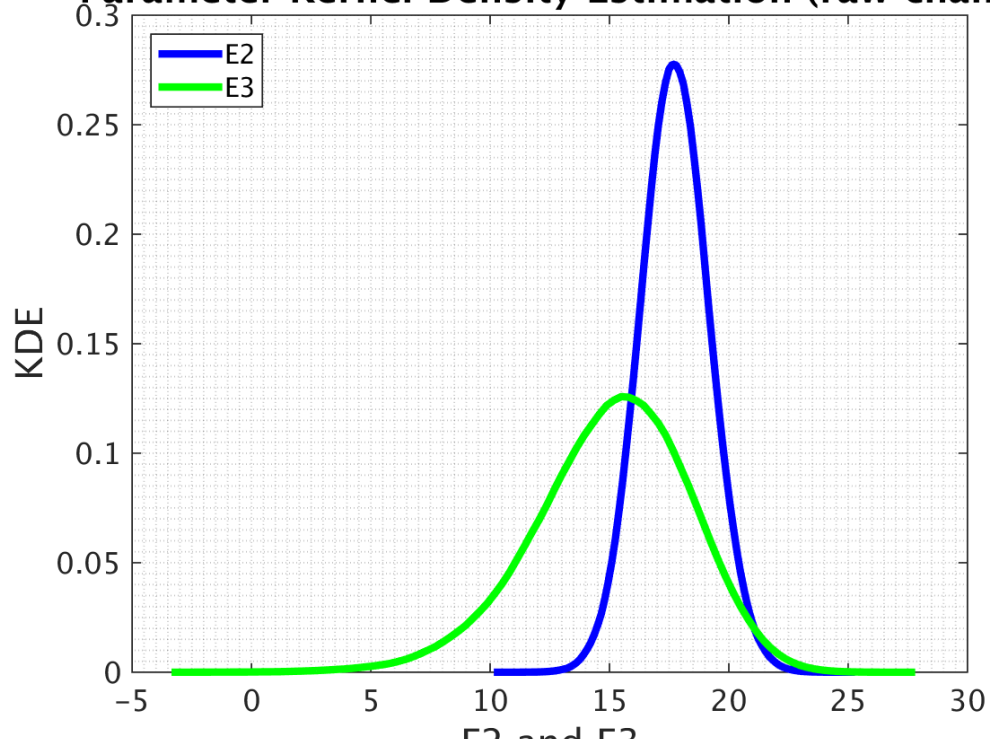
(d) Histogram for E_3

Parameter Cumulative Distribution Function (raw chain)



(e) Cummulative Density Funtion

Parameter Kernel Density Estimation (raw chain)

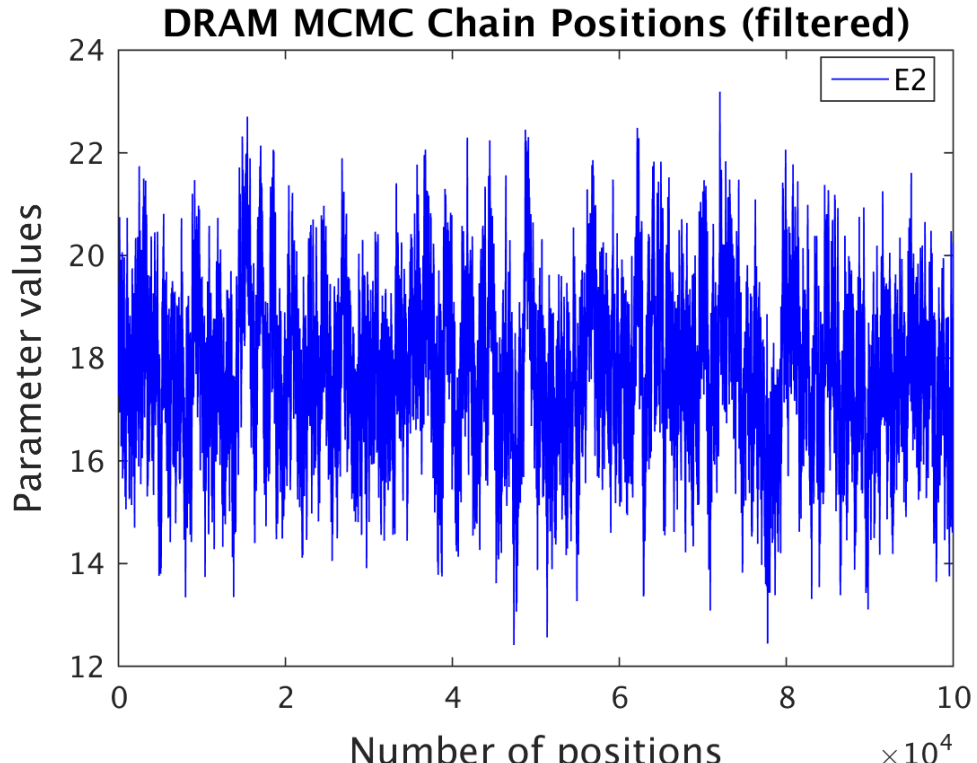


(f) KDE
119

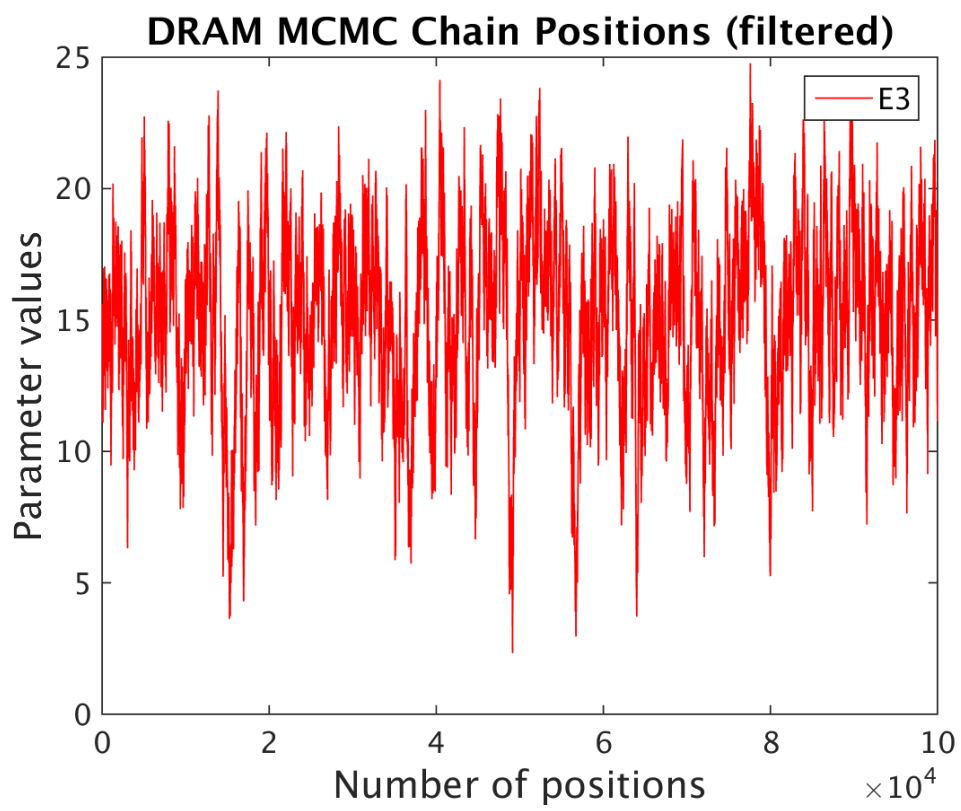
Figure 5.-16: Results for sample size 1e7

Sample size (Surrogate size) 100*100

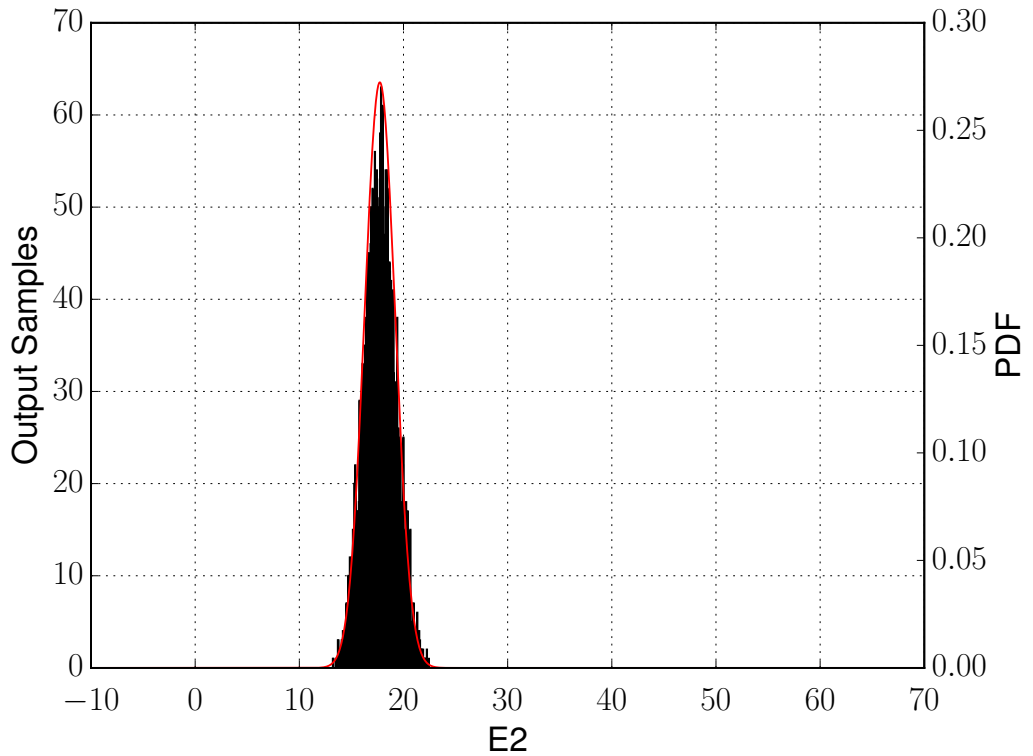
In this section we calculated flamespeed values for 10,000 (100*100) different points in the domain and the remaining values are linear combination of these 10,000 points. The results below are for sample size $1e5$, $5e5$, $1e6$, $5e6$ and $1e7$.



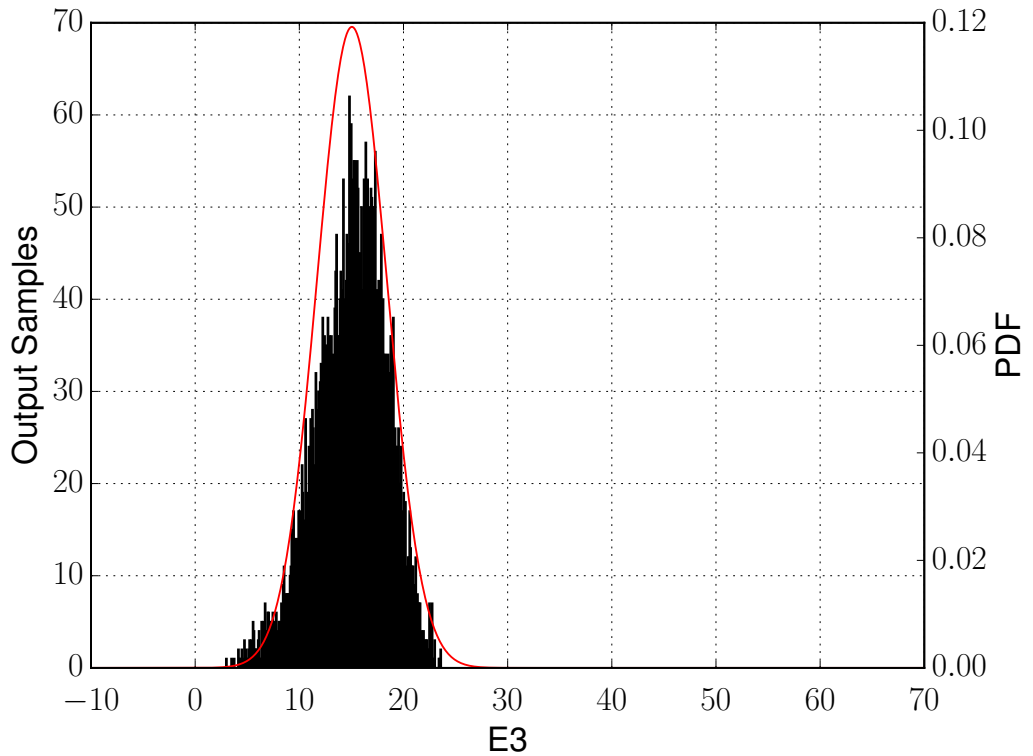
(a) MCMC raw chain of samples of E_2



(b) MCMC raw chain of samples of E_3

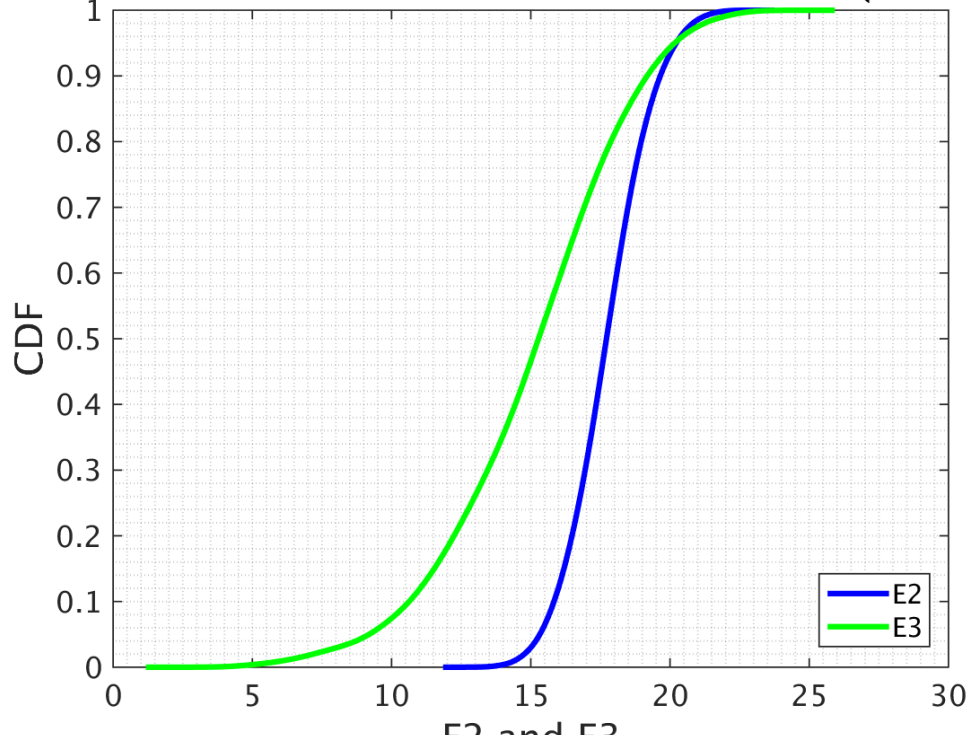


(c) Histogram for E_2



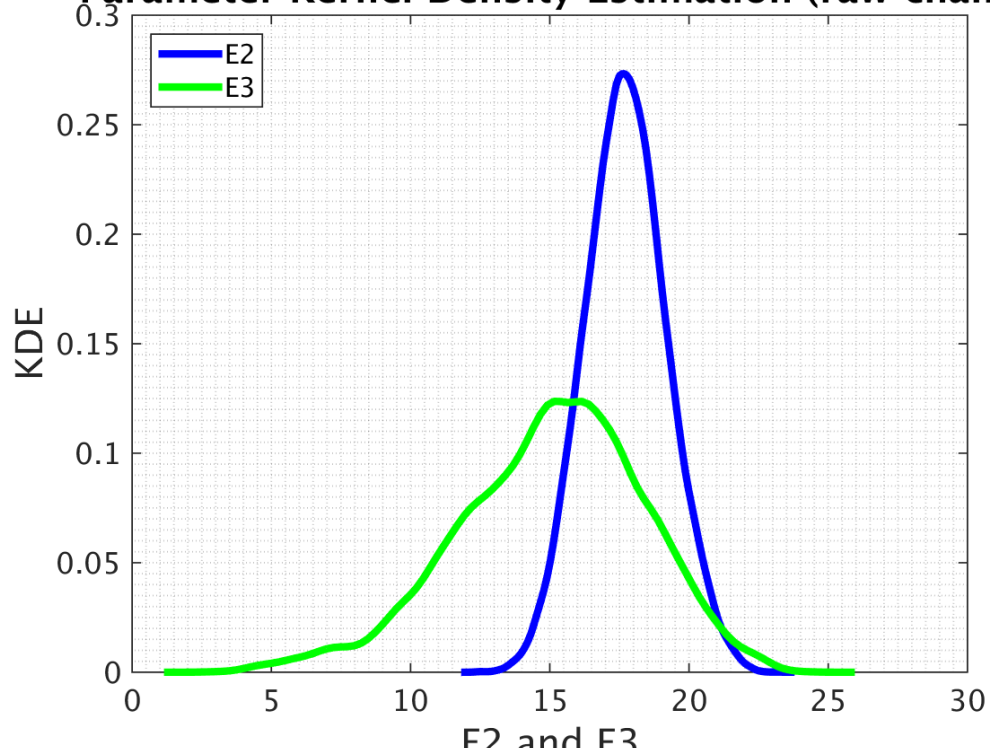
(d) Histogram for E_3

Parameter Cumulative Distribution Function (raw chain)



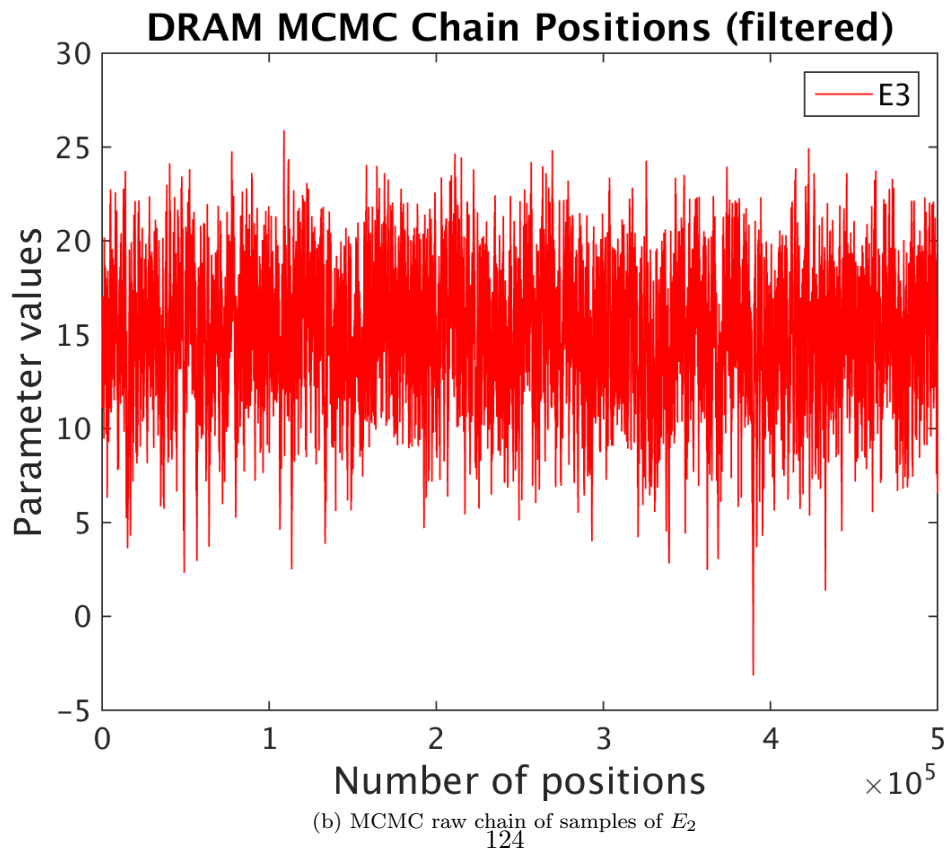
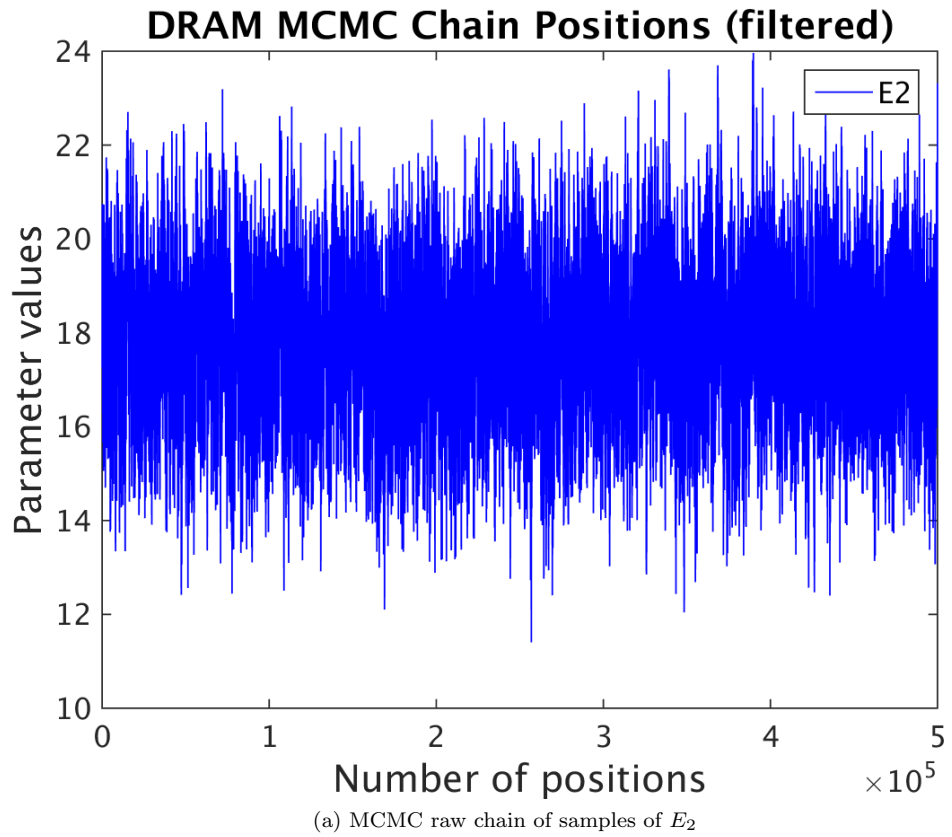
(e) Cummulative Density Funtion

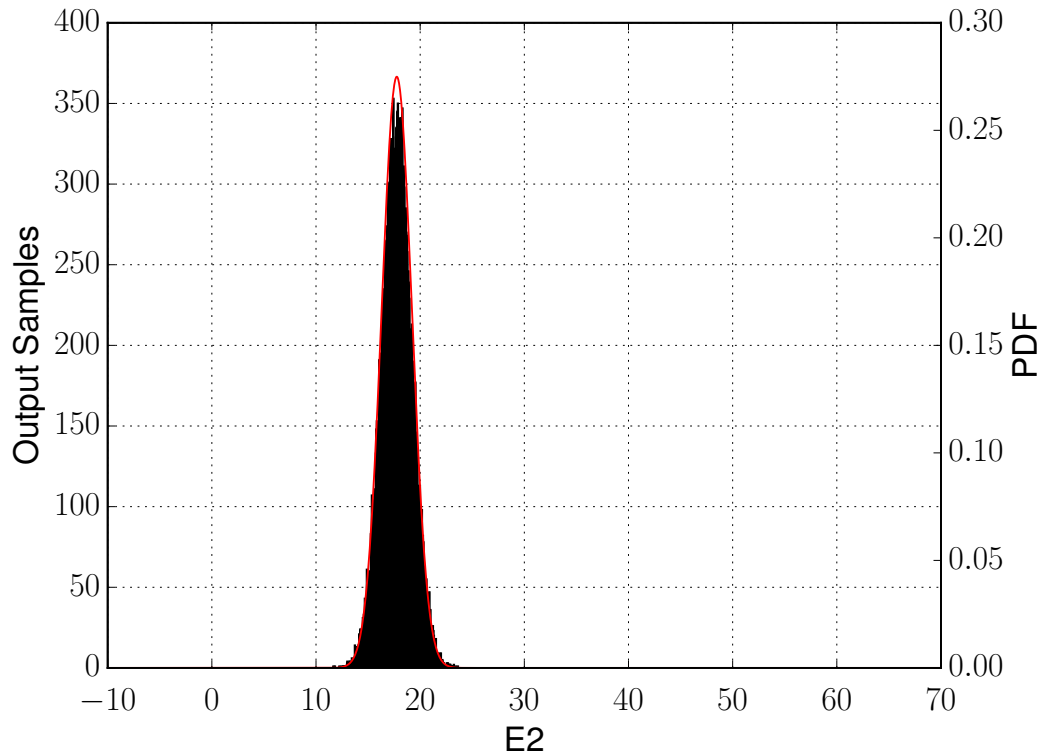
Parameter Kernel Density Estimation (raw chain)



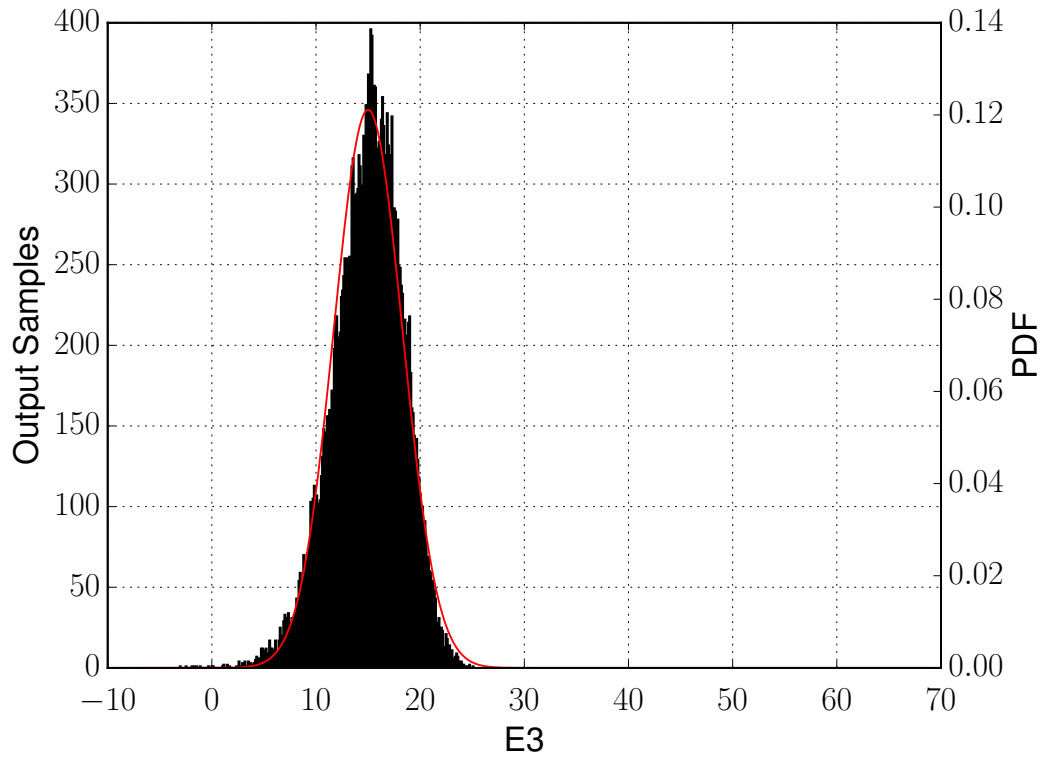
(f) KDE
123

Figure 5.-16: Results for sample size 1e5



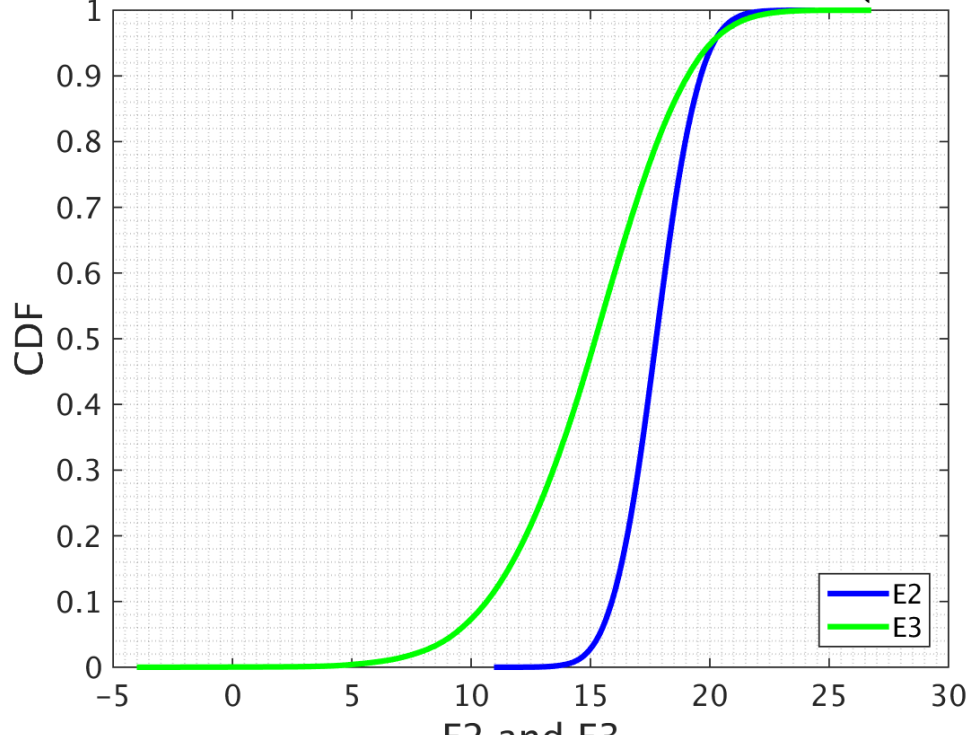


(c) Histogram for E_2



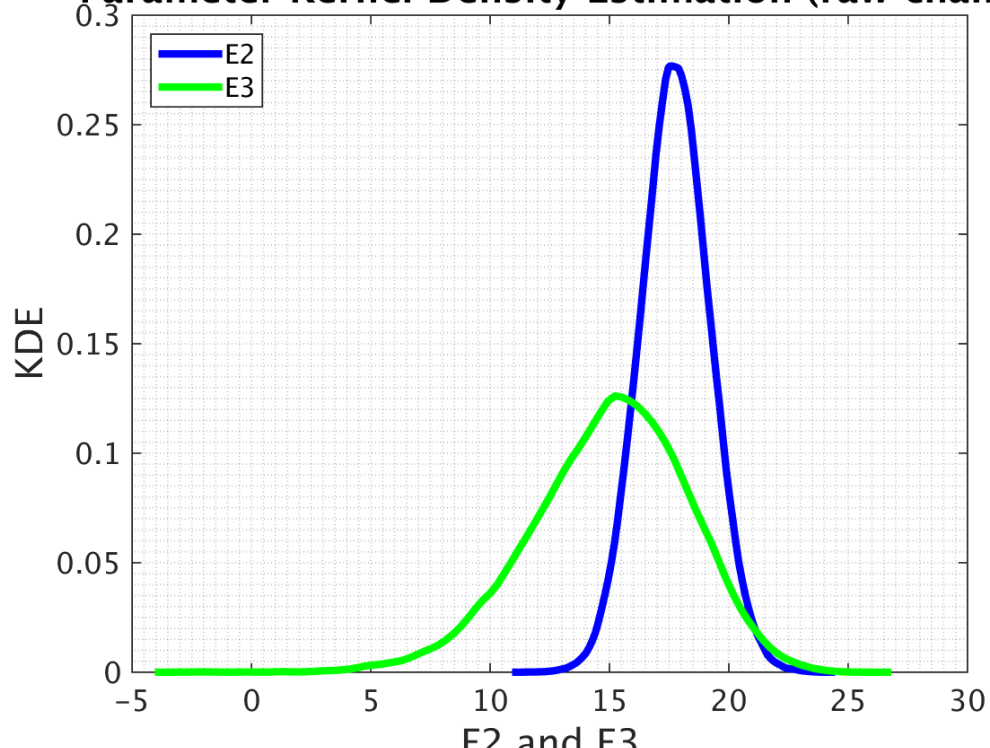
(d) Histogram for E_3

Parameter Cumulative Distribution Function (raw chain)



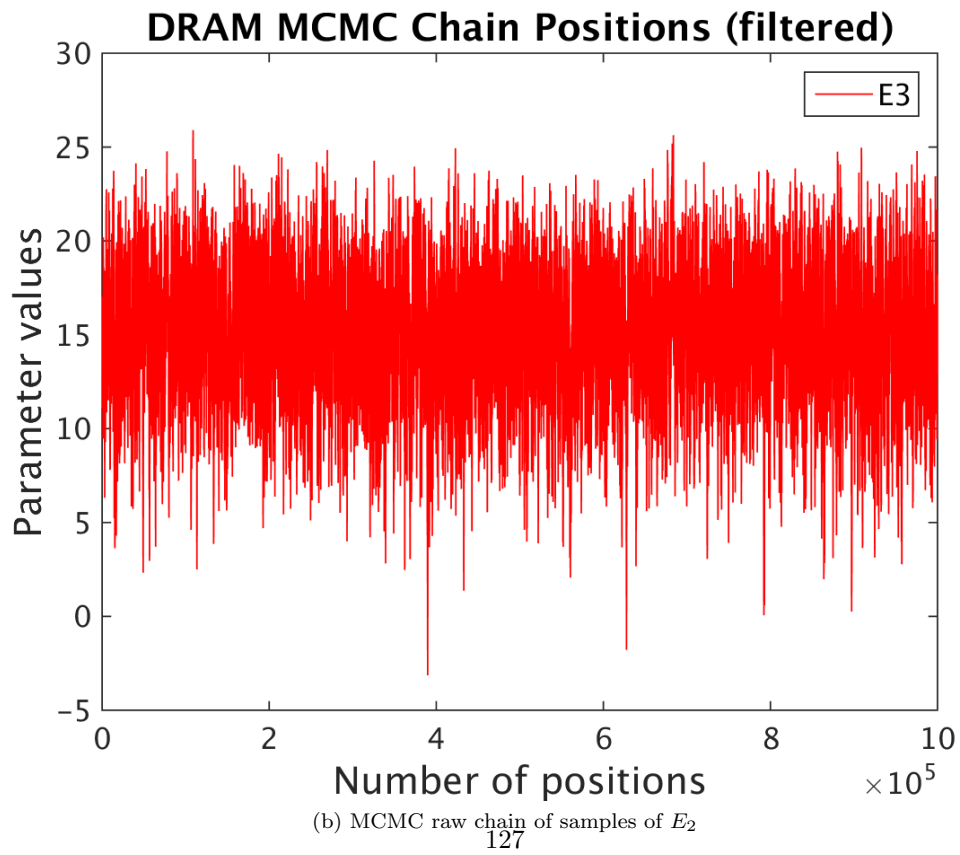
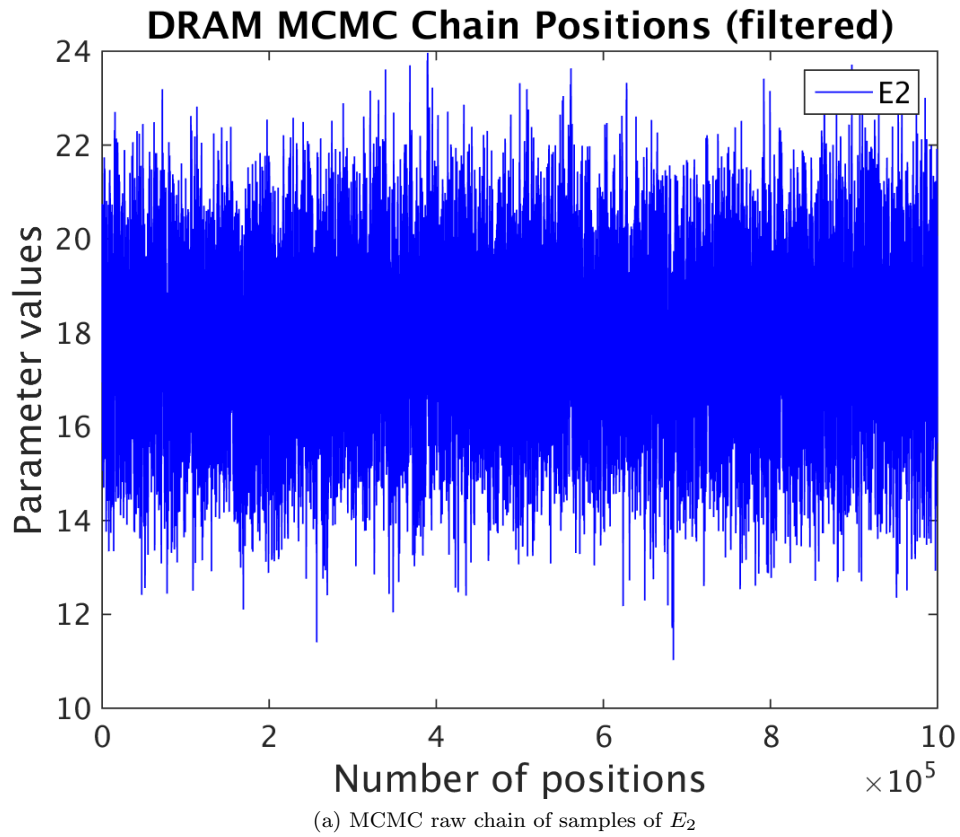
(e) Cummulative Density Funtion

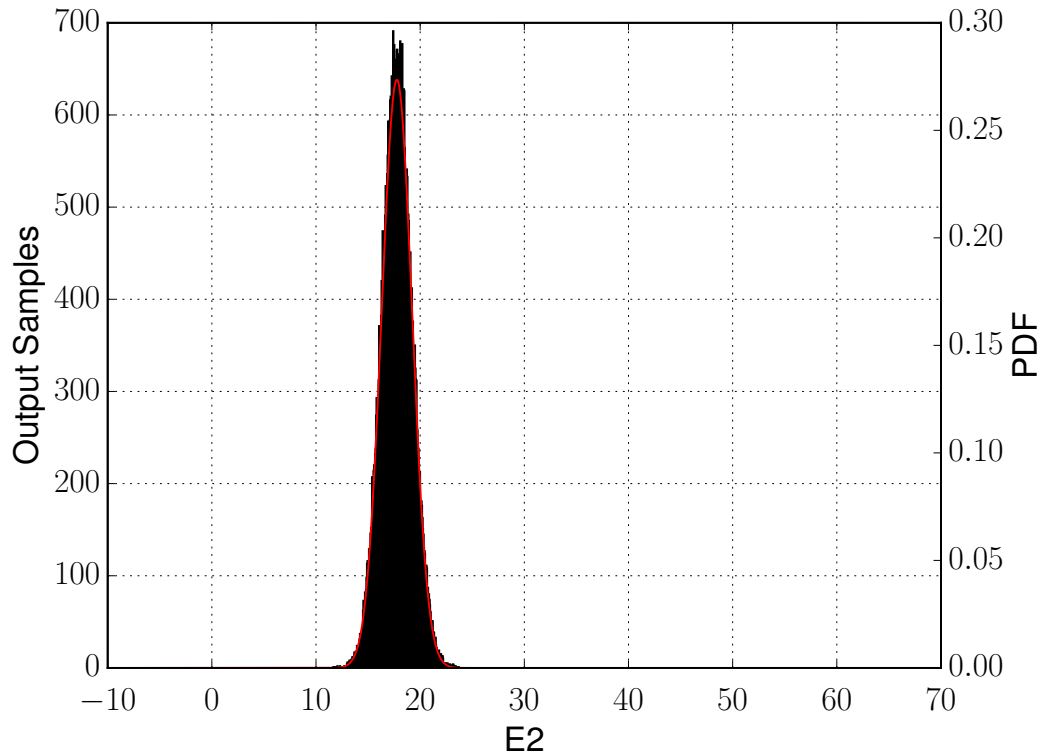
Parameter Kernel Density Estimation (raw chain)



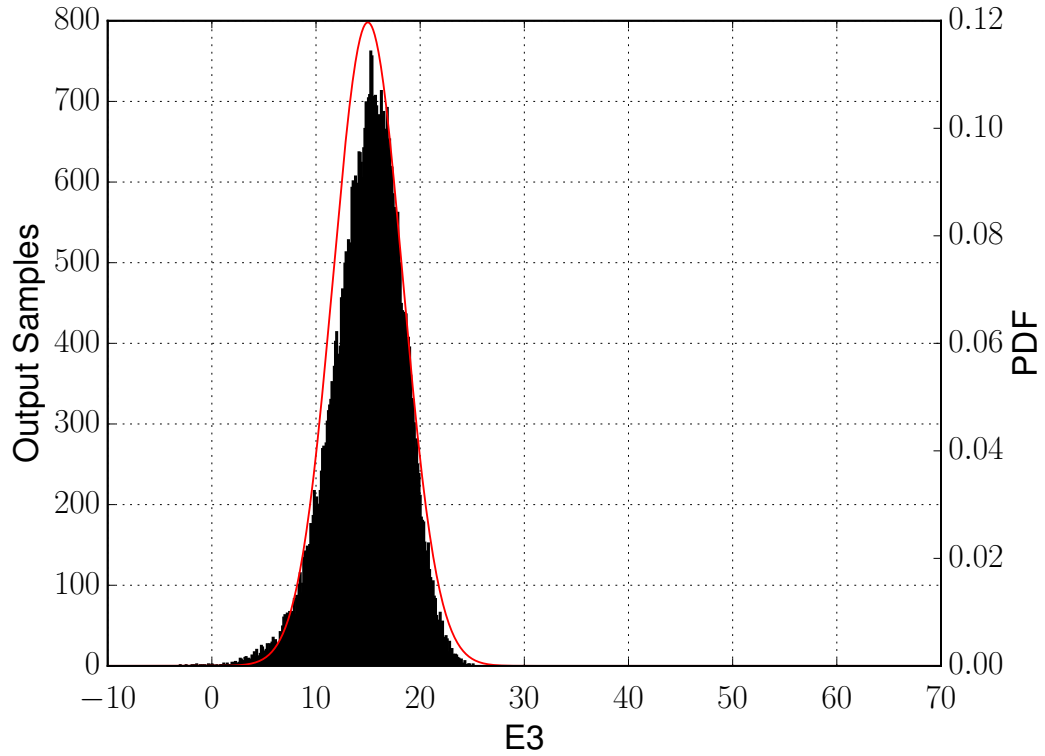
(f) KDE
126

Figure 5.-16: Results for sample size 5e5



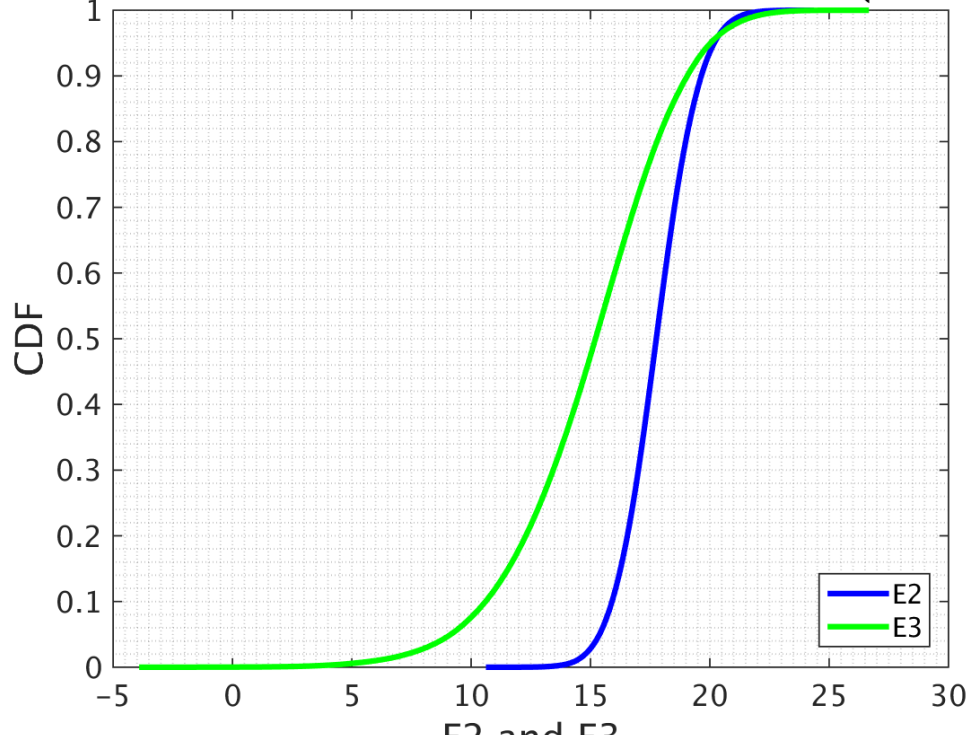


(c) Histogram for E_2



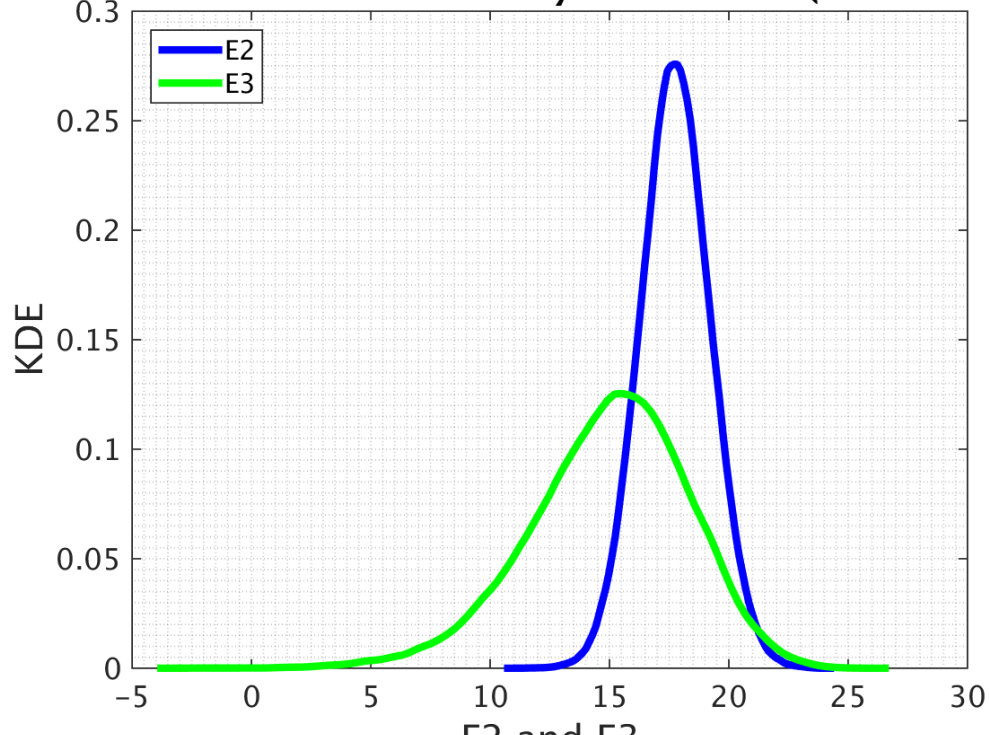
(d) Histogram for E_3

Parameter Cumulative Distribution Function (raw chain)



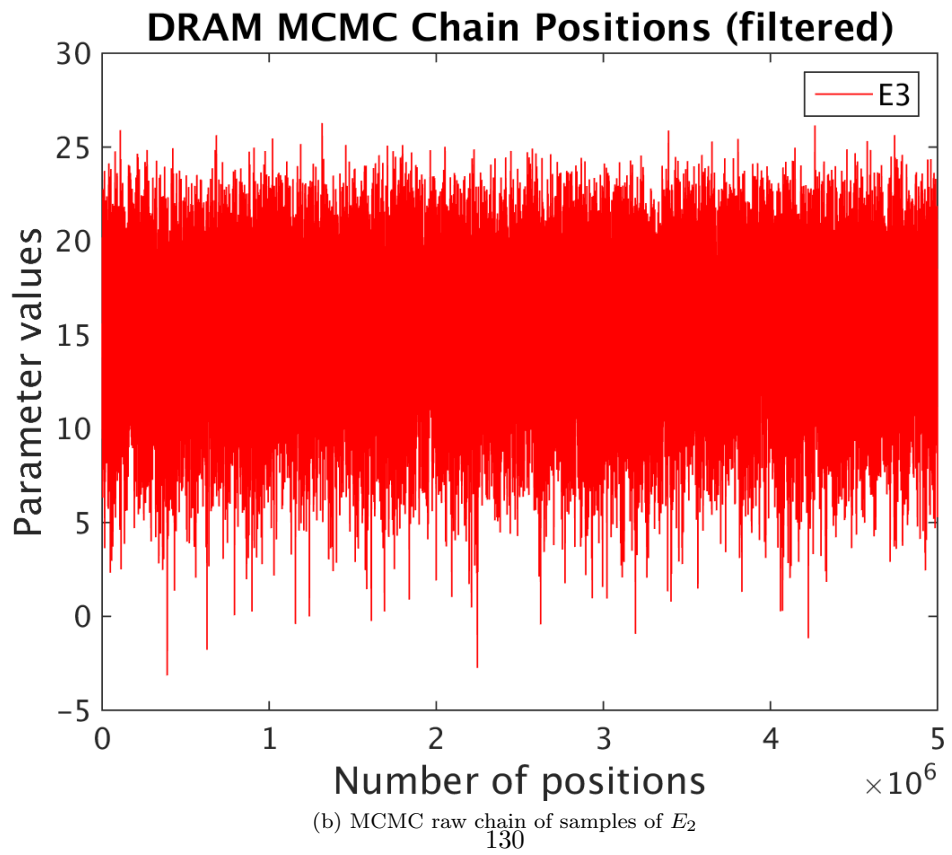
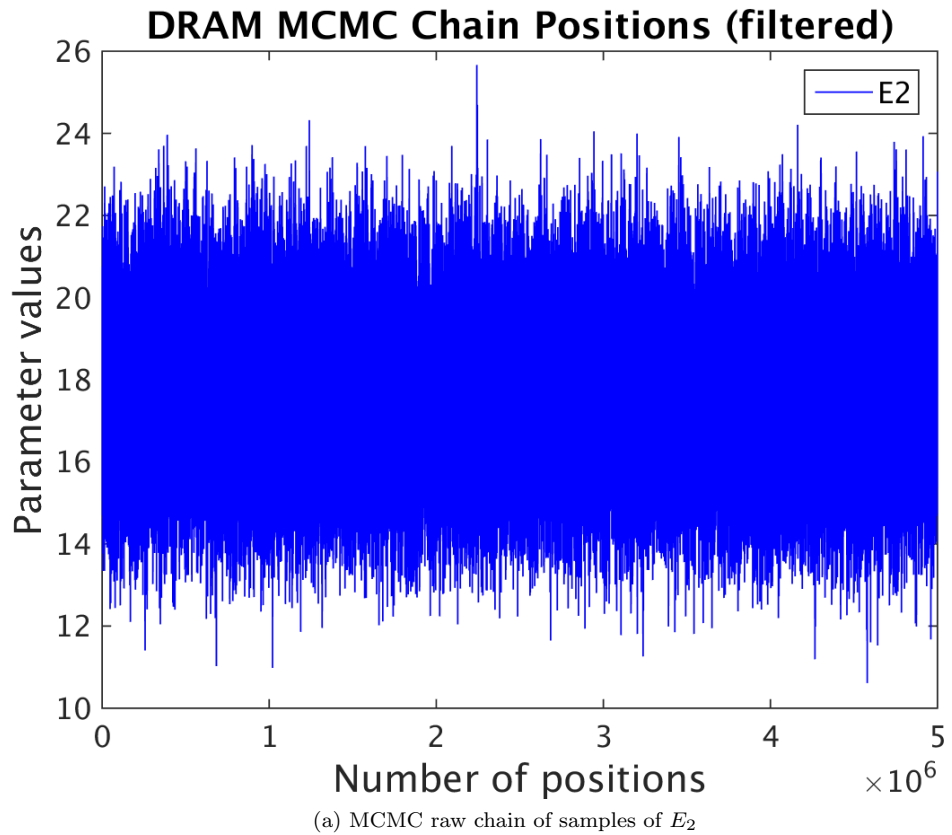
(e) Cummulative Density Funtion

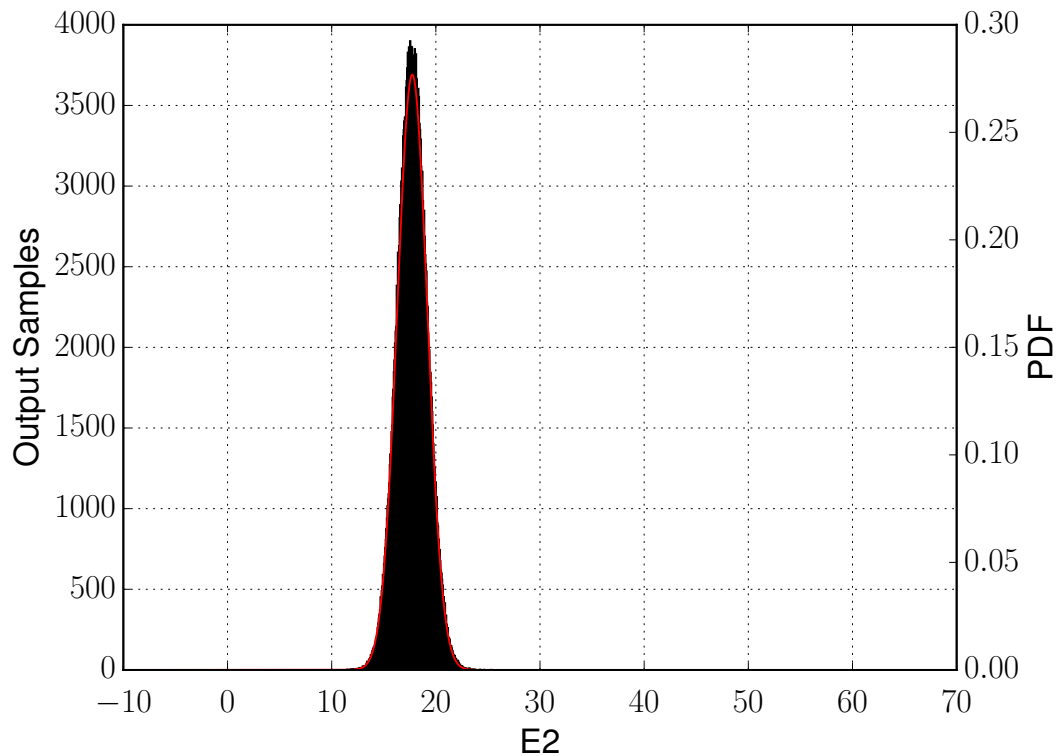
Parameter Kernel Density Estimation (raw chain)



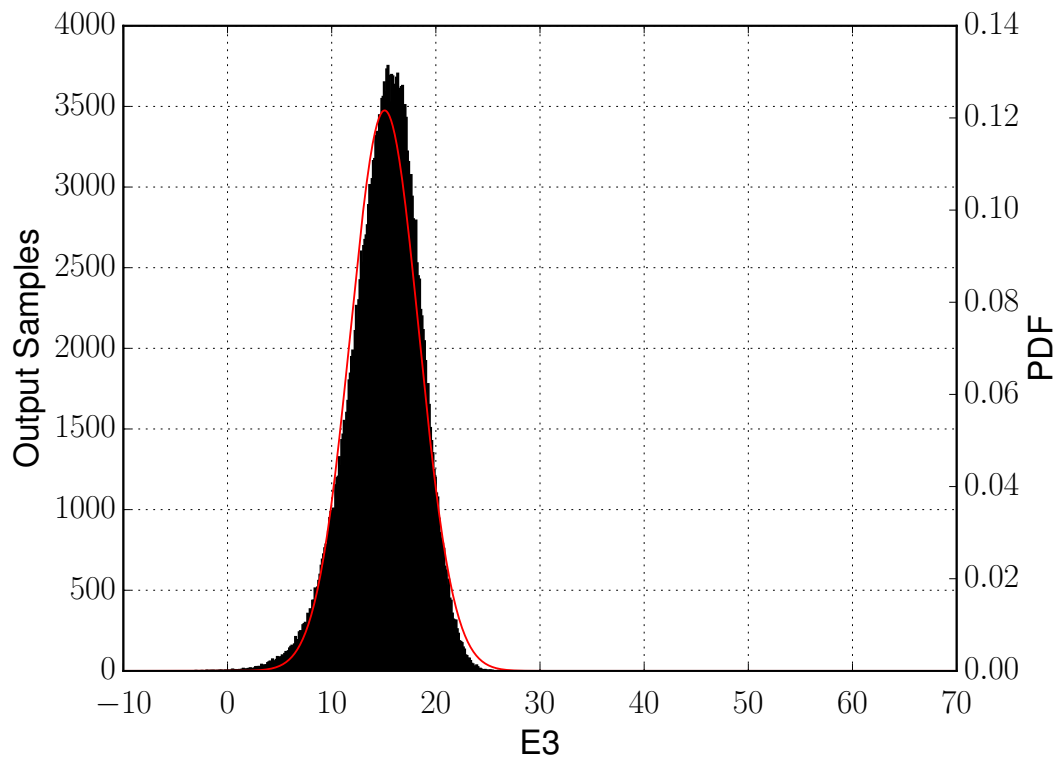
(f) KDE
129

Figure 5.-16: Results for sample size 1e6



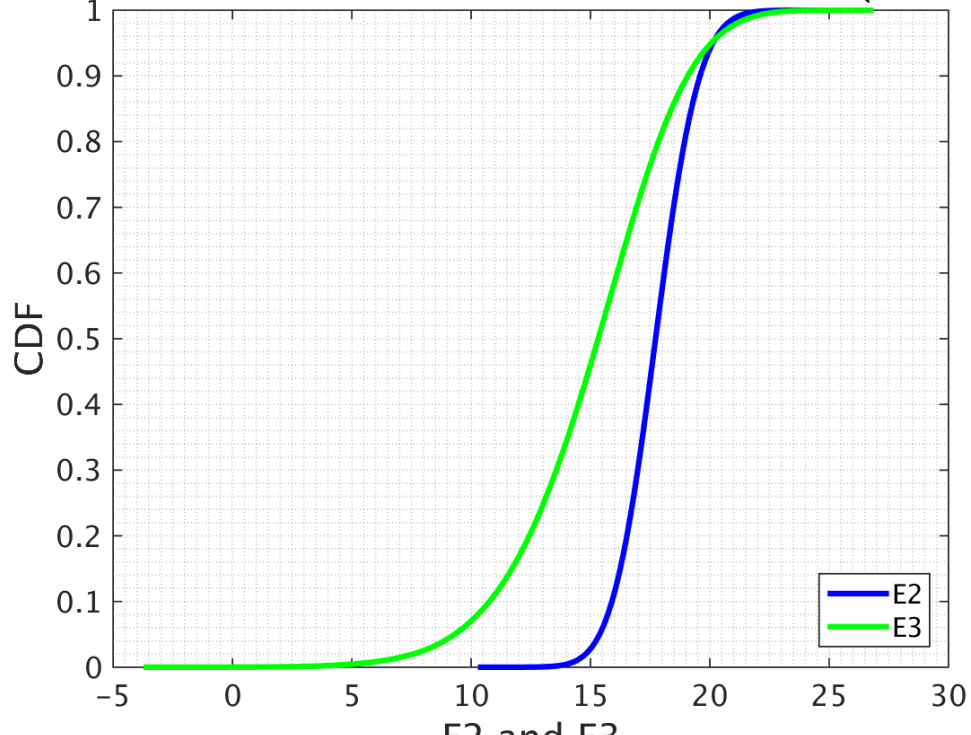


(c) Histogram for E_2



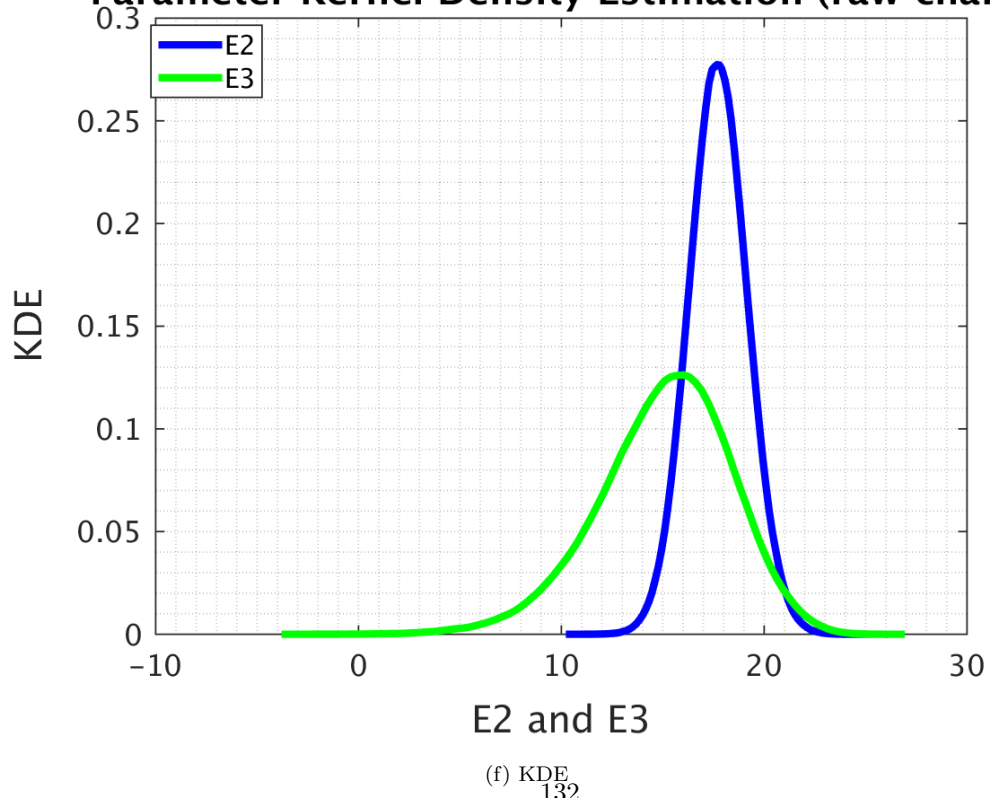
(d) Histogram for E_3

Parameter Cumulative Distribution Function (raw chain)



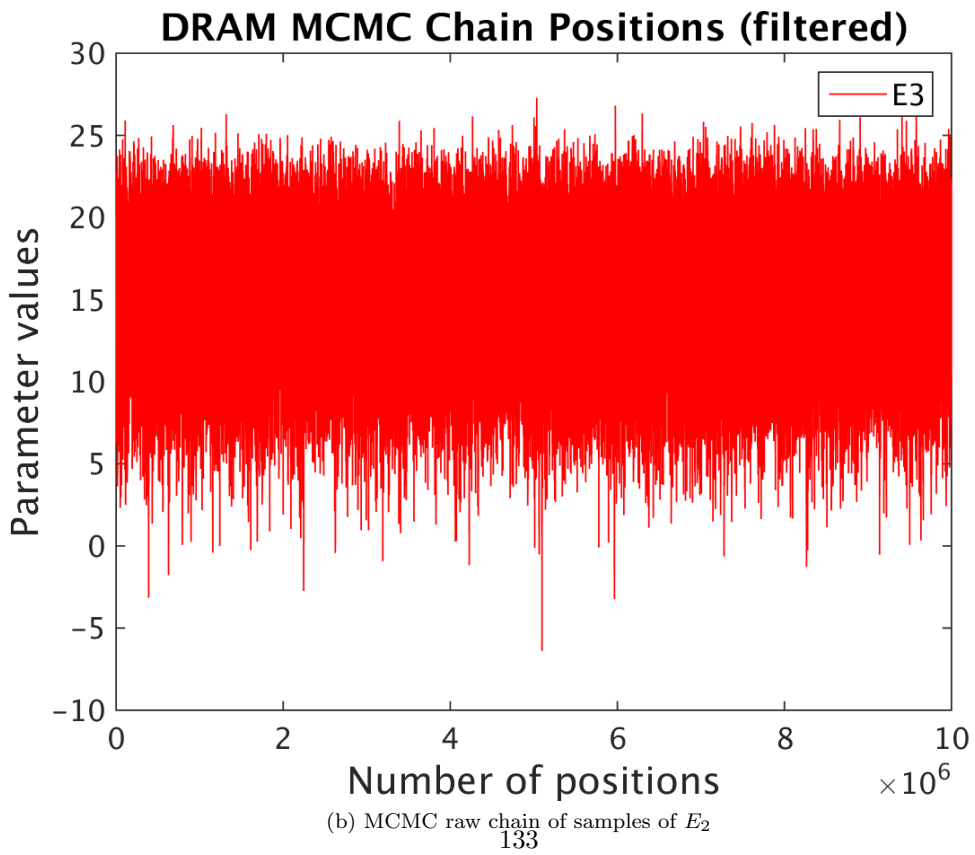
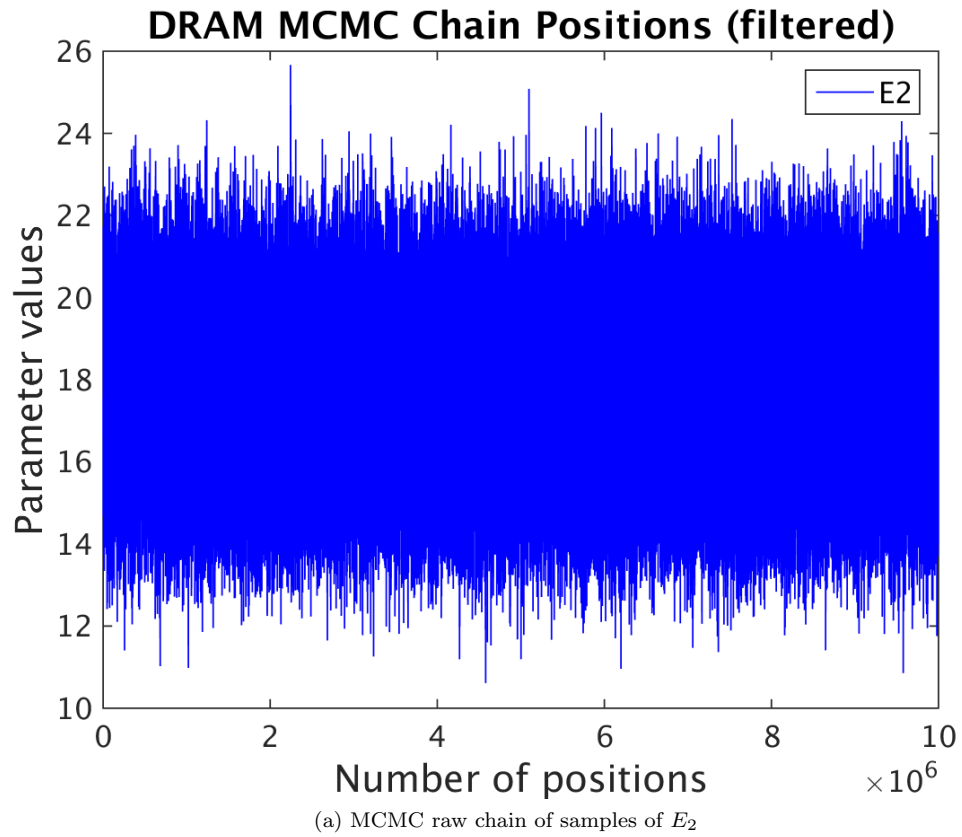
(e) Cummulative Density Funtion

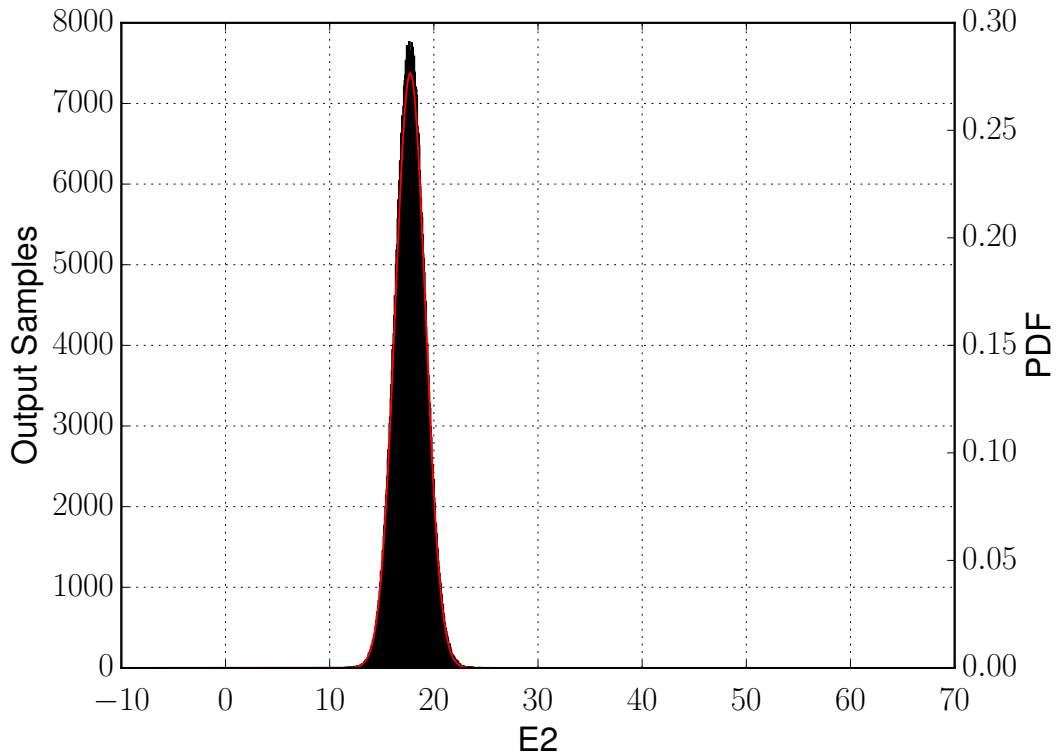
Parameter Kernel Density Estimation (raw chain)



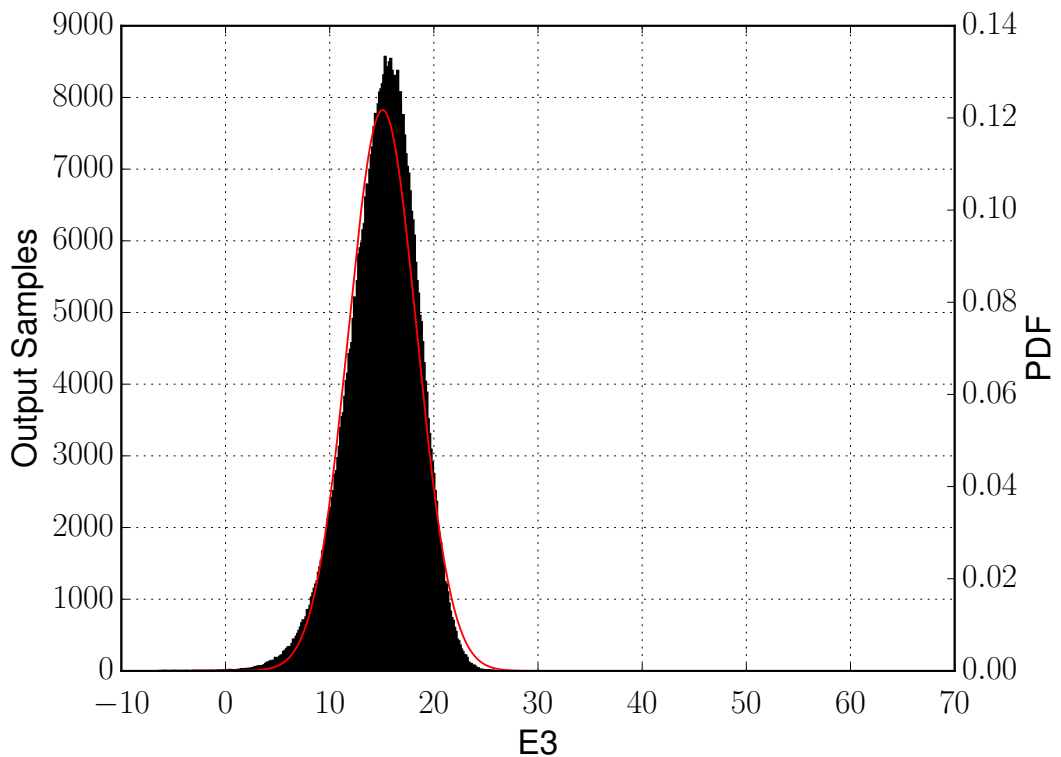
(f) KDE₁₃₂

Figure 5.-16: Results for sample size 5e6



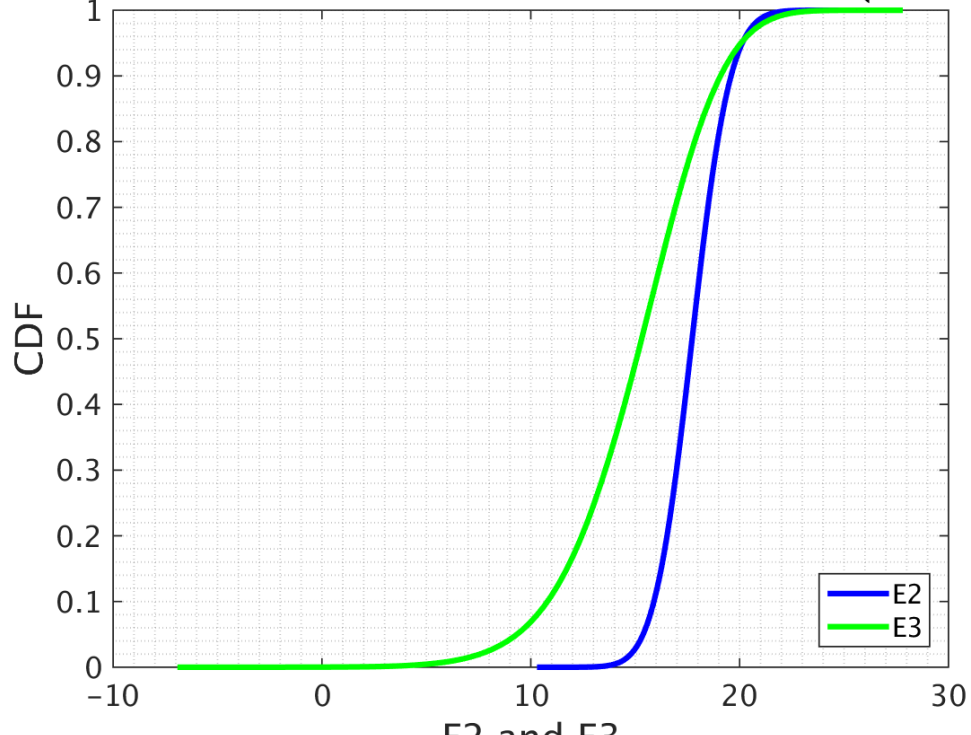


(c) Histogram for E_2



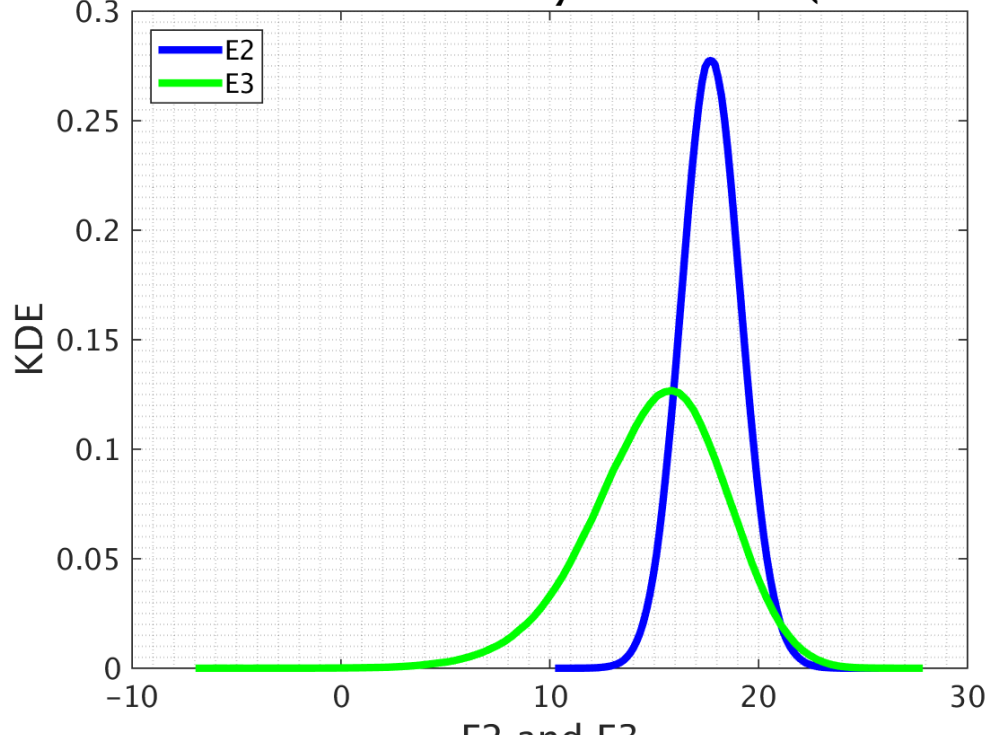
(d) Histogram for E_3

Parameter Cumulative Distribution Function (raw chain)



(e) Cummulative Density Funtion

Parameter Kernel Density Estimation (raw chain)



(f) KDE
135

Figure 5.-16: Results for sample size 1e7

5.2.2 Convergence Study

In this section, we see the convergence of the probability distribution as we increase the raw chain sample size. The plot is done for surrogate size of 100. In this analysis, raw chain size of 1e5, 5e5 , 1e6, 5e6 and 1e7 is taken.

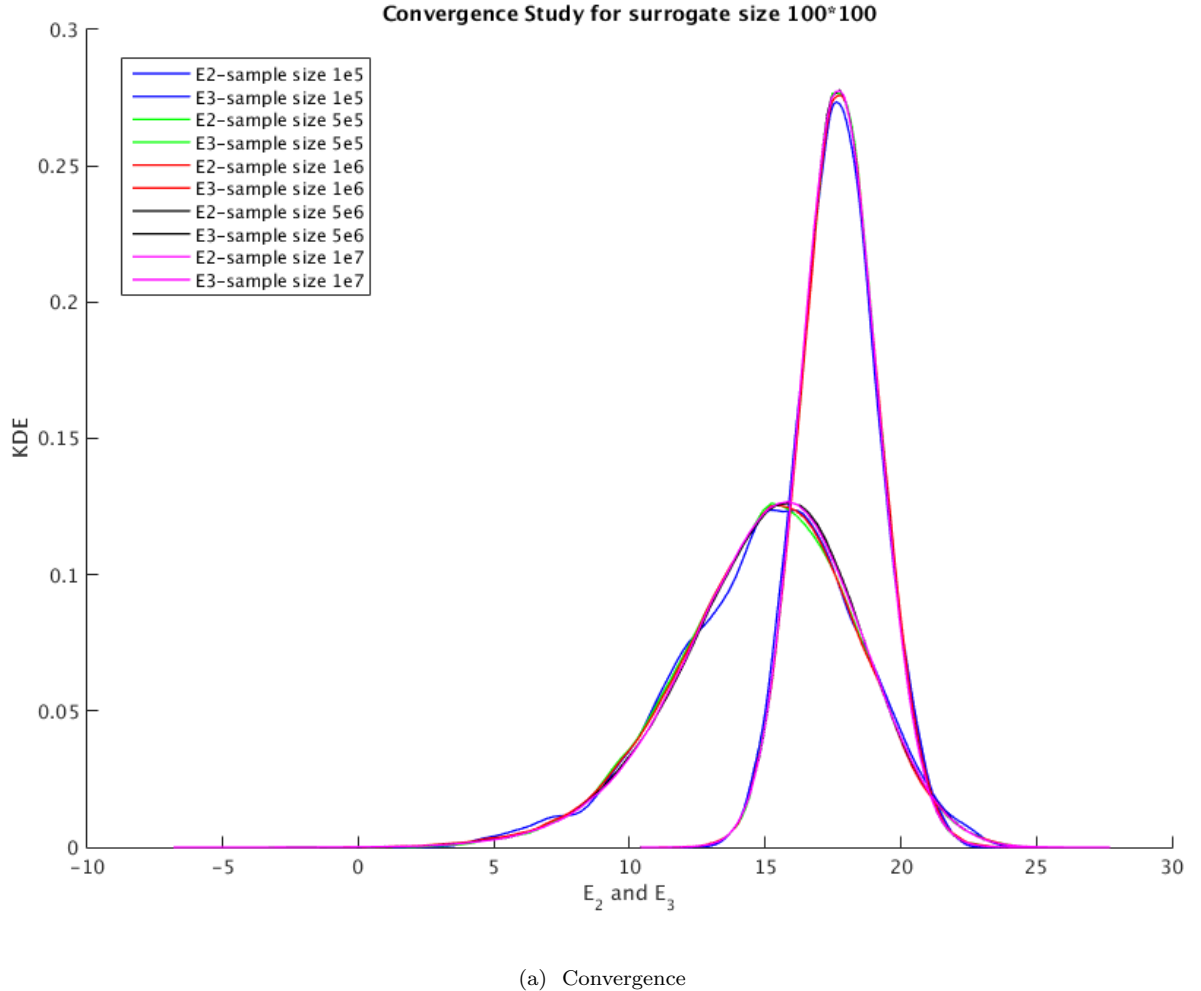
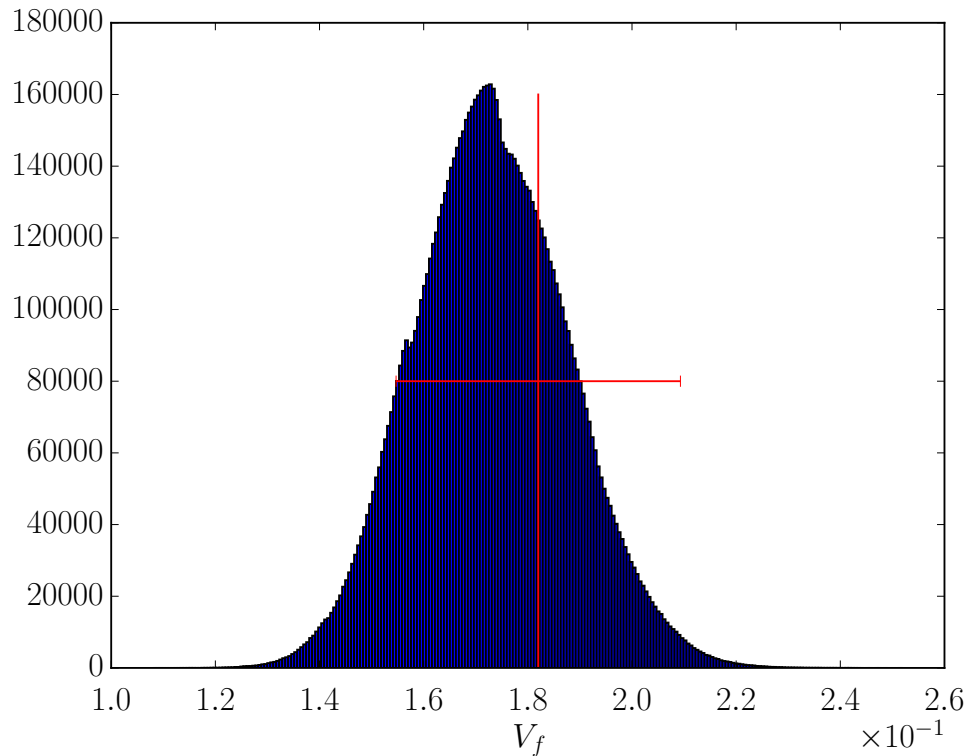


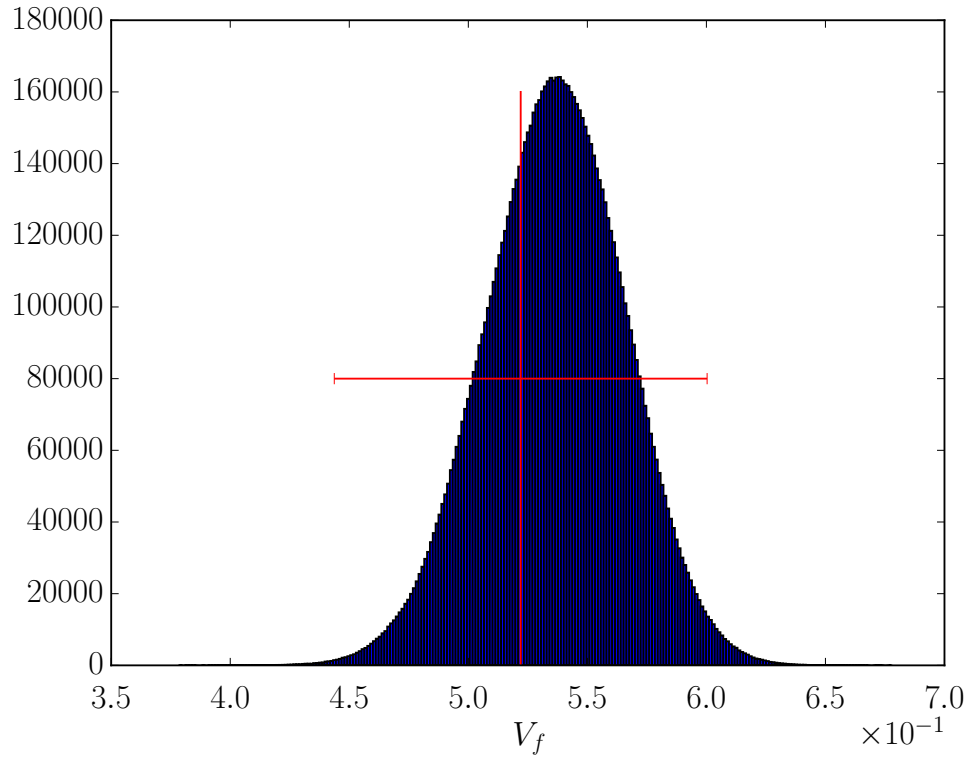
Figure 5.-15: Convergence for surrogate size 100

5.2.3 flamespeed Data fit

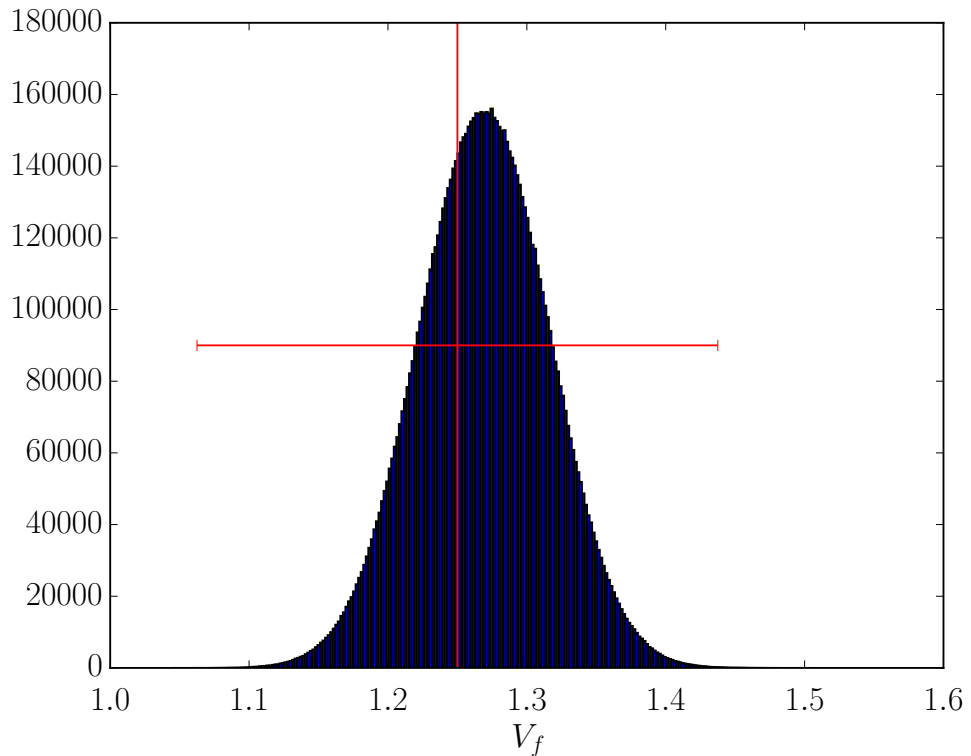
It is necessary to ensure that the samples of the parameters which we are drawing are fitting the flamespeed values of the experimental. In this section, we calculate the flamespeed for all the parameters drawn using the surrogate generated before. We have taken 1e7 sample size and calculated flamespeed for different concentrations of ozone.



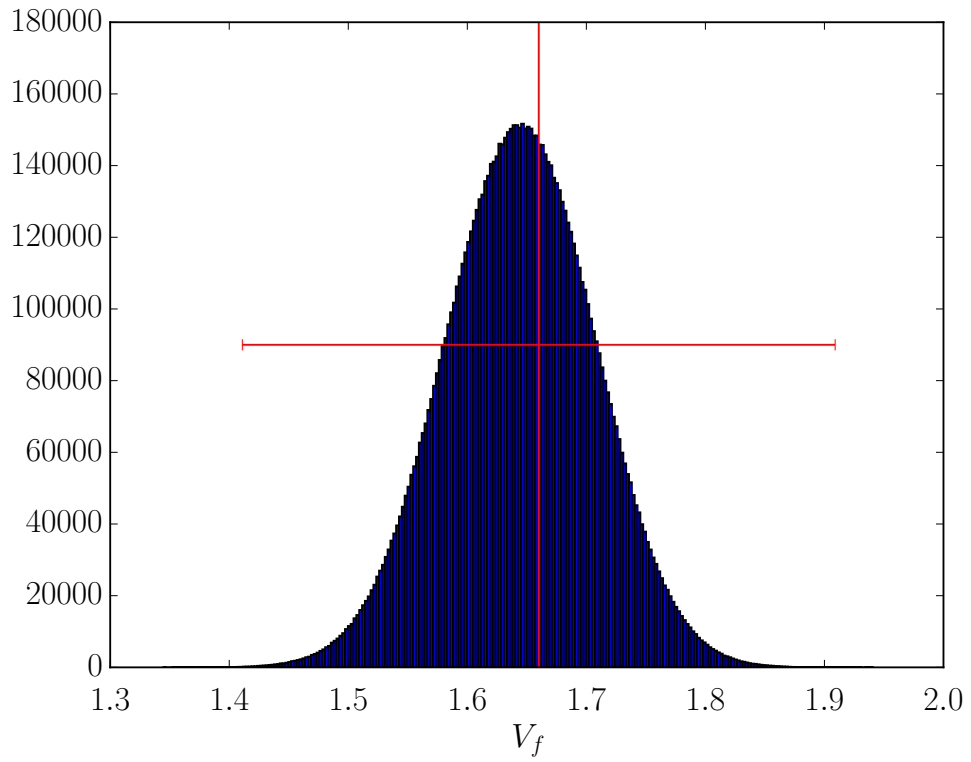
(a) Flame speed for 20 % ozone



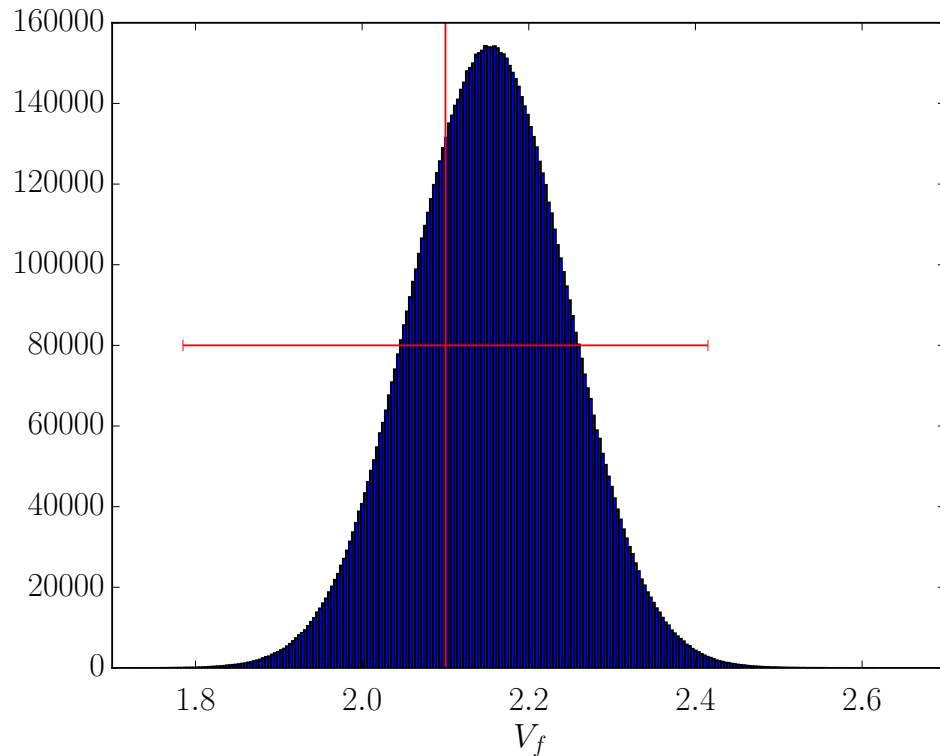
(b) Flame speed for 28 % ozone



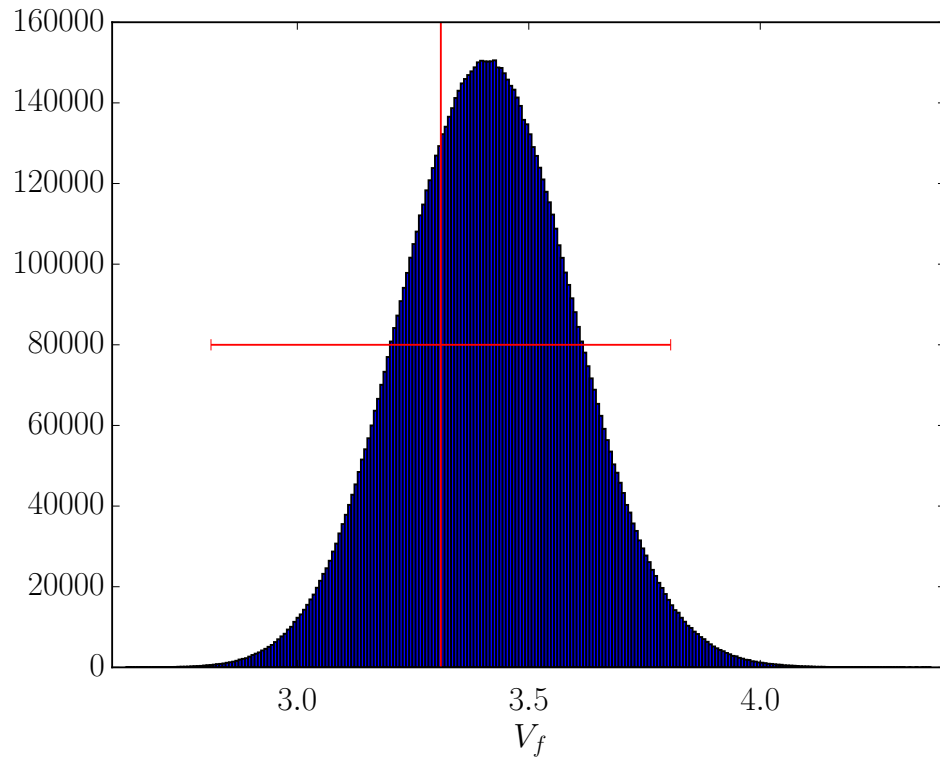
(c) Flame speed for 40 % ozone



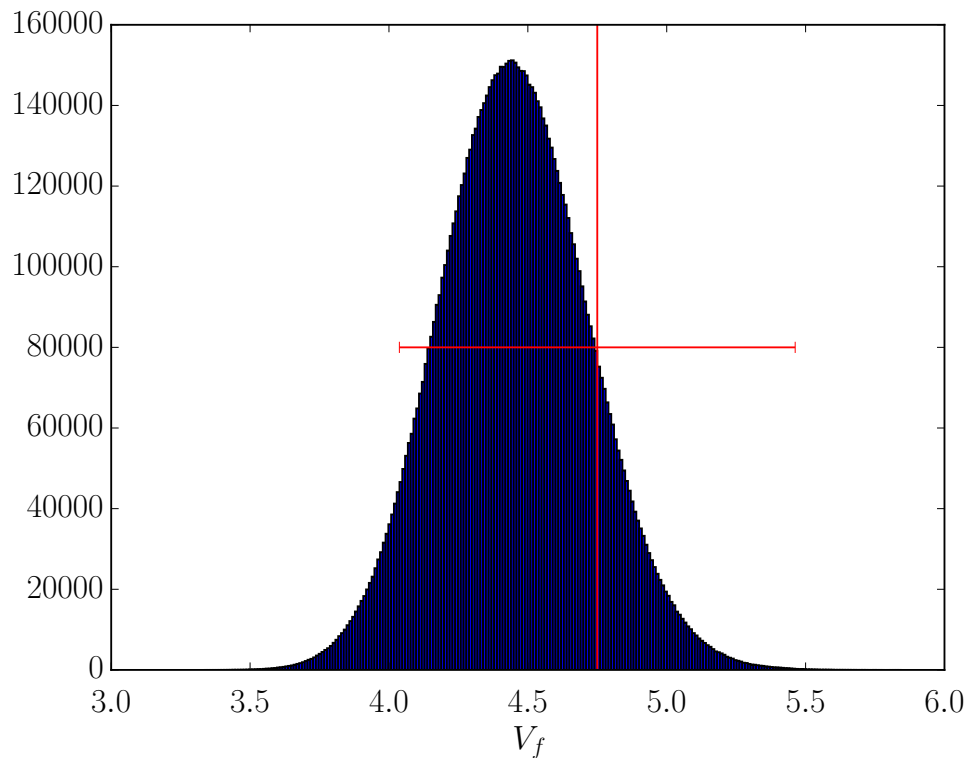
(d) Flame speed for 46 % ozone



(e) Flame speed for 53 % ozone



(f) Flame speed for 75 % ozone



(g) Flame speed for 100 % ozone

Figure 5.-17: Flamespeed Data fit

Chapter 6

Conclusion

Chapter 7

Appendix

7.1 Literature Review

It is shown by Muller [2] that a multiple-time scale, single-space scale asymptotic analysis of the compressible Navier-Stokes equations reveals that the zeroth-order global thermodynamic pressure, the divergence of velocity; and the material change of density are affected by heat-release rate and heat conduction at low-Mach-numbers.

His result show that the acoustic time change of the heat-release rate as the dominant source of sound in low-Mach-number flow. The asymptotic expansion of all flow variables show that the viscous and buoyancy forces enter the computation of the second-order incompressible pressure in low-Mach-number flow in a similar way as they enter the pressure computation in incompressible flow, except that the velocity-divergence constraint is non zero. He averaged flow equation over an acoustic wave period, the averaged velocity tensor described the net acoustic effect on the averaged flow field. Once acoustics were removed from the equations altogether it lead to the low-Mach-number equations.

The incompressibility assumption makes the problem simpler than if a full compressible flow is considered. Codine proposed that for ideal fluids, with isentropic condition, solutions of the incompressible Navier Stokes equations can be found as the limit of solutions of the compressible ones as the Mach number tends to zero under certain assumptions on the initial data.

In this paper, they showed that small Mach number limit gives rise to a separation of the pressure into a constant-in-space thermodynamic pressure and a mechanical pressure that has to be used in the momentum equation. This leads to a removal of the acoustic modes and the flow behaves as incompressible, in the sense that the mechanical pressure is determined by the mass conservation equation and not by the state equation. However, large variations of density due to temperature variations are allowed. They showed that when the Mach number is small the hyperbolic wave equation for the pressure becomes an elliptic equation for the first order pressure $p(2)$, thus showing the implicit (incompressible or mechanical) character of this pressure component.

7.2 Mathematical Model

7.2.1 Governing Equations

The flow of a compressible fluid is described in terms of the velocity (u^*), pressure (p^*), density (ρ^*), and temperature(T^*) fields. These fields are solutions of the compressible Navier Stokes equations that describe the dynamics of the system and that are statements of conservation of mass, momentum and energy and a state equation relating the thermodynamic variables.

The system of equation that needs to be solved reads

$$\frac{D\rho^*}{Dt^*} = -\rho^* \nabla \cdot u^* \quad (7.1)$$

$$\rho^* \frac{Du^*}{Dt} = -\nabla p^* + \nabla \cdot \tau^* + \rho^* g^* \quad (7.2)$$

$$\rho^* C_p^* \frac{DT^*}{Dt^*} = \tau^* \nabla \cdot u^* - \nabla \cdot q^* + \beta^* T^* \frac{Dp^*}{Dt^*} \quad (7.3)$$

$$\frac{D\rho^*}{Dt^*} = -\beta^* T^* \frac{D\rho^*}{Dt^*} + \alpha^* \rho^* \frac{Dp^*}{Dt^*} \quad (7.4)$$

Where u^* is the velocity vector, ρ^* is the density, β^* is the thermal expansion coefficient, p^* is the pressure, τ^* is the viscous stress term, g^* is the gravitational vector, C_p^* is the specific heat, T^* is the temperature, q^* is the heat flux vector.

for Newtonian fluid,

$$\tau^* = \mu^* (\nabla u^* + (\nabla u^*)^T) - \frac{2}{3} \mu^* \nabla \cdot u^* I$$

By fourier law's,

$$q^* = k^* \nabla T^*$$

μ^* is the dynamic viscosity. k^* is the thermal conductivity.

The following are the quantities in equation of state, $\beta^* = -\frac{1}{\rho^*} \frac{\partial \rho^*}{\partial T^*}$ and $\alpha^* = \frac{1}{\rho^*} \frac{\partial \rho^*}{\partial p^*}$.

7.2.2 Low mach number asymptotic analysis

The work below uses low mach number symptotic analysis developed by Muller[2]. We nondimensionalize the Equations by using reference quantities denoted by the subscript ∞ , e.g. farfield or stagnation conditions, and a typical length scale L^* of the considered flow. The thermodynamic reference quantities are assumed to be related by the equation of state for a perfect gas. We have used perfect gas law because we are dealing with gases in combustion environment. We define the nondimensional quantities by:

$$\rho = \frac{\rho^*}{\rho_\infty}, p = \frac{p^*}{p_\infty}, u = \frac{u^*}{u_\infty}, T = \frac{T^*}{T_\infty}, \mu = \frac{\mu^*}{\mu_\infty}, k = \frac{k^*}{k_\infty}, x = \frac{x^*}{L^*}, t = \frac{t^*}{L^*/u_\infty^*}, \beta^* = \frac{\beta}{\beta_\infty},$$

$$C_p^* = \frac{C_p}{C_{p_\infty}^*}.$$

Using the relations above; we may write the nondimensional Navier-Stokes equations and other equations of interest as follows:

$$\frac{D\rho}{Dt} = -\rho \nabla \cdot u \quad (7.5)$$

$$\rho \frac{Du}{Dt} = -\frac{1}{M^2} \nabla p + \frac{1}{Re} \nabla \cdot \tau + \frac{1}{Fr^2} \rho g \quad (7.6)$$

$$\rho C_p \frac{DT}{Dt} = \frac{M^2}{Re\lambda} \tau \nabla \cdot u - \frac{1}{RePr} \nabla \cdot (k \nabla T) + \frac{\beta T}{\lambda} \frac{Dp}{Dt} \quad (7.7)$$

$$\frac{D\rho}{Dt} = -\beta T \frac{D\rho}{Dt} + \alpha \rho \frac{Dp}{Dt} \quad (7.8)$$

Where the following nondimensional quantities are

$$M = \frac{u_\infty}{a_\infty}$$

$$Re = \frac{u_\infty \rho_\infty L}{\mu_\infty}$$

$$Pr = \frac{C_{p\infty} \mu_\infty L}{k_\infty}$$

$$Fr = \sqrt{\frac{u_\infty^2}{g_\infty L}}$$

a_∞ is the reference speed of sound, M is the mach number, Re is the reynolds number, Pr is the prandtl number, Fr is the froude number and λ is defined as $\frac{C_{p\infty} T_\infty}{a_\infty^2}$.

From ideal gas law,

$$\beta^* = -\frac{1}{\rho^*} \frac{\partial \rho^*}{\partial T^*}$$

We non dimensional this term as follows

$$\beta^* = -\frac{1}{\rho_\infty \rho} \frac{\rho_\infty}{T_\infty} \frac{\partial \rho}{\partial T}$$

$$\beta^* = \frac{1}{T_\infty} \beta$$

Where $\beta_\infty = \frac{1}{T_\infty}$.

From ideal gas law,

$$a^{*2} = \frac{\partial p^*}{\partial \rho^*}$$

We non dimensional this term as follows

$$a^{*2} = \frac{p_\infty}{\rho_\infty} \frac{\partial p}{\partial \rho}$$

$$a^{*2} = \frac{p_\infty}{\rho_\infty} a^2$$

Where $a_\infty = \sqrt{\frac{p_\infty}{\rho_\infty}}$.

7.2.3 Asymptotic analysis

We do asymptotic analysis with respect to Mach number. We use the following equation in terms of Mach number

$$\xi(x, t, M) = \xi^0(x, t) + M\xi^1(x, t) + M^2\xi^2(x, t) + O(M^3)$$

Where ξ can be u, p, ρ . We use non dimensional form of navier stokes equation do the asymptotic equation. We show the example of asymptotic analysis for mass conservation.

$$\frac{D}{Dt}(\rho^0 + M\rho^1 + M^2\rho^2 + O(M^3)) + (\rho^0 + M\rho^1 + M^2\rho^2 + O(M^3)) \nabla \cdot (u^0 + Mu^1 + M^2u^2 + O(M^3)) = 0$$

Collecting equal order terms together we get,

$$\left(\frac{D\rho^0}{Dt} + \rho^0 \nabla \cdot u^0 \right) + M \left(\frac{\partial \rho^1}{\partial t} + \rho^1 \nabla \cdot u^0 + \rho^0 \nabla \cdot u^1 \right) + O(M^2) = 0$$

Therefore zeroth order terms can be written.

$$\frac{D\rho^0}{Dt} + \rho^0 \nabla \cdot u^0 = 0 \quad (7.9)$$

The asymptotic relation for momentum are obtained are as follows. The zero, first and second order momentum equation are written as follows respectively

$$M^{-2} \nabla p^{(0)} = 0 \quad (7.10)$$

$$M^{-1} \nabla p^{(1)} = 0 \quad (7.11)$$

$$\rho^0 \frac{Du^0}{Dt} = -\nabla p^2 + \nabla \cdot \tau^0 + \rho^0 g \quad (7.12)$$

The asymptotic relation for momentum are obtained are as follows.

$$\rho^0 C_p \frac{DT^0}{Dt} = -\frac{1}{RePr} \nabla \cdot (k^0 \nabla T^0) + \frac{\beta^0 T^0}{\lambda} \frac{dp^0}{dt} \quad (7.13)$$

We have seen from momentum asymptotic analysis that $p^0 = p^0(t)$ and therefore

$$\frac{Dp^0}{Dt} = \frac{dp^0}{dt}$$

The nondimensional equation of state is same as that of the dimensional form. Now same asymptotic expansion of the state equation is done in order to get zeroth order state equation which is given below.

$$\frac{D\rho^0}{Dt} = -\beta^0 T^0 \frac{D\rho^0}{Dt} + \alpha^0 \rho^0 \frac{Dp^0}{Dt} \quad (7.14)$$

From mass conservation equation and since $p^0 = p^0(t)$, we get the following equation

$$-\nabla \cdot u^0 = -\beta^0 \frac{DT^0}{Dt} + \alpha^0 \frac{dp^0}{dt} \quad (7.15)$$

From energy conservation equation

$$-\rho^0 C_p^0 \nabla \cdot u^0 = \frac{1}{RePr} \nabla \cdot q^0 + \left(\frac{C_p^0 \lambda - 1}{\lambda} \right) \frac{dp^0}{dt} \quad (7.16)$$

The final equation obtained by applying various thermodynamic properties are following

$$-\nabla \cdot u = \frac{1}{p^0} \frac{dp^0}{dt} - \frac{1}{T} \frac{DT}{Dt} \quad (7.17)$$

$$\rho \frac{Du}{Dt} = -\frac{1}{M^2} \nabla p + \frac{1}{Re} \nabla \cdot \tau + \frac{1}{Fr^2} \rho g \quad (7.18)$$

$$\rho C_p \frac{DT}{Dt} = -\frac{1}{RePr} \nabla \cdot (k \nabla T) + \frac{1}{\gamma - 1} \frac{dp^0}{dt} \quad (7.19)$$

$$(7.20)$$

Bibliography

- [1] J.M. Heimerl and T.P. Coffee. The detailed modelling of premixed, laminar steady state flames. i. ozone. *Combustion and Flame*, 39:301 – 315, 1980.
- [2] Bernhard Müller. Low mach number asymptotics of the navier stokes equations. *Journal Of Engineering Mathematics*, 34:97 – 109, 1998.
- [3] A.G. Streng and A.V Grosse. The ozone to oxygen flame. *Symposium, International, on Combustion*, 6:264 – 272, 1957.

Bibliography

- [1] J.M. Heimerl and T.P. Coffee. The detailed modelling of premixed, laminar steady state flames. i. ozone. *Combustion and Flame*, 39:301 – 315, 1980.
- [2] Bernhard Müller. Low mach number asymptotics of the navier stokes equations. *Journal Of Engineering Mathematics*, 34:97 – 109, 1998.
- [3] A.G. Streng and A.V Grosse. The ozone to oxygen flame. *Symposium, International, on Combustion*, 6:264 – 272, 1957.